UNIVERSITY*of*
TASMANIA

CLASS I METHANOL MASERS TOWARD EXTERNAL GALAXIES

by

Tiege P. McCarthy, B.Sc. Hons

Submitted in fulfilment of the requirements
for the Degree of Doctor of Philosophy

School of Natural Sciences
University of Tasmania
January, 2020

I declare that this thesis contains no material which has been accepted for a degree or diploma by the University or any other institution, except by way of background information and duly acknowledged in the thesis, and that, to the best of my knowledge and belief, this thesis contains no material previously published or written by another person, except where due acknowledgement is made in the text of the thesis.

Signed: _____
Tiege P. McCarthy

Date: 08/01/2020

Signed: _____
Tiege P. McCarthy

Date: 08/01/2020

ABSTRACT

The role extragalactic class I methanol masers play in their host galaxies is currently not well understood. With only a few known examples of these masers to date, investigating their nature is very difficult. However, determining the physical conditions and environments responsible for these masers will provide a useful tool for the study of external galaxies. In this thesis we present over a hundred hours of Australia Telescope Compact Array (ATCA) observations aimed at expanding our available sample size, increasing our understanding of the regions in which these masers form, and making comparison with class I methanol emission towards Galactic regions.

We present the first detection of 36.2-GHz class I methanol maser emission toward NGC 4945, which is the second confirmed detection of this masing transition and the brightest class I maser region ever detected. This emission is offset from the nucleus of the galaxy and is likely associated with the interface region between the bar and south-eastern spiral arm. Additionally, we report the first detection of the 84.5-GHz class I maser line toward NGC 253, making NGC 253 the only external galaxy displaying 3 separate masing transitions of methanol. Upper limits on the 36.2- class I and 37.7-GHz class II maser lines are also reported for 12 other galaxies that were searched as part of this project.

Alongside observations of the class I methanol lines, we also observed various thermal and masing molecular lines towards these sources. This includes the imaging of 7-mm HC_3N, CS and SiO lines towards NGC 4945, which had not previously been observed at high resolution before, along with some 3-mm lines, such as HNCO, towards NGC 253.

Long term monitoring of the 36.2-GHz transition from NGC 4945 and NGC 253 was also performed. This monitoring produced detections of new maser regions in both NGC 4945 and NGC 253 and provided the first evidence for variability from these extragalactic class I masers, with the luminosity of the new maser region in NGC 4945 increasing by approximately 300 percent compared to past observations. We determine this is likely the result of excitation changes in the maser environments, however, further monitoring is required to accurately quantify this variability.

We also present interferometric imaging of the 95.2-GHz class I methanol masers towards 32 6.7-GHz class II maser sources along with detailed comparison between the class I (36.2-, 44.1- and 95.2-GHz) and class II (6.7- and 12.2-GHz) lines in these high-mass star formation regions. Flux-density ratios for matched (spatially associated) 44.1- and 95.2-GHz class I masers shows that the 3:1 ratio previously reported in the literature holds true even at parsec scales. Investigation of our statistically complete sample indicates that 95.2-GHz class I methanol masers do not preferentially favour more evolved sources. Our observations reinforce that when using class I methanol masers to investigate shock fronts and star-formation region dynamics, observation of multiple class I transitions is necessary in order to form a complete picture.

ACKNOWLEDGEMENTS

The three and a half years of my candidature has produced many people I would like to thank. First I would like to thank my partner Sophia for supporting me, dealing with my stress and loving me through the past 8 years of my university career. Without you I would not likely be doing what I am today, and for that, I am incredibly grateful.

Next I would like to thank my primary supervisor Simon Ellingsen. Thank you for still giving me another shot despite the disaster that was my honours project. Thank you for being available all the time, for spur of the moment questioning or requests for help. Without your constant support and expertise there is no way I would have finished, let alone enjoyed my candidature as much as I did.

I would also like to thank Maxim Voronkov, my co-supervisor, for despite being incredibly busy, always taking the time to respond to my emails, review/comment on my papers, and explain maser theory in great detail. Also, thank you for helping show me the ropes of ATCA observing as a fresh Ph.D student in Narrabri.

Also, thank you to Shari Breen, who ever since our trip to Narrabri in 2017 has become my unofficial co-supervisor. Thank you for noob checking my CABB schedule files in the early days, teaching me how to compact array, and allowing me to be a part of the StarFISH survey team.

Thank you to Kelly and Karen for taking care of everything on the administration side of things. You made all travel organisation as stress free as possible and always found extra ways to throw more money at us Ph.D students.

Thank you to my office mate Andrew for putting up with my occasional ranting and engaging in regular pointless, yet enjoyable discussions. Thank you to all members

of the regular coffee aquisition crew over the past few years (Andrew, Eloise, Gabor, Jonny, Katie, Lucas, Patrick and others), for the countless hours of enjoyable procrastination both at and outside of university.

Finally, thank you to my family, for supporting me no matter what path I decided to take in life.

STATEMENT OF CO-AUTHORSHIP

The following people and institutions contributed to the publication of work undertaken as part of this thesis:

Candidate – Tiege McCarthy, School of Natural Sciences
Author 1 – Simon Ellingsen, University of Tasmania, Australia
Author 2 – Xi Chen, GuangZhou University, China
Author 3 – Shari Breen, University of Sydney, Australia
Author 4 – Maxim Voronkov, CSIRO Astronomy & Space Science, Australia
Author 5 – Hai-hua Qiao, Shanghai Astronomical Observatory, China
Author 6 – Giuseppe Cimò, Joint Institute for VLBI ERIC, the Netherlands
Author 7 – Christian Henkel, Max-Planck-Institut für Radioastronomie, Germany

Contribution of work by co-authors for each paper:

Paper 1: Located in Chapter 2
This paper was originally published in *Monthly Notices of the Royal Astronomical Society* as *'The relationship between Class I and Class II methanol masers at high angular resolution'* (DOI: 10.1093/mnras/sty694).

Candidate was the primary author and contributed 75% to the planning execution and preparation of the research project and subsequent paper.
Author 4 created field image figures for the paper.
Author 1 and 4 contributed to the interpretation of results from the data reduction, in addition to critically revising the paper prior to submission.
Author 1, 4 and 6 were involved in taking the ATCA observations for the project.

Paper 2: Located in Chapter 3
This paper is originally published in *The Astrophysical Journal* as *'Detection of 36.2-GHz Class I Methanol Maser Emission toward NGC 4945'* (DOI: 10.3847/1538-4357/aa872c).

Candidate was the primary author and contributed 85% to the planning execution and preparation of the research project and subsequent paper.
Author 1, 2, 3 and 4 all contributed to the interpretation of results from the data

reduction, in addition to critically revising the paper prior to submission.
Author 5 was involved in taking observations for the project.

Paper 3: Located in Chapter 4
This paper was originally published in *Monthly Notices of the Royal Astronomical Society* as *'Investigations of the Class I methanol masers in NGC 4945'* (DOI: 10.1093/mnras/sty2192).

Candidate was the primary author and contributed 80% to the planning execution and preparation of the research project and subsequent paper.
Author 4 created field image figures for the paper.
Author 1, 3, 4 and 7 contributed to the interpretation of results from the data reduction, and along with Author 2, critically revised the paper prior to submission.
Author 7 contributed some analysis of thermal CS emission pertinent to discussion Section 4.2 of the paper.
Author 3 and 4 assisted with both planning and setting up ATCA observations.

Paper 4: Located in Chapter 5
This paper is originally published in *The Astrophysical Journal* as *'Detection of 84 GHz Class I Methanol Maser Emission toward NGC 253'* (DOI: 10.3847/2041-8213/aae82c).

Candidate was the primary author and contributed 85% to the planning execution and preparation of the research project and subsequent paper.
Author 1, 3 and 4 contributed to the interpretation of results from the data reduction, and along with Author 2, critically revised the paper prior to submission.
Author 3 and 4 assisted with planning ATCA observations.

Paper 5: Located in Chapter 6
This paper was originally published in *Monthly Notices of the Royal Astronomical Society* as *'Variability in extragalactic class I methanol masers: New maser components toward NGC 4945 and NGC 253'* (DOI: 10.1093/mnras/stz3098).

Candidate was the primary author and contributed 90% to the planning execution and preparation of the research project and subsequent paper.
Author 1, 3 and 4 contributed to the interpretation of results from the data reduction, and along with Author 2, critically revised the paper prior to submission.
Author 2 and 6 assisted with taking some of the observations presented in the paper (observations from the C2879 ATCA project).

We, the undersigned, endorse the above stated contribution of work undertaken for each of the published (or submitted) peer-reviewed manuscripts contributing to this thesis:

Signed: _____ Date: 08/01/2020

Tiege McCarthy
Candidate
School of Natural Sciences
University of Tasmania

Signed: _____ Date: 19/12/19

Professor Simon Ellingsen
Primary Supervisor
School of Natural Sciences
University of Tasmania

Signed: _____ Date: 08/01/2020

Professor Brian Yates
Executive Dean
College of Science and Engineering
University of Tasmania

TABLE OF CONTENTS

TABLE OF CONTENTS **i**

LIST OF TABLES **iv**

LIST OF FIGURES **v**

1 ASTRONOMICAL MASERS, METHANOL, AND STARBURST GALAXIES **1**

1.1 Astronomical Masers 1

1.1.1 Overview of interstellar masing species 3

1.1.2 Megamasers and extragalactic masers 5

1.2 Methanol Masers 8

1.2.1 Class I and class II methanol masers 9

1.2.2 Methanol masers within the Milky Way 10

1.2.3 Methanol masers towards other galaxies 13

1.2.4 Comparison of methanol maser transitions from the same source 16

1.2.5 Probing the fundamental constants of physics 21

1.3 The Extragalactic Targets 22

1.3.1 NGC 4945 22

1.3.2 NGC 253 25

1.4 This project 28

2 The relationship between Class I and Class II methanol masers at high angular resolution **30**

2.1 Introduction 30

2.2 Author Contributions 31

3 Detection of 36.2-GHz Class I methanol maser emission toward NGC 4945 50

3.1 Introduction 50

3.2 Author Contributions 51

4 Investigations of the class I methanol masers in NGC 4945 57

4.1 Introduction 57

4.2 Author Contribution 58

5 Detection of 84-GHz class I methanol maser emission toward NGC 253 70

5.1 Introduction 70

5.2 Author Contribution 71

6 Variability in extragalactic class I methanol masers 79

6.1 Introduction 79

6.2 Author Contribution 80

7 Discussion, conclusions and future work 96

7.1 The methanol maser emission of NGC 4945 96

7.2 Three class I transitions toward NGC 253 98

7.3 Extragalactic methanol masers 100

7.3.1 NGC 253 101

7.3.2 IC 342 101

7.3.3 NGC 6946 102

7.3.4 Maffei 2 103

7.3.5 NGC 1068 103

7.3.6 General discussion on extragalactic class I masers 103

7.4 Future work 105

7.4.1 Searching for new extragalactic 36.2-GHz masers 105

7.4.2 Class I transition follow-up on known maser hosts 108

7.4.3 Radiative transfer modelling 108

7.5 Concluding remarks 111

A 95-GHz Maser Field Images and Spectra **113**

A.1 95-GHz maser field images 114

A.2 95-GHz maser spectra 130

BIBLIOGRAPHY **141**

LIST OF TABLES

7.1 Potential targets for a 36.2-GHz search with the JVLA. 106
7.2 Potential targets for a 36.2-GHz search with the ATCA. 107

LIST OF FIGURES

1.1 Methanol rotational energy level diagram including known class I methanol transitions. 12

1.2 Original detection of 36.2-GHz methanol maser emission towards NGC 253. 14

1.3 Maser optical depth contour diagram as a function of methanol column density and H_2 density at two different temperatures. 17

1.4 Optical depth of the four class I methanol lines vs. temperature across three different H_2 densities. 20

1.5 Optical depth as a function of H_2 density across three different temperatures. 20

1.6 Optical image of NGC 4945 taken using the 2.2-m MPG/ESO telescope in La Silla. 23

1.7 Optical image of NGC 253 as seen by the Wide Field Imager on the 2.2-m MPG/ESO telescope in La Silla. 27

Chapter 1

Astronomical Masers, Methanol and Starburst Galaxies

This chapter will begin with a general overview of astronomical masers, both within our Galaxy and towards extragalactic sources. Following this will be a review of the literature concerning specifically methanol masers (with an emphasis on the class I transitions) and of the extragalactic sources directly relevant to this work.

At the start of my candidature, the field of extragalactic class I methanol masers was relatively new. Over the past few years there has been an increase in research in this area, and therefore, the majority of our current understanding about these extragalactic masers has occurred since the beginning of my candidature. Unfortunately, it is not possible to include this recent research in the literature review without the context of my work. For this literature review, the section relating to extragalactic methanol masers will be written as of the beginning of my PhD (July 4, 2016). A more in-depth review of the field as it is at the end of my candidature will be included as part of the final conclusions chapter.

1.1 Astronomical Masers

Astronomical masers are characterised as bright, radio-frequency, spectral lines found in numerous different astrophysical environments. In order for masing emission to oc-

cur, molecules from a particular species must be experiencing a population inversion. This occurs when more molecules from the population are in higher energy states than lower. This inversion can only be maintained between certain transitions where selection rules provide sufficient lifetimes of the higher energy state. For a population to become inverted, some external energy source is required to 'pump' the majority of the population into higher-energy excited states. This energy source is referred to as the pumping mechanism, and is what allows maser emission to be a useful signpost for other interesting astrophysical phenomena. Once the population is 'inverted', an incident photon of an appropriate wavelength (based on the energy levels of the excited molecules), can stimulate the release of an identical photon, dropping the excited molecule down an energy level. This essentially causes the incident photon to be amplified, and each of these resultant photons can trigger subsequent stimulation events causing large scale amplification of some background source. While these astronomical masers can be extremely luminous, the maser gains for these astronomical sources are much lower than those observed from laboratory masers. Injection of energy from the pumping mechanism ensures a balance of energy loss from amplification, and allows the masing regions to persist for extended periods of time.

The first molecular species to be observed as astronomical masers were detections of interstellar OH and H_2O in the 1960's (Weaver et al., 1965; Cheung et al., 1969). Since then, masing transitions have been observed from a large number of molecular species and research into the field has increased significantly. The intensity of the emission from these lines, along with their association with other astrophysical phenomena, allows masers to be utilised as a powerful tool for studying the universe. Various annual reviews (e.g. Menten, 1991a; Elitzur, 1982, 1992) dedicated to astronomical masers have covered the theory of this phenomenon in great detail. This overview will focus on how astronomical masers from various molecular species have been used in order to further our understanding of the Milky Way, and other galaxies.

1.1.1 Overview of interstellar masing species

Maser emission has been observed towards many different molecular species. The most common of which are water (H_2O), methanol (CH_3OH), hydroxyl (OH) and silicon monoxide (SiO) (Elitzur, 1992). As methanol is the main masing species this project covers, a full section will be dedicated to overviewing methanol masers. The other three common masing species will be briefly covered here.

OH Masers

The strongest and most commonly detected OH line towards Galactic star-forming regions is at 1665-MHz, which is usually observed coming from the same location as the 1667-MHz line, though over a factor of 3 times more luminous (Caswell & Haynes, 1987; Caswell, 1998). These main line OH masers are widely accepted as being pumped via infrared emission from warm dust (Cragg et al., 2002), and are generally observed towards star-formation regions, where they are believed to be associated with the shocked gas around expanding ultra-compact HII regions (UCHII Elitzur & de Jong, 1978; Baart & Cohen, 1985; Fish & Reid, 2006). Similarly to water and class II methanol masers (discussed in later sections), OH masers have been detected towards high-mass protostellar objects (Edris et al., 2007), where they are usually associated with the later evolutionary stages (Forster & Caswell, 1989).

Unlike their main line counterparts, the less common 1612- and 1720-MHz OH maser satellite line transitions are rarely associated with star-formation regions. The former tends to be most commonly observed toward late-type stars and the later supernova remnants (Lockett et al., 1999; Gray et al., 2005). The mechanisms responsible for pumping masers from these satellite lines are still being investigated, however, current understanding is that the 1612-MHz line is radiatively pumped (Gray et al., 2005), while the 1720-MHz line is collisionally pumped via C-shocks (Brogan et al., 2013).

Variability (on the order of years) has been detected from Galactic OH masers, though

others have also been observed to remain stable over periods of multiple decades (Caswell, 1998). Evidence of OH masers in outflows has been reported (Argon et al., 2002), however, more typically OH masers are observed without extreme velocity components (Caswell, 1998). Galactic OH masers also tend to show high levels of circular polarisation, which can be a useful tool for investigating the magnetic field of the regions where they are located (Gray, 2012).

H_2O Masers

First detected by Cheung et al. (1969), water masers are observed from many different transitions across the radio and microwave spectrum, however, the 22.2-GHz line is by far the most populous and brightest. This line is in fact the brightest radio-frequency spectral line. Collisional pumping of the rotational energy levels is the accepted mechanism for the excitation of astronomical water masers (Deguchi, 1977). This pumping can occur in stellar winds associated with low- and high-mass star-formation regions, or molecular outflows (Torrelles et al., 2002; Furuya, 2003). The energetic environment of these masers (high temperatures driven by high velocity shocks; Hollenbach et al., 2013) is prone to variability, with maser components disappearing and appearing on relatively short time-scales (Felli et al., 2007).

SiO Masers

The first detection of a SiO maser was made by Snyder & Buhl (1974), where they reported the presence of an unidentified molecular species masing at 86 GHz toward Orion, tentatively identifying it as the SiO $J = 2 \rightarrow 1$ transition for the first vibrational state ($\nu = 1$). Maser emission has now been detected from a variety of different SiO transitions in five ($\nu = 0, 1, 2, 3$ and 4) different vibrational states (e.g. Buhl et al., 1974; Scalise & Lepine, 1978; Schwartz et al., 1982; Boboltz & Claussen, 2004), however, the strongest masers tend to occur at $\nu = 1$ or 2 (Gray, 2012).

SiO masers are predominantly associated with evolved stars such as asymptotic giant

branch (AGB) stars and are rarely detected towards star-formation regions. SiO masers form in the inner zones of long-period variable (LPV) stars, where they display variability driven by the intrinsic variability of their host stars (Gray, 2012).

1.1.2 Megamasers and extragalactic masers

A handful of the molecular species observed to be masing within our galaxy have also been detected towards external Galaxies. Some of these extragalactic masers may be considered 'megamasers' based on their luminosity, $\sim 10^6$ times brighter than typical Galactic maser of the same species, or in some cases the phenomena they are associated with. Because of the sensitivity limitations of current facilities, and the distances involved, detected extragalactic masers are usually much brighter than typical Galactic masers. However, extremely luminous examples (kilomasers) of Galactic style water and methanol masers have been detected toward many galaxies (Sinclair et al., 1992; Ellingsen et al., 1994, 2010; Beasley et al., 1996; Henkel et al., 2004; Braatz & Gugliucci, 2008; Gorski et al., 2019).

Extragalactic masers have been detected from the H_2O, OH, CH_3OH, SiO, H_2CO, CH and HC_3N molecular species (Churchwell et al., 1977; Gardner & Whiteoak, 1975; Sinclair et al., 1992; Ellingsen et al., 2017b). We will focus the discussion on extragalactic H_2O and OH masers here, as methanol will be extensively covered in an upcoming section. For a more comprehensive review of extragalactic masers, see the review of Lo (2005).

Extragalactic water masers

The first detection of extragalactic methanol emission was reported by Churchwell et al. (1977) towards a star-formation region in M 33. The properties of this maser emission, along with further detections within M 33 and IC 342 (Huchtmeier et al., 1978) are similar to those observed water masers associated with Galactic star formation regions. This is due to the fact that giant HII regions were the original targets

for searching for these water masers. Shortly after these first detections, strong water maser emission was detected towards the nucleus of NGC 4945 (Dos Santos & Lepine, 1979). In the following years more examples of strong water masers were detected towards the nuclei of nearby active galaxies: Circinus, NGC 4258, NGC 1068, NGC 6946 and M 82 (Gardner & Whiteoak, 1982; Claussen et al., 1984; Claussen & Lo, 1986). Claussen & Lo (1986) hypothesised that these water masers are forming in the dense circumnuclear gas clouds, excited by mass outflow from the active galactic nuclei (AGN). The real interest in extragalactic water masers came with the discovery of high velocity red and blueshifted water maser emission (**?**), and subsequent VLBI observations by Greenhill et al. (1995b,a) and Miyoshi et al. (1995) which showed the masers lie in a circumnuclear disk that exhibits Keplarian rotation.

The observation of H_2O megamaser emission from a circumnuclear keplarian disk in NGC 4258 provided some of the most convincing evidence for the existence of supermassive black holes at the centre of galaxies. VLBI observations of the spatial distribution of the maser emission provided constraints on the size of these circumnuclear disks, which allowed the enclosed masses to be calculated. The implied densities from these disk sizes, along with the enclosed masses, can only be explained by the presence of a supermassive black hole (Miyoshi et al., 1995). Extragalactic water masers have also been observed associated with nuclear jets in AGN galaxies. The water maser of NGC 1052 is the prototypical example of this kind of maser, with water maser spots situated along the nuclear jet, and a clear velocity gradient (Claussen et al., 1998).

Extragalactic hydroxyl masers

Emission from extragalactic OH was originally detected toward NGC 253 and M 82, these two sources showed narrow OH maser components with luminosities an order of magnitude greater than Galactic OH masers (Gardner & Whiteoak, 1975; Nguyen-Q-Rieu et al., 1976). A subsequent detection of OH emission toward Arp 220 was

reported by Baan et al. (1982). Compared to the NGC 253 and M 82 detections, this emission was much broader (400 km s^{-1}compared to 10 km s^{-1}) and $\sim 10^7$ times more luminous (Baan et al., 1982). Despite how broad the emission from Arp 220 is, high-resolution observations by Norris (1985) determined a brightness temperature far too high ($> 10^6$K) for the emission to be the result of a thermal process. One thing all three of these original detections of OH masers have in common is that the 1667-MHz line is brighter than the 1665-MHz, and the emission is unpolarised, Which is in stark contrast to typical Galactic OH masers (Gardner & Whiteoak, 1975; Nguyen-Q-Rieu et al., 1976; Baan et al., 1982). This relationship between the 1667- and 1665-MHz lines has remained true as more examples of extragalactic OH masers have been detected (e.g. Parra et al., 2005; Lo, 2005). The vast majority of OH megamasers are detected toward the starburst regions of luminous infrared galaxies (LIRGs), which is expected due to OH pumping relying on far infrared emission (Cragg et al., 2002). A relation of $L_{OH} \propto L_{FIR}^{1.2}$ has been determined for these OH megamasers (Darling & Giovanelli, 2002), however detection rates towards LIRGs and ULIRGS are approximately 20 percent (Lo, 2005, and references therein)

Potential issues with nomenclature

The megamaser/kilomaser nomenclature can create some problems when discussing extragalactic maser emission. Considering extragalactic water masers for example, water megamaser emission has been observed to be associated with the circumnuclear disks of some AGN (Miyoshi et al., 1995). This is a distinct phenomena from typical Galactic water maser emission, which is generally associated with star-formation regions (Torrelles et al., 2002). However, extragalactic water kilomasers have also been observed towards some starburst galaxies, associated with regions of high star-formation (Churchwell et al., 1977; Henkel et al., 2004; Braatz & Gugliucci, 2008). Essentially these kilomasers are simply very bright examples of Galactic-style water masers. This means people associate extragalactic kilomasers with one type of phenomena and megamasers with another. This becomes a problem as masers associated

with these different phenomena are not constrained to specific luminosity cutoffs. This can create confusion when reporting kilomasers that are associated with these larger scale phenomenon (where megamasers are typically observed). While this may not be much of an issue currently, as the majority of extragalactic maser detections are of the extremely luminous megamasers, however, as sensitivity of instruments increases a larger number of lower-luminosity extragalactic masers will be reported and discussed.

1.2 Methanol Masers

The methanol molecule is an asymetric top, which features hindered internal rotation about the C–O bond. These characteristics produce a large array of rotational energy levels, resulting in a plethora of observable transitions towards astrophysical methanol sources. Hydrogenation of CO on icy interstellar grains is the process by which methanol naturally forms within our galaxy (Watanabe & Kouchi, 2002). The theoretically proposed successive hydrogenation is as follows: $CO \rightarrow HCO \rightarrow H_2CO \rightarrow CH_3O \rightarrow CH_3OH$ (Tielens & Whittet, 1997). This has been experimentally confirmed by Watanabe & Kouchi (2002), who determined that this process produces methanol yields of the order of 10%, making it the most likely candidate for the production of methanol in astronomical molecular clouds. Typically, the methanol is released from these grains into the gas phase via shocks within star-formation regions or heating from protostars (Brown et al., 1988; van Dishoeck & Hogerheijde, 1999; Voronkov et al., 2010b).

Maser emission from interstellar methanol was first detected at 25 GHz towards the Orion-KL region by Barrett et al. (1971). Since then, a large number of methanol maser lines have been detected towards various astrophysical sources (e.g. Wilson et al., 1984, 1985; Morimoto et al., 1985; Batrla et al., 1987; Menten, 1991b; Breen et al., 2019), and this rich spectrum of transitions has proven to be a valuable tool for investigating star-formation towards Galactic sources.

1.2.1 Class I and class II methanol masers

The masing transitions of methanol are divided into two separate classes, I and II (Batrla et al., 1987; Menten, 1991b). These classes were originally proposed, based on the fact that the 25-GHz methanol line, and 12-GHz methanol (the first class I and class II lines respectively) transitions had never been found towards the same source (Batrla et al., 1987). Orion-KL was considered a prototypical class I methanol maser source, while class II methanol masers were detected towards compact HII regions, similar to OH masers, with W3(OH) suggested as their prototypical source (Batrla et al., 1987). This empirical difference in the methanol transitions is now known to be caused by the different pumping mechanisms responsible for the population inversion of the methanol molecules (Cragg et al., 1992), with masers from both classes having been detected towards many of the same star-formation sources (e.g. Slysh et al., 1994; Caswell et al., 2010, 2011; Green et al., 2010; Breen et al., 2015; Voronkov et al., 2014). The class II maser lines occur in regions where radiative processes dominate over collisional, whereas class I maser lines favour the reverse (Cragg et al., 1992; Sobolev et al., 1997; Cragg et al., 2005). Maser transitions occur between energy levels with different K quantum numbers, with all the energy level for a particular K quantum number sometimes referred to as a 'K ladder' (see Figure 1.1). Depending on what pumping mechanism (radiative or collisional) is present, different K ladders will become over (or under) populated, switching on either the class I (for collisional) or class II (for radiative) masers (Cragg et al., 1992). This means the two classes are competitive, and anytime masers from both classes are observed towards the same volume of gas, they are considered to be mutually exclusive (Voronkov et al., 2005, 2012). Despite their competitive excitation processes, both classes of methanol masers are frequently observed towards the same Galactic star-forming regions, with the differing pumping mechanisms result in masers from each class being associated with different environments within these regions. The class I masers are typically associated at the interface regions of molecular outflows (e.g Kurtz et al., 2004; Voronkov et al.,

2006; Cyganowski et al., 2012) or associated with shocks from cloud-cloud interactions or expanding HII regions (Cyganowski et al., 2009; Sjouwerman et al., 2010; Voronkov et al., 2010a, 2014). Therefore, class I masers are often observed as multiple discrete components, distributed over scales of up to 1 pc from the high-mass protostar (Kurtz et al., 2004; Voronkov et al., 2006, 2014). Class II masers on the other hand, are found tightly clustered around the location of the young, high-mass star (Caswell, 1997).

1.2.2 Methanol masers within the Milky Way

This difference in pumping mechanisms between the two classes of methanol masers makes them both interesting tools for investigating star-formation regions within the Milky Way. Class II methanol masers at 6.7 GHz are useful signposts for high-mass young stellar objects (YSOs) as they are exclusively associated with high-mass star-formation (HMSF; Breen et al., 2013). Methanol is released from dust grains through heating and mild shocks from the protostar (Brown et al., 1988; van Dishoeck & Hogerheijde, 1999). The radiative pumping required for these class II transitions is provided by the infrared emission from these YSOs, and as the HII region evolves, the class II maser emission rapidly wanes (Walsh et al., 1998; Breen et al., 2010). The mechanism behind this rapid reduction in the class II maser emission is not yet understood, however, it could be the result of destruction of the methanol molecule or major environmental changes (for further discussion see Breen et al., 2010; Ellingsen et al., 2011b). This means the class II transition trace a very specific evolutionary phase of these star-formation regions (Breen et al., 2010, 2011; Ellingsen et al., 2011b). This, combined with their brightness, making them readily detectable, and compactness, meaning they are an accurate locator of these high-mass YSOs, makes them a very useful tool for probing the conditions in these HMSF systems. The Methanol Multibeam (MMB) survey produced the most complete study of 6.7-GHz Class II masers in the southern hemisphere (Green et al., 2009, 2010, 2012; Caswell et al., 2010, 2011; Breen et al., 2015). This survey brought the total number of known Galactic 6.7-GHz class II masers to over 1200 (with 972 of those detected in the MMB survey).

Follow-up observations of the MMB sources have also been conducted at 12.2-GHz, detecting hundreds of 12.2-GHz class II masers towards these HMSF sources (Breen et al., 2010, 2011, 2012b).

In contrast to the class II masers, which have a well understood relationship with star-formation regions, the Galactic class I masers are not exclusively associated with any particular astrophysical phenomena. Their are two major series when considering the class I methanol lines, the $J_0 \rightarrow (J-1)_1\,\mathrm{A}^+$ series containing the 44- and 95-GHz lines and the $J_{-1} \rightarrow (J-1)_0\,\mathrm{E}$ series which has the 36- and 84-GHz transitions (see Figure 1.1). These four methanol transitions are the most widespread class I lines observed in our Galaxy (e.g. Slysh et al., 1994; Val'tts et al., 2000; Ellingsen et al., 2005; Chen et al., 2011). Compared with the class II transitions and the MMB survey, no surveys of comparable size have been undertaken for class I methanol masers, however, this will soon change when the Australia Telescope Compact Array (ATCA) StarFISH survey (Breen et al., in preparation), a full-scale version of the MALT45 survey (Jordan et al., 2015), is completed. This survey will provide a full census of 44-GHz class I methanol masers along the Galactic plane (covering a Galactic coordinate range of $l = 270^\circ \rightarrow 5^\circ$, $b = \pm 0.5^\circ$).

Based on the environments class I masers have been detected towards, the presence of shocks appears to be a very important factor in the production of these masers (Kurtz et al., 2004; Sjouwerman et al., 2010; Cyganowski et al., 2012; Voronkov et al., 2014). These weak shocks have been identified as a production mechanism for releasing methanol from dust grains through heating (Hartquist et al., 1995; Garay et al., 2002). This increased methanol abundance combined with heating and compression of the gas due to the same shocks, produces the required conditions for these class I masers to form (Voronkov et al., 2010b).

Yusef-Zadeh et al. (2013a) discovered widespread 36.2-GHz class I emission towards the Milky Way's central molecular zone (CMZ). Over 350 sites are located within a region with linear size of approximately 160×43 pc with a combined total luminosity

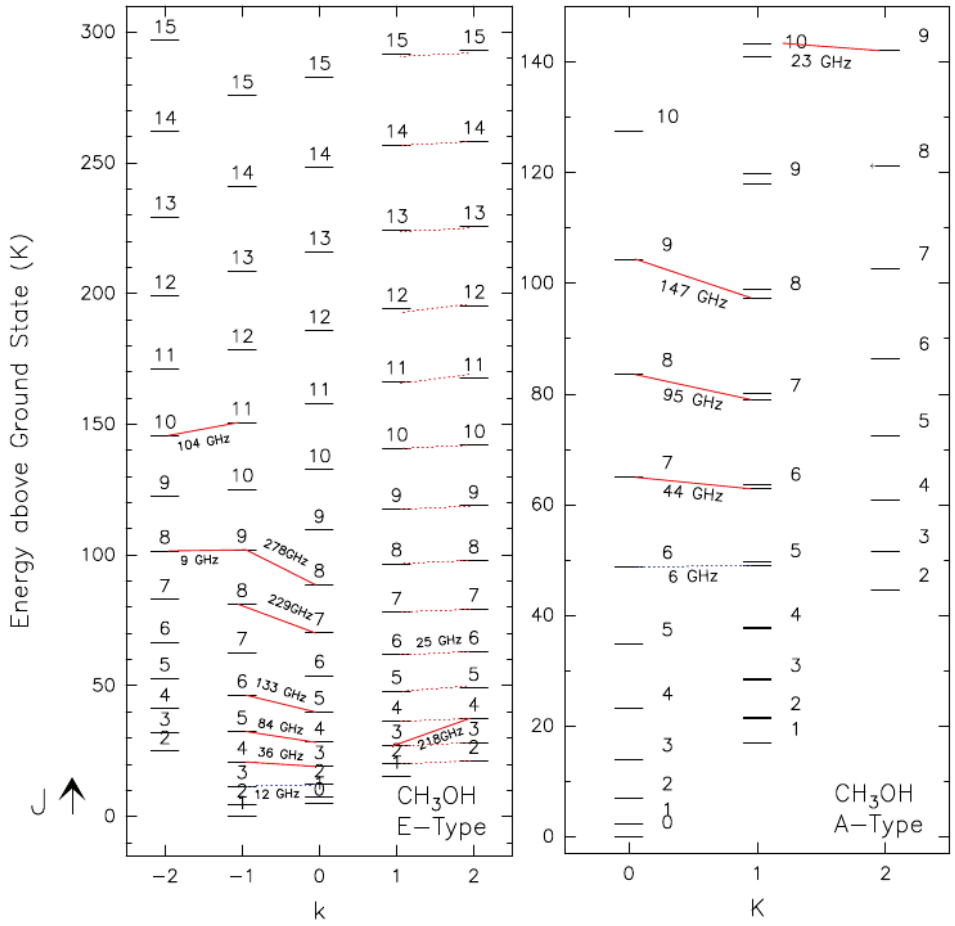

Figure 1.1: Methanol rotational energy level diagram including known class I methanol transitions (connected by red lines) and anti-inverted transitions (connected by blue-dotted lines). Left panel is for E-type transitions, and right panel for A^+-type. Figure is originally presented in Leurini et al. (2016).

of > 5600 Jy km s^{-1}. In order for this widespread emission to occur, methanol must be abundant in this region, however, the production mechanism is not as clear cut as for star-formation regions. The weak shocks generally responsible for methanol production in class I maser sources tend to occur at the edges of molecular clouds (where the interaction is occurring) or due to outflows/expanding HII regions in star-formation sites (e.g Kurtz et al., 2004; Voronkov et al., 2006). In the case of these methanol masers within the CMZ, they are located within the inner regions of giant molecular clouds, and therefore, weak shocks at the outer edges of the clouds are an unlikely mechanism for the release of methanol (Yusef-Zadeh et al., 2013a). Additionally, star-formation in the CMZ giant molecular clouds has low-efficiency (Immer et al., 2012), so shocks local to star-formation sites are also unlikely to release the required abundance of methanol. Therefore, instead of weak shocks, Yusef-Zadeh et al. (2013a) suggest photodesorption of the methanol from cold dust by cosmic rays. The cosmic ray ionisation rate in the inner region of the Milky Way is approximately two orders of magnitude higher than in the Galactic disk (Yusef-Zadeh et al., 2013b). These cosmic rays collide with H_2, producing FUV emission that heats dust grains causing the evaporation of molecular methanol (Roberts et al., 2007).

1.2.3 Methanol masers towards other galaxies

The first detection of an extragalactic methanol maser was towards the N105a/MC23 nebula in the Large Magellanic Cloud(LMC) at 6.7 GHz (Sinclair et al., 1992). Following this, two additional 6.7-GHz class II masers were detected towards other locations within the LMC by Ellingsen et al. (1994) and Beasley et al. (1996). These findings prompted a complete systematic survey of the Small Magellanic Cloud (SMC) and LMC for 6.7-GHz methanol masers using the Parkes 64-m telescope as part of the MMB project (Green et al., 2008). This survey detected a fourth 6.7-GHz methanol maser towards the LMC, alongside the three previously reported. A search for 12.2-GHz class II masers was then conducted towards HMSF regions in the LMC by (Ellingsen et al., 2010). They detected one 12.2-GHz methanol maser in the N105a

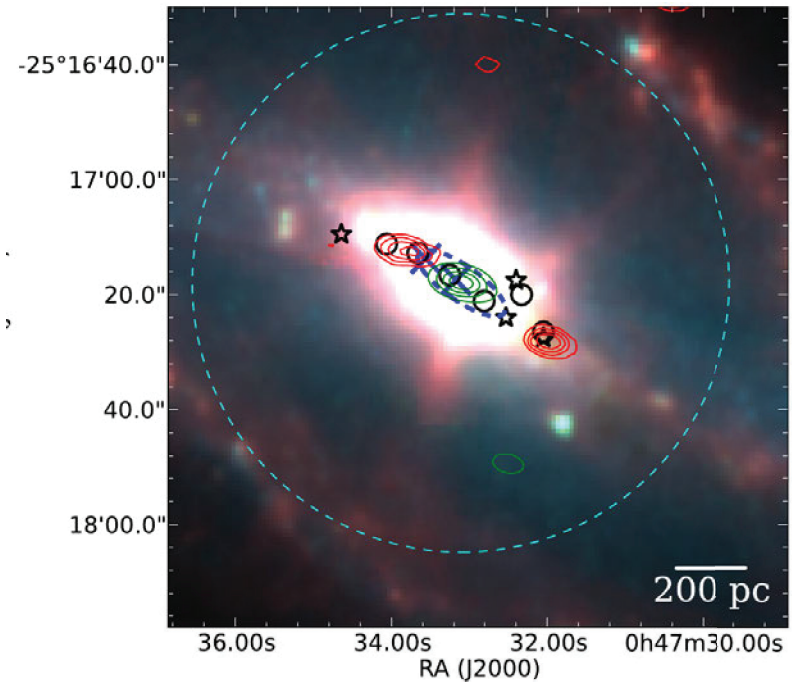

Figure 1.2: Original detection of 36.2-GHz methanol maser emission towards NGC 253 presented in (Ellingsen et al., 2014). Methanol emission is represented by red contours, with 7-mm continuum as green contours. The boundary of the CMZ in NGC 253 given by the dark blue dashed ellipse.

nebula, the same site as the original 6.7-GHz LMC detection. The detection of a 6.7-GHz class II methanol maser towards the 10 kpc ring in M 31, increased the number of extragalactic sources with methanol masers to two (Sjouwerman et al., 2010). The class II masers in both the LMC and M 31 are less luminous than the brightest known 6.7-GHz class II masers in our galaxy (Van Der Walt et al., 2009). In addition to these emission sources, the 6.7-GHz class II transition has also been detected in absorption towards NGC 3079 and Arp 220 (Salter et al., 2007; Impellizzeri et al., 2008). The masers in the LMC and M 31 are also associated with HMSF, just like those observed towards Galactic sources. This seems to indicate that these extragalactic class II masers are simply Galactic-style class II methanol masers which are luminous enough to be detected with current facilities at the larger distances of the LMC and M 31.

The mechanism suggested by Yusef-Zadeh et al. (2013a) for producing the 36.2-GHz

class I emission observed towards the centre of our Galaxy, is not necessarily unique to the Milky Way. It can be reasonably expected that a similar mechanism may exist in other nearby galaxies. This fact spurred the first searches for this transition towards nearby galaxies. The first extragalactic class I methanol maser emission was detected towards the nearby starburst galaxy NGC 253 (Ellingsen et al., 2014). These masers were detected offset either side of the nuclear region in NGC 253. Unlike the previously detected extragalactic class II masers, both of these maser regions have luminosities approximately 5 orders of magnitude greater than a typical Galactic class I maser. When compared to the widespread emission in the Milky Way's CMZ (Yusef-Zadeh et al., 2013a), this emission is both an order of magnitude more luminous and it lies outside of NGC253's CMZ. Ellingsen et al. (2014) suggest three possible explanations for the location of this emission in NGC 253. The first is that the cosmic ray intensities are too high, and gas-phase methanol is destroyed shortly after being created. This was sggested by Yusef-Zadeh et al. (2013a) as a possible explanation for the lack of 36.2-GHz masers within the Milky Way's molecular ring. The second explanation is that the nuclear outflow in NGC 253 is interacting with the edges of the molecular disk in NGC 253. This interaction may release methanol through weak shocks, similar to what is seen in outflows in Galactic star-formation regions. This hypothesis is supported by the association of both 36.2-GHz methanol maser regions with NH_3 cores. The third suggestion is that a large number of high-mass star-formation regions are located within the class I methanol maser sites. However, this hypothesis does not seem likely as densely clustered star-formation regions should have higher mid-infrared and dust-continuum levels (when compared to locations nearby to the nucleus) than are observed towards these two class I methanol masers.

The same observations responsible for the first detection of extragalactic class I methanol masers in NGC 253 (Ellingsen et al., 2014), also produced the second reported detection of extragalactic 36.2-GHz emission in Arp 220 (Chen et al., 2015). This distant galaxy (luminosity distance of 83.5 Mpc; Ashby et al., 2011), is the closest known ultra-luminous infrared galaxy (ULIRG) and major merger system and host

of the first detected OH megamaser (Baan et al., 1982). Emission from the 36.2-GHz class I line appears to be highly correlated with diffuse X-ray emission along the south-east to north-west axis of Arp 220, however, anti-correlated at the nucleus where the X-ray emission is of higher intensity. This X-ray emission is used as a probe for cosmic-ray flux in different locations of the galaxy, therefore, this observed relationship is consistent with the mechanism for gas-phase methanol release in the Milky Way as outlined in Yusef-Zadeh et al. (2013a). Chen et al. also report emission from the 37.7-GHz class II methanol line, which is the first detection of this transition towards an external source. They suggest that both of the class I and class II masers are tracing star-formation and feedback in the circumnuclear starburst region of Arp 220, rather than close to the nucleus like 'Megamasers' observed from other molecules (e.g. OH and H_2O).

In addition to these two galaxies with reported 36.2-GHz clas I masers, emission from the 84.5-GHz class I methanol line was detected towards NGC 1068 (Wang et al., 2014). Wang et al. (2014) argue that this emission results from a maser process associated with shock fronts in NGC 1068, however, to date no interferometric observations have been made of this line towards NGC 1068, nor have any searches for the 36.2-GHz class I line been published.

1.2.4 Comparison of methanol maser transitions from the same source

The rich spectrum of methanol maser lines all have specific conditions under which the pumping mechanism is optimised. Modelling the formation of these masers can help us determine the conditions required for optimal pumping in each transition. Comparison of the flux-density line ratios between multiple maser transitions, towards the same volume of gas, allows us to accurately determine the physical conditions present in this region or the evolutionary phase of the source (Cragg et al., 2001; Sutton et al., 2001; McEwen et al., 2014; Leurini et al., 2016). Interferometric studies have observed methanol maser lines from multiple transitions, spatially coincident within various

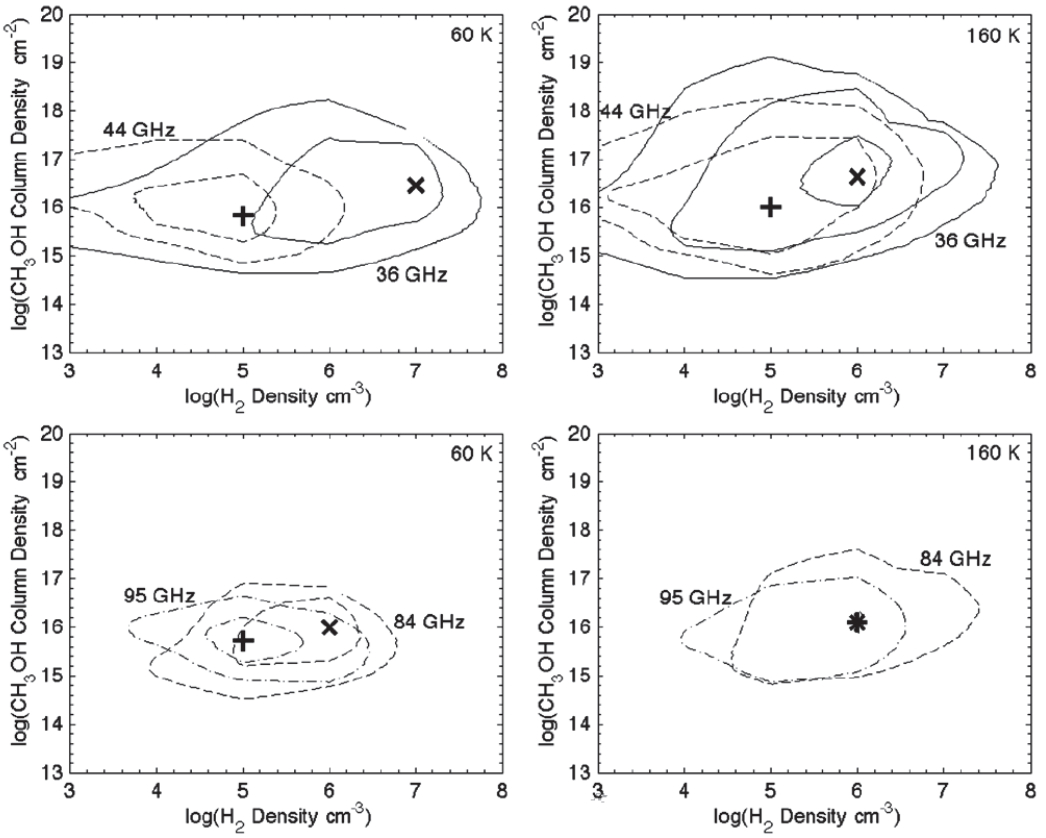

Figure 1.3: Maser optical depth contour diagram as a function of methanol column density and H_2 density at two different temperatures (60 and 160 K). Crosses and pluses mark the highest peak inverted temperature for the A^+- (44.1- and 95.2-GHz) and E-type (36.2- and 84.5-GHz) transitions respectively. Figure is originally presented (as figure 3) in McEwen et al. (2014).

astronomical sources. While we do not see class I and class II maser transitions from the same volumes of gas, we often do see multiple transitions from the same class in these locations (e.g. 6.7- and 12.2-GHz class II masers towards YSOs or 36.2- and 44.2-GHz class I masers in outflows; Breen et al., 2012b; Voronkov et al., 2014).

The two main class II methanol transitions (6.7- and 12.2-GHz), can provide useful information about the evolutionary phase of their associated YSO. 12.2-GHz class II masers are observed towards approximately 40 percent of 6.7-GHz sources (Breen et al., 2011, 2012a,b). These class II masers form in a later stage of the high-mass

star-formation (HMSF) regions lifetime (Breen et al., 2010, 2011). Therefore, older HMSF regions (compared to those with just 6.7-GHz masers) can be identified by detecting this transition. In addition to this, Breen et al. (2011) also identify that both the 6.7- and 12.2-GHz transitions increase in luminosity as the YSO evolves, with the former transition doing so more quickly. This indicates that HMSF regions with very high 6.7-/12.2-GHz line ratios (but importantly still have detected 12.2-GHz maser emission) are likely to be in later evolutionary stages than regions where the ratio is closer to unity (Breen et al., 2010). Similarly, as the sources evolve, both of these maser transitions increase in velocity coverage, again with the 6.7-GHz maser doing so at a more rapid rate (Breen et al., 2011). This provides another basis for comparison between the two transitions in order to probe the underlying evolutionary phase of the HMSF region. Observations of the 37.7-GHz class II methanol line towards Galactic sources have determined that this line is also present in HMSF regions where the 6.7-/12.2-GHz line ratios are high, indicating that the 37.7-GHz transition is a useful signpost for the final few thousand years of the class II methanol phase of these sources (Ellingsen et al., 2011b).

McEwen et al. (2014) present modelling of the physical conditions required for the 36.2-, 44.1-, 84.5- and 95.2-GHz class I methanol maser lines. This modelling pertains to class I methanol masers associated with shock fronts in supernova remnants (SNRs) but is also useful for understanding the conditions present in molecular cloud interactions in star-formation regions. This paper contains some excellent figures, some of which will be included here, for understanding how these four lines behave across a variety of different environmental conditions. Figure 1.3 shows how the optical depth of the E-type transitions (36.2- and 84.5-GHz) favours higher H_2 densities than the A^+ transitions and that methanol column density has less of an impact on the line ratios between transitions of each type. This figure also shows that at higher temperatures the required H_2 density for peak optical depth begin to converge between the two series (E- and A^+-type). The optical depth of maser lines also increases with temperature of the region. This can be seen in Figure 1.4, where, for a fixed density,

the optical depth of the four maser transitions increases as a function of the temperature. The three different panels of this figure also show how the line ratios between the transitions can drastically vary across our parameter space. This is further illustrated by Figure 1.5, which shows the H_2 density break point for which the 44.1 and 36.2-GHz lines flip in relative strength, indicating that the A^+ transitions become quenched at lower densities than the E-type. These relationships, in particular the break points where line ratios flip, allow us to probe the gas conditions of these class I masers. For example, if we observe both 36.2- and 44.1-GHz masers from the same volume of gas, and the 36.2-/44.1-GHz line ratio is > 1 we can infer that the density of this location is likely higher than regions where the inverse is observed. Modelling of class I methanol maser lines is also covered in great detail by Leurini et al. (2016), who particularly investigate a third transition series at 25-GHz, the $J_2 \rightarrow J_1$E family of lines (see red-dotted lines in Figure 1.1). However, as the 36.2-, 44.1-, 84.5- and 95.2-GHz class I methanol maser lines are of primary interest for this project we will only mention that study here as an excellent source of further discussion on this topic.

All of the modeling studies for class I methanol masers has been with reference to Galactic methanol masers. As extragalactic class I methanol masers are a recently discovered phenomenon, with no source having multiple class I lines detected towards it, whether or not the various transitions are related in the same way as their Galactic counterparts is not yet well understood. Detections of multiple class I transitions towards the same external galaxies (and from the same region in those galaxies) may prove a useful tool for understanding their environments, and subsequently their host sources, similarly to how they are used in our Galaxy. In addition to understanding the environments of these extragalactic masers, sources with various methanol maser transitions may also allow us to investigate some fundamental constants of physics, and how they may or may not vary across cosmic time (Levshakov et al., 2011; Jansen et al., 2011; Bagdonaite et al., 2013; Ellingsen et al., 2017a), which will be discussed in the following section.

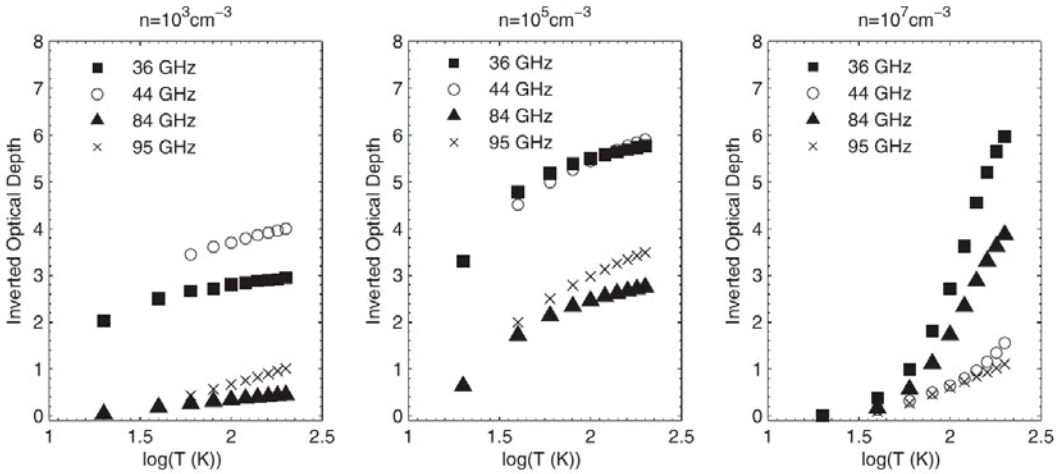

Figure 1.4: Optical depth of the four class I methanol lines vs. temperature across three different H_2 densities. Figure is originally presented (as figure 4) in McEwen et al. (2014).

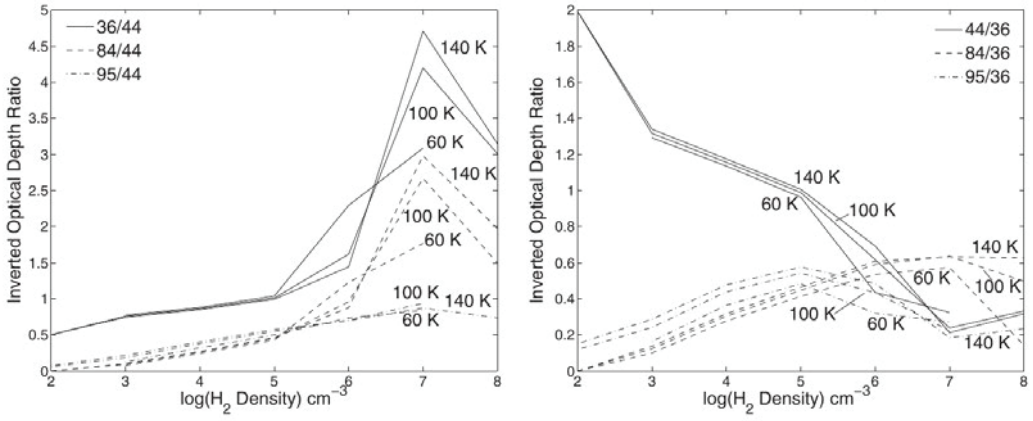

Figure 1.5: Optical depth as a function of H_2 density across three different temperatures (60, 100 and 120 K) with respect to the 44.1-GHz line (left) or 36.2-GHz line (right). Figure is originally presented (as figure 5) in McEwen et al. (2014).

1.2.5 Probing the fundamental constants of physics

The potential for using extragalactic methanol masers for this sort of investigation was originally suggested by Ellingsen et al. (2011a). Further discussion in light of the first detections of extragalactic class I masers was also presented by Ellingsen et al. (2017a).

The hindered internal rotation of the OH radical in methanol makes the rest-frequencies of these rotational transitions sensitive to the proton-electron mass ratio (Levshakov et al., 2011). Comparison of the rest frequencies observed from astronomical methanol, with those observed in the laboratory can reveal variations in these fundamental constants (Kanekar, 2011; Ellingsen et al., 2012; Bagdonaite et al., 2013). Ellingsen et al. (2012) demonstrated how this can be used on the lensing galaxy PKS 1830–211, observing 12.2-GHz methanol absorption using the ATCA and comparing with the 60.5-GHz methanol absorption feature reported by (Muller et al., 2011). A subsequent, more comprehensive investigation by Bagdonaite et al. (2013) utilised the Effelsberg 100-m, Institute de Radio Astronomie Millimétrique 30-m and Atacama Large Millimetre Array, to observe thermal methanol absorption towards this same source, achieving a statistical constrain for the proton-electron mass ratio ($\frac{\Delta\mu}{\mu}$) of $(1.5 \pm 1.5) \times 10^{-7}$. Ellingsen et al. (2017a) identified that the recently discovered extragalactic methanol masers may also be useful for probing these fundamental constants at cosmologically interesting distances. In order for this to viable, we need luminous enough masers to be detectable from multiple methanol maser transitions. Ellingsen et al. identify that the 44.1-GHz class I line is not appropriate for comparison against the 36.2-GHz class I line for this purpose. However, the 84.5-GHz class I maser transition, which has been observed towards an extragalactic source (Wang et al., 2014), may prove more sensitive to these changes. Both the 84.5- and 36.2-GHz class I lines are from the same transition family, making it more likely we will observe both of these lines towards the same region within these extragalactic sources, which is required in order to probe the proton-electron mass ratio.

1.3 The Extragalactic Targets

The majority of the work presented in this thesis focusses on two nearby starburst galaxies, NGC 4945 and NGC 253. The following sections will discuss these sources in further detail to help provide context to the research.

1.3.1 NGC 4945

NGC 4945 is a southern sky galaxy (J2000 right ascension of $13h\ 05m\ 27.4s$ and declination of $-49°\ 28'\ 04\farcs4$) located at a distance of 3.7 Mpc (Tully et al., 2013) in the Centaurus A/M 83 group. Originally discovered by James Dunlop in 1826, this galaxy is observed edge-on from Earth (75° inclination angle). This galaxy is classified as a barred spiral, although due to its edge-on nature, and the presence of prominent dust lanes obscuring the central region, it is difficult to accurately classify its spiral type (see 1.6).

NGC 4945 is bright in the infrared wavelengths, harbouring one of the brightest IRAS point sources (in the far-IR) outside of the local group (Brock et al., 1988). Brock et al. (1988) identified that this far-infrared emission may be the result of starburst activity in the central region of NGC 4945 or, the result of activity from a type II Seyfert active nucleus. The detection of an ionized gas outflow along the minor axis of the galaxy by Nakai (1989) has been interpreted as a super-wind resulting from starburst activity in the nucleus of NGC 4945 (Heckman et al., 1990). X-ray observations of NGC 4945, using *Ginga*, also identified the presence of an obscured Seyfert II active nucleus, making NGC 4945 a starburst/AGN hybrid galaxy (Iwasawa et al., 1993).

22-GHz water megamaser emission was detected towards NGC4945 by Dos Santos & Lepine (1979), making it the first example of a water maser detected in a galactic nucleus. An interferometric follow-up by Greenhill et al. (1997) determined positions for these masers, along with identifying additional components of emission which are blue-shifted with respect to the systemic velocity of NGC 4945. This imaging by

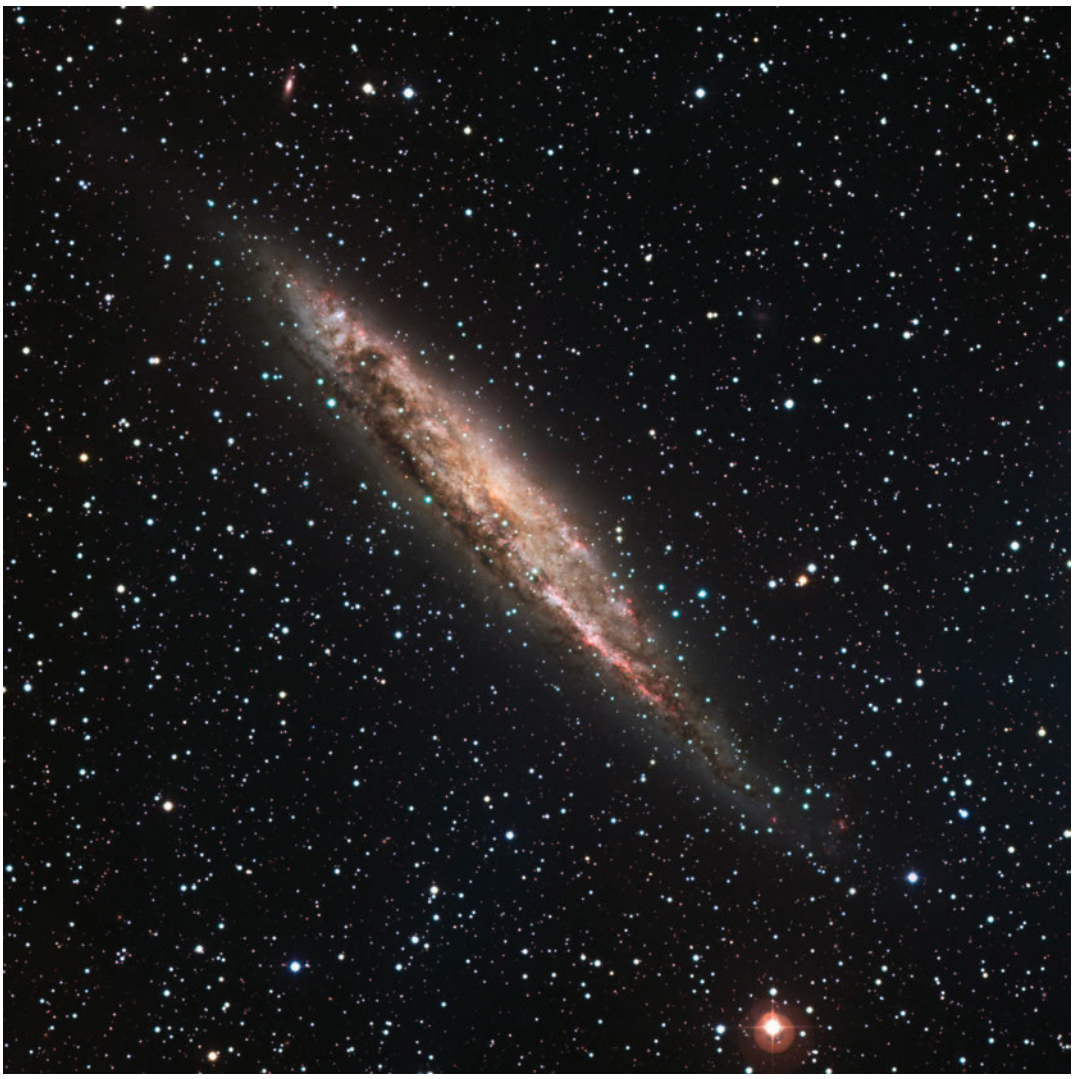

Figure 1.6: Optical image of NGC 4945 taken using the 2.2-m MPG/ESO telescope in La Silla. This image is comprised of data from 5 bands (B, V, R, Hα and S II). The TIFF image was downloaded from the ESO website (https://www.eso.org/public/images/eso0931a/) and then converted to PNG.
[Optical image of NGC 4945 taken using the 2.2-m MPG/ESO telescope in La Silla.]

Greenhill et al. (1997) suggests that the water masers are distributed in an organised structure, similar to that seen in the Keplerian disk of NGC 4258 (Miyoshi et al., 1995). This has yet to be confirmed with no VLBI follow-up ever having been made towards NGC 4945, making it a good future target for the Long Baseline Array (LBA). Two sub-mm wavelength water maser transitions have also been observed towards NGC 4945, the 183-GHz line by Humphreys et al. (2016) and the 321-GHz line by Pesce et al. (2016) and Hagiwara et al. (2016). Humphreys et al. (2016) suggest that the 183-GHz line may be coming from the same locations as the 22-GHz masers mapped by Greenhill et al. (1997), due to these lines sharing similar optimal conditions for masing. The 321-GHz line is also believed to be associated with the circumnuclear accretion disk, however, higher-resolution observations are needed to confirm this (Hagiwara et al., 2016; Pesce et al., 2016).

The significant southern declination of NGC 4945 means it has suffered from a lack of robust molecular line studies, despite it being a relatively nearby starburst galaxy. The Australia Telescope Compact Array (ATCA) has been utilised for a couple of molecular line surveys focussed on the 3-mm lines of HCN, HCO^+ and HNC towards NGC 4945 (Cunningham & Whiteoak, 2005; Green et al., 2016). These lines (and others, most notably 3-mm SiO and CS lines), were imaged in greater detail by Henkel et al. (2018) using the Atacama Large Millimetre Array (ALMA). These three 3-mm surveys, plus some CO surveys by Dahlem et al. (1993) and Ott et al. (2001), make up the only detailed molecular line data of radio-regime gas tracers towards NGC 4945 to date. Recently Eisner et al. (2019) observed cm-wave transitions towards NGC 4945. They detect excited 23.8-GHz OH absorption, along with numerous NH_3 transitions (all 15-mm ammonia lines). Many radio recombination lines (RRLs) between 4- and 25-GHz were targetted during these observations (see Eisner et al. (2019) for full list), however, none were detected towards NGC 4945.

1.3.2 NGC 253

Originally discovered by Caroline Herschel in 1783 and located at a distance of 3.4 Mpc (Dalcanton et al., 2009) in the Sculptor group, NGC 253 is a southern sky (J2000 right ascension of $00h\ 47m\ 33.2s$ and declination of $-25°\ 17'\ 18\overset{''}{.}4$) galaxy, viewed mostly edge-on (inclination angle of $72 - 78°$; Puche et al., 1991). This galaxy is classified as a dusty weakly barred spiral galaxy, with relatively open spiral arms (SAB(s)c type de Vaucouleurs et al., 1991).

Telesco & Harper (1980) first reported an excess of far-infrared emission from the central region of NGC 253. They identified that it was unlikely that this emission was the result of late-type stars, and instead suggested that OB stars may be the power source. It is now widely accepted that NGC 253 contains a starburst type nucleus, and this source has been used to investigate the relationship between star-formation and spiral type galaxies (Carlstrom et al., 1990; Paglione et al., 2004; Bendo et al., 2015; Leroy et al., 2015). Unlike NGC 4945 which is host to a hybrid AGN/starburst nucleus, there is currently no compelling evidence for the existence of a Sgr A* equivalent in NGC 253, indicating that all nuclear activity is driven by starburst (Günthardt et al., 2015). Mapping of SiO and $H^{13}CO^+$ by García-Burillo et al. (2000) revealed a double ringed structure towards the nucleus of NGC 253, with the inner-ring corresponding to the radius of the inner Linblad resonance, the same radius as the inner-end of the galactic bar. A ring at this radius ($\sim$ 200 pc) was also reported by Iodice et al. (2014), and both papers suggest that the bar-potential may help drive star-formation in this inner nuclear ring. In addition to mechanically driving the star-formation, the bar also plays another role, with gas inflow along the bar fueling the starburst in this central nuclear ring (Paglione et al., 2004). A star-formation rate of $\sim 1.7\ M_\odot\ yr^{-1}$ has been reported for this nuclear ring in NGC 253 (Bendo et al., 2015), which corresponds to half of the total star-formation for the whole galaxy (Leroy et al., 2015). Submillimetre ALMA observations by (Leroy et al., 2018) reveal $\sim$ 14 bright and compact knots of dust emission within the central region of NGC 253. They conclude

that these knots, which have sizes on the order of ∼3 pc, correspond to newly formed super star clusters (SSCs), which contain a significant fraction (∼ 20 percent) of the star-formation in this central region (Leroy et al., 2018).

Recently, molecular outflow from the starbursting centre of NGC 253 has also been further investigated, with molecular 'streamers' reported by (Bolatto et al., 2013) and subsequently investigated by Zschaechner et al. (2018) and Krieger et al. (2019). A mass loss rate of $14 - 39 M_{\odot}$ yr^{-1} has been determined for these outflows, an order of magnitude higher than the star-formation rate (Krieger et al., 2019). Research on the outflows of NGC 253 is still ongoing, with many factors such as the geometry and sources of these outflows unknown at this time (Krieger et al., 2019).

Extragalactic maser emission has been observed from five different species towards NGC 253. The nuclear region of the galaxy is host to OH, water and NH_3(3,3) masers (Turner, 1985; Henkel et al., 2004; Ott et al., 2005; Hofner et al., 2006). The OH masers detected by Turner (1985) are located in a nuclear outflow plume extending 1.5 kpc from the equatorial plane, with masers from the 1612-, 1665- and 1667-MHz transitions detected. Later observations of the 1612- and 1720-MHz satellite OH lines by Frayer et al. (1998), also detect the 1720-MHz transition as a maser in the nuclear region of NGC 253. Apart from these two studies, the 18-cm OH lines of NGC 253 have no modern observations. Unlike NGC 4945, the H_2O masers towards NGC 253 are not highly-luminous megamasers tracing a circumnuclear disk (Henkel et al., 2004; Gorski et al., 2019). Gorski et al. (2019) show that the H_2O masers are associated with sites of star-formation throughout the nuclear disk, with the brightest (a kilomaser) located at a known SSC (Leroy et al., 2018; Gorski et al., 2019). A tentative detection of an NH_3(3,3) maser was originally presented by Ott et al. (2005). This maser is located towards the nuclear continuum source where NH_3(1,1), (2,2) and (6,6) were all also observed in absorption and was the first reported detection of an extragalactic ammonia maser (Ott et al., 2005). Gorski et al. (2017) later confirmed this detection and concluded that this maser is being collisionally pumped via interaction between

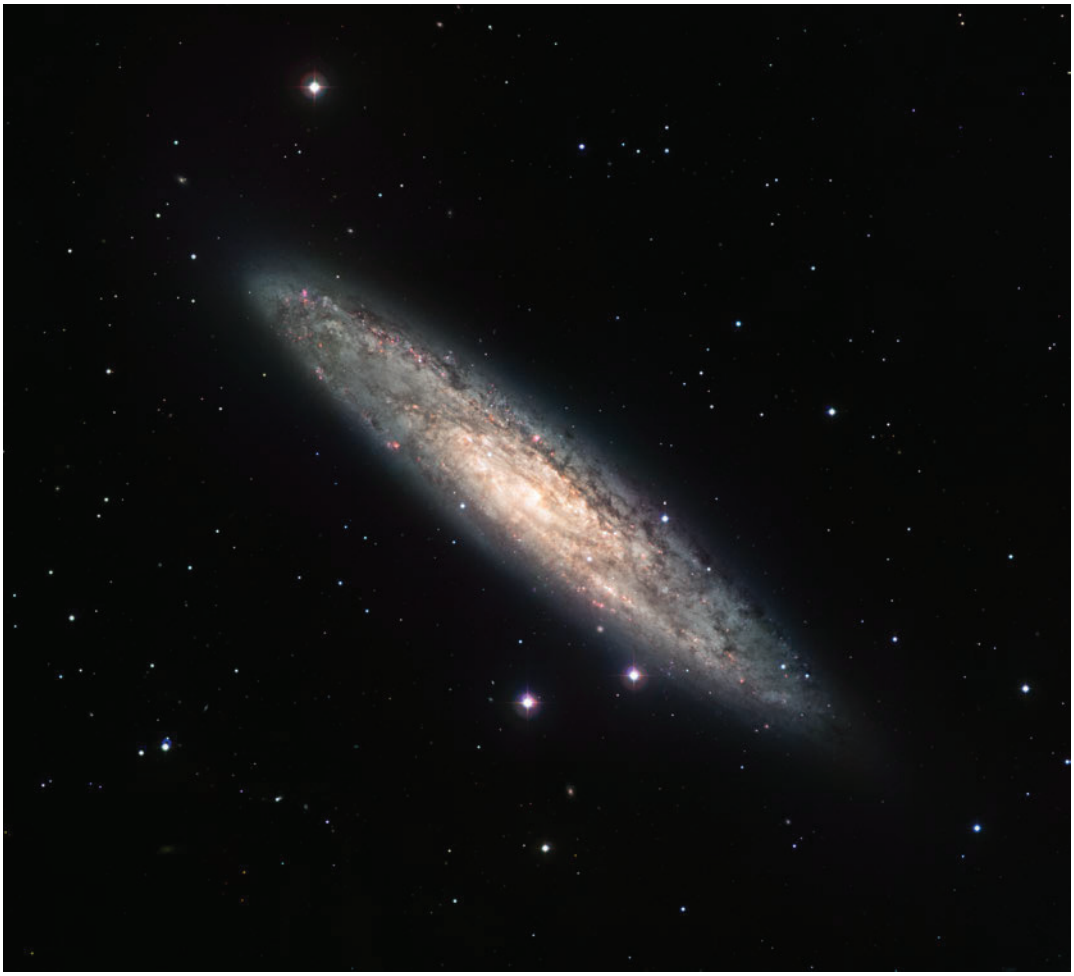

Figure 1.7: Optical image of NGC 253 as seen by the Wide Field Imager on the 2.2-m MPG/ESO telescope in La Silla. This image contains data from 4 different bands (R, V, Hα and OIII). The TIFF image was downloaded from the ESO website (https://www.eso.org/public/images/eso0902c/) and then converted to PNG.

[Image of NGC 253 as seen by the Wide Field Imager on the 2.2-m MPG/ESO telescope in La Silla.]

the base of the molecular outflow and surrounding material. Outside of the central few hundred parsec, masing emission has been detected from two other molecules, methanol and HC_3N (Ellingsen et al., 2014, 2017b). The methanol maser emission has been discussed in detail in Section 1.2.3 and will be omitted here. The HC_3N maser emission marks the first detection of masing emission from this species in either Galactic or extragalactic sources. The HC_3N maser is offset south-west from the nucleus and located towards the inner edge of the galactic bar, which is the same site as the strongest 36.2-GHz class I maser emission (Ellingsen et al., 2017a,b).

In contrast to NGC 4945, NGC 253 has received plenty of attention from the astronomical community. This is largely due to it being a nearby, starburst galaxy, with a declination that allows it to be observed from both southern and northern hemisphere facilities (e.g. ATCA, JVLA and ALMA). Many molecular species have been mapped in millimetre-wavelengths towards the central region of NGC 253 (Martín et al., 2006; Meier et al., 2015; Ellingsen et al., 2017a). The centimetre-wavelength observations of Eisner et al. (2019) detected 18 Hα recombination lines towards NGC 253, which is the highest number of RRLs detected in an extragalactic source to date. Eisner et al. (2019) also detected the presence of an unidentified line towards NGC 253 at 5.737-GHz.

1.4 This project

In this thesis we investigate the relationship between extragalactic class I methanol masers and the properties of their host galaxies. One of the primary goals was to search for new examples of these extragalactic masers, as the sample size at the beginning of this project (two 36.2-GHz sources) was one of the limiting factors in progressing our understanding of the phenomenon. In addition to the maser searches, we made numerous observations of known sources characterising the properties of the maser emission and various other spectral lines indicative of the maser environment.

The vast majority of work in this thesis has now been published across 5 differ-

ent papers in three different journals: *The Astrophysical Journal, The Astrophysical Journal Letters and Monthly Notices of the Royal Astronomical Society.* Each of these published papers will be a chapter of this thesis, with each chapter consisting of an introduction, discussion on author contribution to the paper, and then the manuscript as published.

The first of these five chapters (chapter 2) will focus on a comparison of methanol maser transitions towards Galactic star-formation source. The majority of work for this second paper was actually completed at the start of my candidature, as this Galactic data was used to develop MIRIAD data reduction skills. It was published later due to the detection of another extragalactic class I maser being important for an upcoming conference (IAU S336). After this, the next 4 chapters about extragalactic methanol masers will be ordered by publication data as this makes the most sense regarding the progression of our understanding of the phenomenon. Chapter 3 contains an ATCA detection of 36.2-GHz class I maser emission toward the nearby starburst galaxy NGC 4945. Chapter 4 (paper 3) focusses on follow-up observations of NGC 4945, covering both the 36.2- and 44.1-GHz class I methanol transitions in addition to other 7-mm spectral lines. Chapter 5 (paper 4) is comprised of the detection of 84.5-GHz class I methanol maser emission towards NGC 253, making it the second example of an extragalactic maser from this transition. Finally, the sixth chapter (paper 5) details results from our maser search projects, along with the results of multi-epoch monitoring of NGC 4945 and NGC 253. Further monitoring of these two sources resulted in detections of new maser components and the first evidence of variability in these extragalactic masers.

Chapter 2

The relationship between Class I and Class II methanol masers at high angular resolution

2.1 Introduction

This paper was originally published in *Monthly Notices of the Royal Astronomical Society* as *'The relationship between Class I and Class II methanol masers at high angular resolution'* (DOI: 10.1093/mnras/sty694).

This paper reports an interferometric follow-up of known Galactic 95-GHz class I methanol sources using the Australia Telescope Compact Array (ATCA). The original targets were all Galactic class II methanol masers, and therefore, high mass star formation regions. Across the 32 targets, we identified a total of 172 95-GHz maser components. These 95.2-GHz masers were then compared against similar observations of the 36.2- and 44.1-GHz class I masers in these sources by Voronkov et al. (2014), along with any 6.7- or 12.2-GHz class II masers detected from the Methanol Multibeam survey.

Despite being the second publication, the majority of the work for this paper was completed at the beginning of my candidature. The ATCA data here was used to develop the Miriad data reduction techniques which were required for the rest of

my candidature. Additionally, the analysis for this paper built a foundation for my knowledge of class I and class II methanol masers, which allowed useful comparisons to be drawn between the Galactic and extragalactic class I masers.

2.2 Author Contributions

- Observations were made as part of the C1273 ATCA project led by Simon Ellingsen. ATCA observations were performed by Simon Ellingsen with assistance from Maxim Voronkov and Giuseppe Cimò in September of 2004.
- All data-reduction for this paper was performed by Tiege McCarthy using MIRIAD and PYTHON.
- Analysis was performed by Tiege McCarthy alongside substantive discussion with Simon Ellingsen and Maxim Voronkov.
- Field images for all 30 of the sources were created by Maxim Voronkov using the extracted maser positions provided by Tiege McCarthy.
- All other figures and the vast majority of the writing for the paper were created by Tiege McCarthy, with Simon Ellingsen and Maxim Voronkov providing review and suggestions to improve the final manuscript.

Monthly Notices
of the
ROYAL ASTRONOMICAL SOCIETY

MNRAS **477,** 507–524 (2018)
Advance Access publication 2018 March 16

doi:10.1093/mnras/sty694

The relationship between Class I and Class II methanol masers at high angular resolution

T. P. McCarthy,[1,2]★ S. P. Ellingsen,[1] M. A. Voronkov[2] and G. Cimò[3,4]

[1]*School of Natural Sciences, University of Tasmania, Private Bag 37, Hobart, Tasmania 7001, Australia*
[2]*Australia Telescope National Facility, CSIRO, PO Box 76, Epping, NSW 1710, Australia*
[3]*Joint Institute for VLBI ERIC (JIVE), Postbus 2, NL-7990AA, Dwingeloo, the Netherlands*
[4]*Netherlands Institute for Radio Astronomy (ASTRON), Postbus 2, NL-7990AA, Dwingeloo, the Netherlands*

Accepted 2018 March 1. Received 2018 February 27; in original form 2017 November 10

ABSTRACT

We have used the Australia Telescope Compact Array (ATCA) to make the first high-resolution observations of a large sample of class I methanol masers in the 95-GHz (8_0–7_1A^+) transition. The target sources consist of a statistically complete sample of 6.7-GHz class II methanol masers with an associated 95-GHz class I methanol maser, enabling a detailed study of the relationship between the two methanol maser classes at arcsecond angular resolution. These sources have been previously observed at high resolution in the 36- and 44-GHz transitions, allowing comparison between all three class I maser transitions. In total, 172 95-GHz maser components were detected across the 32 target sources. We find that at high resolution, when considering matched maser components, a 3:1 flux density ratio is observed between the 95- and 44-GHz components, consistent with a number of previous lower angular resolution studies. The 95-GHz maser components appear to be preferentially located closer to the driving sources and this may indicate that this transition is more strongly inverted nearby to background continuum sources. We do not observe an elevated association rate between 95-GHz maser emission and more evolved sources, as indicated by the presence of 12.2-GHz class II masers. We find that in the majority of cases where both class I and class II methanol emission is observed, some component of the class I emission is associated with a likely outflow candidate.

Key words: masers – radio lines: ISM.

1 INTRODUCTION

Interstellar masers are one of the most readily observable signposts of young high-mass star formation regions as strong emission is commonly observed towards them from a range of molecular species and transitions. The most commonly observed maser species in star formation regions are from the OH, water, and methanol molecules, with the latter having the richest centimetre wavelength spectrum of the group. Methanol is an asymmetric top molecule with hindered internal rotation around the C–O bond and it is these characteristics which produce a large number of near-degenerate rotational energy levels. Methanol maser transitions are empirically divided into two classes, known as class I and class II. The class II masers are the better studied methanol masers, with more than 1200 sources having been observed in the 6.7-GHz transition throughout the Milky Way (e.g. Caswell et al. 2010, 2011; Green et al. 2010, 2012, 2017; Breen et al. 2015) and more than 20 different transitions having been detected (see Ellingsen et al. 2012, and references therein). Class II transitions are closely associated with main-line OH masers, water masers and are found in compact clusters (a typical linear scale of less than 0.03 pc; Caswell 1997) close to the infrared sources which mark the location of a young, high-mass star. Class I methanol masers have historically been harder to study as the strongest common transitions are at frequencies of 36- and 44-GHz, which are accessible to less telescopes and furthermore, until recently there was no reliable method for targeting searches for these masers. The class I methanol masers are often observed to be distributed over scales of 0.1–1 pc and are further offset from high-mass stars than class II masers (e.g. Kurtz, Hofner & Álvarez 2004; Voronkov et al. 2006). The empirically observed difference between the two classes of methanol masers is known to be caused by different pumping mechanisms (Cragg et al. 1992; Voronkov et al. 2005), with the class I methanol masers being collisionally pumped, while the class II masers are radiatively pumped (Sobolev, Cragg & Godfrey 1997; Cragg, Sobolev & Godfrey 2005). Class I masers are typically associated with the interface regions of molecular outflows (e.g Kurtz et al. 2004; Cyganowski et al. 2012;

★ E-mail: tiegem@utas.edu.au

Voronkov et al. 2006, 2014). However, these masers may also be associated with shocks resulting from expansion of H II regions, EGOs, or cloud–cloud interactions (Cyganowski et al. 2009, 2012; Sjouwerman et al. 2010; Voronkov et al. 2010, 2014).

Early studies of class I and class II methanol masers led to suggestions that they might be associated with different types of sources, however this turned out to be an observational bias in that some of the best-studied class I (e.g. Orion KL) and class II (e.g. W3(OH)) maser sources show no emission, or only very weak emission in the other class. Slysh et al. (1994) made a search for 44-GHz class I masers towards a sample of star formation regions known to host either OH maser and/or 6.7-GHz class II methanol masers. They detected many new class I methanol masers in this search and claimed an anticorrelation between the velocity ranges and the peak intensity of the class I and class II methanol masers in the same sources. Ellingsen (2005) searched for 95-GHz class I methanol masers towards a statistically complete sample of class II methanol masers, obtaining detections towards approximately 40 per cent of the sample, however Ellingsen found no evidence for the anticorrelations between the two classes claimed by Slysh et al.

The observations of Ellingsen were made with a single dish and so while they established the statistical relationship between the fraction of class II methanol maser sources which also host a class I methanol maser nearby, they did not show whether the two classes of methanol maser are driven by the same young high-mass star, nor the detailed spatial relationship between them. Here we report interferometric observations made with the Australia Telescope Compact Array (ATCA) of the 95-GHz class I methanol masers towards the sources detected by Ellingsen (2005). The locations of the class II methanol masers in all of these sources are known to sub-arcsecond precision from previous observations (Caswell et al. 2011; Green et al. 2012) and so we have the opportunity to make the first study of the relationship between class I and class II methanol masers at high resolution in a statistically complete sample.

2 OBSERVATIONS

The observations were undertaken with the ATCA between 2004 September 24 and 26 (project code C1273). The array was in the H75 configuration, with minimum and maximum baselines of 30.6 and 89.2 m, respectively, and the synthesized beam width for the observations at 95-GHz was approximately 6 × 5 arcsec. The correlator was configured with 256 spectral channels across a 32-MHz bandwidth. At an observing frequency of 95-GHz, this corresponds to a total velocity range of 100 km s^{-1} with a velocity resolution of 0.47 km s^{-1} for uniform weighting of the lag function (a channel width of 0.4 km s^{-1}).

The target sources were the detected 95-GHz class I methanol masers from Ellingsen (2005). Ellingsen used the Mopra telescope to search for 95-GHz class I methanol masers towards a statistically complete sample of 6.7-GHz methanol masers in the Galactic longitude range $l = 325° - 335°$, $b = \pm 0.53°$. We observed every source within the aforementioned Galactic longitude range that were observed to have 95-GHz emission in Ellingsen (2005). Not every source observed by Ellingsen was member of their statistically complete sample of 6.7-GHz methanol masers. Therefore, 11 of the 32 sources reported here are not within the statistically complete sample due to them falling outside the coordinate/LSR velocity range or being excluded for reasons described in Ellingsen (2005). These 11 sources have been clearly noted in the observation tables, and are not included in analysis where a statistically complete sample is described.

The data were reduced with MIRIAD using the standard techniques for ATCA 3 mm spectral line observations. Amplitude calibration with respect to Uranus and PKS B1921-293 was observed as the bandpass calibrator. The data were corrected for atmospheric opacity and the absolute flux density calibration is estimated to be accurate to 20 per cent. This was estimated by comparing the measured flux density of the bandpass and phase calibrator sources over each of the 3 d of the observations. The observing strategy interleaved 5 min on-source for each of the maser targets with 2.5 min observations of a phase calibrator, alternating between two different phase calibrator sources 1600-44 and 1613-586. The data were self-calibrated (phase-only) using the emission from the brightest 95-GHz methanol maser in each pointing. After self-calibration we used continuum subtraction (modelled using the spectral channels without maser emission) to isolate the spectral line and continuum emission components.

The 95-GHz maser emission was then subsequently imaged with a velocity plane width of 0.25 km s^{-1}. Imaging at higher than the spectral resolution of our observations does not affect our results due to the restrictions we place on determination of individual components. The pointing centre for each of the observations is listed in Table 1, along with information on the total time on-source for each source and the RMS noise for both the continuum data and a 0.25 km s^{-1} spectral resolution image cube. We adopted a rest frequency of 95.169489-GHz for the 8_0–7_1A$^+$ transition of methanol (Müller, Menten & Mäder 2004).

3 RESULTS

We detected 95-GHz methanol maser emission towards all 32 of our target sources. A continuum source was detected in 14 out of 32 target pointings. The majority of continuum sources detected were point sources, however, more extended continuum emission was observed in four cases (G 326.641+0.61, G 331.132−0.24, G 333.068−0.44, and G 333.163−0.10). Table 2 contains details of the location and flux density of these continuum sources, along with information on whether the 6.7-GHz pointing target or 95-GHz class I masers were associated. An association was considered to exist between the 95-GHz continuum emission and the two maser species, if the maser components were within 3 s of arc from the peak continuum emission.

In all observed sources the methanol maser emission was detected in many spectral channels. Emission in consecutive spectral channels is often at a similar location and is therefore considered a single component. In order to describe the maser emission as a series of 'spots, we have to define a set of criteria for when we consider emission adequately separated in space and velocity to be considered a unique maser component. Here we are considering emission regions to be independent if they are separated by at least 1.4 arcsec (upper 3σ positional error across all sources) or separated by at least 1 km s^{-1} in LSR velocity. If the angular separation criteria were met, the component was considered unique; If only the velocity separation criterion was met, the spectrum of the component was closely considered in order to determine that it was unique, and not the result of broad emission from another component it shares a position with. The 95-GHz components detected in the target sources are listed within Table 3. In total, 172 unique 95-GHz maser components were detected across our 32 class II targets. The absolute position of these components has been listed, along with their corresponding alphabetized location, as defined by Voronkov et al. (2014).

Table 1. The coordinates of the pointing centre for each of the 6.7-GHz class II maser sites observed, along with on-source time and RMS noise for the observations. Distance estimates to the target sources along with their associated error (values in parenthesis are the negative error bars in cases where errors are asymmetrical) are also included and drawn from Green & McClure-Griffiths (2011). Three sources (G 331.13−0.24, G 333.128−0.44, and G 333.466−0.16) did not have previously estimated linear distances, for these sources a near kinematic distance has been assumed using the same parameters and methodology presented in Green & McClure-Griffiths (2011) and their distances denoted with an asterisk. The final column reports the linear offset between each class II pointing target and the closest detected 95-GHz maser component with velocity coincident to the velocity range of the class II emission (for the estimated distance). Velocity range values for the class II sources are drawn from Caswell et al. (2011) and Green et al. (2012).

Source name	RA (J2000) *h m s*	Dec. (J2000) ° ′ ″	Time on-source (min)	RMS noise Cont (mJy beam^{-1})	RMS noise Line (mJy beam^{-1})	Dist. (kpc)	Dist. error (kpc)	Class I offset (pc)
G 326.48+0.70	15 43 16.60	−54 07 12.70	29.9	4.5	150	11.8	0.4	0.076
G 326.64+0.61[a]	15 44 32.90	−54 05 28.60	29.9	2.0	60	2.3	0.4	0.037
G 326.86−0.67[a]	15 51 14.20	−54 58 04.90	24.6	1.5	45	3.2	0.3(0.4)	–
G 327.39+0.19	15 50 18.50	−53 57 06.40	24.6	2.1	42	4.5	0.4(0.3)	0.072
G 327.63−0.11	15 52 50.20	−54 03 00.70	24.6	1.9	45	8.9	0.4	–
G 328.24−0.54[a]	15 57 58.40	−53 59 23.10	29.9	1.7	50	12.0	0.4	0.053
G 328.25−0.53	15 57 59.80	−53 58 00.90	29.9	2.3	45	2.6	0.4	0.007
G 328.81+0.63[a]	15 55 48.60	−52 43 06.20	30.9	4.7	55	2.6	0.4	0.028
G 329.03−0.20	16 00 31.80	−53 12 49.70	24.8	2.5	50	12.0	0.4	0.112
G 329.03−0.19	16 00 30.30	−53 12 27.30	24.9	1.5	65	12.0	0.4	0.077
G 329.07−0.30	16 01 09.90	−53 16 02.70	21.4	1.5	48	11.8	0.4	0.312
G 329.18−0.31	16 01 47.00	−53 11 44.20	25.2	1.8	48	3.3	0.3	0.037
G 329.47+0.50	15 59 40.70	−52 23 27.70	24.6	1.4	44	10.8	0.3	0.026
G 331.13−0.24	16 10 59.70	−51 50 22.70	25.2	1.7	45	5.2∗	0.3	0.032
G 331.34−0.34	16 12 26.50	−51 46 16.90	24.6	2.2	45	3.9	0.3	0.048
G 331.44−0.18[a]	16 12 12.50	−51 35 10.30	24.6	2.0	42	10.1	0.3	0.033
G 332.30−0.09	16 15 45.40	−50 55 53.90	24.6	1.6	45	3.0	0.3(0.4)	0.011
G 332.60−0.16	16 17 29.30	−50 46 12.50	24.6	1.8	50	2.8	0.3(0.4)	0.013
G 332.94−0.68[a]	16 21 19.00	−50 54 10.40	24.6	2.6	48	3.2	0.3(0.4)	–
G 332.96−0.67[a]	16 21 22.90	−50 52 58.70	24.6	1.7	45	2.8	0.3(0.4)	0.006
G 333.03−0.06[a]	16 18 56.70	−50 23 54.20	24.6	1.7	48	2.5	0.4	0.009
G 333.07−0.44	16 20 49.00	−50 38 40.70	24.6	1.8	45	3.3	1.5	–
G 333.12−0.43	16 20 59.70	−50 35 52.30	25.2	2.2	60	3.0	1.5	0.025
G 333.13−0.44	16 21 03.30	−50 35 49.80	24.6	3.3	55	3.3∗	0.3(0.4)	0.143
G 333.13−0.56[a]	16 21 35.40	−50 40 57.00	24.6	1.7	50	3.3	0.3	0.066
G 333.16−0.10[a]	16 19 42.70	−50 19 53.20	24.6	1.7	50	4.9	0.3	0.208
G 333.18−0.09	16 19 45.60	−50 18 35.00	24.6	2.0	45	4.6	0.3	0.032
G 333.23−0.06	16 19 51.30	−50 15 14.10	24.6	1.7	400	4.6	0.3	0.035
G 333.32+0.10	16 19 29.01	−50 04 41.50	24.6	1.7	50	12.3	0.4(0.3)	0.099
G 333.47−0.16	16 21 20.20	−50 09 48.60	24.9	3.0	60	3.2∗	0.3(0.4)	0.030
G 333.56−0.02	16 21 08.80	−49 59 28.30	24.9	2.3	80	12.6	0.4	0.093
G 335.06−0.42[a]	16 29 23.10	−49 12 27.30	24.9	1.8	55	2.4	0.4	0.028

Note. [a]Sources are not within the statistically complete sample of 6.7-GHz methanol masers

We aim to compare our observations to those presented in Voronkov et al. (2014), who imaged 71 southern class I methanol maser sources at 36- and 44-GHz with the ATCA, with typical 1σ RMS noise levels of ∼70 and ∼120 mJy at 36- and 44-GHz, respectively. Voronkov et al. identified class I components that were roughly spatially associated and assigned them a letter name for ease of reference. We have used these same locations for grouping and referring to the components presented here. The 95-GHz components, along with the 36- and 44-GHz components from Voronkov et al. (2014), have been plotted on a series of field images (see Fig. 1). There are 30 field images total, covering the 32 targets sources from our observations, as two fields have multiple pointings (G329.03–0.20 and G333.13–0.44). In addition to these field images, Fig. 2 shows scalar averaged spectra for all sources (except G328.25−0.53 where scalar averaging prevented emission from being clearly identifiable). These spectra all appear very similar to those presented in Ellingsen, Shabala & Kurtz (2005) for the same sources, albeit with generally higher SNR.

In all but three instances, locations containing 95-GHz components also harbour 44-GHz emission (as specified by Voronkov et al. 2014). The exceptions occur in the sources G328.25−0.53 and G328.81+0.63, where the 95-GHz masers are located within ∼4 arcsec of a class II 6.7-GHz maser, but do not have an associated 44-GHz class I component.

A close association between 95- and 44-GHz methanol masers is expected because the two transitions belong to the same transition series ($J_0 - (J - 1)_1A^+$) and there is a reported correlation between the observed flux density of the two transitions (Val'tts et al. 2000).

All, except one (G333.07−0.45), of our target sources had previously observed class I maser emission (from the 36-GHz and 44-GHz transitions) reported by Voronkov et al. (2014). Due to the significantly smaller primary beam at 95-GHz (∼30 arcsec), along with the expected flux density of the 95-GHz masers being half of that observed in associated 44-GHz masers, there are likely other 95-GHz components located outside the half-power range of our primary beam that we are unable to detect (specifically in regions with strong 44-GHz emission).

Table 2. Details of the continuum sources detected in 14 of the pointing targets. Including location of the peak emission, peak flux density, integrated flux density and whether any association is observed with either class II 6.7-GHz masers or detected 95-GHz masers.

Source name	RA (J2000) *h m s*	Dec. (J2000) ° ′ ″	Peak flux density (mJy)	RMS noise (mJy)	Integrated flux density (mJy)	Associations Class II	Class I
G 326.48+0.70	15:43:16.48	−54:07:14.0	94	4.3	105.2	y	y
G 326.64+0.61[a]	15:44:32.85	−54:05:28.6	23.2	2.1	41.9	y	y
G 326.86−0.67			<5				
G 327.39+0.19			<7				
G 327.62−0.11			<6				
G 328.24−0.54[a]	15:57:58.37	−53:59:21.9	63.9	1.6	66.2	y	y
G 328.25−0.53			<8				
G 328.81+0.63[a]	15:55:48.48	−52:43:07.2	973.3	4.8	1007	y	y
G 329.03−0.20			<9				
G 329.03−0.19			<5				
G 329.07−0.30	16:01:07.86	−53:16:05.8	9.6	1.6	9.7	n	n
	16:01:09.99	−53:16:00.3	7.4	1.6	7.2	y	n
G 329.18−0.31	16:01:47.99	−53:11:58.6	9.4	1.9	11.6	n	n
	16:01:47.22	−53:11:41.3	9.8	1.9	10.0	y	y
G 329.47+0.50			<4				
G 331.13−0.24	16:10:59.67	−51:50:23.8	122.7	1.7	147.2	y	y
G 331.34−0.34			<7				
G 331.44−0.18[a]	16:12:12.75	−51:35:10.4	26.1	2.0	28.1	y	y
G 332.30−0.09	16:15:45.58	−50:55:55.3	17.9	1.6	27.4	y	y
G 332.60−0.16			<7				
G 332.94−0.68[a]			<9				
G 332.96−0.67[a]			<6				
G 333.03−0.06[a]			<6				
G 333.07−0.44	16:20:48.88	−50:38:39.6	11.6	1.8	30.6	y	y
G 333.12−0.43	16:20:59.78	−50:35:50.6	14.0	2.4	14.0	y	y
G 333.13−0.44	16:21:02.46	−50:35:57.1	42.3	3.6	48.1	y	y
G 333.13−0.56[a]			<6				
G 333.16−0.10[a]	16:19:42.43	−50:19:53.3	16.0	1.8	30.7	y	y
G 333.18−0.09			<7				
G 333.23−0.06	16:19:51.08	−50:15:13.9	10.7	1.9	11.6	y	y
G 333.32+0.10			<5				
G 333.47−0.16			<9				
G 333.56−0.02			<8				
G 335.06−0.42[a]			<6				

NOte. [a]Sources are not within the statistically complete sample of 6.7-GHz met ısers.

3.1 Notes on individual sources

With the exception of G333.07−0.44, all the sources reported here have previous high resolution observations of the 36- and 44-GHz transitions by Voronkov et al. (2014). In the comments below, we have not repeated the information given by Voronkov et al. relating to the general class I maser distribution, we comment only on the specifics of the new 95-GHz methanol maser information.

The field images presented in this study are created in the same way as those previously presented by Voronkov et al. (2014) and therefore any prior comment on the *Spitzer* background images for individual sources will apply here.

3.1.1 G326.48+0.70

The majority of 95-GHz methanol maser emission is associated with site A, close to the north-west class II 6.7-GHz maser. 95-GHz components trace the same linear structure, beginning at A and extending south-west, observed in the 36- and 44-GHz transitions. Within the FWHM of the 95-GHz primary beam, there are two EGOs, both considered likely outflow candidates (Cyganowski et al. 2008). There is an EGO located at A (obscured by maser ıols at this location in Fig. 1), along with a larger region sev- arcseconds to the east. Class I methanol maser emission is ıiated with both of these EGOs (only the western edge of the r EGO), however, 95-GHz methanol maser emission is only ally associated with the EGO at A. In addition to these two s, there is another infrared source with 4.5-μm excess within alf-power range of our observations, located south-east of G. ɜ is 3.5-mm continuum source detected at A, with peak inten- ɔoincident with the densest cluster of class I methanol maser sion. 36- and 44-GHz emission has been detected in a second ɔy 6.7-GHz maser, located in the south-east of this field and ıiated with a strong infrared source. However, this region is far nd the half-power point of our 95-GHz pointing. A follow-up ɾvation of this south-eastern class II source would likely pro- additional detections of 95-GHz class I methanol emission in egion.

G326.64+0.61

6.7-GHz target source is located on the edge of a large 8.0-μm ent (seen in the south-east corner of the field). Class I emission is field is widely spread, however, the half-power range of

Table 3. Detailed list of the 95 GHz components detected in each maser site, including their alphabetical location as defined by Voronkov et al. (2014), positions, and flux density. Source names have been converted from those of the individual pointings to those used by Voronkov et al. (2014); This results in two cases where two 95‘GHz pointings have been combined into one source.

Source name	Location	LSR velocity ($km\,s^{-1}$)	RA (J2000) *h m s*	Dec. (J2000) ° ′ ″	Flux density (Jy)
G 326.48+0.70	A	−47.0	15:43:16.67	−54:07:16.9	0.31
	A	−46.3	15:43:16.38	−54:07:16.6	0.33
	A	−45.2	15:43:16.49	−54:07:14.5	0.85
	A	−44.0	15:43:16.46	−54:07:14.3	6.04
	A	−41.7	15:43:16.37	−54:07:15.1	8.18
	A	−40.5	15:43:16.15	−54:07:16.7	14.62
	A	−37.7	15:43:16.22	−54:07:16.1	1.96
	B	−39.5	15:43:15.98	−54:07:12.9	3.56
	B	−39.3	15:43:15.84	−54:07:11.3	4.31
G 326.64+0.61[a]	B	−43.0	15:44:33.60	−54:05:20.9	0.50
	B	−37.3	15:44:33.60	−54:05:23.0	1.57
	D	−41.0	15:44:32.96	−54:05:31.0	0.99
	D	−40.8	15:44:32.72	−54:05:33.2	1.27
	D	−40.0	15:44:32.95	−54:05:30.8	3.17
	D	−38.2	15:44:32.85	−54:05:32.3	6.45
G 326.86−0.67	A	−67.3	15:51:13.84	−54:58:04.7	3.22
	A	−66.7	15:51:13.73	−54:58:05.0	8.31
	A	−66.0	15:51:13.76	−54:58:05.1	5.79
	A	−65.5	15:51:13.91	−54:58:05.2	1.44
	B	−68.8	15:51:14.11	−54:58:03.8	0.53
	B	−67.8	15:51:14.05	−54:58:03.9	2.04
G 327.39+0.19	B	−88.8	15:50:18.53	−53:57:06.3	3.30
	B	−87.3	15:50:18.32	−53:57:07.8	1.96
	B	−86.5	15:50:18.13	−53:57:07.4	0.57
G 327.62−0.11	A	−88.0	15:52:50.20	−54:03:00.9	6.78
	B	−86.8	15:52:50.31	−54:03:05.5	0.88
G 328.24−0.54[a]	A	−42.3	15:57:58.38	−53:59:22.9	0.99
	A	−41.7	15:57:58.34	−53:59:20.3	1.12
	A	−40.8	15:57:58.27	−53:59:17.7	7.55
	A	−40.0	15:57:58.39	−53:59:20.5	0.42
	A	−39.3	15:57:58.55	−53:59:19.5	0.54
	A	−37.7	15:57:58.66	−53:59:19.8	0.42
	B	−44.0	15:57:58.46	−53:59:31.3	0.49
	B	−43.2	15:57:58.28	−53:59:31.3	1.86
G 328.25−0.53	-	−44.0	15:57:59.93	−53:57:57.4	0.53
	-	−43.5	15:57:59.82	−53:58:01.5	0.47
	-	−41.7	15:57:59.81	−53:58:00.5	1.67
G 328.81+0.63	A	−42.0	15:55:50.23	−52:43:21.7	4.72
	B	−42.5	15:55:49.15	−52:43:23.6	3.66
	C	−41.0	15:55:48.25	−52:43:19.8	2.46
	C	−40.3	15:55:48.49	−52:43:19.5	14.89
	J	−44.7	15:55:48.48	−52:43:06.5	1.22
	J	−43.5	15:55:48.53	−52:43:05.8	1.66
	J	−38.0	15:55:48.84	−52:43:07.1	0.50
G 329.03−0.20[a b]	A	−46.5	16:00:30.33	−53:12:28.7	1.65
	F	−43.2	16:00:31.98	−53:12:45.7	18.87
	F	−42.0	16:00:31.84	−53:12:47.2	9.09
	G	−41.2	16:00:31.90	−53:12:55.8	3.67
	G	−40.5	16:00:31.76	−53:12:51.5	3.12
	G	−39.7	16:00:31.81	−53:12:52.6	3.13
	G	−38.2	16:00:32.05	−53:12:53.7	1.40
	G	−37.5	16:00:32.01	−53:12:54.7	4.15
G 329.03−0.19[b]	A	−46.5	16:00:30.29	−53:12:28.6	16.06
	A	−44.7	16:00:30.06	−53:12:26.0	1.09
	B	−45.5	16:00:30.45	−53:12:13.5	2.99
	D	−44.2	16:00:30.46	−53:12:19.6	0.67
G 329.07−0.30	D	−41.7	16:01:08.95	−53:16:07.8	2.87
	D	−40.5	16:01:09.33	−53:16:03.5	0.37
	D	−40.2	16:01:09.18	−53:16:07.7	0.37

Table 3 – *continued*

Source name	Location	LSR velocity ($km\,s^{-1}$)	RA (J2000) *h m s*	Dec. (J2000) ° ′ ″	Flux density (Jy)
G 329.18−0.31	C	−49.2	16:01:46.70	−53:11:49.2	0.56
	E	−50.2	16:01:47.26	−53:11:43.8	0.70
	E	−48.5	16:01:47.15	−53:11:42.1	0.56
	E	−47.2	16:01:47.33	−53:11:42.3	2.54
	E	−46.2	16:01:47.17	−53:11:42.0	0.39
G 329.47+0.50	B	−66.2	15:59:40.15	−52:23:35.7	2.64
	E	−69.0	15:59:40.66	−52:23:27.5	0.53
	E	−68.8	15:59:40.74	−52:23:29.3	0.53
	E	−67.3	15:59:40.69	−52:23:28.4	0.36
	F	−68.2	15:59:40.91	−52:23:30.4	0.78
G 331.13−0.24	A	−90.8	16:10:59.59	−51:50:25.7	35.43
	A	−86.8	16:10:59.74	−51:50:24.5	4.18
	A	−85.8	16:10:59.69	−51:50:23.7	4.35
	A	−84.8	16:10:59.73	−51:50:24.3	3.28
	A	−82.5	16:10:59.90	−51:50:25.6	2.67
	A	−80.3	16:11:00.00	−51:50:26.7	0.71
	B	−88.3	16:11:00.74	−51:50:23.9	10.42
	C	−84.0	16:11:00.25	−51:50:25.9	5.08
G 331.34−0.34	A	−66.5	16:12:26.41	−51:46:18.9	0.60
	A	−65.2	16:12:26.50	−51:46:20.6	15.17
G 331.44−0.18[a]	A	−91.3	16:12:12.28	−51:35:13.3	5.05
	A	−89.5	16:12:12.23	−51:35:13.0	1.02
	C	−87.3	16:12:11.41	−51:35:18.3	1.99
	D	−90.5	16:12:12.32	−51:35:10.8	0.28
	D	−90.3	16:12:12.35	−51:35:12.3	0.91
	D	−89.0	16:12:12.33	−51:35:11.0	0.75
	D	−88.5	16:12:12.44	−51:35:09.6	0.52
	D	−87.5	16:12:12.57	−51:35:08.5	3.21
	D	−86.5	16:12:12.55	−51:35:08.6	0.83
	D	−86.0	16:12:12.39	−51:35:07.4	0.44
	D	−85.5	16:12:12.51	−51:35:09.2	0.42
G 332.30−0.09	A	−52.2	16:15:45.30	−50:55:54.9	0.31
	A	−51.7	16:15:45.72	−50:55:55.0	0.64
	A	−50.5	16:15:45.86	−50:55:55.2	5.71
	A	−49.2	16:15:45.78	−50:55:55.3	19.11
	A	−48.0	16:15:45.65	−50:55:55.8	7.21
	A	−47.2	16:15:45.45	−50:55:55.7	1.23
	A	−47.0	16:15:45.29	−50:55:56.3	1.16
	A	−46.5	16:15:45.45	−50:55:54.3	0.77
	C	−45.5	16:15:44.21	−50:55:56.6	1.50
G 332.60−0.16	A	−46.2	16:17:29.27	−50:46:14.6	0.70
	A	−45.5	16:17:29.22	−50:46:12.8	8.52
G 332.94−0.68[a]	A	−50.0	16:21:19.32	−50:54:13.7	1.52
	A	−48.2	16:21:19.44	−50:54:13.0	4.34
	A	−46.7	16:21:19.32	−50:54:13.8	1.01
G 332.96−0.67[a]	A	−50.7	16:21:22.93	−50:52:56.7	0.42
	A	−50.2	16:21:22.71	−50:52:55.7	0.76
	A	−50.0	16:21:22.84	−50:52:57.5	0.49
	A	−48.7	16:21:22.88	−50:52:58.7	0.71
	A	−48.2	16:21:22.84	−50:52:56.9	2.06
	A	−46.7	16:21:22.76	−50:52:56.7	11.13
G 333.03−0.06[a]	A	−41.7	16:18:56.64	−50:23:53.4	1.17
	A	−40.3	16:18:56.77	−50:23:54.9	4.27
G 333.07−0.44	-	−53.7	16:20:48.83	−50:38:40.2	0.47
	-	−51.2	16:20:48.64	−50:38:39.1	2.75
G 333.13−0.56[a]	A	−59.5	16:21:34.33	−50:41:06.8	1.13
	B	−57.2	16:21:35.91	−50:40:49.1	1.45
	B	−56.5	16:21:36.10	−50:40:48.7	1.74
	B	−56.3	16:21:36.33	−50:40:48.3	1.64
	B	−55.3	16:21:36.43	−50:40:47.4	4.65
	B	−54.0	16:21:36.08	−50:40:48.1	8.69
	D	−58.8	16:21:35.79	−50:40:55.1	7.51

Table 3 – *continued*

Source name	Location	LSR velocity ($km\,s^{-1}$)	RA (J2000) *h m s*	Dec. (J2000) ° ′ ″	Flux density (Jy)
G 333.12−0.43[c]	B	−58.0	16:20:59.75	−50:35:51.3	0.32
	B	−56.3	16:20:59.71	−50:35:51.7	0.49
	B	−55.0	16:20:59.73	−50:35:50.9	1.43
	B	−52.3	16:20:59.49	−50:35:50.5	9.31
	B	−50.2	16:20:59.42	−50:35:49.0	8.10
	B	−49.3	16:20:59.63	−50:35:50.2	1.02
	B	−45.3	16:20:59.64	−50:35:51.5	1.74
G 333.13−0.44[c]	A	−48.7	16:21:02.58	−50:35:54.5	18.44
	A	−48.0	16:21:02.18	−50:35:50.8	18.85
	A	−47.7	16:21:02.41	−50:35:53.0	17.54
	A	−47.0	16:21:02.63	−50:35:54.0	19.87
	A	−46.2	16:21:02.35	−50:35:53.1	10.64
	A	−44.5	16:21:02.39	−50:35:52.9	0.49
	E	−51.5	16:21:03.32	−50:35:45.1	0.41
	E	−50.7	16:21:03.16	−50:35:45.9	1.91
	DF	−49.7	16:21:03.73	−50:35:38.8	12.21
	F	−51.2	16:21:03.18	−50:35:38.4	0.90
G 333.16−0.10[a]	A	−92.0	16:19:42.12	−50:20:00.2	0.93
	B	−91.0	16:19:42.71	−50:19:55.3	4.74
G 333.18−0.09	A	−86.8	16:19:45.54	−50:18:32.4	0.80
	A	−86.3	16:19:45.65	−50:18:33.6	3.25
	A	−85.3	16:19:45.96	−50:18:31.9	0.68
G 333.23−0.06	A	−89.5	16:19:49.52	−50:15:14.1	0.89
	A	−86.8	16:19:49.49	−50:15:14.3	35.57
	C	−85.0	16:19:51.41	−50:15:14.1	4.90
	C	−83.8	16:19:51.28	−50:15:12.5	0.40
G 333.32+0.10	A	−49.2	16:19:28.74	−50:04:38.7	1.11
	A	−45.5	16:19:29.26	−50:04:43.6	0.38
	A	−44.0	16:19:28.85	−50:04:40.7	3.78
	B	−48.0	16:19:28.14	−50:04:38.7	0.86
	B	−47.2	16:19:28.34	−50:04:39.1	0.56
	B	−46.7	16:19:27.98	−50:04:42.8	0.56
	B	−46.0	16:19:28.09	−50:04:37.4	0.47
	D	−44.7	16:19:28.62	−50:04:53.5	0.73
G 333.47−0.16	A	−45.0	16:21:19.94	−50:09:42.0	3.19
	B	−41.0	16:21:20.10	−50:09:38.1	2.13
	C	−42.3	16:21:20.55	−50:09:55.5	1.80
	D	−43.0	16:21:20.15	−50:09:46.7	5.38
	D	−40.5	16:21:20.42	−50:09:48.8	0.43
	E	−42.5	16:21:19.69	−50:09:33.7	1.42
G 333.56−0.02	A	−40.8	16:21:08.77	−49:59:49.5	0.81
	A	−39.5	16:21:08.74	−49:59:49.5	9.35
	A	−38.2	16:21:08.59	−49:59:47.8	0.73
G 335.06−0.42[a]	A	−41.7	16:29:23.50	−49:12:23.2	1.13
	A	−41.2	16:29:23.46	−49:12:22.5	0.57
	A	−40.5	16:29:23.42	−49:12:21.0	3.70
	B	−39.7	16:29:22.98	−49:12:32.8	0.31
	B	−38.8	16:29:22.80	−49:12:32.4	4.83
	B	−37.7	16:29:23.04	−49:12:32.1	3.25
	B	−37.3	16:29:23.07	−49:12:30.5	0.53
	B	−37.0	16:29:23.19	−49:12:29.4	0.47

Note. [a]Sources are not within the statistically complete sample of 6.7-GHz methanol masers.
[b]Components from this target are included in the multipointing field image G 329.03−0.20.
[c]Components from this target are included in the multipointing field image G 333.13−0.44.

our observations contains the majority of locations of previously detected methanol maser emission (A, B, D, E, G, and J). 95-GHz maser emission is observed in two locations (B and D). A 3.5-mm continuum source is detected near D and E (∼3 arcsec north-west of the 6.7-GHz maser), with the majority of class I maser emission at D associated with the southern edge. Additionally the 95-GHz masers at this location are arranged in a line extending from the edge of this continuum emission towards the south-west.

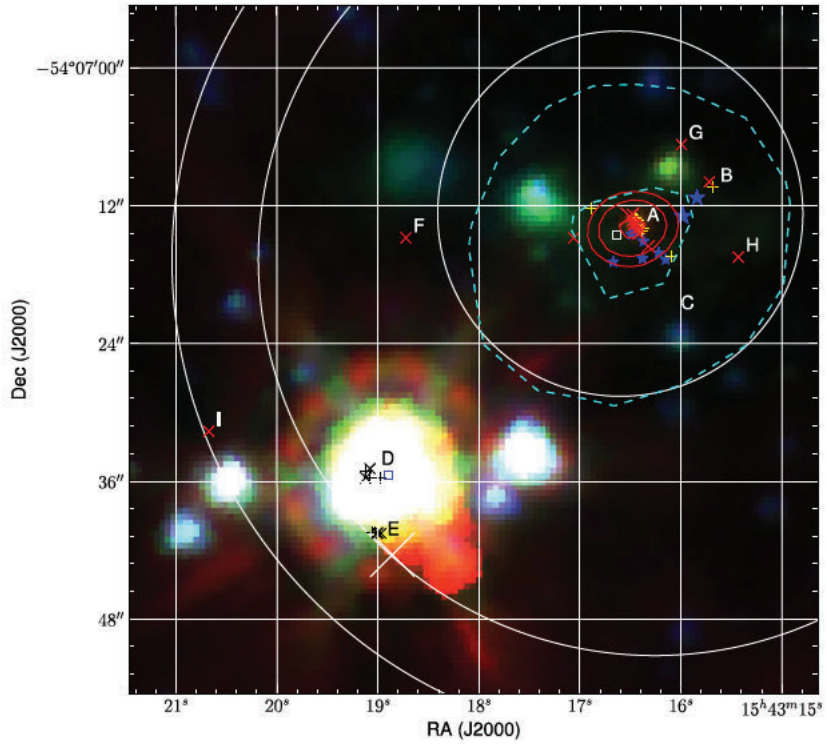

Figure 1. Field image for G 326.48+0.70 and field images for the remaining 29 class I sources are available online. Four different symbols are projected on the *Spitzer* background images, a square symbol represents a 6.7-GHz class II methanol maser, and the cross, plus, and star symbols represent 36-, 44-, and 95-GHz class I maser emission, respectively. Solid contours on the images represent 95-GHz continuum emission where applicable. Dashed contours represent the 50 per cent and 90 per cent levels of the ATLASGAL emission. The white circles, in order of increasing size, represent the full width at half-maximum (FWHM) of the primary beam and are centred on the pointing direction for the 95-, 44-, and 36-GHz observations.

3.1.3 G326.86−0.68

Class I emission is relatively tightly clustered in this source, with locations B and A containing all the observed 95-GHz maser components. The class I emission at B is associated with a 6.7-GHz class II maser. East of the class II maser is a dark cloud, with class I emission at B and C located at the interface of this region (Peretto & Fuller 2009). The 95-GHz masers in this source are located at the south-east edge of an EGO (likely outflow candidate according to Cyganowski et al. 2008).

3.1.4 G327.39+0.20

The methanol maser emission is separated into two separate locations (A and B), both with 6.7-GHz masers and associated with strong infrared sources. The 95-GHz pointing was centred on the westernmost 6.7-GHz maser (327.392+0.199) within this field. Although both locations are within the FWHM of the 95-GHz primary beam, 95-GHz maser emission is only observed at B. The infrared source associated with B also contains a 4.5-μm halo that has been classified as an EGO and considered a possible outflow candidate in Cyganowski et al. (2008).

3.1.5 G327.62−0.11

The centre of this field contains a strong infrared source where the 6.7-GHz maser target and class I maser location A is situated. Only two 95-GHz components were observed in this source, one component tightly co-located with the 6.7-GHz maser, and one component at B on the southern edge of the infrared source. Similar to what is observed in the other class I transitions, the 95-GHz maser emission at location A is considerably stronger than that observed in B (Voronkov et al. 2014).

3.1.6 G328.24−0.55

The 6.7-GHz pointing target is in the south-western corner of the field, with the majority of class I maser emission located nearby in A and B. The 95-GHz masers at A are loosely clustered, with the majority of these components being associated with other class I maser emission. The 6.7-GHz maser is a few arcseconds south of A and associated with a 95-GHz component. A 3.5-mm continuum source is observed, co-spatially associated with the class II 6.7-GHz maser. The 95-GHz masers at A appear to follow some sort of arc that may be related to the 8.0-μm PDR situated north-east of these masers.

3.1.7 G328.25−0.53

The class II 6.7-GHz maser in this source is associated with a strong infrared source in the south-west of the field. The 36- and 44-GHz emission in this source is spread between six locations spanning over 1 arcmin squared, only one of which (A) is within the FWHM of the 95-GHz primary beam. The 95-GHz masers in this source are not associated with any of the locations where 36- and 44-GHz masers are detected, and instead they are associated with the 6.7-GHz maser target. This is one of only two cases across all of our sources where 95-GHz masers are observed offset from the other

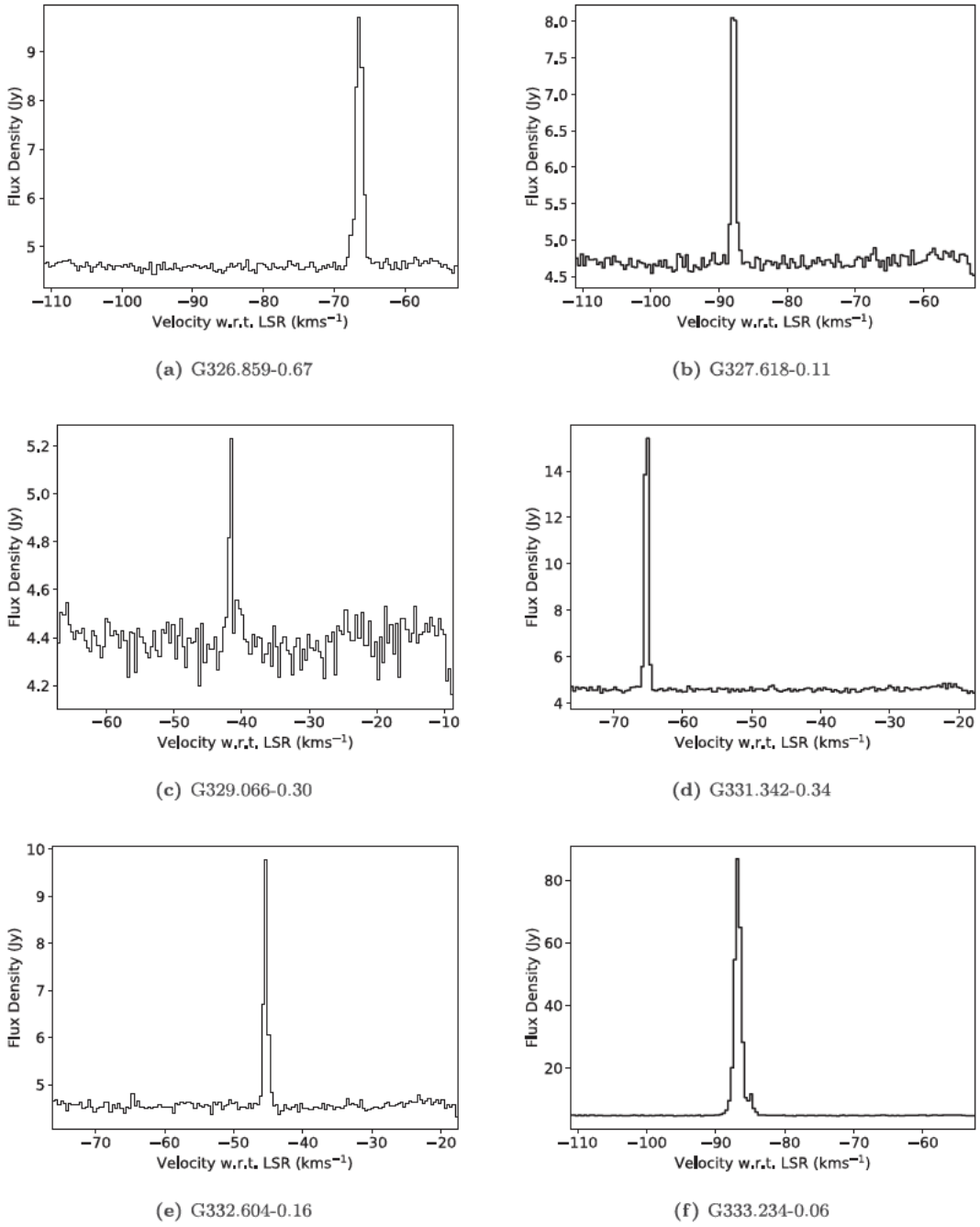

(a) G326.859-0.67 (b) G327.618-0.11

(c) G329.066-0.30 (d) G331.342-0.34

(e) G332.604-0.16 (f) G333.234-0.06

Figure 2. Representative spectra of 95-GHz class I methanol masers from the current observations. Spectra for the remaining sources in the sample are available online. The spectra were extracted from scalar averaging of the self-calibrated ultraviolet (UV)-data used to create spectral line image cubes. Scalar averaged spectra allow us to see maser emission from all class I locations in the primary beam, but have a positive offset baseline because of contributions from the system temperature of the receivers and any continuum emission in the primary beam.

transitions of class I emission. An EGO is also nearby to this class II source (likely outflow candidate according to Cyganowski et al. 2008), with one 95-GHz component located at the interface of the EGO and the infrared source.

3.1.8 G328.81+0.63

Two strong class II 6.7-GHz masers, separated by 2″.5, are projected on to a H II region in the centre of this field (Walsh et al. 1998; Green et al. 2012). The 95-GHz maser emission is spatially associated with the two 6.7-GHz masers at J. A 3.5-mm continuum source is detected at J, with peak emission at the location of the western 6.7-GHz maser. Interestingly there is no 44-GHz maser emission associated with the 95-GHz masers in this location, however, indicating the continuum source may be seeding the emission of these masers. This may occur due to the 95-GHz masers amplifying the underlying continuum emission, which may differ significantly between 7- and 3.5-mm, which boosts the expected ratio of 95–44-GHz

flux densities at these projected locations. 95-GHz masers at B and C trace the southern edge of the diffuse 8.0-μm excess south of the H II region.

3.1.9 G329.03−0.20

This field contains two separate 95-GHz pointings, one centred on the north-western 6.7-GHz maser 329.031-0.198 and the other on the south-eastern 6.7-GHz maser 329.029−0.205. Class I maser emission in the south-east pointing is organized in a linear structure (from F to H), extending north and south from the class II pointing target. The majority of the 95-GHz emission in the north-west pointing is clustered about the 6.7-GHz maser (location A). An EGO is present in this field (classified as likely outflow candidate by Cyganowski et al. 2008), several arcseconds south of A, with a single 36-GHz component located on its western edge.

3.1.10 G329.07−0.31

The class II 6.7-GHz maser target is located in the centre of a strong infrared source. An additional strong infrared source is on the eastern edge of the FWHM of the 95-GHz primary beam. Extended 4.5-μm emission is present near both of the infrared sources, with both being classified as possible outflow candidates by Cyganowski et al. (2008). All detected 95-GHz maser components are located south-west of the 6.7-GHz maser, at the interface of the EGO between the western infrared source and location D. Interestingly we see the second case of a 95-GHz maser being offset from any previously observed class I maser emission, with the maser spot associated with the western edge of the infrared source. There are two weak continuum sources detected in this field, the weaker continuum source is spatially associated with the 6.7-GHz maser, and the stronger (40 per cent brighter) continuum source is located north-west of D, with no associated methanol emission or infrared source.

3.1.11 G329.18−0.31

The 6.7-GHz maser target's location is projected on to a prominent EGO (likely outflow candidate according to Cyganowski et al. 2008). The 95-GHz masers at E appear to trace the eastern boundary of the YSO and the EGO. The 95-GHz component at C is also located on the south-western edge of the EGO. Two weak continuum sources are detected in this region. The northern-most is positionally associated with the class I emission and 6.7-GHz maser at E. The southern-most continuum source is outside the FWHM of the 95-GHz primary beam with no visible associations. Both locations D and F contain comparatively bright 44-GHz class I methanol masers and are within the half-power range of the 95-GHz primary beam, however, no 95-GHz emission was detected in either of these regions.

3.1.12 G329.47+0.50

The majority of class I maser emission is clustered around the 6.7-GHz maser in the centre of the field. This class II source is on the eastern edge of an EGO (classified as a likely outflow candidate by Cyganowski et al. 2008). The majority of 95-GHz maser emission in this source is arranged in a line extending from the position of the 6.7-GHz maser towards the south-east.

3.1.13 G331.13−0.24

The 6.7-GHz source is located on the north-eastern edge of one of the northern-most H II regions in the field. This class II source is positioned at the interface between an EGO (likely outflow candidate according to Cyganowski et al. 2008) and this H II region. 95-GHz masers are located at the three locations nearby to this H II region. The 95-GHz maser components are organized into a curve starting at the position of the 6.7-GHz maser, going through C and ending to the east at location B. A 3.5-mm continuum source is detected, encompassing the entire northern H II region, including the majority of 95-GHz emission.

3.1.14 G331.34−0.35

A strong infrared source dominates the centre of this compact class I maser. The 6.7-GHz maser is situated centrally to this infrared source. A class I masing component with emission from 36-, 44-, and 95-GHz is situated at the interface between the strong infrared source and an EGO (classified as a possible outflow candidate by Cyganowski et al. 2008). We observe another component at 95 GHz to the north-west, closer to the location of the 6.7-GHz maser.

3.1.15 G331.44−0.19

The 6.7-GHz class II target source is projected on to the edge of a compact H II region. 95-GHz masers are detected at all three locations (A, C, and D) that fall within the half power point of the 95-GHz primary beam. A second 6.7-GHz maser is also located within the FWHM of the 95-GHz primary beam at C. 95-GHz emission in A and D trace a line across the H II region, connecting the two locations. The majority of 36- and 44-GHz components reported by Voronkov et al. (2014) form a line extending to the south-west from A through to E. Due to the line of 95-GHz components connecting D and A, class I maser emission from locations A through E may be all part of the same linear structure. A 3.5-mm continuum source is detected near D, with the emission between D and A tracing the outer edge of the emission.

3.1.16 G332.30−0.09

Two closely separated 6.7-GHz masers are within this field, the western 6.7-GHz maser (332.2950.094, the pointing target for this source), is located at the southern edge of an EGO (possible outflow candidate according to Cyganowski et al. 2008), and the second maser (332.296−0.094) is approximately 3 arcsec to the east. All but one of the 95-GHz maser components in this source are clustered between the northern edge of a H II region and the EGO to the north-west, with the other component situated ∼15 arcsec west. The 95-GHz components close to the eastern 6.7-GHz maser appear to be systematically offset by ∼1 arcsec south of the nearby 44-GHz maser components. An elongated 3.5-mm continuum source is detected at the location of the two 6.7-GHz masers, and encompasses all the 95-GHz maser emission at A.

3.1.17 G332.60−0.17

There are two sites of class I methanol emission within this source. The 6.7-GHz maser is associated with the southern class I emission and a faint EGO (classified as likely outflow by Cyganowski et al. 2008). Both 95-GHz maser components are situated on the western edge of this EGO, nearby (within 2 arcsec) to the class II maser.

3.1.18 G332.94−0.69

The class II 6.7-GHz maser is located on the eastern edge of an infrared source, surrounded by an EGO (classified as likely outflow candidate by Cyganowski et al. 2008) extending towards the south-east. All 95-GHz masers are situated at location A within the south-eastern region of the EGO. No 95-GHz maser emission is detected in location B, despite the relative brightness of the detected 44-GHz components.

3.1.19 G332.96−0.68

Location A, at the northern edge of a infrared point source with associated EGO (likely outflow candidate according to Cyganowski et al. 2008), contains the majority of class I emission in this source. The EGO extends to the south-east, ending near B. The 6.7-GHz target maser is projected on this infrared point source, with the bulk of the observed 95-GHz emission clustered closely associated.

3.1.20 G333.03−0.06

The 6.7-GHz maser along with class I emission in this source is tightly clustered between a strong infrared source and a region of 4.5-μm excess (not classified as EGO by Cyganowski et al. 2008). The 95-GHz masers here have a close association with the 44-GHz maser components.

3.1.21 G333.07−0.45

This is the source with no previous observation made by Voronkov et al. (2014). The 6.7-GHz maser pointing target is projected on to the centre of a bright infrared region, surrounded by a region of 4.5-μm excess. There are two detected 95-GHz masers in this source, both offset to the north-west of the class II maser. An elongated 3.5-mm continuum source is detected, with peak emission co-located with the 6.7-GHz masers and an extension towards the south-east.

3.1.22 G333.13−0.44

Four 6.7-GHz class II masers are present in this field, with two separate 95-GHz pointings covering the densest regions of class I emission (targets 333.128-0.440 in the east and 333.121-0.434 in the west). The half-power range of the eastern pointing contains four distinct regions of class I emission (A, D, E, and F), with a secondary 6.7-GHz maser associated with a strong infrared source at A. All 95-GHz masers from the eastern pointing form a line, starting at the position of the 6.7-GHz maser at A and extending towards the north-west. A 3.5-mm continuum source is also detected a few arcseconds south-west of this secondary 6.7-GHz maser.

The western pointing contains a single compact region of class I emission, clustered about the 6.7-GHz maser target (B), and located near the edge of a dark cloud. A 3.5-mm continuum source is also detected at this location, encompassing the 6.7-GHz maser and all but one of the 95-GHz maser components at B.

3.1.23 G333.13−0.56

The pointing target for this class I source was the southern-most of the two closely spaced 6.7-GHz masers, 333.128−0.560. 95-GHz masers are seen at three separate locations within this source, with the majority associated with an EGO (classified as possible outflow candidate by Cyganowski et al. 2008) north-east of the northern 6.7-GHz maser (B). These 95-GHz components appear to be distributed in a line across the EGO. Bright 95-GHz emission is also observed at D, equidistant from both class II masers. Emission from all three different class I transitions is projected at this location (D), with the masers potentially being associated with a slight 4.5-μm excess. Voronkov et al. (2014) suggested that B and D might be connected with a curved 4.5-μm structure going through the nearby 6.7-GHz maser.

3.1.24 G333.16−0.10

6.7-GHz maser is associated with the eastern side of a strong infrared source, and H II region in the centre of the field. Class I maser emission is observed in two compact locations (A and B) in this source. The masers at B are close to the 6.7-GHz maser (∼2 arcsec), whereas class I emission at A is offset to the south of the infrared source. An elongated 3.5-mm continuum source is detected, encompassing the infrared source and class I and class II emission at B.

3.1.25 G333.18−0.09

The 6.7-GHz maser target is associated with an infrared point source surround by a prominent EGO (classified as likely outflow candidate by Cyganowski et al. 2008) extending to the south-east. The 95-GHz maser components are spatially associated with the location of previously reported 36- and 44-GHz components at A along the northern edge of the EGO.

3.1.26 G333.23−0.06

The south-eastern 6.7-GHz maser (333.234−0.062) is the pointing target of the 95-GHz observations in this source. A secondary 6.7-GHz maser (333.234−0.060) is located a few arcseconds north-west, and is associated with a bright infrared source. 95-GHz emission is distributed between two locations, A and C. The former is outside the FWHM of the 95-GHz primary beam, however, it contains a very bright 95-GHz component (35.57 Jy, strong relative to the typical 95-GHz flux density values we observe). The 95-GHz masers at region C have a close spatial association with the position of the south-eastern 6.7-GHz maser. 3.5-mm continuum emission is detected, situated between the two 6.7-GHz masers on the south-eastern edge of the infrared source.

3.1.27 G333.32+0.11

The 6.7-GHz maser in this field is projected on to a strong infrared source, with an EGO (classified as likely outflow candidate by Cyganowski et al. 2008) at the north-western edge. 95-GHz maser components at location A are projected across the infrared source, with one component of 95-GHz emission located significantly south-east of any previously reported class I emission. Interestingly in this source there does not appear to be a close spatial association between the 95-GHz components and the 36- and 44-GHz components. This may be due to evolution in the source, over the 2.5 yr between observations.

3.1.28 G333.47−0.16

The 6.7-GHz maser pointing target in this source is located within the southern half of an EGO (classified likely outflow candidate by Cyganowski et al. 2008). Voronkov et al. (2014) note a curved distribution of class I emission at locations A, B, D, and F tracing a bow shock with the 6.7-GHz maser situated at the apex. The 95-GHz masers are consistent with the positions of the previously observed class I masers at A and B. However, at D one 95-GHz maser is located with the previously observed emission, and another is observed east of the 6.7-GHz maser at the edge of the EGO. No 95-GHz masers are observed at F, possibly due to the 44-GHz maser here being relatively weak compared to other locations in this source. 95-GHz masers are located at E and C also, making it appear that these masers trace the entire eastern edge of the EGO.

3.1.29 G333.56−0.02

A mistake in the observations of this source caused the pointing to be ∼18 arcsec north of the intended 6.7-GHz maser target. Therefore, all the class I emission is outside the FWHM of the 95-GHz primary beam to the south. All class I maser emission in this source is compactly clustered about this 6.7-GHz class II maser. One of the 95-GHz masers is offset to the north-east from the other class I emission.

3.1.30 G335.06−0.43

The class II maser is within the central region of an EGO (classified as a likely outflow candidate by Cyganowski et al. 2008). The 95-GHz masers at B and D closely trace the southern edge of the EGO. Voronkov et al. note that the class I emission at A appears to trace the northern edge of the EGO and the 95-GHz components at this location are consistent with this observation.

4 DISCUSSION

Throughout our discussion we will directly compare the 36- and 44-GHz methanol maser properties presented by Voronkov et al. (2014) to the current 95-GHz data. However, before doing that, it is important to highlight the differences in sample selection between the Voronkov et al. study and our investigation. Voronkov et al. selected almost all southern sources with previously detected class I maser emission from the single-dish searches of Slysh et al. (1994); Val'tts et al. (2000); Ellingsen (2005). The target sources for these original single-dish observations were highly varied, with a mix of known 6.7-GHz class II masers and H II regions. Comparatively, the targets for our investigation are based on the Ellingsen (2005) sample, which was more restrictive and consisted of all 6.7-GHz class II methanol masers with associated 95-GHz emission (a lower detection limit of ∼4.5 Jy) within the Galactic longitude range $l = 325° - 335°$, $b = \pm 0.53°$. This means that our sample is statistically complete with a different set of selection biases present than the Voronkov et al. sample. Due to all of our targets (except 333.07-0.45) being previously observed at high-resolution by Voronkov et al. (2014), we can compare all three of the observed class I transitions in our statistically complete maser target sample. Although we have 32 pointing targets total for our data, four of these pointings are associated with two class I sources (two pointings each source), therefore, in general, we will refer to a set of 30 class I sources throughout the discussion, except in cases where we are directly discussing relations between class I emission and the class II sources.

4.1 Diversity in class I methanol masers

In comparison to the complex spectra observed from class II methanol masers, class I emission appears to be considerably simpler. The spectra from multiple class I transitions observed from the same masing region often appear as single components with peak emission occurring at a common velocity. This contrasts with the typical spectrum of a class II region, with multiple bright components spread across a large velocity range. However, despite the similarities in appearance of the spectra of class I transitions, our investigation, combined with that of Voronkov et al. (2014), reveals significant differences between the three considered transitions. Our high-resolution observations, when compared to the 36- and 44-GHz observations of Voronkov et al. (2014), reveal frequent differences between the physical associations of the 95-GHz maser components with other phenomenon in the star-formation regions. 95-GHz masers are observed tracing ordered structures, both independently or coinciding with other class I transitions. We observe a stronger preference towards co-location with the class II maser position in the 95-GHz masers compared with the 36- or 44-GHz components. This observation is particularly interesting due to the shared optimal conditions for masing between the 95- and 44-GHz components (McEwen, Pihlström & Sjouwerman 2014; Leurini, Menten & Walmsley 2016). In addition, we see significant offsets in LSR velocity between matched components from the two A^+-type transitions (44-GHz blue-shifted compared to 95 GHz), which is not observed between the matched 95- and 36-GHz components. This diversity between transitions will be discussed further in the following sections.

4.2 General associations

The angular resolution of our observations allows us to determine the association of class I methanol masers and other phenomena observed in star-formation regions. The high angular resolution of the maser data combined with the *Spitzer* infrared images enables us to investigate association rates between the class I emission and EGOs and other 4.5-μm excess regions (Cyganowski et al. 2008). These regions of enhanced 4.5-μm emission can result from shocked gas (De Buizer & Vacca 2010), therefore, we expect to see high association rates with class I methanol masers. Voronkov et al. (2014) reported association rates of ∼54 and ∼82 per cent between class I emission and EGOs or any 4.5-μm excess source, respectively, across their entire sample of 64 class I sources. They considered an association to exist if a class I component was within a few arcseconds of the relevant region. Using this criterion for our observations, we found close spatial associations between 95-GHz class I emission and EGOs in 19 out of 30 sources (∼63 per cent). In 4 out of our 30 sources (G326.48+0.70, G328.24−0.55, G332.30−0.09, and G333.03−0.06), 95-GHz class I emission is associated with 4.5-μm excess sources that were not determined to be EGOs by Cyganowski et al. (2008), two of these (G326.48+0.70 and G332.30−0.09) have associations with EGOs in addition to these other 4.5-μm excess regions. Therefore, we see 21 out of 30 sources (∼70 per cent) have some sort of 95-GHz maser emission associated with regions of excess 4.5-μm emission. If we instead consider any class I emission (95-GHz masers combined with 36- and 44-GHz masers reported by Voronkov et al. 2014), we determine the following association fractions: 21 out of 30 target sources (∼70 per cent) contain class

I masers spatially associated with EGOs as defined by Cyganowski et al. (2008) and 24 out of 30 sources (80 per cent) have class I masers spatially associated with any 4.5-μm excess source. Therefore, we can conclude that in the majority of cases where both class I and class II methanol maser emission is observed, there is some component of class I maser emission is associated with a likely outflow candidate. Additionally, when comparing the association rates between EGOs and the class I transitions, we see the 95-GHz maser components have an increased association rate with confirmed EGOs compared to the other two class I transitions combined (Cyganowski et al. 2008; Voronkov et al. 2014). A review of single dish surveys of class I maser sources identified that approximately 50 per cent of class I maser sources have emission (44 or 95-GHz) within an arcminute of an outflow source (EGO or otherwise) (Chen, Ellingsen & Shen 2009), and subsequent searches for class I methanol masers targeted towards EGOs have achieved high detection rates (Chen et al. 2011). Our association rate between outflows and class I emission is significantly higher than this (80 per cent when considering any class I emission in our sources) and unlike the single-dish data, our high-resolution data allow us to directly confirm the presence of class I maser components within these outflow sources.

There are 57 reported EGOs within the Galactic longitude range of our statistically complete sample (Cyganowski et al. 2008). 22 (∼39 per cent) of these EGOs have 6.7-GHz class II methanol maser associations and 14 (∼25 per cent) have class I methanol maser detections in one or more of the discussed class I transitions (Cyganowski et al. 2008; Voronkov et al. 2014). Indicating that EGOs with associated 6.7-GHz methanol masers make good targets for observing class I methanol masers.

Twenty of the 6.7-GHz class II methanol masers that were observed here have associated 12.2-GHz class II methanol masers (Breen et al. 2012a,b). When considering our statistically complete sample 12 of 21 targets (∼57 per cent) are detected in the 12.2-GHz transition. Including all 6.7-GHz masers within the statistically complete sample, our targets were drawn from (all 6.7-GHz masers, regardless of presence of 95-GHz emission) we see an association rate between the two class II transitions (6.7 and 12.2 GHz) of 60 per cent. Comparing these two rates, we see that 6.7-GHz masers also displaying emission at 95-GHz do not appear to have a significantly different association rate with 12.2-GHz class II masers. Sources with emission present from 12.2-GHz class II methanol masers tend to be at a later evolutionary stage than those without (Breen et al. 2010, 2011). This indicates that 95-GHz class I emission does not appear to favour these more evolved sources.

4.3 Continuum association

In addition to the observations of 95-GHz maser emission, we also searched for 3.5-mm continuum in each of our targets. We detected 3.5-mm continuum emission in 14 of our 32 pointings, with two of these pointings corresponding to the one class I methanol maser source. Therefore, 3.5-mm continuum emission is observed in 13 of the 30 (∼43 per cent) class I methanol maser sources (typical 3σ upper limit is ∼7 mJy for non-detections). 7 of our 30 class I sources have previously reported cm-wavelength continuum emission (18-cm emission for all except G328.24−0.55, which has a 3-cm continuum detection) and we detect 3.5-mm continuum in all but one (G333.47−0.16). Voronkov et al. (2014) report an association rate of ∼24 per cent between their class I maser sources and cm-wavelength continuum emission. This is significantly lower than the association rate we observe between the 95-GHz and mm-wavelength continuum sources. However, it should be noted that their rate was reported as a lower limit due to the inhomogeneous nature of their continuum data with respect to their sample of sources. It is likely that mm-wavelength continuum emission, such as the observed 3.5-mm emission results from thermal dust, in contrast to cm-wavelength continuum emission which is mostly free–free emission from H II regions. This indicates that class I sources displaying mm- and not cm-wavelength continuum emission may be at an earlier evolutionary phase.

In all of these sources we observe 95-GHz masers closely co-located (to within a few arcseconds) with the continuum emission. Additionally, in all sources where continuum emission is observed, at least some component of it was observed within several arcseconds of the class II pointing target. Considering both cm- and mm-wavelength continuum data for our sources, we obtain an association rate between class II masers and radio continuum emission (∼47 per cent) consistent with those previously reported (Phillips et al. 1998; Walsh et al. 1998).

4.4 ATLASGAL association

The ATLASGAL survey mapped continuum emission from cold, dense dust and gas throughout the Galactic Plane. All class I methanol maser sources we have observed are within the bounds of the ATLASGAL survey. All of our class I maser regions are closely associated (within 30 arcsec of peak emission) with ATLASGAL sources with the 95-GHz maser spots appearing to be slightly offset from the central peak of the dust emission, which is consistent with the class I masers being associated with gas outflows. We observe a positive linear correlation between the dust mass of these ATLASGAL sources, and the luminosity of the associated 6.7-GHz class II masers with a correlation coefficient (r) of 0.85.

In the majority of sources that we observe strong 3.5-mm continuum emission, we observe the location of the ATLASGAL point source coinciding with the position of this continuum emission. Additionally, we consider whether sources where 3.5-mm continuum emission or IR sources are associated with the class I maser emission affects the dust masses of the ATLASGAL sources. This was done by using the ANOVA statistical function to determine the significance of the various categorical variables (e.g. presence of EGO, 8-μm IR source, etc.) in predicting ATLASGAL dust mass. The ANOVA function is robust to the normality assumption of the continuous variable (ATLASGAL dust mass) allowing us to be reasonably confident in the output despite the skewed distribution of the dust masses. The presence of continuum emission and 4.5-μm excess sources (whether EGO or other) do not correspond to distributions of ATLASGAL masses with statistically different means. Conversely, association with 8-μm emission does result in a statistically significant difference in the mean, with sources displaying 8-μm emission generally displaying lower dust masses.

In targets where no IR source was observed at the location of the class II maser, the ATLASGAL source likely pinpoints the location of the young star driving the methanol emission. However, in the eight sources where this is the case, we do not observe a close coincidence between the peak of the ATLASGAL emission and the location of the class II masers. We also do not observe any statistically significant difference between the luminosity of class II masers in sources where no IR source is identified versus those with IR sources detected.

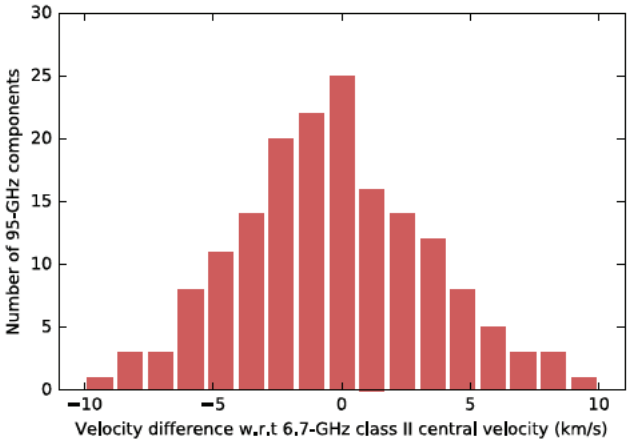

Figure 3. The histogram representing the distribution of velocity separations between the 95-GHz class I masers and the central velocity range value of the 6.7-GHz class II target sources.

4.5 Velocity separation

Voronkov et al. (2014) compared relative velocities of the 36-/44-GHz class I methanol masers with the quiescent gas in the same region. Their results were consistent with the expected result that class I methanol masers have a closely related radial velocity to the systemic velocity. We follow up this analysis with a similar comparison using the detected 95-GHz masers. In the Voronkov et al. (2014) study, the velocity of the quiescent gas was approximated by the central velocity value of 6.7-GHz class II methanol maser velocity range. As the pointing targets for our observations are 6.7-GHz class II masers, we will use this same convention in our analysis. Creating a histogram (Fig. 3) of relative velocities, we see that the distribution can be reasonably approximated by a normal distribution with a mean of $-0.33 \pm 0.28\,\mathrm{km\,s^{-1}}$ and a standard deviation of $3.62 \pm 0.20\,\mathrm{km\,s^{-1}}$. Qualitatively the histogram for the 95-GHz masers appears to have a minor blueshift asymmetry, similar to the 36- and 44-GHz transitions, however, this shift cannot be considered statistically significant in our data (tested with a one-sample *T*-Test). The ratio of negative to positive relative velocities is 1.34; this is statistically significant from unity, however, it requires a simplification of the problem to a binomial distribution and is thus not a rigorous test. Follow-up observations at higher spectral resolution are required in order to conclude whether this is a real result. Unlike the 36- and 44-GHz transitions, we observed no components with extreme relative velocities, with all relative velocities falling within a range of approximately -10 to $10\,\mathrm{km\,s^{-1}}$. The 3σ range of our results is very similar to that observed from the other class I transitions presented by Voronkov et al. (2014). Due to the nature of our observing (covering a fixed range of -100 to $0\,\mathrm{km\,s^{-1}}$), some sources such as G 333.16–0.10, with velocities close to the edge of this range ($\sim -92\,\mathrm{km\,s^{-1}}$), will not be sensitive to high-velocity blue-shifted components. This same limitation is not an issue at the opposite end of our velocity range, as we do not observe any sources with systemic velocities higher than $-37\,\mathrm{km\,s^{-1}}$.

4.6 Comparison with 36-/44-GHz class I masers

Voronkov et al. (2014) presented a detailed comparison between spatially associated 36- and 44-GHz methanol maser components. Combining these data with our observations allows for an analysis of the relationship between all three class I methanol maser transitions within our sample. In order to appropriately compare emission from each transition, we need to determine which maser components display emission in more than one transition. This was achieved by matching components between transitions that were co-associated both spatially and with respect to LSR velocity. 95-GHz components were matched with components from the other class I transitions if they are co-located within 1.5 arcsec and separated by $1\,\mathrm{km\,s^{-1}}$ or less in LSR velocity. It is worth noting that while the Voronkov et al. observations of the two different class I transitions occurred quasi-simultaneously, our observations were made 3 yr prior. Therefore, any comparison between matched 95-GHz masers and 36-/44-GHz masers will have inherently more uncertainty than comparison between matched 36- and 44-GHz transitions as variability within class I methanol maser sources is not currently well understood or studied. The 36-/44-GHz masers were grouped using the same method outlined by Voronkov et al., where components from the same transition that were co-located within 3σ (in fit uncertainty) of both position and velocity were considered a single component for the purpose of analysis. Across all 172 95-GHz components, we find matches with 36-GHz components in 51 cases ($\sim$30 per cent) and matches with 44-GHz components in 85 ($\sim$49 per cent). 97 out of the 172 ($\sim$56 per cent) total components had a match in either of the other class I methanol maser transitions, with 39 components ($\sim$22 per cent) displaying emission in all three transitions. Note that the LSR velocity of 36-GHz masers was adjusted in accordance with the rest-frequency corrections described by Voronkov et al. (2014) ($-0.215\,\mathrm{km\,s^{-1}}$) before being matched with the 95-GHz masers.

When considering 95-/44-GHz pairs, we find that 57 of 85 cases ($\sim$67 per cent) have higher flux density in the 44-GHz transition (left-hand plot, Fig. 5). In the 95-/36-GHz matched pairs, we find that the 95-GHz transition is brighter in 39 out of 51 ($\sim$76 per cent) cases (right-hand plot, Fig. 5). The relationship between the 95- and 44-GHz maser pairs is expected due to both of these transitions belonging to the same transition series (both are J_0 —(J-1)$_1$A$^+$ transitions with consecutive J numbers).

Flux density scatter plots were created between the matched components of each pair of transitions (Fig. 6). Only 36- and 44-GHz maser components from within our source sample were considered, therefore, the comparison between the paired 36- and 44-GHz masers here is a smaller sample size than that in Voronkov et al. (2014). A first-order polynomial line of best fit was determined for each of these plots. Considering the flux density scatter plot of 95- and 44-GHz matched components (plot (a) of Fig. 6), the linear fit had a slope of 0.35 ± 0.10 (and intercept value of 2.1 ± 0.5) with a modest correlation coefficient (r) of 0.78. This relationship is similar to the 3:1 ratio between 44- and 95-GHz flux density reported by Val'tts et al. (2000). We find reasonable coefficients of correlation ($r = 0.78$ for 95-/36-GHz and 95-/44-GHz and $r = 0.79$ for 44-/36-GHz) in the linear fits of all three of our transition pairs. It is important to note that these comparisons were made using the flux density peak values for each transition. This introduces velocity resolutions effects when comparing our 95-GHz data to the 36- and 44-GHz values, as the velocity resolution of our observations are approximately a factor of 8 coarser. The observed relationship between frequency of association and flux density is consistent with the expected relationships between these transitions (Cragg et al. 1992; McEwen et al. 2014; Leurini et al. 2016).

When considering the velocity separation between matched class I transitions, we observe a red-shift between the 95-GHz

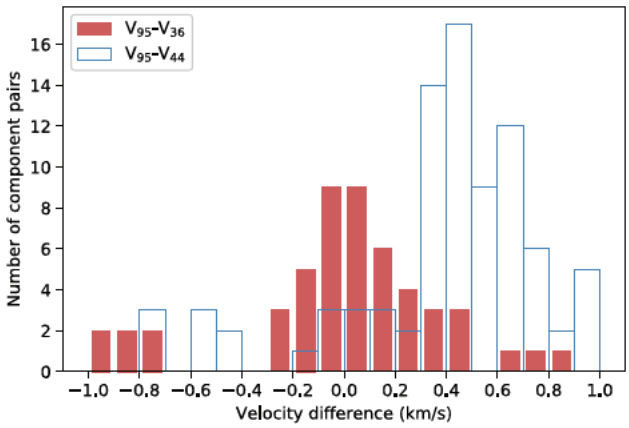

Figure 4. Histograms of velocity offset between matched 95- and 36-GHz masers (red filled) and 95- and 44-GHz masers (blue outline).

components with respect to their matched 44-GHz components in 73 out of 85 (∼86 per cent) pairs with a mean red-shift of 0.385 km s^{-1} over all pairs (see Fig. 4). The velocity separations between the 95- and 36-GHz matched pairs has a mean of 0.005 km s^{-1}. The distribution of the velocity separation between both pairs of transitions is approximately Gaussian.

It is interesting to consider the number of regions where 95-GHz masers are detected which also contain emission from either, or both, of the other two class I transitions. To do this, we considered the original spatial association of maser components represented by the letter symbols in our images (originally defined in Voronkov et al. 2014). In most cases these locations have a maximum spread of approximately 4 arcsec, which is close enough to assume co-location in the same general environment. In a few cases 95-GHz masers were seen to be offset from an alphabetized location; in these situations they were considered their own region. This resulted in 64 groupings of 95-GHz class I masers over the 30 class I sources. In 52 of the 64 (∼81 per cent) clusters of 95-GHz masers, both 36- and 44-GHz masers are also present. When considering cases where only 36- or 44-GHz are co-located with the 95-GHz masers, this reduces down to ∼1.5 per cent (1 region) and ∼14 per cent (9 regions), respectively, with the remaining two regions (∼3 per cent; regions in G 328.25–0.53 and G 329.07–0.31) only containing 95-GHz class I masers. Therefore, the vast majority of regions where 95-GHz masers are detected have 36- and 44-GHz masers in relatively close proximity. Different environmental conditions favour different class I methanol transitions (Cragg et al. 1992; McEwen et al. 2014; Leurini et al. 2016). For the three transitions considered here, the 44-GHz and 95-GHz emission are related and share similar optimal masing conditions, whereas the 36-GHz emission prefers denser environments. All three transitions favour temperatures ≥50 K, however, the optimal density range (of molecular hydrogen) for the two A^+ type transitions is between 10^4 and 10^6 cm^{-3}, compared with $10^5 - 10^7$ cm^{-3} for the 36-GHz transition (McEwen et al. 2014). Masers from the 36- and 44-GHz transitions can be observed co-spatially due to overlapping optimal conditions for masing (Voronkov et al. 2010, 2014; Pihlström, Sjouwerman & Fish 2011; McEwen, Pihlström & Sjouwerman 2014). Therefore, as the 95-GHz masers have similar optimal conditions as the 44-GHz transition, this explains why we tend to observe spatial associations between all three transitions in regions where 95-GHz components are located (which are in general optimal for 44-/95-GHz masing, allowing 95-GHz to be observable).

4.7 YSO range of influence

Due to the nature of their pumping mechanism, 6.7-GHz class II methanol masers are located close to high-mass YSOs. This allows the positions of these class II masers to be used as an accurate indicator of the location of a YSO. As all of our target sources were 6.7-GHz class II masers, we can determine linear offsets between all our detected maser components and nearby YSOs. Kinematic distance estimates to each source were taken from Green & McClure-Griffiths (2011) or computed using similar methodology (see Table 1). Similar analysis for the 36- and 44-GHz class I emission was conducted by Voronkov et al. (2014) and concluded that 1 pc is a good estimate of the range of influence of YSOs in producing class I methanol masers. In the case of our 95-GHz observations, we have a much smaller primary beam which does not allow us to accurately determine whether the 1 pc estimate applies to the 95-GHz masers we observed. Instead, with our data we considered a range out to 0.46 pc, this range was determined from the mean linear radius of the primary beam over all of our sources. Considering only the subset of 95-GHz components within this range limit allows for a sample with reduced bias towards detections close to the pointing centre. This reduced sample can be compared against the 36- and 44-GHz maser components, which satisfy the same criteria, in order to investigate any positional preference of 95-GHz masers towards YSOs relative to the 36- and 44-GHz masers.

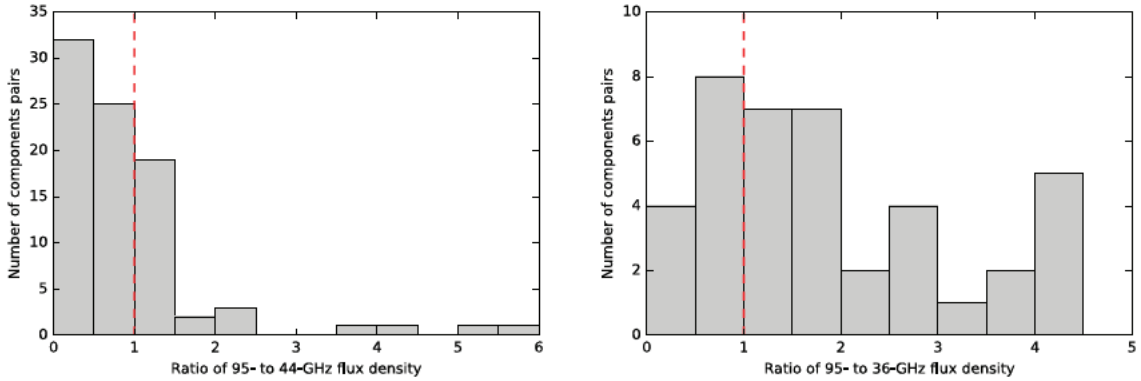

Figure 5. Distribution of the flux density ratio of 95- to 44-GHz masers in matched pairs (left) and 95- to 36-GHz pairs (right). There are 85 and 51 matched pairs in the 95-/44-GHz and 95-/36-GHz distributions, respectively. Vertical dashed line separates the pairings where 95-GHz component is brighter than the other paired class I methanol maser transition.

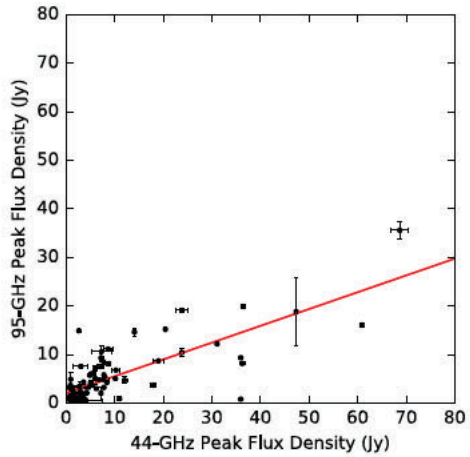

(a)

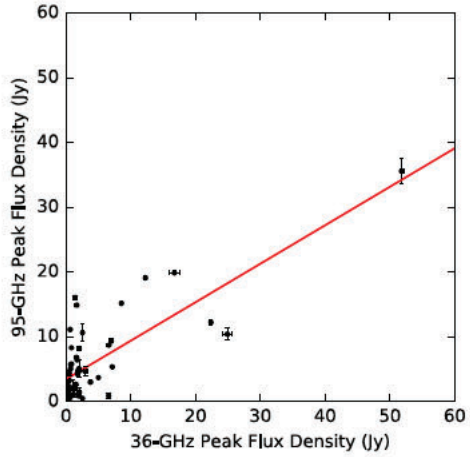

(b)

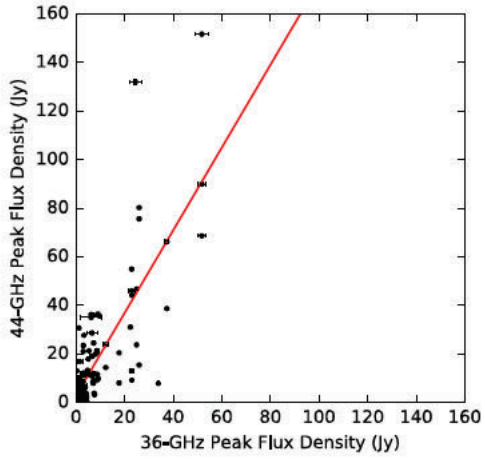

(c)

Figure 6. Scatter plots of peak flux density between matched class I components, 95- and 44-GHz (a), 95- and 36-GHz (b) and 44- and 36-GHz (c). Line in each plot is a first-order polynomial best fit: $y = (0.35 \pm 0.10)x - (2.1 \pm 0.5)$ (a), $y = (0.59 \pm 0.17)x - (3.4 \pm 0.7)$ (b), $y = (1.70 \pm 0.49)x - (2.8 \pm 1.3)$ (c).

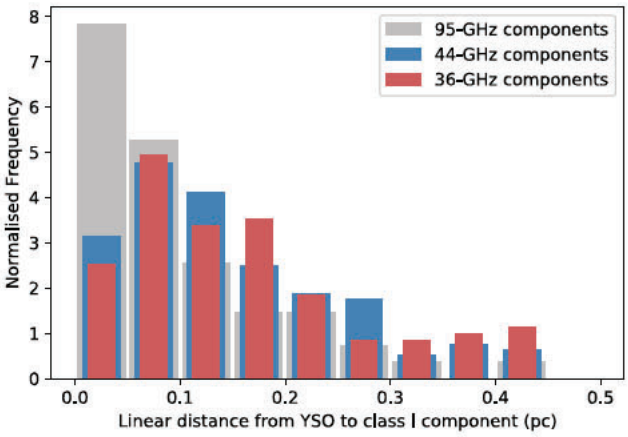

Figure 7. The normalized histogram of class I components linear separation from the 6.7-GHz (indicative of the position of the YSO). This is the reduced sample, of only components within 0.46 pc of the excitation source (see Section 4.7). The histogram for each frequency has been normalized so that the y-axis is the value of the probability density function for each bin, ensuring across the entire sampled range this integrates to 1. This allows comparison between the three samples of class I masers, despite sample sizes not being equal.

Five of our 32 target sources were excluded from this analysis: one due to a missed pointing (G 333.56−0.02) and another four due to multiple close 6.7-GHz class II masers present in the field (G 332.30−0.09, G 333.13-0.44, G 333.13−0.56, and G 333.23−0.06). Sources with multiple 6.7-GHz masers are excluded as we are unable to determine which class II source the class I masers are associated with. In the remaining 27 sources, we determined linear offsets for 138 components, with 127 of these falling within the range of 0.46 pc from a YSO. Within this subset of 127 components, we observe 81 (∼59 per cent) with projected distances less than 0.1 pc and 107 (∼78 per cent) less than 0.2 pc. Therefore, we observe more than an ∼68 per cent drop in the number of components when comparing those from between 0.1 and 0.2 pc and those within 0.1 pc of the YSO. Considering a 2-dimensional density determined as the number of components per projected area, the density of the region between 0.1 and 0.2 pc from the YSO is ∼89 per cent lower than that of the inner region. When considering components from all three class I transitions within this same 0.46 pc range, we must exclude three additional sources (G 329.03−0.20, G 329.03−0.19, and G 333.12−0.43) as these have multiple 6.7-GHz class II masers within the FWHM of the 36- and 44-GHz primary beam. In this reduced sample, we observe ∼65 per cent of 95-GHz class I masers within 0.1 pc of the YSO, compared to the ∼37 and ∼39 per cent observed for the 36- and 44-GHz transitions, respectively (see Fig. 7). Despite considering a reduced sample to alleviate bias towards 95-GHz maser components nearby to YSOs, this sample is only appropriate for comparing between the three transitions and are not indicative of the true distribution of 95-GHz maser emission in these sources. In order to accurately determine the distribution of 95-GHz maser spots with respect to the YSO, multiple pointings of each source would need to be made or an instrument with a much larger primary beam utilized.

The result that 95-GHz masers appear to be found closer to the exciting source than the other two transitions would seem to indicate that the 95-GHz transition prefers a comparatively higher energy environment. However, the both 44- and 95-GHz share similar conditions for ideal population inversion (Cragg et al. 1992;

McEwen et al. 2014), and we do not see as strong a preference for higher energy environments in the former. There is one observational factor that may be responsible for the perceived difference between these two related transitions. The 44-GHz maser transition is generally the stronger of the two transitions, so if the 95-GHz needs a higher energy environment for observable masing to occur, we may see a steeper decline in detected components when in lower energy areas, due to the sensitivity bias of our observations. This will have the effect of making 95-GHz masers seem proportionally closer to the excitation source than the 44-GHz masers. Additionally, we see no correlation between the flux density of a component (of any class I transition) and its linear separation from the associated YSO, which is consistent with the findings of Voronkov et al. (2014).

4.8 Class I–Class II association at high resolution

While the vast majority of class I methanol maser components are generally located within 1 pc of a YSO (Voronkov et al. 2014), typically, class I emission is not observed coincident with class II methanol maser features. Kurtz et al. (2004) observed examples of spatial association between 44-GHz class I and 6.7-GHz class II masers, and suggested that the mutual exclusivity between the two classes may not be as strong as previously supposed. In Section 4.7 we observe the majority of 95-GHz emission nearby (<0.2 pc) to the YSO (marked by the location of the 6.7-GHz masers) and Fig. 3 shows the distribution of velocities for our components is approximately Gaussian about the class II central velocity. Therefore, we should observe some 95-GHz maser components, both spatially associated and within the velocity range of the 6.7-GHz class II masers. Observation of components matching these two conditions does not conclusively mean that masers from the two classes are associated with the same environment and could instead result simply from chance alignment.

We include in Table 1 the linear offset between each class II maser and the closest 95-GHz component coincident with the class II maser velocity range. In 8 (of 32) class II sources we observe class I maser emission both: closer than 1 arcsec in position and within the velocity range of the 6.7-GHz masers (Caswell et al. 2011). The median angular separation and projected linear separation of all 95-GHz components satisfying the aforementioned criteria is 0.71 arcsec and 0.013 pc, respectively. G 328.25−0.53 and G 333.03−0.06 host the two most accurately positioned components within this subset, with 3σ angular errors in their fitted positions of <0.2 arcsec. The line-of-site distance to these sources is less than 3 kpc (see Table 1), therefore, these small angular offsets correspond to projected linear distances of less than 0.01 pc. In contrast to the 95-GHz masers, similar spatial alignment between class I maser components and 6.7-GHz masers was only observed in three sources from our sample, for both the 36- and 44-GHz transitions. Such a considerable difference between the 95- and 44-GHz masers is interesting due to their shared optimal environment conditions (Cragg et al. 1992; McEwen et al. 2014), however, it is worth noting that we are only considering 44-GHz emission from sources we have observed at 95 GHz.

From our observations it is not possible to definitively determine whether these components are anything other than aligned with the line of sight to the class II source. In order to properly investigate coincidence between class I and class II masers, high-resolution astrometry must be performed. However, these close angular offsets combined by the general trend that 95-GHz masers appear preferentially towards the driving source (discussed in Section 4.7) may indicate that masers from this transition are more strongly inverted when close to a background continuum source.

5 CONCLUSIONS

We present 95-GHz imaging results from 32 pointings of a statistically complete sample of 6.7-GHz class II methanol masers. We detected 95-GHz maser emission in all pointings and across all 32 pointings we detected a total of 172 95-GHz class I methanol components. Due to two cases with dual pointings, these 32 pointings represent coverage of 30 individual class I methanol maser sources. In many cases we observe similar associations between these 95-GHz maser components and ordered structures, as is seen in 36-/44-GHz components in the same sources (Voronkov et al. 2014). We observe associations between 95-GHz components and 4.5-μm excess sources in 21 out of 30 sources (70 per cent) or 24 out of 30 sources (80 per cent) when considering all class I methanol emission (inclusion of 36-/44-GHz components). Additionally, in 19 of 30 sources (∼63 per cent) we observe associations with 8.0-μm emission, increasing to 22 of 30 sources (∼73 per cent) with the inclusion of all class I methanol data for these sources. 3.5-mm continuum sources were detected in 13 of our 30 sources (∼43 per cent) and in all of these sources we see co-location (within a few arcseconds) between the continuum emission, the 95-GHz class I masers, and the 6.7-GHz class II maser.

When considering our statistically complete sample (all 6.7-GHz class II sources with observed 95-GHz maser emission), we observe a 57 per cent association rate with 12.2-GHz class II masers). This is not significantly different from the 60 per cent association rate observed between the two class II transitions in the larger complete sample that our targets were drawn from. As 12.2-GHz masers generally appear at later evolutionary stages, the 95-GHz masers do not seem to prefer more evolved sources.

We observe component matches between the 44-GHz and 95-GHz transitions in 85 (∼49 per cent) of our detected 95-GHz components and matches between 36- and 95-GHz transitions in 51 (∼30 per cent) 95-GHz components. Only 39 of our 172 observed 95-GHz components have matching components from all three transitions. These matches were made by cross-matching every 95-GHz maser with its nearest 36- and 44-GHz masers, then filtering these matches with a limit of 1.5 arcsec of angular separation and 1 km s^{-1} of LSR velocity separation. Additionally when considering broader environmental associations between the two transitions, we find that in ∼81 per cent of regions containing 95-GHz components, 36- and 44-GHz components are also observed. Indicating that the vast majority of environments with suitable conditions for 95-GHz masing are also suitable for 36- and 44-GHz masing. When comparing the flux densities between matched 44- and 95-GHz components, we observe a similar relationship to the 3:1 ratio reported by Val'tts et al. (2000). Indicating that this relationship holds when considering high-resolution data of both transitions where individual maser components can be matched together.

When comparing the velocities of matched class I components, we observe a red-shift of 0.385 km s^{-1} on average between 95- and 44-GHz components. No significant shift is observed between the 95- and 36-GHz matched components.

When considering the offset from the YSOs (position defined as location of the 6.7-GHz masers), 95-GHz maser spots appear to be preferentially closer than the other considered class I transitions. This could be explained by the 95-GHz methanol transition being more strongly inverted when closer to a background continuum source. Additionally, we observe some 95-GHz components at very

small linear offsets from class II 6.7-GHz masers, however, high-resolution astrometry is required to determine whether any real association exists.

The distribution of velocity offsets between 95-GHz components and the systematic source velocity (defined by the central velocity value of the 6.7-GHz class II emission in each source) has a mean of $-0.33 \pm 0.28\,\mathrm{km\,s^{-1}}$. We observe no high-velocity features in any of our sources at 95 GHz.

Similar to the complementary nature of the 36- and 44-GHz components observed in our target sources (Voronkov et al. 2014), there are many cases where the 95-GHz components trace the same morphological structures in a particular source. In several of these cases, the 95-GHz components extend along paths not covered by 36- or 44-GHz components. Therefore, observations in all three transitions can be useful in determining the exact structure of particular morphological features. Our investigation rejects the notion that the class I maser transitions of the methanol species are simpler than class II, with diversity in relationships and associations being observed between closely related transitions (95-GHz and 44-GHz *A*-type).

ACKNOWLEDGEMENTS

We thank the anonymous referee for useful suggestions which helped to improve this paper. The ATCA is part of the Australia Telescope, which is funded by the Commonwealth of Australia for operation as a National Facility managed by CSIRO. This research has made use of NASA's Astrophysics Data System Abstract Service. This research has made use of data products from the GLIMPSE survey, which is a legacy science programme of the Spitzer Space Telescope, funded by the National Aeronautics and Space Administration, and the NASA/IPAC Infrared Science Archive, which is operated by the Jet Propulsion Laboratory, California Institute of Technology, under contract with the National Aeronautics and Space Administration. This research also utilized APLPY, an open-source plotting package for PYTHON hosted at http://aplpy.github.com. This research made use of Astropy, a community-developed core PYTHON package for Astronomy (Astropy Collaboration 2013).

REFERENCES

Astropy Collaboration, 2013, A&A, 558, A33
Breen S. L., Ellingsen S. P., Caswell J. L., Lewis B. E., 2010, MNRAS, 401, 2219
Breen S. L., Ellingsen S. P., Caswell J. L., Green J. A., Fuller G. A., Voronkov M. A., Quinn L. J., Avison A., 2011, ApJ, 733, 80
Breen S. L., Ellingsen S. P., Caswell J. L., Green J. A., Voronkov M. A., Fuller G. A., Quinn L. J., Avison A., 2012a, MNRAS, 421, 1703
Breen S., Ellingsen S., Caswell J., Green J., Voronkov M., Fuller G., Quinn L., Avison A., 2012b, MNRAS, 426, 2189
Breen S. L. et al., 2015, MNRAS, 450, 4109
Caswell J. L., 1997, MNRAS, 289, 203
Caswell J. L. et al., 2010, MNRAS, 404, 1029
Caswell J. L. et al., 2011, MNRAS, 417, 1964
Chen X., Ellingsen S. P., Shen Z.-Q., 2009, MNRAS, 396, 1603
Chen X., Ellingsen S. P., Shen Z.-Q., Titmarsh A., Gan C.-G., 2011, ApJS, 196, 9
Cragg D. M., Johns K. P., Godfrey P. D., Brown R. D., 1992, MNRAS, 259, 203
Cragg D. M., Sobolev A. M., Godfrey P. D., 2005, MNRAS, 360, 533
Cyganowski C. J. et al., 2008, AJ, 136, 2391
Cyganowski C. J., Brogan C. L., Hunter T. R., Churchwell E., 2009, ApJ, 702, 1615
Cyganowski C. J., Brogan C. L., Hunter T. R., Zhang Q., Friesen R. K., Indebetouw R., Chandler C. J., 2012, ApJ, 760, L20
De Buizer J. M., Vacca W. D., 2010, AJ, 140, 196
Ellingsen S. P., 2005, MNRAS, 359, 1498
Ellingsen S. P., Shabala S. S., Kurtz S. E., 2005, MNRAS, 357, 1003
Ellingsen S. P., Sobolev A. M., Cragg D. M., Godfrey P. D., 2012, ApJ, 759, L5
Green J. A., McClure-Griffiths N. M., 2011, MNRAS, 417, 2500
Green J. A. et al., 2010, MNRAS, 409, 913
Green J. A. et al., 2012, MNRAS, 420, 3108
Green J. A. et al., 2017, MNRAS, 469, 1383
Kurtz S., Hofner P., Álvarez C. V., 2004, ApJS, 155, 149
Leurini S., Menten K. M., Walmsley C. M., 2016, A&A, 592, A31
McEwen B. C., Pihlström Y. M., Sjouwerman L. O., 2014, ApJ, 793, 133
Müller H. S. P., Menten K. M., Mäder H., 2004, A&A, 428, 1019
Peretto N., Fuller G. A., 2009, A&A, 505, 405
Phillips C. J., Norris R. P., Ellingsen S. P., McCulloch P. M., 1998, MNRAS, 300, 1131
Pihlström Y. M., Sjouwerman L. O., Fish V. L., 2011, ApJ, 739, L21
Sjouwerman L. O., Murray C. E., Pihlström Y. M., Fish V. L., Araya E. D., 2010, ApJ, 724, L158
Slysh V. I., Kalenskii S. V., Valtts I. E., Otrupcek R., 1994, MNRAS, 268, 464
Sobolev A. M., Cragg D. M., Godfrey P. D., 1997, A&A, 324, 211
Val'tts I. E., Ellingsen S. P., Slysh V. I., Kalenskii S. V., Otrupcek R., Larionov G. M., 2000, MNRAS, 317, 315
Voronkov M. A., Sobolev A. M., Ellingsen S. P., Ostrovskii A. B., 2005, MNRAS, 362, 995
Voronkov M. A., Brooks K. J., Sobolev A. M., Ellingsen S. P., Ostrovskii A. B., Caswell J. L., 2006, MNRAS, 373, 411
Voronkov M. A., Caswell J. L., Ellingsen S. P., Sobolev A. M., 2010, MNRAS, 405, 2471
Voronkov M. A., Caswell J. L., Ellingsen S. P., Green J. A., Breen S. L., 2014, MNRAS, 439, 2584
Walsh A. J., Burton M. G., Hyland A. R., Robinson G., 1998, MNRAS, 301, 640

SUPPORTING INFORMATION

Supplementary data are available at *MNRAS* online.

field_images_pdf.tar.gz
spectra.tar.gz

Please note: Oxford University Press is not responsible for the content or functionality of any supporting materials supplied by the authors. Any queries (other than missing material) should be directed to the corresponding author for the article.

This paper has been typeset from a TEX/LATEX file prepared by the author.

Chapter 3

Detection of 36.2-GHz Class I methanol maser emission toward NGC 4945

3.1 Introduction

This paper was originally published in *The Astrophysical Journal* as *'Detection of 36.2-GHz Class I Methanol Maser Emission toward NGC 4945'* (DOI: 10.3847/1538-4357/aa872c).

In this paper we report the third (at the time) detection of a 36.2-GHz class I methanol maser from an external galaxy using Australia Telescope Compact Array (ATCA) observations from 2015 August. The maser emission was identified as coming from a single region, offset from the galactic nucleus by approximately 10 arcseconds, with a FWHM of ~ 10 km s^{-1}. The isotropic luminosity of the maser emission is five orders of magnitude higher than what is typical from a Galactic 36.2-GHz maser. Similarly to the previous detections reported by Ellingsen et al. (2014) and Chen et al. (2015), it was identified that this maser emission does not appear to be the result of cumulative emission from many star-formation regions in a compact cluster.

Based on results from Ellingsen et al. (2017a), we believed the maser emission is likely to be associated with some source of large-scale low-velocity shocks. Molecular inflow, identified in HF absorption (Monje et al., 2014), had a compatible velocity range of

560–720 km s^{-1} and radial upper limit of 200 pc and was suggested as a potential candidate for producing these large-scale shocks.

3.2 Author Contributions

- The observations for this paper were the result of an ATCA project (C2879) led by Xi Chen and Simon Ellingsen. With Hai-hua Qiao responsible for observing this source in August of 2015.
- All data-reduction for this paper was performed by Tiege McCarthy using MIRIAD and PYTHON. Analysis was performed by Tiege McCarthy, alongside discussion with Simon Ellingsen, Shari Breen and Maxim Voronkov.
- Tiege McCarthy was responsible for approximately 90% of the writing in this paper, with Simon Ellingsen, with all other co-authors reviewing, discussing and offering suggestions to improve the final product.

Chapter 4

Investigations of the class I methanol masers in NGC 4945

4.1 Introduction

This paper was originally published in *Monthly Notices of the Royal Astronomical Society* as *'Investigations of the Class I methanol masers in NGC 4945'* (DOI: 10.1093/mnras/sty2192).

This paper reports the results of three 7-mm observing epochs toward NGC 4945 using hybrid array configurations with the Australia Telescope Compact Array (ATCA). Two of these epochs were focussed on the 36.2-GHz class I transition, with the other searching for 44.1-GHz class I emission. These hybrid configuration observations allowed us to more accurately map the 36.2-GHz maser emission towards this source, compared to the previous observations presented in McCarthy et al. (2017). Under the assumption that the maser emission is in line with the galactic disk, the 36.2-GHz maser emission would be located at a galactocentric radius of approximately 670 pc. Improvements in understanding of the bar-dynamics in NGC 4945 by Henkel et al. (2018) indicate that the maser emission may be located at the interface region between the south-eastern spiral arm and galactic bar. This dynamical situation would be a good candidate for the production of the large-scale, low-velocity shocks believed to pump these masers. Alongside the observations of these class I maser lines, we also

included various other 7-mm spectral lines. This resulted in detections and mapping of 36.4-GHz HC_3N, 43.4-GHz SiO and 49-GHz CS toward NGC 4945. This paper then presents a comparison of the maser emission from NGC 4945, with that of NGC 253 and G 1.6-0.025, a giant molecular cloud in the Milky Way.

The observations presented in this paper were the first from proposals I was personally the primary investigator for (ATCA project code C3167). With the approximately 20 hours of ATCA observing being my introduction into observing with the ATCA.

4.2 Author Contribution

- Observations were made as part of the C3167 ATCA project led by Tiege McCarthy. ATCA observations were performed by Tiege McCarthy in June, July and October of 2017 with support from Maxim Voronkov and Shari Breen.
- All data-reduction for this paper was performed by Tiege McCarthy using MIRIAD and PYTHON.
- Majority of analysis was performed by Tiege McCarthy alongside substantive discussion with Simon Ellingsen, Shari Breen and Christian Henkel. Some analysis of line ratios betwen CS (1–0) and CS (2–1) was performed by Christian Henkel.
- All figures and the vast majority of the writing for the paper were created by Tiege McCarthy, with Simon Ellingsen, Shari Breen, Christian Henkel, Xi Chen and Maxim Voronkov providing review and suggestions to improve the final manuscript.

Monthly Notices of the ROYAL ASTRONOMICAL SOCIETY

MNRAS **480,** 4578–4588 (2018) doi:10.1093/mnras/sty2192
Advance Access publication 2018 August 9

Investigations of the Class I methanol masers in NGC 4945

T. P. McCarthy [1,2★] S. P. Ellingsen [1] S. L. Breen,[3] C. Henkel,[4,5] M. A. Voronkov[2] and X. Chen[6,7]

[1]*School of Natural Sciences, University of Tasmania, Private Bag 37, Hobart, Tasmania 7001, Australia*
[2]*Australia Telescope National Facility, CSIRO, PO Box 76, Epping, NSW 1710, Australia*
[3]*Sydney Institute for Astronomy (SIfA), School of Physics, University of Sydney, NSW 2006, Australia*
[4]*Max-Planck-Institut für Radioastronomie, Auf dem Hügel 69, D-53121 Bonn, Germany*
[5]*Astronomy Department, Faculty of Science, King Abdulaziz University, PO Box 80203, Jeddah 21589, Saudi Arabia*
[6]*Center for Astrophysics, GuangZhou University, Guangzhou 510006, China*
[7]*Shanghai Astronomical Observatory, Chinese Academy of Sciences, Shanghai 200030, China*

Accepted 2018 August 3. Received 2018 July 24

ABSTRACT

We have used the Australia Telescope Compact Array (ATCA) to conduct further observations of the 36.2-GHz ($4_{-1} \rightarrow 3_0$E) methanol transition towards the nearby active galaxy NGC 4945. These observations have led to a more accurate determination of the offset between the maser emission and the nucleus of NGC 4945 with a typical synthesized beam of 6 arcsec × 4 arcsec (108 × 72 pc). This corresponds to a factor of 4 improvement with respect to the major axis of the beam. Other transitions of methanol and lines of other molecular species were obtained alongside the 36.2-GHz methanol emission, with strong detections of HC_3N (J = 4 → 3) and CS (J = 1 → 0) presented here. We do not detect thermal methanol (5σ upper limit of 5 mJy in a 6 km s^{-1} channel) from the 48.4-GHz ($1_0 \rightarrow 0_0$A$^+$) ground-state transition, nor emission from the 44.1-GHz ($7_0 \rightarrow 6_1$A$^+$) class I maser transition (5σ upper limit of 6 mJy in a 3 km s^{-1} channel). We also present a comparison of the class I maser emission observed towards NGC 4945 with that from NGC 253 and towards the Galactic giant molecular cloud G 1.6-0.025.

Key words: masers – galaxies: starburst – radio lines: galaxies.

1 INTRODUCTION

Methanol maser emission is divided into two classes based on pumping mechanism. Methanol masers pumped via collisional processes are defined as class I, while those that are radiatively pumped are considered class II (Batrla et al. 1987; Menten 1991). Both classes of methanol masers are commonly observed throughout the Milky Way, with over 1200 unique sources discovered (Ellingsen, Shabala & Kurtz 2005; Caswell et al. 2010, 2011; Voronkov et al. 2014; Breen et al. 2015; Green et al. 2010, 2012, 2017). In contrast with this, outside of our Galaxy we have relatively few detections of methanol maser emission. Extragalactic class II masers have been detected in the Large Magellanic Cloud and M31 (Green et al. 2008; Ellingsen et al. 2010; Sjouwerman et al. 2010). These extragalactic class II masers appear to be extremely luminous examples of their Galactic counterparts. Conversely, the extragalactic class I methanol masers are not yet a well-understood phenomenon, with observed emission unable to simply be considered large-scale emission from Galactic-style class I masers. Currently, there are six reported examples of class I maser emission towards extragalactic sources, 36.2-GHz emission in NGC 253, Arp 220, IC 342, NGC 6946, and NGC 4945 (Ellingsen et al. 2014; Chen et al. 2015; McCarthy et al. 2017; Gorski et al. 2018) and 84.5-GHz emission in NGC 1068 (Wang et al. 2014). Of these six sources, only NGC 253 has been detected in multiple epochs with multiple telescopes (Ellingsen et al. 2014, 2017a; Chen et al. 2018; Gorski et al. 2018).

Class I methanol emission is a powerful tool for understanding star formation within our Galaxy. More than 600 unique sources of class I maser emission are observed within the Milky Way (Slysh et al. 1994; Val'tts et al. 2000; Ellingsen et al. 2005; Chen et al. 2011; Gan et al. 2013; Jordan et al. 2017). Galactic class I masers are generally associated with shocked gas driven by the expansion of H II regions or molecular outflows (Kurtz, Hofner & Álvarez 2004; Cyganowski et al. 2009, 2012; Voronkov et al. 2010, 2014). However, it is not yet known if, or how, these highly luminous extragalactic class I masers relate to the star formation of their host galaxies. In Galactic star formation regions the two most commonly observed class I methanol maser transitions are the 36.2- and the 44.1-GHz, with the latter generally being the stronger of the two (Voronkov et al. 2014). Ellingsen et al. (2017a) detected weak 44.1-GHz methanol maser emission associated with two of the 36.2-

★ E-mail: tiegem@utas.edu.au

GHz sites in NGC 253. They suggest that the low intensity of the 44.1-GHz transition compared to the 36.2-GHz in NGC 253 is a strong evidence that extragalactic class I methanol maser emission cannot be explained as being due a large number of Galactic-like star formation regions within a small volume, but is rather a new and different extragalactic masing phenomenon. It appears that the extragalactic variants may evolve from large-scale molecular inflow inside their host galaxies (Ellingsen et al. 2017a). However, this has so far only been verified in the case of NGC 253. Developing an understanding of the pumping environments responsible for this phenomenon is one of the most important factors in determining its usefulness as a probe of galactic properties.

NGC 4945 is a nearby (assumed distance of 3.7 ± 0.3 Mpc, Tully et al. 2013) spiral galaxy, with a hybrid AGN and starburst nucleus. The starburst is the primary source of energy for exciting photoionized gas, due to heavy obscuration of the AGN by dust (Marconi et al. 2000; Spoon et al. 2000, 2003; Pérez-Beaupuits et al. 2011). The star formation rate in NGC 4945 is more than three times that of the Milky Way (4.35 ± 0.25 $M_\odot$ yr^{-1} for the nuclear region of NGC 4945 only, compared to 1.65 ± 0.19 $M_\odot$ yr^{-1} for the entire Milky Way, Licquia & Newman 2015; Bendo et al. 2016) and approximately 20 per cent higher than that of the similar (in terms of galactic properties and maser luminosity) extragalactic class I maser host galaxy, NGC 253 (Strickland et al. 2004). NGC 4945 is also host to various transitions of water megamasers, predominantly located in a circumnuclear accretion disc (Greenhill, Moran & Herrnstein 1997; Hagiwara et al. 2016; Humphreys et al. 2016; Pesce, Braatz & Impellizzeri 2016).

We have undertaken new observations of the 36.2-GHz methanol maser transition in NGC 4945 to better determine its location with respect to the host galaxy and other molecular gas. In addition to the 36.2-GHz methanol transition we have also observed the 44.1-GHz class I methanol maser transition to determine if the NGC 4945 shows a similar pattern to NGC 253 with this transition being relatively much weaker than is observed towards Galactic class I methanol masers associated with high-mass star formation regions. We were able to include observations of a number of thermal molecular transitions simultaneously with the maser observations and we present the results of those observations and compare them with the recent, sensitive high-resolution molecular line ALMA observations at 3-mm made by Henkel et al. (2018). We currently have a sample of only six known extragalactic class I methanol maser sources and by obtaining a range of complementary spectral line and other data and comparing the results for NGC 4945 with other sources we hope to improve understanding of this new phenomenon and its relationship to the properties of the host galaxy.

2 OBSERVATIONS

The Australia Telescope Compact Array (ATCA) was utilized for observations of NGC 4945 on 2017 June 29 and 2017 October 22 (project code C3167). Both the observations used hybrid array configurations, H214 for the June session (minimum and maximum baselines of 82 and 247m, respectively) and H168 for the October session (minimum and maximum baselines of 61 and 192m, respectively), and we excluded antenna 6 from our analysis. The Compact Array Broadband Backend (Wilson et al. 2011) was configured in CFB 64M-32k mode for these sessions. This mode consists of two 2-GHz IF bands (consisting of 32×64 MHz channels) and up to 16 of these 64-MHz channels can be configured as zoom bands consisting of 2048×31.2 kHz channels. The October-observing session consisted of two separate frequency setups, splitting the transitions below and above 40 GHz. Multiple zoom bands were 'stitched' together in order to obtain the appropriate velocity coverage for each transition. Table 1 describes all the molecular transitions, along with which epochs they were observed in. The two class I maser lines at 36.2- ($4_{-1} \rightarrow 3_0E$) and 44.1-GHz ($7_0 \rightarrow 6_1A^+$) were the primary science targets, for which we adopted rest frequencies of 36.169265 and 44.069410 GHz, respectively. The 31.2-kHz spectral resolution corresponds to 0.259 km s^{-1} and 0.213 km s^{-1} at 36.2 and 44.1 GHz, respectively.

The following refers to the observing strategy for the 2017 June and 2017 October epochs. Details regarding the previously reported 2015 August observations (EW352 array configuration) can be found in McCarthy et al. (2017). PKS B1934-648 was used for flux density calibration for both epochs and the bandpass was calibrated with respect to PKS B0537-441 and PKS B1921-293. PMN J1326-5256 was utilized as the phase calibrator, with 2 min on the calibrator interleaved with 10 min on-source. The data were corrected for atmospheric opacity and the absolute flux density calibration is estimated to be accurate to better than 30 per cent. Poor weather during the latter half of the 2017 October observations negatively affected the transitions above 48 GHz to a more significant degree. This, combined with representing only single epoch data, causes a significantly higher RMS noise in these higher frequency transitions (see Table 2).

MIRIAD was used for data reduction, following standard techniques for the reduction of ATCA 7-mm spectral line observations. Phase and amplitude self-calibration was performed on the data using the continuum emission from the core of NGC 4945. The continuum emission was subtracted from the self-calibrated uv data with the uvlin task, which estimates the intensity on each baseline from the line-free spectral channels. This enables us to isolate any spectral line emission from continuum emission. Data from all relevant epochs were combined prior to imaging (for on-source times see Table 1). Molecular line emission in NGC 4945 is observed between approximately 300 and 800 km s^{-1} in the local standard of rest velocity reference frame (Ott et al. 2001). The velocity range of our imaging was dependent on the number of stitched zoom bands utilized for each observed transition. However, all observed transitions were covered at least in the 350 to 780 km s^{-1} range. The spectral line data for each transition was resampled and imaged with a variety of channel widths. Table 2 shows the velocity range, channel width, and RMS per channel for a typical spectral line cube of each transition. Positions were determined using the MIRIAD task imfit that reports the peak value and location of a two-dimensional Gaussian fit for the emission in a given velocity plane within the spectral line cube. This task was also utilized for reporting peak flux density values for our emission, which may result in minor differences between the apparent flux density seen in extracted spectra and those tabulated. Combining data from all three array configurations results in a typical synthesized beam size of 6 arcsec $\times$ 4 arcsec.

3 RESULTS

The previously reported 36.2-GHz maser emission from NGC 4945 was clearly detected in both the 2017 June and 2017 October epochs, along with a strong 7-mm continuum source. In addition to methanol, 36.4-GHz HC_3N ($J = 4 \rightarrow 3$) line emission was detected in both epochs and 49-GHz CS $J = 1 \rightarrow 0$ and 43.4-GHz SiO $J = 1 \rightarrow 0$, $v = 0$ emission was also detected in the October session (where frequencies greater than 40 GHz were covered). Below we describe, in more detail, each of these detected

Table 1. Details of the observed transitions in NGC 4945. All rest frequencies were taken from the online database: *NIST Recommended Rest Frequencies for Observed Interstellar Molecular Microwave Transitions by Frank J. Lovas.*[1]

Species	Transition	Rest Frequency (GHz)	Array Configuration	Epoch	Integration Time (min)	Detection
Methanol	$4_{-1} \rightarrow 3_0$E	36.169265	EW352, H168, H214	2015 Aug, 2017 Jun, 2017 Oct	265.2	detection
	$7_{-2} \rightarrow 8_{-1}$E	37.703696	EW352, H168, H214	2015 Aug, 2017 Jun, 2017 Oct	265.2	non-detection
	$7_0 \rightarrow 6_1$A$^+$	44.069476	H214	2017 Oct	178.2	non-detection
	$1_0 \rightarrow 0_0$A$^+$	48.372456	H214	2017 Oct	138.2	non-detection
HC_3N	$J = 4 \rightarrow 3 F = 4 \rightarrow 3$	36.392332	H168, H214	2017 Jun, 2017 Oct	197.4	detection
HC_5N	$J = 12 \rightarrow 11$	31.951777	H168, H214	2017 Jun, 2017 Oct	197.4	non-detection
NH_3	$12_{12} \rightarrow 12_{12}$	31.424943	H168, H214	2017 Jun, 2017 Oct	197.4	non-detection
	$13_{13} \rightarrow 13_{13}$	33.156849	H168, H214	2017 Jun, 2017 Oct	197.4	non-detection
CH_3CN	$2_0 \rightarrow 1_0, F = 3 \rightarrow 2$	36.795568	H168, H214	2017 Jun, 2017 Oct	98.4	non-detection
SiO	$J = 1 \rightarrow 0$, v = 0	43.423853	H214	2017 Oct	178.2	detection
CS	$J = 1 \rightarrow 0$	48.990955	H214	2017 Oct	138.2	detection

[1] https://physics.nist.gov/cgi-bin/micro/table5/start.pl

Table 2. Details of the final spectral line cubes for each molecular line observed. Image cubes were created out of all available data. Methanol and continuum imaging included previously reported 2015 August observations, whereas, other transitions use both 2017 epochs where applicable. All details given refer to self-calibrated image cubes. RMS noise value is per channel, of width given in the relevant column. All velocities are with respect to the barycentric reference frame.

Species	Rest Frequency (GHz)	Velocity Range (km s^{-1})	Channel Width (km s^{-1})	RMS (mJy)
Methanol	36.169265	80–840	1.0	2.0
	37.703696	200–860	3.0	0.9
	44.069476	180–810	3.0	1.2
	48.372456	150–810	6.0	1.7
HC_3N	36.392332	200–950	3.0	1.1
HC_5N	31.951777	80–980	3.0	0.7
NH_3	31.424943	250–850	3.0	0.7
	33.156849	270–870	3.0	0.9
CH_3CN	36.795568	350–800	3.0	0.8
SiO	43.423853	180–780	3.0	1.3
CS	48.990955	270–930	3.0	3.4

transitions (listed in Table 1). All velocities referenced and reported in this work are relative to the barycentric coordinate system ($V_{\rm barycentric} - V_{\rm LSR} = 4.6$ km s^{-1}). Properties of the emission from detected transitions are tabulated in Table 3.

3.1 Continuum

Using the imfit MIRIAD task on our combined array data gives a beam deconvolved angular size of $4.8 \pm 0.04 \times 1.8 \pm 0.04$ arcsec, with a position angle of $41.4° \pm 0.3°$ for the major axis. This is of similar size, and identical position angle, compared to the 3-mm continuum source dimensions reported by Henkel et al. (2018).

The bulk of the nuclear continuum emission observed at millimetre wavelengths is the result of free–free emission from star formation regions (Bendo et al. 2016). We detect a 7-mm continuum source towards the nuclear region of NGC 4945, with peak and integrated flux densities of 299 mJy and 436 mJy km s^{-1}, respectively (see Table 3 for position). This continuum emission was extracted by combining the line-free continuum data from all three epochs (and array configurations). The zoom band for the 36.2-GHz methanol line was used, in order to remain consistent with the previous value reported in McCarthy et al. (2017). This zoom band covers the frequency range 35.99–36.18GHz. Our integrated flux density is in good agreement with the modelled values for 7-mm from Bendo et al. (2016). The SED model of Bendo et al. (see their figure 5) predicts 75 per cent of the 7-mm emission is from free–free emission, so the good agreement we obtain suggests that at this frequency, the majority of the continuum emission is due to star formation.

The dynamical centre, as defined by the position of the circumnuclear H_2O megamaser accretion disc, is located at $\alpha_{2000} = 13^{\rm h}05^{\rm m}27^{\rm s}.48$ and $\delta_{2000} = -49°28'05''.6$ (Greenhill et al. 1997; Henkel et al. 2018). Comparing the peak of our 7-mm continuum source, we see an offset of −0.13 arcsec in right ascension and 0.8 arcsec in declination (projected linear offset of 15 pc), indicating our continuum source is offset to the north-west from the dynamical centre. However, this offset is of the same order as the nominal astrometric accuracy of our observations, 0.4 arcsec. The 3-mm continuum source detected by Henkel et al. (2018) with a beam size of ∼2 arcsec shows a similar angular offset, though to the north-east, instead of north-west. We also identify an asymmetry between the angular offsets of the two CS $J = 1 \rightarrow 0$ peaks to the south-west and north-east when compared to the 7-mm continuum peak (4.4 arcsec and 5.7 arcsec for the south-west and north-east components, respectively). In addition to the main continuum source, we observe a minor emission feature (at a 6σ level) roughly aligned with the position of the maser emission to the south-east (see Fig. 1).

3.2 Methanol spectral lines

The 36.2-GHz (class I) methanol maser emission (see Table 3) is observed from the same position as reported in McCarthy et al. (2017) in both follow up epochs, offset south-east from the galactic nucleus. The hybrid array configuration used for both 2017 observations allows for more accurate imaging of the methanol masing region, which was not possible with previous observations. All emission is located at this offset region, which corresponds to the location of some weak HCN emission (see Fig. 1), and consists of multiple components with narrow line widths. The 55 mJy primary component has a velocity of 673 km s^{-1}, redshifted with respect to the systemic velocity of NGC 4945 (585 km s^{-1}, Chou et al. 2007), with two significantly lower flux density (∼15 mJy) components at 643 and 705 km s^{-1} (see Fig. 1). Whether these minor components were real based on the observations in McCarthy et al. (2017) was

Table 3. Combined array flux density, velocity, and positional information for all molecular transitions (and continuum) observed in NGC 4945. The locations and peak flux densities given are those of the peak emission components in each transition. They were extracted using the imfit MIRIAD task on the spectral line cubes tabulated in Table 2. The integrated flux density of methanol emission tabulated here is an artefact of a minor velocity redshift in the peak emission (between the 2017 epochs and the 2015 epoch, see Section 4.1). This causes a higher apparent integrated flux than observed in any individual epoch (see Table 4).

	Location	RA (J2000) *h m s*	Dec (J2000) ° ′ ″	S_{pk} (mJy)	S (mJy km s^{-1})	V_{pk} (km s^{-1})	V_{Range} (km s^{-1})
Methanol	SE	13 05 28.167	−49 28 12.1	55 ± 6	516 ± 10	673	660–720
HC_3N	south-west	13 05 26.936	−49 28 07.9	13.5 ± 3	399 ± 14	479	390–550
	north-east	13 05 27.621	−49 28 02.1	8.4 ± 3	177 ± 14	686	550–720
CS	north-east	13 05 27.961	−49 28 01.9	63.0 ± 10	2692 ± 300	705	640–750
	south-west	13 05 27.196	−49 28 08.3	46.2 ± 10	3346 ± 300	465	400–550
Continuum	-	13 05 27.467	−49 28 04.8	295 ± 15	436 ± 33		

not clear. However, we now are able to confirm that these components exist independently in all three of our epochs covering a time interval of more than two years. Fig. 2 shows the relative difference between the spectra from each epoch of observation. No significant differences are observed, however, there is a small shift in velocity of the peak component (∼1 km s^{-1}) when comparing the 2015 August epoch and the 2017 October epoch (top panel of Fig. 2). This, and the other features of the difference spectra, is likely caused by differing array configurations between the three epochs of observation, rather than variability in the source. All strong maser emission (channels >10σ) is confined to a region smaller than approximately 1 arcsec (projected linear size of 18 pc at our assumed distance of 3.7 Mpc for NGC 4945).

We did not detect any emission from the 44.1-GHz $7_0 \rightarrow 6_1A^+$ class I methanol maser transition (5σ upper limit of 6 mJy at 3 km s^{-1} spectral resolution), or the 48.4-GHz thermal methanol line (5σ upper limit of 5 mJy at 6 km s^{-1} spectral resolution) in our observations. Assuming an identical line profile between the two class I maser transitions (36- and 44-GHz) we can put an upper limit on the 44/36-GHz integrated line intensity ratio of 0.07 ± 0.01. Similar to the 2015 August epoch (described in McCarthy et al. 2017), the 37.7-GHz class II methanol line was not detected in either of our follow up observations (5σ upper limit of ∼4.5 mJy at 3 km s^{-1} spectral resolution).

3.3 Additional 7-mm spectral lines

3.3.1 HC_3N

The HC_3N emission (see Fig. 3) is situated within the galactic plane, along the major axis of the galactic disc, near the nucleus. Two point sources with moderately broad emission are located south-west and north-east of the galactic core, covering velocity ranges of 410–560 km s^{-1} and 630–730 km s^{-1}, respectively. These components have projected linear offsets from the nucleus of 56 pc and 110 pc for the south-west and north-east components, respectively (assuming a distance of 3.7 Mpc for NGC 4945). The emission from the south-west region seems to have multiple bright components peaking above the broad underlying pedestal, the highest of which has a flux density of 13 mJy. Conversely, the north-west region appears to be simply broad emission, with a peak flux density of 8 mJy and a strong absorption trough at 636 km s^{-1} (see Fig. 3). This absorption feature at 636 km s^{-1} is observed at the same velocity as the largest absorption trough observed by Henkel et al. (2018) in their 3-mm molecular lines. We can put a 5σ upper limit of 5 mJy (at 3kms^{-1} spectral resolution) on the presence of HC_3N emission at the location of the class I methanol maser emission.

3.3.2 SiO

The SiO $J = 1 \rightarrow 0$, $v = 0$ spectral line is most obvious in absorption towards NGC 4945. Two relatively strong absorption features are observed, one at 528 km s^{-1} (–8 mJy) and the other at 636 km s^{-1} (–9 mJy). The former is located at the 7-mm continuum peak and the latter is marginally offset (<3 arcsec; $\alpha_{2000} = 13^h05^m27.654^s$, $\delta_{2000} = -49°28'04.0''$) to the north-east (see top panel of Fig. 4). The stronger absorption feature at 636 km s^{-1} is in good agreement with the feature observed by us in HC_3N emission, and therefore, also with the large absorption troughs seen in the 3-mm molecular lines by Henkel et al. (2018). In addition to these two absorption sources, there is emission observed to the south-west of the nucleus, consisting of a series of narrow peaks covering the velocity range 450–540 km s^{-1} (lower panel of Fig. 4). Compared to the other spectral lines detected in our observations these are relatively weak, with the emission not easily identifiable prior to self-calibration.

3.3.3 CS

Similar to HC_3N, CS ($J = 1 \rightarrow 0$) is also mainly arising from the galactic plane, covering the region from north-east to south-west of the galactic nucleus. The majority of emission comes from two bright regions located on either side of the nucleus within the galactic plane (see Table 3). Both of these regions consist of broad emission covering velocity ranges of 400–550 and 640–750 km s^{-1} for the south-west and north-east locations, respectively (see Fig. 3). The velocity ranges covered by the peaks of these components aligns well with those observed in the higher frequency CS $J = 2 \rightarrow 1$ line towards this same source (Henkel et al. 2018). As for HC3N (Section 3.3.1), we identify an asymmetry between the angular offsets of the two CS $J = 1 \rightarrow 0$ peaks when compared to the 7-mm continuum peak. This offset is 4.4 arcsec and 5.7 arcsec for the south-west and north-east components, respectively (corresponding to a projected linear separations of 79 and 102 pc). The lack of emission observed towards the nucleus (and in the velocity range 550–640 km s^{-1}) is due to absorption. The strong absorption feature observed in HC_3N and SiO is also present in CS and is also seen towards the position slightly north-east of the 7-mm continuum peak (see Section 3.3.1 and 3.3.2). This absorption is also observed in both the HCN $J = 1 \rightarrow 0$ and CS $J = 2 \rightarrow 1$ 3-mm lines reported by Henkel et al. (2018).

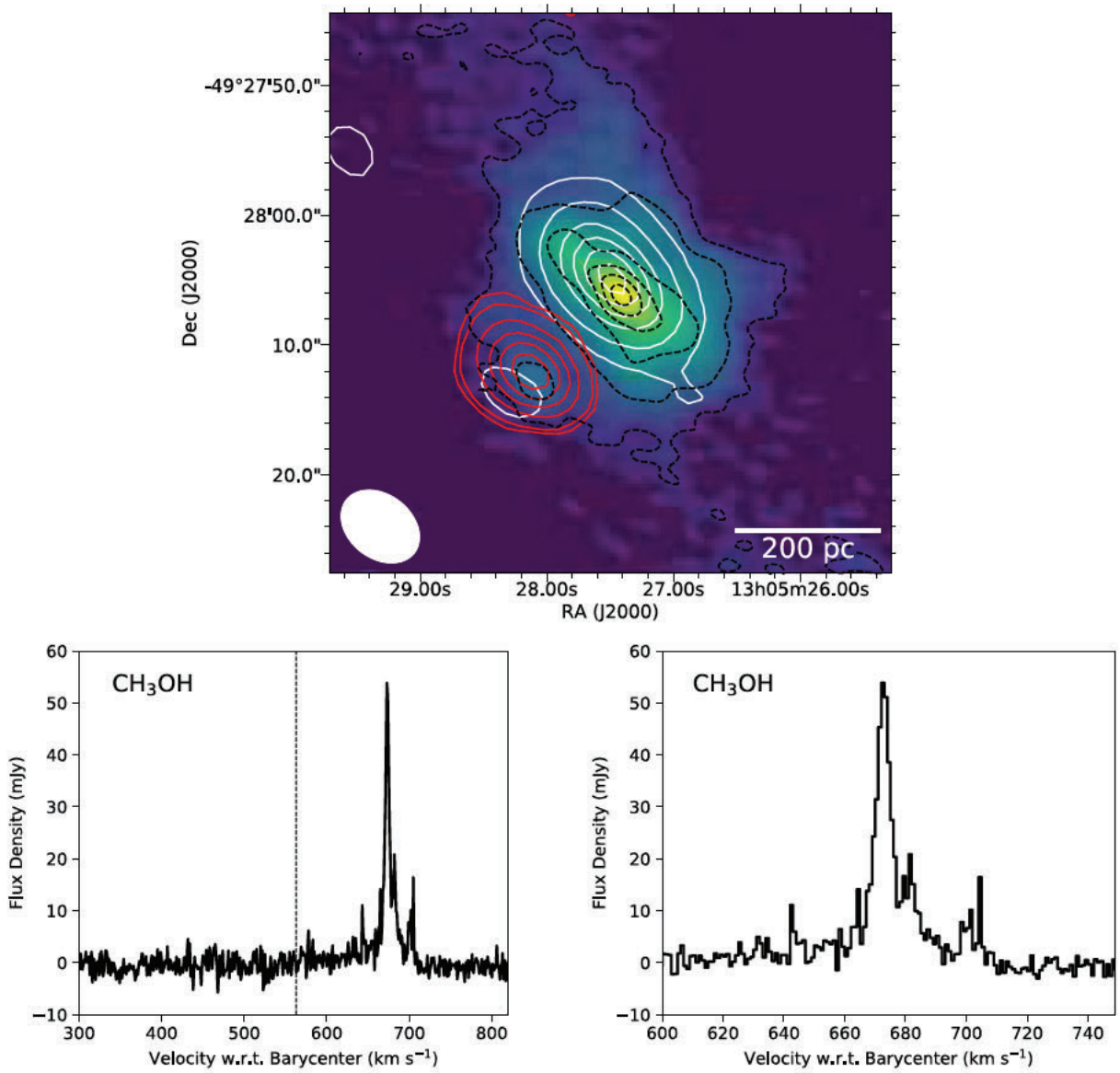

Figure 1. Top: Integrated 36.2-GHz methanol emission (red contours 2.5 per cent, 10 per cent, 30 per cent, 50 per cent, 70 per cent, and 90 per cent of the peak of 516 mJy km s^{-1} beam^{-1}) and the 7-mm continuum emission (white contours 2.5 per cent, 10 per cent, 30 per cent, 50 per cent, 70 per cent, and 90 per cent of the peak of 538 mJy beam^{-1}) with background colour map and black dashed contours of HCN $J = 1 \rightarrow 0$ integrated intensity from Henkel et al. (2018) (2 per cent, 10 per cent, 30 per cent, 50 per cent, 70 per cent, and 90 per cent of the peak of 27.6 Jy km s^{-1} beam^{-1}). Methanol and continuum emission were extracted from the combined image cube including all data from 2015 August and 2017 June/October. The white ellipse in the lower left describes the synthesized beam size for our combined observations (6.6 × 4.9 arcsec). Bottom left: 36.2 GHz spectrum from the region of peak emission within our spectral line cube (channel spacing 1 km s^{-1}). The vertical dashed line indicates the systemic velocity of NGC 4945 (Chou et al. 2007). Bottom right: Same spectrum with a cropped velocity range to allow for easier differentiation between spectral features.

4 DISCUSSION

4.1 The masing methanol of NGC 4945

Follow up observations of the $4_{-1} \rightarrow 3_0E$ methanol transition in NGC 4945 have allowed for higher fidelity imaging of the masing region. The main advantage with respect to the data previously presented by McCarthy et al. (2017) is the significantly improved uv coverage. We find good agreement (to within an arcsec) between the previously reported class I maser location (α_{2000} = 13^{h}05^{m}28.093^s, δ_{2000} = −49°28′12.3″) and the position determined using all three epochs of observation (α_{2000} = 13^{h}05^{m}28.167^s, δ_{2000} = −49°28′12.1″; see Table 3), with the standard deviation in our fit more than an order of magnitude lower (∼0.02 arcsec compared to the previous ∼0.4 arcsec). The astrometric accuracy to which we can determine the maser position is limited by the systematics of our observing configuration (array configuration etc.), rather than by errors in our position fitting.

When the initial detection of 36.2-GHz maser emission in NGC 4945 was reported in McCarthy et al. (2017), its galactic bar was thought to have a position angle of 33° with an azimuth angle with respect to the plane of the galaxy of 40° based on CO and HI observations by Ott et al. (2001). Recent investigations by Henkel et al.

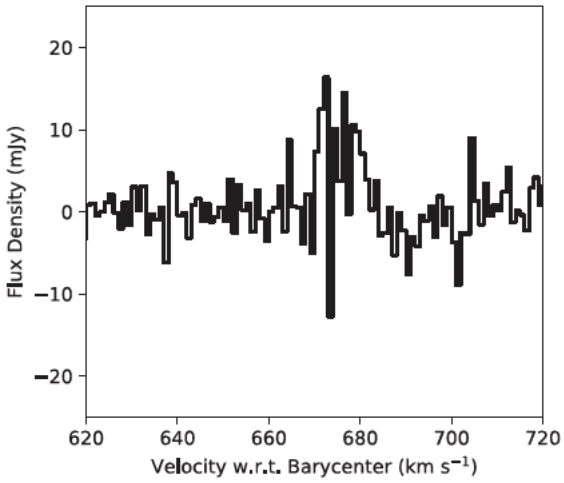

(a) October 2017 – August 2015

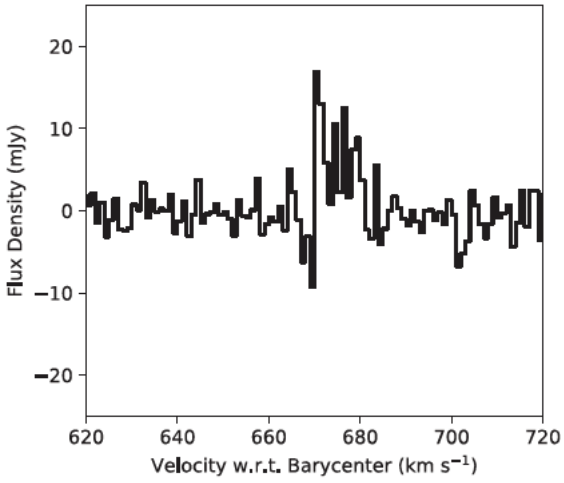

(b) October 2017 – June 2017

Figure 2. Differences between 36.2-GHz methanol maser spectra between individual epochs. Both 2015 August and 2017 June were subtracted from the 2017 October spectrum with the top panel (a) corresponding to the former case and bottom panel (b) to the latter. Vertical scales for each panel are identical for ease of comparison. Emission from the 2017 October epoch appears broader than either of the other epochs of observations (likely due to the more compact array configuration). Additionally, the 1 km s^{-1} peak shift can be seen in panel (a).

(2018) have concluded that the bar dynamics are drastically different than previously thought, with the bar elongated approximately east–west in the plane of the sky. Henkel et al. suggest that the class I methanol maser is likely associated with the front side of the bar or the southeastern spiral arm, also being part of the front side of the galaxy. Assuming the maser emission is exactly in the plane of the galactic disc and that the inclination of NGC 4945 is approximately 75°, the class I maser would have a galactocentric radius of ∼650 pc (note that if you consider a disc with some thickness, a range of valid radii about this value should be considered). This puts it outside of the estimated 300 pc maximum radius that the bar extends, indicating the masing region is likely instead located within the inner southeastern spiral arm. This is consistent with what is observed towards other extragalactic class I methanol maser sources, such as NGC 253 and IC 342, where the class I masers are offset from their dynamical centre, but close to the interfacing regions of the galactic bar (Ellingsen et al. 2017a; Gorski et al. 2018). If the masing methanol is located in this interface environment, it is consistent with the hypothesis that these masing regions result from large-scale low-velocity shocks (Ellingsen et al. 2014, 2017a; Gorski et al. 2018).

The methanol maser emission appears to be spatially coincident with the southeastern hotspot (see HCN colour map in Fig. 1) observed in the HCN and CS ($J = 2 \rightarrow 1$) dense gas tracers by Henkel et al. (2018). This hotspot is also nearby the location of 'Knot B', a structure observed previously in both Hα and Paschen-alpha (Moorwood et al. 1996; Marconi et al. 2000). Henkel et al. (2018, their section 4.1.3) find a small offset between Knot B and this secondary molecular peak, i.e. the secondary molecular peak is offset by (+3 arcsec, −2 arcsec) from knot B. This corresponds to about 3.5 arcsec or about 70 pc. They speculate that this hotspot is a giant molecular cloud complex and that Knot B is the star-forming front side of this region. We find the 36.2-GHz methanol maser emission is located closer (offset by ∼1 arcsec) to the molecular peak, rather than the region of star formation represented by Knot B. The peak velocity of the class I maser emission is redshifted relative to the velocity of this hotspot (∼660 km s^{-1}), however, only by approximately 15 km s^{-1}. Interestingly, we do not see any sign of a CS hotspot in the lower frequency CS transition that we have observed (see Section 4.2). This is not entirely unexpected, as the feature is not strong in the $J = 2 \rightarrow 1$ transition and may, due to lower statistical weights, be even weaker in the $J = 1 \rightarrow 0$ line we observe here.

In Galactic sources, 36.2- and 44.1-GHz masers are often observed together, with the 44.1-GHz transition generally being brighter (Voronkov et al. 2014). The lack of observed 44.1-GHz emission towards NGC 4945, alongside the narrowness of the observed emission, reinforces the conclusion that the class I maser in NGC 4945 is not due to a large number of Galactic-like star formation regions in a confined area.

As our observations were made over three independent epochs, this gives us the chance to compare and contrast the properties of the observed 36.2-GHz emission from NGC 4945 at different times and array configurations. The peak and integrated flux densities from each epoch are tabulated in Table 4 for the 36.2-GHz emission zoom band (both masing and continuum). The flux density of the maser emission across all three epochs is consistent with what we expect from a compact region, with the difference in peak and integrated flux density between the least and most compact array configurations (EW352 and H168, respectively) only varying by approximately 10 per cent. Comparison of the continuum emission across the different array configurations is not as straightforward, with the 2017 June epoch showing a significant drop in flux density (both integrated and peak) compared to the other two epochs (see Table 4). This same decrease in flux density is not observed in any of the calibrator sources for this epoch, with only the continuum emission of NGC 4945 lower than expected. Higher levels of decorrelation due to suboptimal observing conditions may be the cause of this, as this can affect continuum and line emission differently.

The secondary 36.2-GHz component (redshifted with respect to the peak) mentioned in McCarthy et al. (2017) has been observed independently in all three epochs, increasing confidence that it is a real component of maser emission (7σ in combined epoch data). When combining data from all three epochs, we can discern additional features in the 36.2-GHz spectrum. First, another low flux-

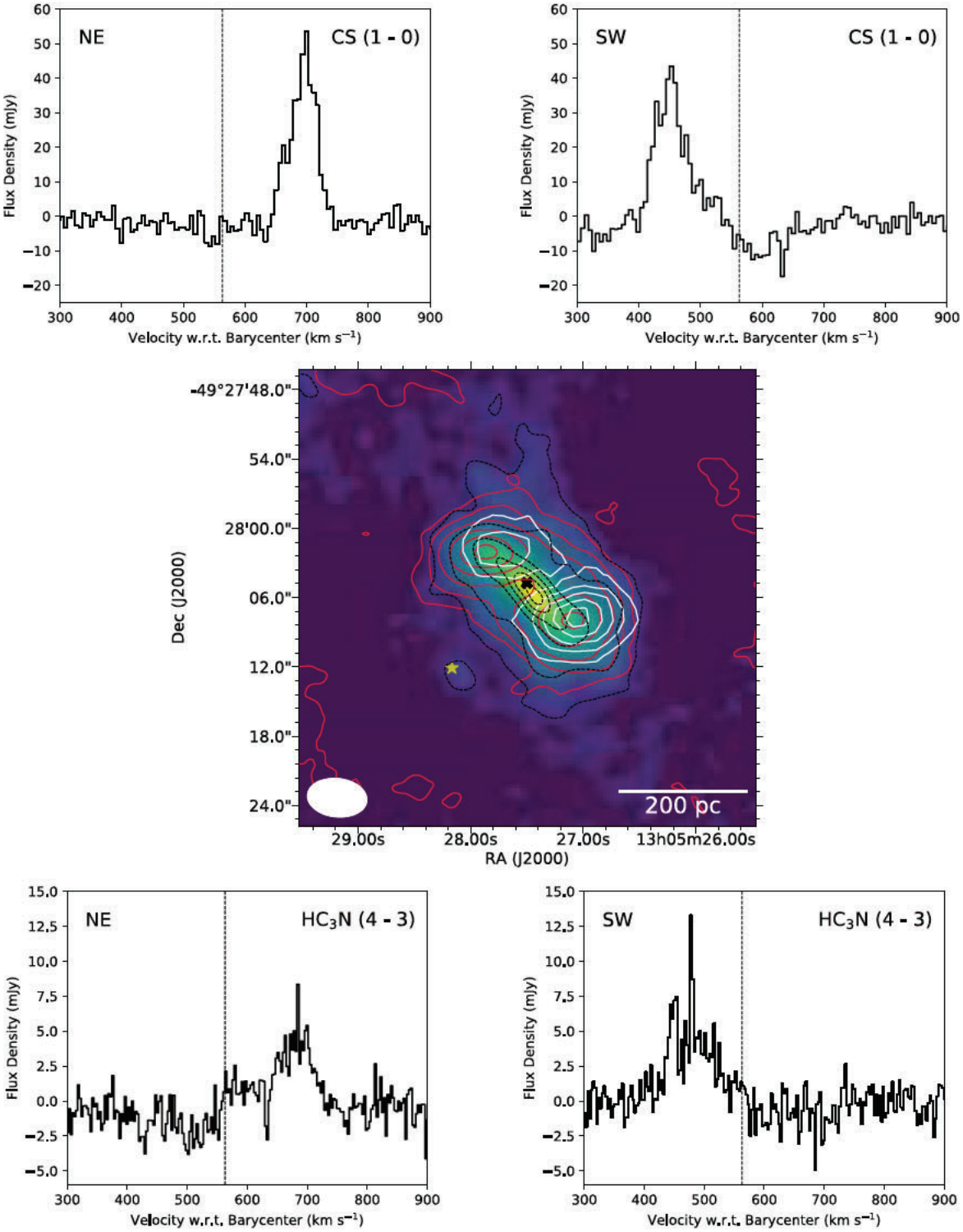

Figure 3. Centre: 36.4-GHz HC_3N integrated emission (white contours 10 per cent, 30 per cent, 50 per cent, 70 per cent, and 90 per cent of the 399 mJy km s^{-1} beam^{-1} peak, restored beam: 6.3 × 4.8 arcsec) and CS $J = 1 \rightarrow 0$ emission (red contours 10 per cent, 30 per cent, 50 per cent, 70 per cent, and 90 per cent of the 2130 mJy km s^{-1} beam^{-1} peak, restored beam: 5.2 × 3.3 arcsec), overlaid on a colour map (with accompanying dashed black contours) of the CS $J = 2 \rightarrow 1$ integrated intensity from Henkel et al. (2018) (contour levels 2 per cent, 10 per cent, 30 per cent, 50 per cent, 70 per cent, and 90 per cent of the peak of the 11.5 Jy km s^{-1} beam^{-1}). The black cross and yellow star indicate the position of the 7-mm continuum peak and 36.2-GHz maser location, respectively. The white ellipse represents the synthesized beam of the CS $J = 1 \rightarrow 0$ observations. Top: Spectra of the north-east and south-west CS $J = 1 \rightarrow 0$ components (from left to right) extracted at the locations of peak emission from the image cube with a spectral resolution of 6 km s^{-1}. Bottom: Spectra of the north-east and south-west HC_3N $J = 4 \rightarrow 3$ components (from left to right) extracted at the location of peak emission from the image cube with a spectral resolution of 3 km s^{-1}.

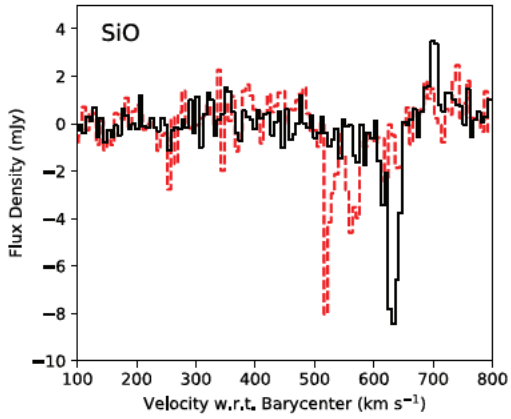

(a) SiO absorption

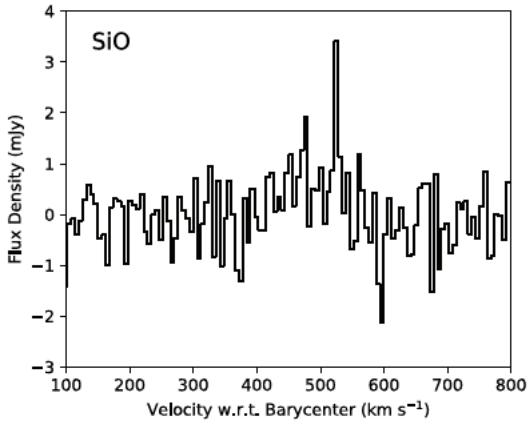

(b) SiO emission

Figure 4. Top: SiO absorption spectra for the two main components in NGC 4945. The red-dashed spectrum represents absorption towards the 7-mm continuum peak (see Table 3). The black spectrum represents absorption from the component offset 3 arcsec to the north-east of the continuum peak. Both spectra have a spectral resolution of 6 km s^{-1}. Bottom: Spectrum of weak SiO emission from south-west of the continuum peak taken from a spectral line cube with spectral resolution of 6 km s^{-1}.

Table 4. 36.2 GHz methanol and continuum emission towards NGC 4945 from individual observation epochs.

	Epoch	Array	S_{pk} (mJy)	S (mJy km s^{-1})
Methanol	2015 Aug	EW367	49	294 ± 23
	2017 June	H214	48	306 ± 40
	2017 Oct	H168	54	339 ± 18
Continuum	2015 Aug	EW367	313	414 ± 40
	2017 June	H214	236	348 ± 45
	2017 Oct	H168	385	489 ± 18

density component (5σ detection in combined epoch data) appears blueshifted in relation to the peak emission. Interestingly, these two minor components, are roughly symmetrically distributed about the central peak emission. Additionally, in the combined data set, the central peak appears to split into two components of maser emission with a small relative velocity offset. This symmetric distribution of masing emission is suggestive of the spectra seen towards edge on disc structures, similar to those observed from H_2O megamasers towards the nucleus, with the bright emission at the systemic velocity and the red- and blueshifted components at the approaching and receding edges of the disc. Assuming an edge on disc, we identify a rotational velocity of $V_{rot} = 30$ km s^{-1} and a velocity drift of 0.5 km s^{-1} yr^{-1} (obtained from peak shift discussed in Section 3.2). These values correspond to a disc with radius of ∼380 au with enclosed mass of ∼390 $M_\odot$ (Ishihara et al. 2001). However, this is highly speculative as our resolution is not high enough to satisfactorily determine whether the positions of these individual components show any ordered structure.

4.2 CS: comparison with 3-mm observations

With the recent addition of ALMA to the southern hemisphere's astrophysical toolbox, the dynamics and molecular structure of the central region of NGC 4945 are now beginning to be more clearly understood (Bendo et al. 2016; Henkel et al. 2018). Our observations of the CS $J = 1 \rightarrow 0$ emission towards NGC 4945 show strong agreement, in terms of position and velocity of the bright regions north-east and south-west of the galactic nucleus, when compared to the CS and HCN emission reported by Henkel et al. (2018). We identify a line ratio of approximately 4 between the CS $J = 2 \rightarrow 1$ and CS $J = 1 \rightarrow 0$ emission (Henkel et al. 2018). This indicates the CS $J = 1 \rightarrow 0$ emission is optically thin and highly excited. As mentioned in Section 4.1, we see no evidence for the southeastern hotspot in the CS $J = 1 \rightarrow 0$ transition (5σ upper limit of 15 mJy in a 3 km s^{-1} channel), likely due to the large discrepancy in flux densities between the two CS transitions. Possibly, longer on-source integration times would reveal some weak emission from this location. It should also be noted that the synthesized beam of our observations is significantly larger than that of the ALMA observations presented by Henkel et al. (5.2 × 3.3 compared to 2.6 × 1.4 arcsec).

Henkel et al. (2018) propose that the east–west oriented bar in NGC 4945 can be directly seen in their CS $J = 2 \rightarrow 1$ and HCN $J = 1 \rightarrow 0$ lines, when integrating over that narrow velocity range near the systemic velocity of the galaxy, which is least affected by absorption. A direct connection can be seen in their HCN-integrated intensity map, and the same east–west structure is even more clearly seen in the CS emission. Comparing our lower frequency CS $J = 1 \rightarrow 0$ emission across this velocity range (585–612km s^{-1}), we are also able to clearly see this bar structure (see Fig. 5), though not as extended as evident in the higher frequency transitions.

4.3 Nature of HC_3N emission in NGC 4945

Determining the nature of the HC_3N $J = 4 \rightarrow 3$ emission in NGC 4945 is difficult as there are not many known Galactic or extragalactic sources displaying maser emission from this species. The Sgr B2 complex has been observed in various HC_3N transitions, with maser emission detected in the $J = 1 \rightarrow 0$ transition (Hunt et al. 1999). McGee, Newton & Balister (1977) report $J = 4 \rightarrow 3$ emission in Sgr B2 with an integrated flux density of ∼660 Jy km s^{-1}. Comparing this flux density to the total integrated intensity across both the north-east and south-west components in NGC 4945, we see that NGC 4945 is approximately a factor of 190 times more luminous than Sgr B2 (assuming a distance of 7.9 kpc for Sgr B2 and 3.7-Mpc for NGC 4945, Reid et al. 2009; Tully et al. 2013). Comparing the individual components to the HC_3N $J = 4 \rightarrow 3$ emission in Sgr B2, we see that the southeastern HC_3N component in NGC 4945 is ∼130 times more luminous.

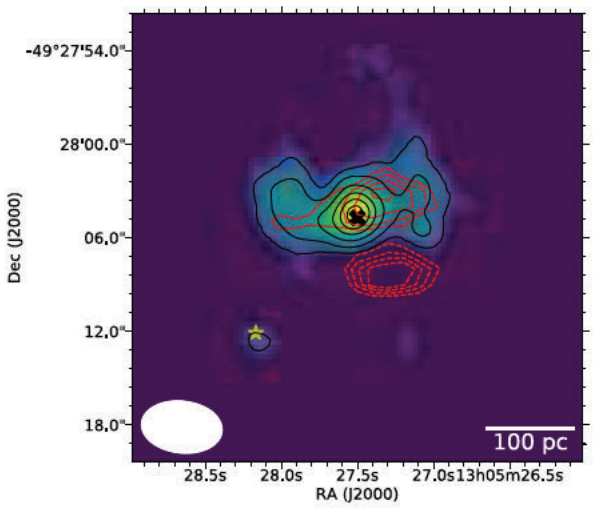

Figure 5. Integrated intensity of 49-GHz CS $J = 1 \rightarrow 0$ emission over the velocity range 585 –612km s^{-1} (red contours 30 per cent, 50 per cent, 70 per cent, and 90 per cent of the 187 mJy km s^{-1} beam^{-1} peak, dashed contours represent the same levels for absorption). This is the same velocity range where the east–west structure of the bar is visible in the CS $J = 2 \rightarrow 1$ emission presented by Henkel et al. (2018). The background colour map represents CS $J = 2 \rightarrow 1$ integrated intensity across this same reduced velocity range (black contours 30 per cent, 50 per cent, 70 per cent, and 90 per cent of the 2.4 Jy km s^{-1} beam^{-1} peak; Henkel et al. 2018). The black cross and yellow star indicate the position of the 7-mm continuum peak and 36.2-GHz maser location, respectively.

Recently, HC_3N $J = 4 \rightarrow 3$ emission towards NGC 253 has been reported to be the result of maser processes (Ellingsen et al. 2017b). The emission we observe towards NGC 4945 bares some similarities to that seen in NGC 253, especially when comparing it on a component-to-component scale. The total integrated flux of the HC_3N $J = 4 \rightarrow 3$ emission in NGC 4945 is almost a factor of 10 lower than that observed in NGC 253 (Ellingsen et al. 2017b). However, when looking at the individual HC_3N components (2 in NGC 4945, 7 in NGC 253) across both sources, we see that the integrated flux densities of individual components are very similar. The most luminous component observed towards NGC 253 is 443 mJy km s^{-1} (Ellingsen et al. 2017b). This would correspond to a flux density of 374 mJy km s^{-1} in NGC 4945 (assuming a distance of 3.4 Mpc for NGC 253 and 3.7 Mpc for NGC 4945, Dalcanton et al. 2009; Tully et al. 2013), very similar to the highest flux density HC_3N component (the southwestern one) observed towards NGC 4945. Likewise, the northeastern HC_3N component in NGC 4945 also shows a flux density which is similar to the individual spots observed in NGC 253. It is important to note that the flux density values reported for NGC 253 in Ellingsen et al. (2017b) are using the combined EW367 and 1.5A array configurations, both of which have longer maximum baselines than the two array configurations used for our observations (H168 and H214). Therefore, missing flux from extended emission makes comparison of flux densities unreliable.

The two regions of HC_3N emission in NGC 4945 have close spatial correlations with the observed CS $J = 1 \rightarrow 0$ emission (see Fig. 3). Emission from the two HC_3N point sources appears to heavily overlap with the most luminous regions of CS north-east and south-west of the core, with similar velocities for peak emission (see Table 3). This is similar to what is seen in NGC 253, where the HC_3N spots correlate with the position of molecular clouds (Leroy et al. 2015; Ellingsen et al. 2017b). These molecular clouds are defined by regions of excess emission from dense gas tracers such as CS and HCN (Leroy et al. 2015; Meier et al. 2015). The linear offsets from the nucleus (110 and 56 pc towards the south-west and north-east, respectively) for the HC_3N spots in NGC 4945, puts them close to the radius of the outer nuclear disc and inner bar interface (Henkel et al. 2018).

Ellingsen et al. (2017b) concluded that at least one of the HC_3N spots they observed in NGC 4945 was due to a maser process. However, it is difficult to evaluate whether this is also the case for either region observed towards NGC 4945. This is partly because of the limited angular resolution of our observations, which prevents us from determining how compact these regions are. Unlike the actively studied maser species such as methanol and H_2O, the maser process of HC_3N is much less clear. Therefore, we do not know whether a typical HC_3N maser forms in a compact region, as observed in those other molecular species. If we assume it does, based on the maser emission detected towards NGC 253, then a follow up of the HC_3N observations in NGC 4945 at higher angular resolution will help us determine the nature of these regions. Additionally, detailed investigation into the nuclear molecular clouds has not been conducted in NGC 4945. Information about the environments housing these spots would provide useful insight into the processes governing the HC_3N emission.

4.4 Comparison of the CH_3OH masing environment in NGC 4945 to other relevant sources

In the absence of direct information regarding the physical conditions responsible for these extragalactic masers, comparisons with similar sources may reveal useful properties of the masing regions. These comparisons can both help understand the phenomenon and allow for future searches with better constrained source samples.

This section will first compare the masing region of NGC 4945 to those observed within NGC 253, and subsequently compare both of these sources to the Galactic giant molecular cloud G 1.6-0.025.

4.4.1 NGC 253

The sample size of known extragalactic class I methanol masers is currently very small. This makes the nature of such emission difficult to discern. The best match up of host galaxies from the available sample is between NGC 253 and NGC 4945. Similar to NGC 4945, NGC 253 is a nearby-barred spiral starburst galaxy, with recently detected class I methanol maser emission at 36.2-GHz (Sakamoto et al. 2011; Ellingsen et al. 2014). These two sources are similarly distant (3.4 Mpc for NGC 253 and 3.7 Mpc for NGC 4945, Dalcanton et al. 2009; Tully et al. 2013), and have methanol maser emission of comparable luminosity. Due to these factors, these two sources are the best candidates for a direct comparison of environments hosting the masing methanol.

Our follow up observations have allowed us to more accurately compare the integrated intensity of NGC 4945 to NGC 253, as both sources have been observed with the same array configuration (H168) and are at similar distances. We find that the single region of class I maser emission in NGC 4945 has an integrated flux density 50 per cent greater than either emission region in NGC 253 (Ellingsen et al. 2014, 2017a). In addition to being brighter, the 36.2-GHz methanol maser component towards NGC 4945 has a much narrower linewidth, $\sim$8 km s^{-1} compared to those observed towards any of the regions in NGC 253 ($\gtrsim$ 20 km s^{-1} at comparable angular and spectral resolution, Ellingsen et al. 2017a).

There is a strong correlation between the masing regions of NGC 253 and the presence of large molecular clouds (Leroy et al. 2015; Ellingsen et al. 2017a). As mentioned in Section 4.1, images presented by Henkel et al. (2018) show the methanol masing region in NGC 4945 is projected on to an HCN and CS hotspot. This hotspot may mark the location of a molecular cloud complex, similar to those identified in NGC 253 (Leroy et al. 2015). 36.4-GHz HC_3N emission is observed towards all of the class I methanol maser emission regions in NGC 253 (Ellingsen et al. 2017b). This same relationship is not observed towards NGC 4945, where we place a 5σ upper limit of 5 mJy (in a 3 km s^{-1} channel) on the existence of HC_3N (from this same transition) at the maser location.

A very significant difference between these two class I maser hosts is the lack of 44.1-GHz emission observed towards NGC 4945. Ellingsen et al. (2017a) detected 44.1-GHz masers in two of the regions host to 36.2-GHz masers in NGC 4945. Despite the relative weakness of the 44.1-GHz emission in NGC 253, our 3σ upper limit from NGC 4945 is a factor of 2 lower. Assuming our 5σ upper limit (6 mJy peak) on the existence of 44.1-GHz emission, we place a lower limit on the 36.2:44.1 GHz integrated line intensity ratio of 15:1. Comparatively, the two regions in NGC 253 displaying emission from both transitions have ratios of 11:1 and 17:1 (for regions 'MM1' and 'MM4', respectively; Ellingsen et al. 2017a), with lower limits on the regions without detections at 44.1-GHz ranging from 4:1 up to 18:1. Therefore, despite a potentially much lower peak flux density, 44.1-GHz emission may exist towards NGC 4945 at similar relative intensities as observed in NGC 253.

Given that the region of 36.2-GHz emission in NGC 4945 is significantly brighter than any of the regions in NGC 253 also hosting 44.1-GHz emission, we would expect any 44.1-GHz emission to be above this threshold assuming similar ratios to what is observed in NGC 253.

Extended thermal methanol (48.4-GHz transition) is clearly visible in NGC 253, covering all sites where the 36.2-GHz maser emission is observed (Ellingsen et al., in preparation). A similar relationship is observed towards IC 342, with extended 96-GHz thermal methanol observed across all class I maser locations (Meier & Turner 2005; Gorski et al. 2018). Conversely, we see no thermal methanol from the 48.4-GHz transition towards NGC 4945. This, combined with differences in the 36.2- to 44.1-GHz flux density ratios and a small line width (indicating a compact region), suggests that the optical depth of the masing line in NGC 4945 is likely much higher than in any region in NGC 253.

4.4.2 G 1.6-0.025

G 1.6-0.025 (referred to hereafter as G 1.6) is a giant molecular cloud located at the easternmost edge of the Milky Way's CMZ cloud complex (Whiteoak & Gardner 1979; Bally et al. 1987, 1988). This region displays maser emission from various class I methanol transitions. However, unlike typical methanol maser sources, it lacks any significant high-mass star formation (Haschick & Baan 1993; Menten et al. 2009). The nature of the maser emission from G 1.6 is unlike that observed from typical Galactic class I maser sites, and appears to be somewhat similar to those observed in the extragalactic class I regions of NGC 4945 and NGC 253. Here, we will make a comparison between G 1.6 and these extragalactic sources, and discuss the possibility of them resulting from similar physical conditions.

Much like NGC 4945 (and to a lesser extent NGC 253), emission from the 44.1-GHz methanol transition is much weaker than the accompanying 36.2-GHz methanol emission in G 1.6 (Jones et al. 2013). As previously mentioned, this is atypical for Galactic class I maser sources, where these two transitions are often observed together, with the 44.1-GHz line being generally more luminous (Voronkov et al. 2014). This may indicate that G 1.6 and these extragalactic class I maser regions share a common pumping regime, which results in emission from the 36.2-GHz transition dominating. G 1.6 is also host to maser emission from the 84.5-GHz methanol transition (Salii, Sobolev & Kalinina 2002). This transition is related to the 36.2-GHz line, and is additionally observed tentatively as a megamaser in the starburst galaxy NGC 1068 (Wang et al. 2014). We suggest that it is likely that this 84.5-GHz methanol transition will be visible towards the extragalactic class I regions in NGC 4945 and NGC 253. If future observations discover this to be correct, a comparison of flux densities between the 36.2- and 84.5-GHz lines in G 1.6 and these extragalactic sources may reveal further similarities.

The broader environment of G 1.6 also shares similarities with the extragalactic maser sources. G 1.6 is a dense giant molecular cloud, easily visible in emission from the same dense gas tracers that identified similar clouds in NGC 253 (Leroy et al. 2015). Each independent region of 36.2-GHz maser emission from NGC 253 is associated with one of these giant molecular clouds (Ellingsen et al. 2017a). We also discuss in Section 4.1, that the southeastern HCN and CS hotspot in NGC 4945 also indicate the presence of a giant molecular cloud at the location of the class I maser emission (Henkel et al. 2018). In addition, the class I masing regions of NGC 253 are bright in the 43.4-GHz SiO and 48.4-GHz thermal methanol transitions, which are some of the strongest 7-mm spectral lines observed towards G 1.6 (Jones et al. 2013). However, these same transitions are not observed towards the masing region of NGC 4945, with emission from the 48.4-GHz thermal methanol not detected, and weak 43.4-GHz SiO only observed close to the galactic nucleus.

One of the most interesting properties of G 1.6 is the lack of star formation from a region displaying such prominent 36.2-GHz class I maser emission. However, this lack of star formation does not appear to be mirrored in the environment of the class I maser emission in NGC 4945, with enhanced star formation (Knot B) observed nearby to the region of dense gas at the masers location (Marconi et al. 2000; Henkel et al. 2018). This star formation is offset from the maser emission, however, it may be part of the same molecular cloud complex (Henkel et al. 2018). If an association with Knot B does exist, this would indicate that the class I maser emission from NGC 4945 and G 1.6 may not result from the same phenomenon and leaves open the possibility between a direct connection between the maser emission and star formation.

5 CONCLUSIONS

Our high-resolution imaging follow up of the 36.2-GHz class I methanol maser emission in NGC 4945 has confirmed its offset position from the galactic nucleus. Assuming the region is part of the disc, it would be located at a galactocentric radius of approximately 670 pc and is likely associated with the interface region between galactic bar and southeastern spiral arm on the front side of the galaxy. This position corresponds to the position of a hotspot observed in dense gas tracers, likely indicating an association between the masing region and a giant molecular cloud. We detect methanol emission from neither the 44.1-GHz masing transion nor the 48.4-GHz thermal transition towards NGC 4945 and this indicates a high optical depth for the 36.2-GHz class I masing region.

The 7-mm continuum source is offset by 0.8 arcsec $\pm$ 0.4 arcsec to the north-west of the dynamical centre of NGC 4945 (α_{2000} = $13^{h}05^{m}27^{s}.467 \pm 0^{s}.032$ and $\delta_{2000} = -49°28'04''.8 \pm 0''.3$).

Emission from the HC_3N $J = 4 \rightarrow 3$, CS $J = 1 \rightarrow 0$, and SiO $J = 1 \rightarrow 0$ transitions were also detected towards NGC 4945. All of these thermal transitions were observed towards the central region of NGC 4945 (consistent with the 3-mm ALMA observations). Additionally, all of these species display strong absorption towards the continuum source, with a peak absorption component at 636 km s^{-1}. None of these molecular species were detected towards the offset location where the methanol masers are observed.

We identify many similarities between the class I methanol masers of NGC 4945 and NGC 253. There is a possibility that the optical depth of the maser in NGC 4945 is higher, leading to particularly high-intensity ratios between the 36.2- and 44.1-GHz methanol lines. A comparison with the giant molecular cloud G 1.6-0.025 revealed similar line ratios between the 36.2- and 44.1-GHz methanol maser transitions, though unlike G 1.6-0.025, the maser region in NGC 4945 may be associated with a region of enhanced star formation.

ACKNOWLEDGEMENTS

We thank the referee for useful suggestions which helped improve this paper. We thank the authors Henkel et al. (2018) for allowing the use of their images cubes in the creation of our figures. The ATCA is part of the Australia Telescope which is funded by the Commonwealth of Australia for operation as a National Facility managed by CSIRO. This research has used NASA's Astrophysics Data System Abstract Service. This research also utilized APLPY, an open-source plotting package for PYTHON hosted at http://aplpy.github.com. This research used Astropy, a community-developed core Python package for Astronomy (Astropy Collaboration et al. 2013).

REFERENCES

Astropy Collaboration et al., 2013, A&A, 558, A33
Bally J., Stark A. A., Wilson R. W., Henkel C., 1987, ApJS, 65, 13
Bally J., Stark A. A., Wilson R. W., Henkel C., 1988, ApJ, 324, 223
Batrla W., Matthews H. E., Menten K. M., Walmsley C. M., 1987, Nature, 326, 49
Bendo G. J., Henkel C., D'Cruze M. J., Dickinson C., Fuller G. A., Karim A., 2016, MNRAS, 463, 252
Breen S. L. et al., 2015, MNRAS, 450, 4109
Caswell J. L. et al., 2010, MNRAS, 404, 1029
Caswell J. L. et al., 2011, MNRAS, 417, 1964
Chen X., Ellingsen S. P., Shen Z.-Q., Titmarsh A., Gan C.-G., 2011, ApJS, 196, 9
Chen X., Ellingsen S. P., Baan W. A., Qiao H.-H., Li J., An T., Breen S. L., 2015, ApJ, 800, L2
Chen X., Ellingsen S. P., Shen Z.-Q., McCarthy T. P., Zhong W.-Y., Deng H., 2018, ApJ, 856, L35
Chou R. C. Y. et al., 2007, ApJ, 670, 116
Cyganowski C. J., Brogan C. L., Hunter T. R., Churchwell E., 2009, ApJ, 702, 1615
Cyganowski C. J., Brogan C. L., Hunter T. R., Zhang Q., Friesen R. K., Indebetouw R., Chandler C. J., 2012, ApJ, 760, L20
Dalcanton J. J. et al., 2009, ApJS, 183, 67
Ellingsen S. P., Shabala S. S., Kurtz S. E., 2005, MNRAS, 357, 1003
Ellingsen S. P., Breen S. L., Caswell J. L., Quinn L. J., Fuller G. A., 2010, MNRAS, 404, 779
Ellingsen S. P., Chen X., Qiao H.-H., Baan W., An T., Li J., Breen S. L., 2014, ApJ, 790, L28
Ellingsen S. P., Chen X., Breen S. L., Qiao H.-H., 2017a, MNRAS, 472, 604
Ellingsen S. P., Chen X., Breen S. L., Qiao H.-h., 2017b, ApJ, 841, L14
Gan C.-G., Chen X., Shen Z.-Q., Xu Y., Ju B.-G., 2013, ApJ, 763, 2
Gorski M., Ott J., Rand R., Meier D., Momjian E., Schinnerer E., 2018, ApJ, 856, 134
Green J. A. et al., 2008, MNRAS, 385, 948
Green J. A. et al., 2010, MNRAS, 409, 913
Green J. A. et al., 2012, MNRAS, 420, 3108
Green J. A. et al., 2017, MNRAS, 469, 1383
Greenhill L. J., Moran J. M., Herrnstein J. R., 1997, ApJ, 481, L23
Hagiwara Y., Horiuchi S., Doi A., Miyoshi M., Edwards P. G., 2016, ApJ, 827, 69
Haschick A. D., Baan W. A., 1993, ApJ, 410, 663
Henkel C. et al., 2018, A&A, 615, A155
Humphreys E. M. L., Vlemmings W. H. T., Impellizzeri C. M. V., Galametz M., Olberg M., Conway J. E., Belitsky V., De Breuck C., 2016, A&A, 592, L13
Hunt M. R., Whiteoak J. B., Cragg D. M., White G. L., Jones P. A., 1999, MNRAS, 302, 1
Ishihara Y., Nakai N., Iyomoto N., Makishima K., Diamond P., Hall P., 2001, PASJ, 53, 215
Jones P. A., Burton M. G., Cunningham M. R., Tothill N. F. H., Walsh A. J., 2013, MNRAS, 433, 221
Jordan C. H., Walsh A. J., Breen S. L., Ellingsen S. P., Voronkov M. A., Hyland L. J., 2017, MNRAS, 471, 3915
Kurtz S., Hofner P., Álvarez C. V., 2004, ApJS, 155, 149
Leroy A. K. et al., 2015, ApJ, 801, 25
Licquia T. C., Newman J. A., 2015, ApJ, 806, 96
Marconi A., Oliva E., van der Werf P. P., Maiolino R., Schreier E. J., Macchetto F., Moorwood A. F. M., 2000, A&A, 357, 24
McCarthy T. P., Ellingsen S. P., Chen X., Breen S. L., Voronkov M. A., Qiao H.-h., 2017, ApJ, 846, 156
McGee R. X., Newton L. M., Balister M., 1977, MNRAS, 180, 585
Meier D. S., Turner J. L., 2005, ApJ, 618, 259
Meier D. S. et al., 2015, ApJ, 801, 63
Menten K., 1991, in Haschick A. D., Ho P. T. P., eds, ASP Conf. Ser. , Vol. 116, Atoms, Ions and Molecules: New Results in Spectral Line Astrophysics, Astron. Soc. Pac., San Francisco, p. 119
Menten K. M., Wilson R. W., Leurini S., Schilke P., 2009, ApJ, 692, 47
Moorwood A. F. M., van der Werf P. P., Kotilainen J. K., Marconi A., Oliva E., 1996, A&A, 308, L1
Ott M., Whiteoak J. B., Henkel C., Wielebinski R., 2001, A&A, 372, 463
Pérez-Beaupuits J. P., Spoon H. W. W., Spaans M., Smith J. D., 2011, A&A, 533, A56
Pesce D. W., Braatz J. A., Impellizzeri C. M. V., 2016, ApJ, 827, 68
Reid M. J. et al., 2009, ApJ, 700, 137
Sakamoto K., Mao R.-Q., Matsushita S., Peck A. B., Sawada T., Wiedner M. C., 2011, ApJ, 735, 19
Salii S. V., Sobolev A. M., Kalinina N. D., 2002, Astron. Rep., 46, 955
Sjouwerman L. O., Murray C. E., Pihlström Y. M., Fish V. L., Araya E. D., 2010, ApJ, 724, L158
Slysh V. I., Kalenskii S. V., Valtts I. E., Otrupcek R., 1994, MNRAS, 268, 464
Spoon H. W. W., Koornneef J., Moorwood A. F. M., Lutz D., Tielens A. G. G. M., 2000, A&A, 357, 898
Spoon H. W. W., Moorwood A. F. M., Pontoppidan K. M., Cami J., Kregel M., Lutz D., Tielens A. G. G. M., 2003, A&A, 402, 499
Strickland D. K., Heckman T. M., Colbert E. J. M., Hoopes C. G., Weaver K. A., 2004, ApJ, 606, 829
Tully R. B. et al., 2013, AJ, 146, 86
Val'tts I. E., Ellingsen S. P., Slysh V. I., Kalenskii S. V., Otrupcek R., Larionov G. M., 2000, MNRAS, 317, 315
Voronkov M. A., Caswell J. L., Ellingsen S. P., Sobolev A. M., 2010, MNRAS, 405, 2471
Voronkov M. A., Caswell J. L., Ellingsen S. P., Green J. A., Breen S. L., 2014, MNRAS, 439, 2584
Wang J., Zhang J., Gao Y., Zhang Z.-Y., Li D., Fang M., Shi Y., 2014, Nature Commun., 5, 5449
Whiteoak J. B., Gardner F. F., 1979, MNRAS, 188, 445
Wilson W. E. et al., 2011, MNRAS, 416, 832

This paper has been typeset from a TEX/LATEX file prepared by the author.

Chapter 5

Detection of 84-GHz class I methanol maser emission toward NGC 253

5.1 Introduction

This paper is originally published in *The Astrophysical Journal* as *'Detection of 84 GHz Class I Methanol Maser Emission toward NGC 253'* (DOI: 10.3847/2041-8213/aae82c).

In this paper we report the results of 3-mm observations towards NGC 253 with the Australia Telescope Compact Array (ATCA). We report the second detection of a 84.5-GHz methanol maser towards an external galaxy. This maser emission is spatially coincident with previously reported 36.2- and 44.1-GHz class I methanol emission by Ellingsen et al. (2017a). All three of these methanol maser transitions show differing distributions across NGC 253, indicating that each of the maser environments likely have differing physical conditions. Included in this paper is imaging of the 87.9-GHz HNCO line (a tracer of shocked gas), and some coarse resolution observations of the 36.2-GHz class I line.

The 84.5-GHz class I methanol transition is the most sensible next line to search for (after the 36.2-GHz transition). In Galactic sources a strong correlation is observed between these two maser lines, with both belonging to the same transition family

$(J_{-1} \rightarrow (J-1)_0)$. Additionally, a detection of this transition had already been made toward NGC 1068 by Wang et al. (2014). Whilst writing this paper, we actually realised that this 84.5-GHz transition had been detected towards NGC 253 previously by Hüttemeister et al. (1997), who observed it alongside some thermal methanol lines. They were unable to reconcile the properties of the emission when compared to the thermal lines they had observed and did not consider that it may instead be a result of a maser process. Our interferometric observations with the ATCA allow us to confidently determine that the emission from this region is indeed masing.

5.2 Author Contribution

- Observations were made as part of the C3167 ATCA project led by Tiege McCarthy. ATCA observations were performed by Tiege McCarthy in July of 2018 with support from Shari Breen and Maxim Voronkov.
- All data-reduction for this paper was performed by Tiege McCarthy using MIRIAD and PYTHON.
- Analysis was performed by Tiege McCarthy alongside substantive discussion with Simon Ellingsen, Shari Breen and Maxim Voronkov.
- All figures and the vast majority of the writing for the paper were created by Tiege McCarthy, with Simon Ellingsen, Shari Breen, Xi Chen and Maxim Voronkov providing review and suggestions to improve the final manuscript.

Chapter 6

Variability in extragalactic class I methanol masers: New maser components toward NGC 4945 and NGC 253

6.1 Introduction

This paper was originally published in *Monthly Notices of the Royal Astronomical Society* as *'Variability in extragalactic class I methanol masers: New maser components toward NGC 4945 and NGC 253'* (DOI: 10.1093/mnras/stz3098).

This is the final paper relating to my candidature, and reports the results of further Australia Telescope Compact Array (ATCA) observations toward NGC 4945 and NGC 253, along with upper-limits on 36.2-GHz methanol emission from all sources searched as part of ATCA projects C2879 and C3263 over the past 5 years.

This further monitoring of the methanol maser emission toward NGC 4945 detected the presence of a new masing region (named M2). This new maser region provides the first evidence for variability from an extragalactic methanol maser. Additionally, we detect tentative new maser components toward NGC 253, which are spatially coincident with the 3-mm HNCO emission reported in the previous chapter (McCarthy

et al., 2018b). In total upper-limits on the 36.2- and 37.7-GHz methanol maser lines were reported for 12 sources observed as part of the C2879 and C3263 projects. The latter project is a recent search for extragalactic 36.2-GHz masers based on our current understanding of these sources.

During the process of reducing data from the C2879 sources, it was discover that the detection of 36.2-GHz (and 37.7-GHz) methanol maser emission toward Arp 220 by Chen et al. (2015) may have been the result of sub-optimal imaging procedures. Subsequent analysis of follow up ATCA data also shows no evidence for the maser emission. Recent Effelsberg 100m observations by Humire et al. (submitted) also do not show evidence of the methanol maser emission toward Arp 220.

6.2 Author Contribution

- Observations were made as part of the C3167 and C3263 ATCA projects led by Tiege McCarthy, along with previous observations from the C2879 project led by Xi Chen. All C3167 and C3263 observations were performed by Tiege McCarthy in July 2017, December 2018 and March 2019. The C2879 observations were performed by Xi Chen and Hai-hua Qiao in March 2014 and August 2015.
- All data-reduction for this paper was performed by Tiege McCarthy using MIRIAD and PYTHON.
- Analysis was performed by Tiege McCarthy alongside substantive discussion with Simon Ellingsen, Shari Breen and Maxim Voronkov.
- All figures and the vast majority of the writing for the paper were created by Tiege McCarthy, with Simon Ellingsen, Shari Breen, Xi Chen and Maxim Voronkov providing review and suggestions to improve the final manuscript.

MNRAS **000**, 000–000 (0000) Preprint 1 November 2019 Compiled using MNRAS LATEX style file v3.0

Variability in extragalactic class I methanol masers: New maser components toward NGC 4945 and NGC 253

T. P. McCarthy,[1,2]⋆ S. P. Ellingsen,[1] S. L. Breen,[3] M. A. Voronkov,[2] X. Chen[4,5] and H-h. Qiao[5,6]

[1] *School of Natural Sciences, University of Tasmania, Private Bag 37, Hobart, Tasmania 7001, Australia*
[2] *Australia Telescope National Facility, CSIRO, PO Box 76, Epping, NSW 1710, Australia*
[3] *Sydney Institute for Astronomy (SIfA), School of Physics, University of Sydney, NSW 2006, Australia*
[4] *Center for Astrophysics, GuangZhou University, Guangzhou 510006, China*
[5] *Shanghai Astronomical Observatory, Chinese Academy of Sciences, Shanghai 200030, China*
[6] *National Time Service Center, Chinese Academy of Sciences, Xi'An, Shaanxi 710600, China*

1 November 2019

ABSTRACT

We have used the Australia Telescope Compact Array (ATCA) to make new observations of the 36.2-GHz ($4_{-1} \rightarrow 3_0$E) methanol transition toward NGC 4945 and NGC 253. These observations have revealed the presence of new maser components toward these galaxies, and have provided the first clear evidence for variability in extragalactic class I methanol masers. Alongside the new observations of NGC 4945 and NGC 253, we present the results of recent 36.2-GHz methanol maser searches toward 12 galaxies, placing upper limits on the emission from the 36.2-GHz class I transition and the 37.7-GHz ($7_2 \rightarrow 8_1$E) class II maser line toward these sources. Flux density values for the 7-mm continuum emission toward these sources are also reported where applicable. A re-analysis of the published 36.2-GHz methanol observations of Arp 220 undertaken as part of the search revealed some issues with previous imaging procedures. The re-analysis, combined with non-detections in independent follow-up observations suggest that there is no 36.2-GHz methanol emission toward Arp 220 stronger than 3.5 mJy in a 10 km s^{-1} channel (5σ upper limit).

Key words: masers – radio lines: galaxies – galaxies: starburst

1 INTRODUCTION

The properties of galaxies (particularly those that are very distant) are often unable to be directly measured. Instead, we rely on indirect measurements through observations of some proxy. Historically, maser emission has proven to be a powerful tool for both direct and indirect investigation of various astrophysical phenomena both within our Galaxy and in others (e.g. star-formation, outflows, black-hole accretion disks; Moran et al. 1999; Kurtz et al. 2004). Galactic methanol masers, in particular, allow insight into the various stages of star-formation regions. Their compact and generally highly luminous nature, allows for conditions or evolutionary stages to be detected and accurately ascribed to certain locations within these star-forming regions (e.g. Cyganowski et al. 2009, 2012; Breen et al. 2013; Voronkov et al. 2014). Extragalactic methanol masers may prove to be a similarly interesting tool for investigation of external galaxies, however, at this stage they are a relatively newly discovered and not well understood phenomenon.

The majority of known extragalactic methanol masers have been detected in the past five years. Class I methanol masers have been reported in NGC 253, Arp 220, NGC 4945, NGC 1068, IC 342 and NGC 6946 (Ellingsen et al. 2014; Wang et al. 2014; Chen et al. 2015; McCarthy et al. 2017, 2018b; Gorski et al. 2018) and class II masers in the Large Magellanic Cloud (LMC) and M31 (Green et al. 2008; Ellingsen et al. 2010; Sjouwerman et al. 2010). Considering these extragalactic examples, the class II masers appear to be highly luminous examples of regular Galactic-type class II masers (Ellingsen et al. 2010), however, this is not the case with the current detections of class I masers. Instead, they appear to be associated with large-scale regions of low-velocity shocks, such as molecular in-fall, within their host galaxies (Ellingsen et al. 2017; Gorski et al. 2018; McCarthy et al. 2018a).

⋆ Email: tiegem@utas.edu.au

NGC 253 and NGC 4945 are two nearby, southern, barred spiral galaxies with starburst nuclei. These sources are considered the prototypical examples of extragalactic class I methanol masers. The methanol masers in these sources are associated with the galactic bars of their host. The masers in NGC 253 appear to be associated with the inner bar-nucleus interface, where molecular in-fall along the bar is interacting with the central starburst zone, resulting in large-scale low velocity shocks (Ellingsen et al. 2017). The single maser region in NGC 4945 appears to be located at the interface region between the galactic bar and the south-eastern spiral arm (Henkel et al. 2018; McCarthy et al. 2018a).

Currently, there is no direct evidence for variability toward any extragalactic methanol maser sources. In Galactic sources, variability has been detected in numerous class II masers (e.g. Goedhart et al. 2003; Olech et al. 2019). However, the same has not been reported for Galactic class I sources. Variability in these class II sources has been suggested to be related to either changes in the pump rate (Araya et al. 2010), or variations in seed photon flux of the masers (van der Walt 2011).

In this paper we report the results of new 7-mm observations toward NGC 4945 and NGC 253. Additionally we report upper-limits on the luminosity of 36.2-GHz class I and 37.7-GHz class II methanol emission toward twelve extragalactic sources (see Table 1), from data taken with the ATCA over the past few years. The initial search for extragalactic class I methanol masers was made towards a sample of luminous extragalactic OH and H_2O megamasers (9 of the 12 sources reported here). These targets were selected before the first detection of an extragalactic class I methanol maser had been reported. This initial search was responsible for the first successful detections of 36.2-GHz class I masers reported in Ellingsen et al. (2014, 2017) and McCarthy et al. (2017). The remaining three sources (NGC 1097, NGC 1792 and NGC 1808) were observed as part of a follow up search, and as such selected targets are based on the general properties of NGC 253 and NGC 4945 (elevated star-formation rates, barred spirals etc.). We also provide a discussion of the entire sample, both detections and non-detections, which will allow a more focussed approach to target selection, allowing a higher success rate for future searches.

2 OBSERVATIONS

The 7-mm observations reported in this paper were all made using the Australia Telescope Compact Array (ATCA) across multiple epochs between 2014 and 2019 (see Table 2). We adopted rest frequencies of 36 169.238±0.001 MHz (Voronkov et al. 2014) and 37 703.700±0.030 MHz (Tsunekawa et al. 1995) for the class I 36.2- and class II 37.7-GHz transitions of methanol respectively.

Our observations are single pointings toward the centre of each galaxy (see Table 1). At 36.2-GHz the FWHM of the ATCA primary beam is 84 arcseconds. This corresponds to a linear radius from the pointing centre of ∼700 pc for our nearest source (NGC 253 at 3.4 Mpc) and ∼47 kpc for our furthest (IRAS 10173+0829 at 231 Mpc). This range is sufficient for detecting class I methanol masers at similar spatial offsets from the nucleus of the galaxies as those reported in previous reported detections.

Either PKS B1921–293 or PKS B1253–055 was utilised as a bandpass calibrator dependent on the epoch. The 10 minute scans of the target source were interleaved with 2 minute phase calibrator scans throughout the observations, with flux density calibration using PKS B1934–638 and Uranus. All sources observed in each epoch, and their relevant calibrators are listed in Table 2.

The details of the Compact Array Broadband Backend (CABB; Wilson et al. 2011) configurations for each epoch are detailed in the following subsections.

2.1 2014 March

Observations were made on 2014 March 26 and 28 (project code C2879), using the H168 hybrid array configuration (minimum and maximum baselines of 61 and 192m respectively). CFB 1M CABB mode was utilised for these observations, resulting in 2 × 2048 MHz IF bands, with centre frequencies of 35.3 GHz and 37.3 GHz respectively. The channel width for these IF bands was 1 MHz (∼8.2 km s^{-1} at 36.2-GHz) resulting in 2048 spectral channels for each IF band. A typical synthesised beam for this hybrid array at 36.2-GHz is approximately $9'' \times 5''$ (dependent on source declination).

Dependent on the day, the observing strategy utilised PKS B1934-638 or Uranus as flux density calibrators, with bandpass calibrated with respect to PKS B1921-293 or PKS B1253-055 (see Table 2). Scans of target sources were interleaved with phase calibration scans on nearby appropriate sources.

The weather for this epoch of observation was particularly bad which, when combined with low on-source times, resulted in bad data quality. We have only reported detection upper-limits for those sources which we could image to a sufficient standard. This generally includes sources where we could get continuum detections (see Table 6) in order to self-calibrate the data and achieve higher sensitivity. As an example of the data quality, NGC 4945 was originally observed during this epoch, and the data quality is too poor to detect the strong 36.2-GHz emission observed toward this source in observations since. A table of sources that were also observed, but with too low data quality (RMS over an order of magnitude higher than expected) to draw any useful conclusions, is included in the appendix (Table A.1).

2.2 2015 August

Observations were made on 2015 August 25 and 26 (project code C2879), using an EW352 east-west array configuration (minimum and maximum baselines of 31 and 352m respectively). The CABB was configured in the CFB 1M/64M hybrid mode, consisting of 2 × 2048 MHz IF bands. The first IF band has a channel width of 1 MHz resulting in 2048 spectral channels, with a centre frequency for the band of 36.85 GHz. The second IF is 32 × 64 MHz channels (also centred on 36.85 GHz) with the ability to define up to 16×2048 channel zoom bands with a fine resolution of 32 kHz (resulting in a channel width of ∼0.26 km s^{-1} at 36.2-GHz). Two sets of five zoom bands were combined ('stitched') together to cover each of the two lines of primary interest (36.2-GHz class I

Table 1: Details for target sources. Recession velocities have been taken from the *NASA/IPAC Extragalactic Database*† (NED). Redshift-independent distances have been provided where possible, otherwise distances reported are the luminosity distances provided by NED.

Target Source	Right Ascension h m s	Declination $^\circ$ $'$ $''$	V_{helio} (km s^{-1})	D (Mpc)	Type
NGC 253	00 47 33.10	–25 17 18.00	243	3.4[1]	SAB(s)c
IRAS 01417+1651	01 44 30.50	+17 06 05.00	8214	119	pair of galaxies
NGC 1097	02 46 19.06	–30 16 29.68	1271	9.51[2]	SB(s)b, Sy1
NGC 1792	05 05 14.45	–37 58 50.70	1211	9.6[3]	SA(rs)bc
NGC 1808	05 07 42.34	–37 30 46.98	995	6.8[3]	(R′)SAB(s)a, Sy2
ESO 558-g009	07 04 21.02	–21 35 19.20	7674	118	Sc
IC 2560	10 16 18.70	–33 33 50.00	2925	32.5[4]	(R′)SB(r)b
IRAS 10173+0829	10 20 00.20	+08 13 34.00	14716	231	LIRG
IRAS 11506-3851	11 53 11.70	–39 07 49.00	3232	30.3[5]	(R′)SAB(r)a
ESO 269-g012	12 56 40.50	–29 34 02.81	5014	78.8	S0, Sy2
NGC 4945	13 05 27.50	–49 28 06.00	563	3.7[6]	SB(s)cd, Sy2
Circinus	14 13 09.30	–65 20 21.00	434	4.21[7]	SA(s)b
NGC 5793	14 59 24.70	–16 41 36.00	3491	55	Sb, Sy2
IIZw 96	20 57 23.90	+17 07 39.00	10822	159	pair of galaxies

Note: [1]Dalcanton et al. (2009), [2]Bottinelli et al. (1985), [3]Sorce et al. (2014), [4]Yamauchi et al. (2012), [5]Tully et al. (2016), [6]Tully et al. (2013) and [7]Tully et al. (2009)

Table 2: Details of the observations for all target sources reported in this paper. The asterisk denotes an observation epoch previously reported in McCarthy et al. (2018a). The details for this epoch have been reproduced here as it is important for the discussion of variability in Section 4.3.

Target Source	Epoch	Array Configuration	Flux Calibrator	Bandpass Calibrator	Phase Calibrator	On-source Time
NGC 253	2019 March	H214	PKS B1934-638	PKS B1921-293	0116-219	4.84h
IRAS 01417+1651	2014 March	H168	Uranus	PKS B1921-293	0221+067	0.50 h
NGC 1097	2018 November	H168	PKS B1934-638	PKS B1921-293	0237-233	4.61h
NGC 1792	2018 December	H168	PKS B1934-638	PKS B1921-293	0521-365	3.72h
NGC 1808	2018 November	H168	PKS B1934-638	PKS B1921-293	0521-365	1.97h
ESO 558-g009	2014 March	H168	Uranus	PKS B1921-293	0648-165	0.49 h
IC 2560	2014 March	H168	PKS B1934-638	PKS B1253-055	1034-293	0.20 h
IRAS 10173+0829	2015 August	EW352	PKS B1934-638	PKS B1921-293	1036+054	4.02h
IRAS 11506-3851	2014 March	H168	PKS B1934-638	PKS B1253-055	1144-379	0.50 h
ESO 269-g012	2014 March	H168	PKS B1934-638	PKS B1253-055	1322-427	0.20 h
NGC 4945	2017 June*	H214	PKS B1934-638	PKS B1921-293	j1326-5256	1.64h
	2017 July	H75	Uranus	PKS B1253-055	j1326-5256	1.92h
	2019 March	H214	PKS B1934-638	PKS B1921-293	j1326-5256	3.93h
Circinus	2015 August	EW352	PKS B1934-638	PKS B1921-293	1414-59	2.80 h
NGC 5793	2014 March	H168	PKS B1934-638	PKS B1253-055	1510-089	0.20 h
IIZw 96	2015 August	EW352	PKS B1934-638	PKS B1921-293	2121+053	2.32 h

and 37.7-GHz class II methanol). A typical synthesised beam for these 36-GHz EW352 observations is $26'' \times 4''$.

2.3 2017 July

Observations were made on 2017 July 7 (project code C3617), using the ATCA H75 hybrid array configuration (minimum and maximum baselines of 30.6 and 89.2m respectively). The CABB was configured in CFB 1M-0.5k mode, resulting in 2×2048 MHz IF bands (with centre frequencies of 36.85 and 32.20 GHz), each with 1 MHz spectral resolution (∼8.2 km s^{-1} at 36.2-GHz) and the option of configuring 16 zoom bands per IF, with 2048 channels and a fine resolution of 0.5 kHz ($<$ 0.01 km s^{-1} at 36.2-GHz). We did not use zoom bands for these observations, due to the fine resolution producing insufficient velocity coverage for extragalactic sources at this frequency. These H75 array observations at 36.2-GHz had a synthesised beam size of approximately $27'' \times 12''$.

2.4 2018 November and December

Observations were made on 2018 November 28 and 29, and December 3 (project code C3263) using the H168 hybrid ar-

ray configuration (minimum and maximum baselines of 61 and 192m respectively). The CFB 64M-32k CABB configuration was used, consisting of two 32×64 MHz IF bands (centre frequencies of 32.2 and 36.85 GHz respectively), with both bands additionally allowing up to 16×2048 channel zoom bands to be defined with a fine resolution of 32 kHz. Each target methanol line (36.2-GHz class I and 37.7-GHz class II methanol), was covered by 4 stitched zoom bands (the 32 kHz channel width corresponds to $\sim$0.26 km s^{-1} at this frequency). The synthesised beams of these observations are approximately $6'' \times 4''$.

It should be noted that due to frequency configuration issues, the flux density calibration for NGC 1097 required approximation based on levels seen from the other recent observations. NGC 1097 and NGC 1808 were observed one day apart and comparison of the flux density values for the bandpass calibrator used for both these sets of observations (PKS B1921–293) allowed for an approximate flux density calibration for NGC 1097. Therefore, both RMS values reported in Table 3 and continuum flux density values in Table 6 have higher levels of uncertainty ($\sim$40 percent) than all other sources.

2.5 2019 March

Observations were made on 2019 March 3 (project code C3167), using the H214 hybrid array configuration minimum and maximum baselines of 82 and 247 m respectively). The CFB 64M-32k CABB configuration was used, consisting of two 32×64 MHz IF bands (centre frequencies of 36.8 and 38.00 GHz respectively), with both bands additionally allowing up to sixteen 2048 channel zoom bands to be defined with a fine resolution of 32 kHz. The target 36.2-GHz methanol line was covered by 4 stitched zoom bands (the 32 kHz channel width corresponds to 0.26 km s^{-1} at this frequency). These observations had a synthesised beam of $6\farcs3 \times 4\farcs4$ and $5\farcs6 \times 4\farcs3$ for NGC 4945 and NGC 253 respectively.

The bandpass calibrator PKS B1921-293 was used with flux density calibrated against PKS B1934-638. A nearby quasar was selected for interleaved phase calibration scans for each source. Details on these sources can be found in Table 2.

The weather during this session was not ideal for mm-wavelength observing, with high ambient temperatures and patchy cloud cover. This results in higher RMS noise levels than would be expected for our on-source time. However, a combination of manual flagging (for scans affected by clouds passing through the line of sight) and self-calibration allows us to achieve a sensitivity similar to past observations of these sources (McCarthy et al. 2018a; Ellingsen et al. 2017).

2.6 Data Reduction

Data were reduced with MIRIAD using standard techniques for the reduction of 7-mm ATCA spectral line data. The data were corrected for atmospheric opacity and we estimate the absolute flux density calibration to be accurate to better than 30%. For targets with continuum source detections, multiple iterations of phase-only self-calibration was performed. Any potential spectral line emission was isolated from the data by using the uvlin MIRIAD task. This task subtracts any potential continuum emission by estimating the correlated flux density on each baseline via polynomial interpolation based on line-free spectral channels. The velocity ranges and channels widths for our spectral line cubes varied depending on the source and CABB configuration/frequency setup that was utilised for the observations. When searching for spectral line emission, the data were resampled using many different channel widths, in order to appropriately identify both broad and narrow emission. Typical channel widths searched were 1, 3, 8, 10 and 20 km s^{-1} as the native spectral-resolution allows (dependent on the CABB configuration). Spectral line cubes are produced with a cell (pixel) sizes of 1×1 arcseconds and a Brigg's visibility weighting robustness parameter of 1. Details of the final spectral line cubes are listed in Table 3, with image cube noise levels reported for a consistent channel width of 10 km s^{-1} for ease of comparison.

Table 3: Details for the spectral line cubes used to search for methanol spectral lines. Sources highlighted in bold text are those from project C3167, while the rest are from the maser search projects. Velocity ranges and channel widths are identical for the 36.2- and 37.7-GHz spectral lines. The two RMS noise values correspond to the noise for the 36.2- and 37.7-GHz cubes respectively (not applicable to C3167 sources where only 36.2-GHz is observed). RMS noise values are reported post self-calibration where relevant. The RMS values for NGC 1097 (denoted by an asterisk) have a higher level of uncertainty due to less accurate flux density calibration (see Section 2.4).

Target Source	Velocity Range (km s^{-1})	Channel Width (km s^{-1})	RMS Noise (mJy beam^{-1})
NGC 253	0–500	1	1.9
IRAS 01417+1651	7100 – 9100	10	1.6/1.6
NGC 1097	750 – 1750	10	0.5*/0.4*
NGC 1792	700 – 1700	10	0.4/0.4
NGC 1808	600–1600	10	0.2/0.2
ESO 558-g009	6800 - 9600	10	2.2/2.2
IC 2560	2000 – 3600	10	6.5/6.7
IRAS 10173+0829	13500 – 14900	10	1.2/1.3
IRAS 11506-3851	1900 – 4100	10	2.2/2.5
ESO 269-g012	4000 – 6000	10	6.6/6.2
NGC 4945 (H214)	250–850	1	1.9
NGC 4945 (H75)	200–1020	8.2	0.3
Circinus	0 – 800	10	0.5/0.6
NGC 5793	2500 – 4400	10	6.4/5.4
IIzw96	10000 – 12000	10	0.6/0.6

2.6.1 Identification of maser sources

Spectral line cubes were visually inspected for strong maser emission. The DUCHAMP source finder software (Whiting 2012) was then used to search each cube with a 3σ threshold. Such a low threshold produces many false positives ($\sim$100), however the vast majority of these are on the outer edges of our images (which are typically $256'' \times 256''$). Any candidate within 2 times the FWHM of the primary beam (cor-

Table 4: NGC 4945 36.2-GHz methanol emission details from the 2019 March H214 observations. All reported velocities are with respect to the barycentric reference frame. Uncertainties in the reported flux density values result from the random errors in fitting using the MIRIAD task imfit. Please note the integrated flux density for the continuum emission has units of mJy rather than mJy km s^{-1}.

#	Label	RA (J2000) h m s	Dec (J2000) $^\circ$ $'$ $''$	S_{pk} (mJy)	S (mJy km s^{-1})	V_{pk} (km s^{-1})	$V_{\rm Range}$ (km s^{-1})
1	M1	13 05 28.0	−49 28 12.67	55±2	500±40	673	630–710
2	M2	13 05 27.1	−49 28 07.39	5±1	250±30	490	420–560

Table 5: NGC 253 36.2-GHz methanol emission details from the 2019 March H214 observations. All reported velocities are with respect to the barycentric reference frame. Labels here are based on those presented in Ellingsen et al. (2017). Uncertainties in the reported flux density values result from the random errors in fitting using the MIRIAD task imfit.

#	Label	RA (J2000) h m s	Dec (J2000) $^\circ$ $'$ $''$	S_{pk} (mJy)	S (mJy km s^{-1})	V_{pk} (km s^{-1})	$V_{\rm Range}$ (km s^{-1})
1	MM6	00 47 33.9	−25 17 11.65	25±2	605.3±50	207	160–260
2	MM5/MM4	00 47 33.7	−25 17 12.39	24±1	655.9±50	195	140–250
3	-	00 47 32.8	−25 17 22.19	5±2	75.5±20	300	255–345
4	-	00 47 32.3	−25 17 19.06	5±2	69.6±20	336	300–360
5	MM1/MM2	00 47 32.0	−25 17 28.98	30.0±4	1100±60	318	260–400

responding to a radius of ∼84″ from the pointing centre at 36.2-GHz) were manually inspected to determine if they were potential maser components. Generally with data of reasonable quality, very few false positives (less than two and typically none) were present within this central region of the image.

3 RESULTS

This paper contains observations from three different projects, two involving searching for new extragalactic class I methanol maser sources (C2879 and C3263), and one studying known maser hosts (C3167). In order to facilitate easier reading we will separate the results based on project goal.

3.1 Project C3167: the methanol masers of NGC 253 and NGC 4945

3.1.1 NGC 4945

The previously reported bright 36.2-GHz methanol maser offset to the south-east from the nucleus of NGC 4945 was readily detected in the latest 2019 March epoch observation (M1 in Figure 1). In addition to this primary region, we identify another region of 36.2-GHz emission south-west of the galactic centre. This emission is offset by approximately 3 arcseconds to the south-west of the galactic nucleus (M2 in Figure 1). This location corresponds to the south-west component of 36.4-GHz HC_3N and CS (1 − 0) emission reported in McCarthy et al. (2018a) and the methanol emission covers the same velocity range. When compared to the primary region, this new emission has a much lower peak flux density and a significantly broader spectral profile. This emission is clearly visible in the data prior to any self-calibration, indicating it is not an artefact of this process.

7-mm continuum emission was detected toward the nucleus of NGC 4945. As in McCarthy et al. (2018a), this continuum measurement was obtained using the line-free data in the 36.2-GHz zoom band. The measured flux density is in agreement with the previously reported measurement. The integrated flux density agrees with the modelled 7-mm continuum values from Bendo et al. (2016), which predicts that 75 percent of this 7-mm continuum emission is from free-free emission.

The flux density values for the methanol and 7-mm continuum emission toward NGC 4945 are recorded in Table 4 and 6 respectively..

3.1.2 NGC 253

We detect the same 36.2-GHz methanol maser regions toward NGC 253 as have been reported by Ellingsen et al. (2014, 2017), though the resolution of the new observations does not allow us to resolve all of the individual features at the locations of the brightest emission. We also identify two tentative new components of methanol emission (see Figure 2) not formerly detected by Ellingsen et al. (2017) or Gorski et al. (2017). These components are only approximately 4σ detections, however, they are located at the same positions and velocities as emission in the 87.9 GHz transition of HNCO emission (location C and D in figure 1 of McCarthy et al. 2018b). The previous 36.2-GHz ATCA observations of NGC 253 by Ellingsen et al. (2017) have a high enough sensitivity (1.1 mJy beam^{-1} in a 3 km s^{-1} channel), however, their observations make use of more extended array configurations. Both components have sufficiently high peak flux densities (∼5 mJy) that they should have been detected by previous observations of NGC 253.

7-mm continuum emission was detected toward the nucleus of NGC 253. Continuum emission was extracted from the line-free data in the 36.2-GHz zoom band, flux density

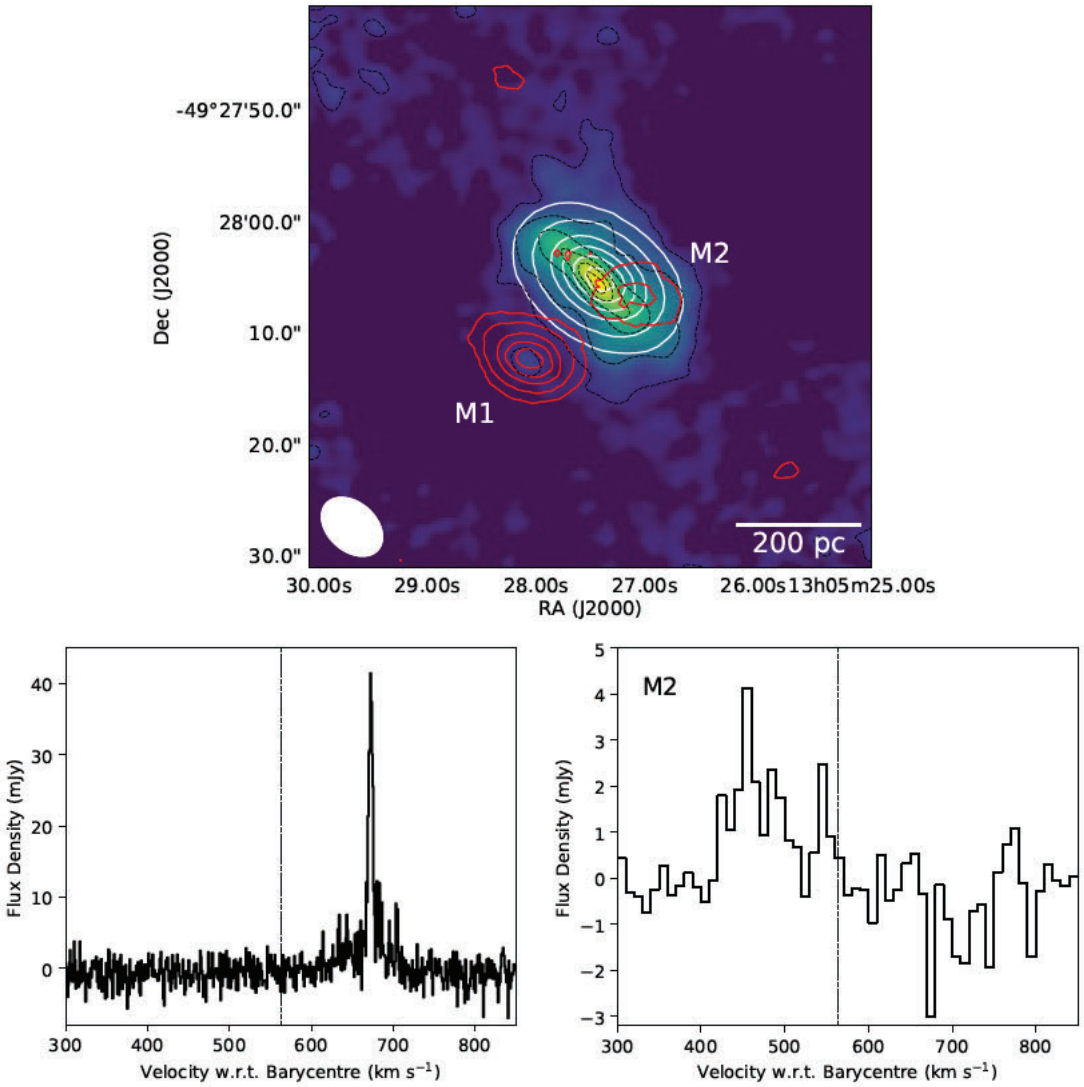

Figure 1: Top: NGC 4945 integrated 36.2-GHz methanol emission (red contours at 10, 25, 50, 70 and 90 per cent of peak 560 mJy km s^{-1} beam^{-1}) and 7-mm continuum emission (white contours at 2, 10, 30, 50, 70, 90 per cent of peak 290 mJy beam^{-1}) with background colour map and black dashed contours of CS $J = 2 \rightarrow 1$ integrated intensity from Henkel et al. (2018) (2%, 10%, 30%, 50%, 70%, and 90% of the peak of 11.5 Jy km s^{-1} beam^{-1}). Methanol and continuum emission data extracted from the 2019 March spectral line cubes with a synthesised beam size of $6\farcs3 \times 4\farcs4$ (white ellipse). Bottom left: Spectrum of 36.2-GHz methanol taken from the location of peak emission at M1 (channel width of 1 km s^{-1}). The vertical dashed line indicates the systemic velocity of NGC 4945 (Chou et al. 2007). Bottom right: Spectrum of 36.2-GHz methanol emission taken from the location of peak emission in region M2 (channel width of 12 km s^{-1}).

values for this continuum emission, along with those for the maser components are recorded in Table 5.

3.2 Projects C2879 & C3263: searching for masers

No additional extragalactic methanol maser sources have been detected in any of the targets of these projects and RMS noise levels for the 36.2-GHz class I and 37.7-GHz class II spectral line cubes are listed in Table 3. Results for NGC 1097 have a higher uncertainty due to flux-calibration issues, as outlined in Section 2.4.

7-mm continuum emission was detected toward the centre of many of these galaxies (see Table 6), many of which have no previously reported values in the literature.

4 DISCUSSION

4.1 New methanol emission toward NGC 4945

The new methanol emission from region M2 shares overlapping position and velocities with the south-western CS (1–0) and HC_3N (4–3) emission reported in McCarthy et al. (2018a). This increases our confidence that despite a relatively low-SNR, the emission at this location is indeed real. Before we can discuss what this new region of methanol emission means for our understanding of extragalactic class I methanol masers, we must first justify that it is reasonable to consider this emission the result of maser processes.

While not as narrow as the linewidths seen toward the primary maser region (M1), M2 appears to consist

Table 6: Details for the continuum emission from all sources. The horizontal line separates the maser search targets from the new (2019 March) H214 observations of NGC 253 and NGC 4945 (above and below respectively). The flux density values for NGC 1097 (denoted by an asterisk) have a higher level of uncertainty due to less accurate flux density calibration (see Section 2.4). For sources with no detected continuum source, the location of the pointing centre and a 5σ upper limits on peak flux density are provided. Uncertainties in the reported flux density values result from the random errors in fitting using the MIRIAD task imfit.

Target Source	Right Ascension	Declination	S_{pk}	S
	h m s	$^\circ$ $\prime$ $\prime\prime$	(mJy beam^{-1})	(mJy)
ESO 269-g012	12 56 40.5	–46 55 34.00	< 2.3	-
IC 2560	10 16 18.7	–33 33 50.00	< 1.8	-
IRAS 11506-3851	11 53 11.8	–39 07 49.18	10.0±0.2	10.7±0.3
NGC 5793	14 59 24.8	–16 41 36.70	18.8±0.1	19.3±0.2
ESO 558-g009	07 04 21.0	–21 35 19.20	< 0.6	-
IRAS 01417+1651	01 44 30.5	+17 06 05.00	< 0.7	-
Circinus	14 13 10.0	–65 20 20.74	56.6±0.6	63±1
IIzw96	20 57 24.4	+17 07 40.47	5.8±0.2	5.8±0.3
IRAS 10173+0829	10 20 00.2	+08 13 32.07	7.1±0.9	8±2
NGC 1097	02 46 18.9	-30 16 28.69	8.1±0.1*	8.4±0.1*
NGC 1792	05 05 14.5	–37 58 49.87	4.4±0.1	4.4±0.1
NGC 1808	05 07 42.3	–37 30 45.64	4.5±0.1	6.2±0.4
NGC 253	00 47 33.2	−25 17 17.77	214.3±8	335.7±20
NGC 4945	13 05 27.4	−49 28 05.43	296±3	430.8±7

of two or more components with FWHM of ∼20 km s^{-1}. These linewidths are much narrower than those observed from thermal emission toward the same regions (FWHM of > 60 km s^{-1}; Henkel et al. 2018; McCarthy et al. 2018a), and are comparable to the masing regions toward NGC 253 (Ellingsen et al. 2017). Similarly to the main 36.2-GHz methanol masing region, no methanol from the ground state 48 GHz transition has been reported toward M2 (McCarthy et al. 2018a).

When investigating the emission at M2 in the three epochs of observation originally presented in McCarthy et al. (2018a), it should be noted that all were made in relatively compact ATCA array configurations (2016 Aug, 2017 Jun and Oct; see Table 7). Looking at these three array configurations we see the integrated flux density of M2 increasing as the array configuration gets more compact. This relationship may indicate thermal emission from this region, however, there are a few important caveats to this interpretation. The first is that the detections of emission from M2 in these epochs is very marginal, with only a channel or two above the noise level (see Figure 5). This means the extracted integrated flux density values from these locations with marginal detections is less reliable. Secondly, a similar relationship is observed toward M1, where integrated flux density increases as they array becomes more compact. Finally, it is hard to determine the true integrated flux density for M2 from the 2017 July H75 observations, as the emission from the primary component M1 is also captured within the larger synthesised beam.

The emission from this new methanol region also displays evidence of variability. This is the best evidence that the emission does not result from a thermal process. This variability is discussed in more detail in Section 4.3, as it is the first compelling evidence for variability in extragalactic class I methanol masers.

Due to the broad spectral profile of the emission and the larger velocity range, the integrated flux density of M2 is only approximately 50% lower than the primary masing region, despite a much lower peak flux density (by a factor of ∼10). This integrated intensity is approximately 5 orders of magnitude higher than that of a typical Galactic style 36.2-GHz emission, and over an order of magnitude (a factor of ∼40) higher than the combined 36.2-GHz emission from the Milky Way CMZ (Yusef-Zadeh et al. 2013). As this region is unresolved by our synthesised beam (6.3×4.4 arcseconds), we can put an upper limit on its angular size. This angular size corresponds to a linear size of 113×79 pc at the 3.7 Mpc distance of NGC 4945 (likely a vast over-estimate based on variability timescale, see Section 4.3). This implies we have over 40 times the 36.2-GHz emission coming from an area on the sky which is at most 30% larger than the CMZ would be at this distance.

Considering all these factors together, we conclude that the most reasonable explanation is that this emission is masing. McCarthy et al. (2018a) also put an upper limit of 6 mJy on the presence of any 44-GHz methanol emission from NGC 4945. This means the 36.2-GHz methanol emission from this region is unlikely to be resulting from the cumulative effect of Galactic-style class I masers, as otherwise we would expect to also see evidence of 44.1-GHz maser emission (Voronkov et al. 2014).

4.2 Tentative new methanol emission in NGC 253

The angular resolution of our observations does not allow us to separate the methanol emission into the individual components as reported in previous interferometeric studies (Ellingsen et al. 2017; Gorski et al. 2017; Chen et al. 2018). However, despite this we observe two new components of emission (labelled 3 and 4 in Figure 2). These components are only 4σ detections, however, their location and velocity strongly correlate with the components of HNCO emission

reported in McCarthy et al. (2018b). Ellingsen et al. (2017) observe a close correlation between the location of 36.2-GHz methanol masers and thermal emission from HNCO, a low-velocity shock tracer. This indicates that despite being a marginal detection, these components are likely real.

Comparison of our new observations with past ATCA observations of the 36.2-GHz methanol masers toward NGC 253 (Ellingsen et al. 2014, 2017), the whole spectrum (combining all regions) is more similar to what is reported in the original detection paper. The 'intermediate resolution' observations displayed in figure 1 of Ellingsen et al. (2017) shows significantly higher peak flux density values then what we see from our observations or their past observations (Ellingsen et al. 2014). However, upon re-analysis of the data, this appears to be an error (with flux density values out by a factor of 2) in how the spectrum has been extracted from their 'intermediate resolution' spectral line cube (and it does not affect the spectra taken from the combined array cube in figure 2 of Ellingsen et al. (2017)), and the data is consistent across all 3 epochs.

4.3 Evidence for variability in extragalactic methanol masers

We currently have five epochs of observations of the 36.2-GHz methanol transition toward NGC 4945, three of which were originally reported in McCarthy et al. (2017) and McCarthy et al. (2018a), with the remaining 2 reported in this paper. This allows us to compare the methanol emission over a time baseline of approximately 3.5 years. Tabulated flux density values for the primary methanol maser component (M1), newly discovered central region (M2) and 7-mm continuum emission can be found in Table 7.

The detection of the new emission at M2 in NGC 4945 is the first strong evidence for variability in an extragalactic class I methanol maser source. This is most evident when comparing the two observations made using the H214 array configuration, one in 2019 March and the other in 2017 June (see Figure 5 for spectra and Table 7 for flux density values). Due to the difficulties of comparing emission observed with different array configurations, the comparison of these two H214 epochs will be the main focus of this section. We see a 330 percent increase in integrated flux density across the velocity range of the new component (420–560 km s^{-1}) when comparing these two epochs (see Table 7). We also see evidence of this emission in the much lower resolution (synthesised beam size of 26.6×12.0 arcseconds) H75 array data from 2017 July, which is bracketed by the higher resolution observations in both 2017 June and October, neither of which show significant emission. This may indicate that emission from this region was much more diffuse during this period, with it becoming significantly more compact sometime prior to the most recent observation. However, if we assume a time-scale of 21 months for the variability (based on the time period between the H214 observations), this puts an upper limit on the size of the emitting region of 21 light-months (∼0.53 pc). At a distance of 3.7 Mpc, this corresponds to an angular size of 0.03 arcseconds, meaning the emission would be compact enough to be detectable on any ATCA baseline. It is therefore more likely that the change in luminosity of the region is instead related to an excitation change. Combining all data from the three intermediate resolution observations reported in McCarthy et al. (2018a) (see Figure 6), we can clearly see this emission at M2 (despite the the individual epochs showing no clear evidence) with a peak flux density of ∼ 3 mJy and integrated flux density of 185 mJy km s^{-1}. This further supports the interpretation that the variability is a result of an excitation change, rather than the emission simply being more diffuse during these earlier epochs.

The angular size of 0.03 arcseconds also allows us to put a lower limit of ∼6500 K on the brightness temperature of the emission from M2 based on the peak spectral channel (channel width 10 km s^{-1}), or $> 3 \times 10^5$ K integrated over a 140 km s^{-1} velocity range. This brightness temperature provides further evidence that this emission is the result of a non-thermal process, as discussed in Section 4.1.

The brighter region to the south-east of the nucleus (M1 in Figure 1) also shows some evidence of variability. The multiple spectral components reported in McCarthy et al. (2018a) are all present without any measurable shift in their velocities. When directly comparing the emission from the south-eastern bright region to the 2017 June observations in the same array configuration (H214), we observe a decrease in peak flux density of ∼6 percent and increase in integrated flux density of ∼30 percent. The integrated flux density of this primary region is also significantly higher (∼15 percent) than that observed using a more compact array configuration (H168) in 2017 October.

Our previous 2017 June H214 observations, when compared to other 7-mm observations toward NGC 4945, had lower continuum values than expected (McCarthy et al. 2018a). However, here we observe the same values of peak and integrated flux density for the 7-mm continuum source as reported from the previous H214 observations of NGC 4945 (see Table 7 for values). This suggests that instead of the 2017 June continuum levels being anomalously low, the 2015 August EW367 continuum levels may be higher than expected. This is likely related to the poor uv-coverage (highly elongated beam) of these observations preventing accurate imaging (flux density values are extracted from images using the imfit miriad task). The consistency of the 7-mm continuum measurements between these two H214 observations increases the confidence in our flux density calibration, which strengthens our comparisons of the maser emission between these two epochs.

It can be difficult to measure variability in the weak millimetre spectral line emission from these extragalactic sources. It is difficult to isolate what is variability in the source, and what is variability caused by differing array configurations, weather and uv-coverage between observations. With that said, the increased integrated flux density observed from M2 in our recent observations (2019 March) when compared to past observations (in particular the 2017 Jun H214 epoch) is far too large to be the result of weather or systematic effects.

The tentative new components detected toward NGC 253 also may indicate variability in this emission. The previous observations of NGC 253 at 36.2-GHz (Ellingsen et al. 2017) have appropriate sensitivity to detect these components, however, these observations use a higher-resolution east-west oriented array without complete uv-coverage. The resulting synthesised beam of those observations makes determining component separation along the north-east to

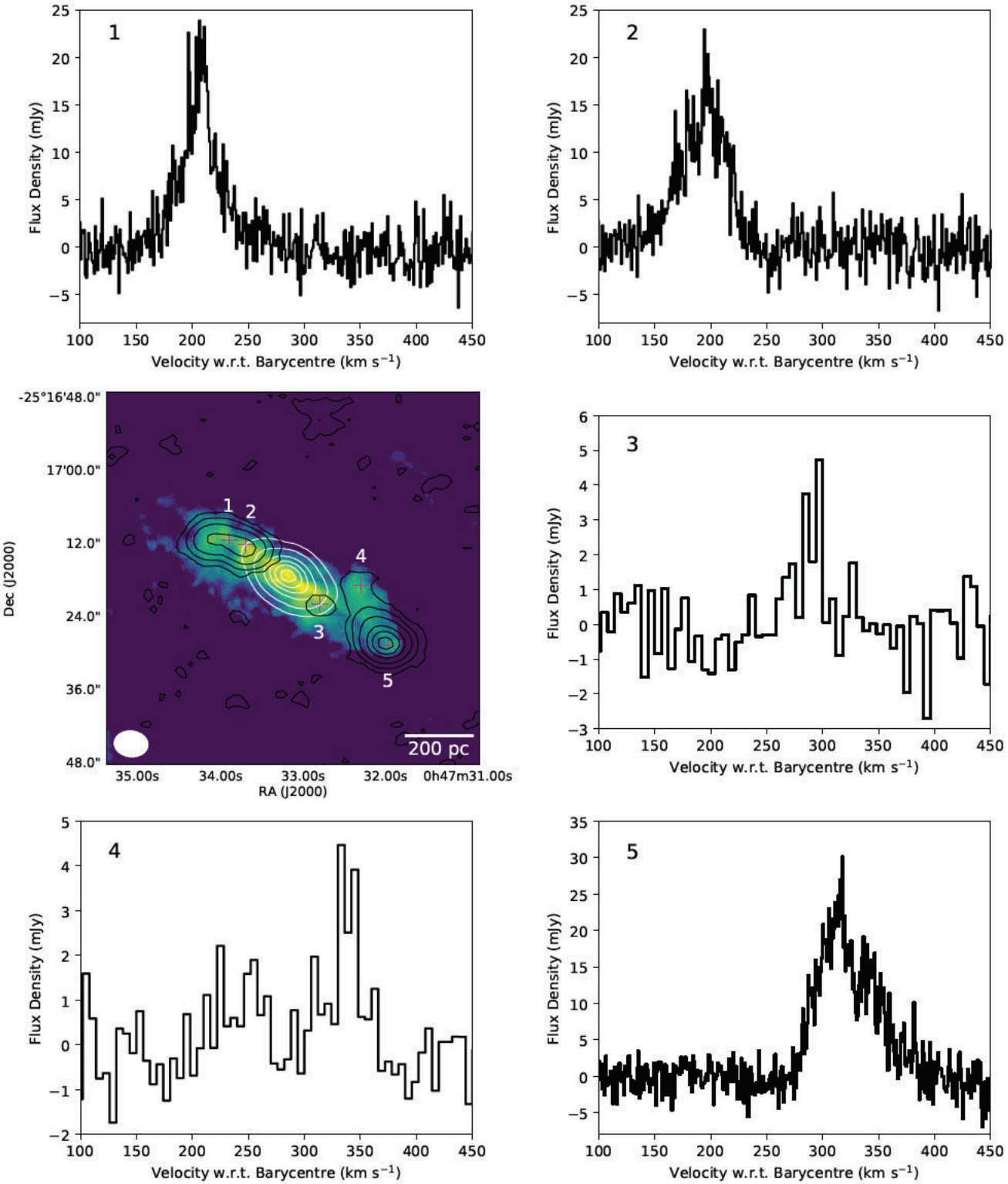

Figure 2: All data in this figure is from the 2019 March epoch, in the ATCA H214 array configuration. Field image: NGC 253 integrated 36.2-GHz methanol emission (black contours 2.5, 10, 25, 50, 70, and 90 per cent of the 1364 mJy km s^{-1} beam^{-1} peak) and 7-mm continuum emission (white contours 2.5, 10, 30, 50, 70, and 90 per cent of the 215 mJy beam^{-1} peak) with background image of integrated CO $J = 2 \rightarrow 1$ emission from Sakamoto et al. (2011) on a logarithmic scale. Magenta plus signs indicate the peak components of the methanol emission and have been labelled 1 through 5 moving from high right ascension to low. Spectra: Surrounding spectra from the 36.2-GHz spectral line cube at the location of each magenta plus sign. Synthesised beam size for our observations is $5\farcs6 \times 4\farcs3$ (white ellipse). Spectra 1, 2 and 5 have a channel width of 1 km s^{-1}, while 3 and 4 have 10 km s^{-1} channel width in order to better show the velocity range of the weaker emission from these regions.

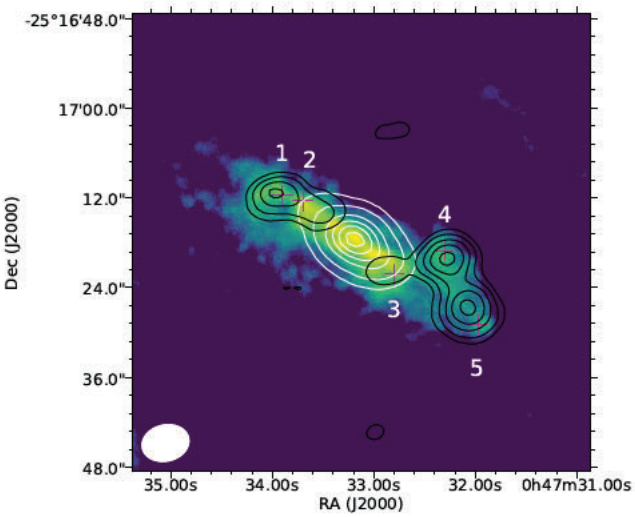

Figure 3: NGC 253 integrated 87.9 GHz HNCO emission (black contours 15, 30, 50, 70, and 90 per cent of the 1.9 Jy km s^{-1} beam^{-1}) and the 7-mm continuum emission (white contours 2.5, 10, 30, 50, 70, and 90 per cent of the 215 mJy beam^{-1} peak) with background image of integrated CO $J = 2 \rightarrow 1$ emission from Sakamoto et al. (2011) on a logarithmic scale. Magenta plus signs indicate the peak components of the 36.2-GHz methanol emission and have been labelled 1 through 5 moving from high right ascension to low. Synthesised beam for the 87.9-GHz HNCO emission is approximately $6\farcs4 \times 4\farcs9$.

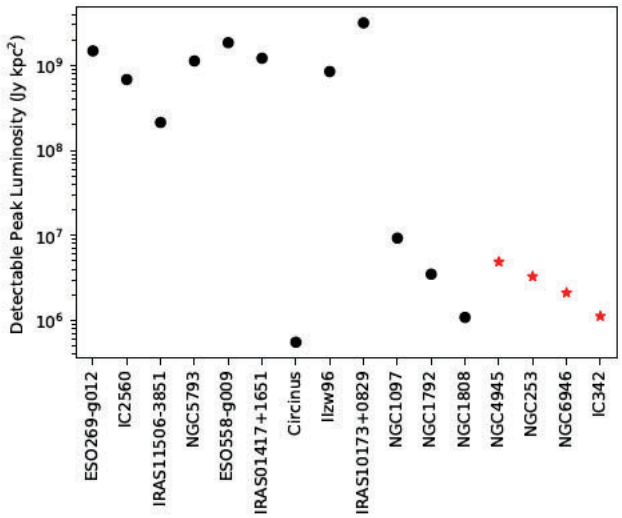

Figure 4: Black dots indicate the detectable peak emission levels for each target source in the maser search projects. Red stars represent the peak luminosity levels in each of the four sources with detected 36.2-GHz class I methanol masers. All peak emission levels are given for a 10 km s^{-1} velocity channel. Peak or integrated luminosity values for this figure (and throughout the rest of the paper) are given with units of Jy kpc^2 (or Jy km s^{-1} kpc^2 for integrated luminosity), which is the flux-density value multiplied by the squared distance to the source (in kpc).

south-west axis difficult, which is required to resolve the individual south-western components.

The mechanism driving such significant variation in these masers is mostly a mystery, especially because at this stage we do not understand the nature of the variability. It could be that it is a periodic phenomenon, or instead we may be observing the creation of new masers at these locations which will eventually stabilise. In Galactic sources, class I methanol masers are observed to exist for long periods of time, remaining relatively stable (Kurtz et al. 2004). This stability is consistent with the expected variability timescales for saturated class I masers, where the low-velocity shocks have long relaxation times (15 years; Leurini et al. 2016). However, it should be noted that long-term monitoring of class I methanol maser sources has not been undertaken to date, and our understanding of variability in these Galactic class I masers is lacking. Another collisionally pumped maser species is water, which is observed to be highly variable in both Galactic and extragalactic sources (e.g. Haschick & Baan 1990; Felli et al. 2007; McCallum et al. 2007). These water masers trace more energetic environments, with higher velocity shocks (Hollenbach et al. 2013). It may be that extragalactic class I methanol masers also trace higher-energy environments than their Galactic counterparts, though this is largely speculation as all modelling of the class I methanol lines is based on our understanding of Galactic sources (Sobolev et al. 2007; McEwen et al. 2014; Leurini et al. 2016). In order to confirm variability in these extragalactic class I methanol masers and develop our understanding of the phenomenon, constant and consistent monitoring is required. This monitoring should ideally be made with the same spatial resolution in order to accurately quantify any variability observed toward these sources.

4.4 Non-detection in Arp 220 follow-up

The weather during the 2014 March observations, was quite poor (particularly on March 28). During the processing of the data from this epoch we found that certain imaging parameters were causing spurious emission to appear in the spectral line cubes of targets with relatively low on-source time (and therefore, high noise). This realisation prompted re-analysis of the Arp 220 data published in Chen et al. (2015), as the data reported in that paper was from this observing session, and has not been confirmed in any subsequent observations. Upon reanalysing with more robust imaging parameters we find a similar spectral profile to that which is reported in Chen et al. (2015), however, at much lower flux density than that reported ($\sim$6 mJy peak compared with $\sim$25 mJy). The RMS noise in the cube is 4.3 mJy, so we can not be confident that this is real emission. Additionally, we see no evidence for the reported 37.7-GHz emission (Chen et al. 2015) in the re-analysed data. We have also reduced data from an ATCA follow-up observation in 2014 November (EW367 array configuration), with much longer integration times (4.8 hours). Analysis of these data does not show any 36.2-GHz methanol emission toward the central region of Arp 220 comparable to that reported in Chen et al. (2015). Based on these follow up observations, we put a 5σ upper limit on emission from the 36.2-GHz methanol line of 3.5 mJy. A recent 36.2-GHz search by Henkel et al. (submit-

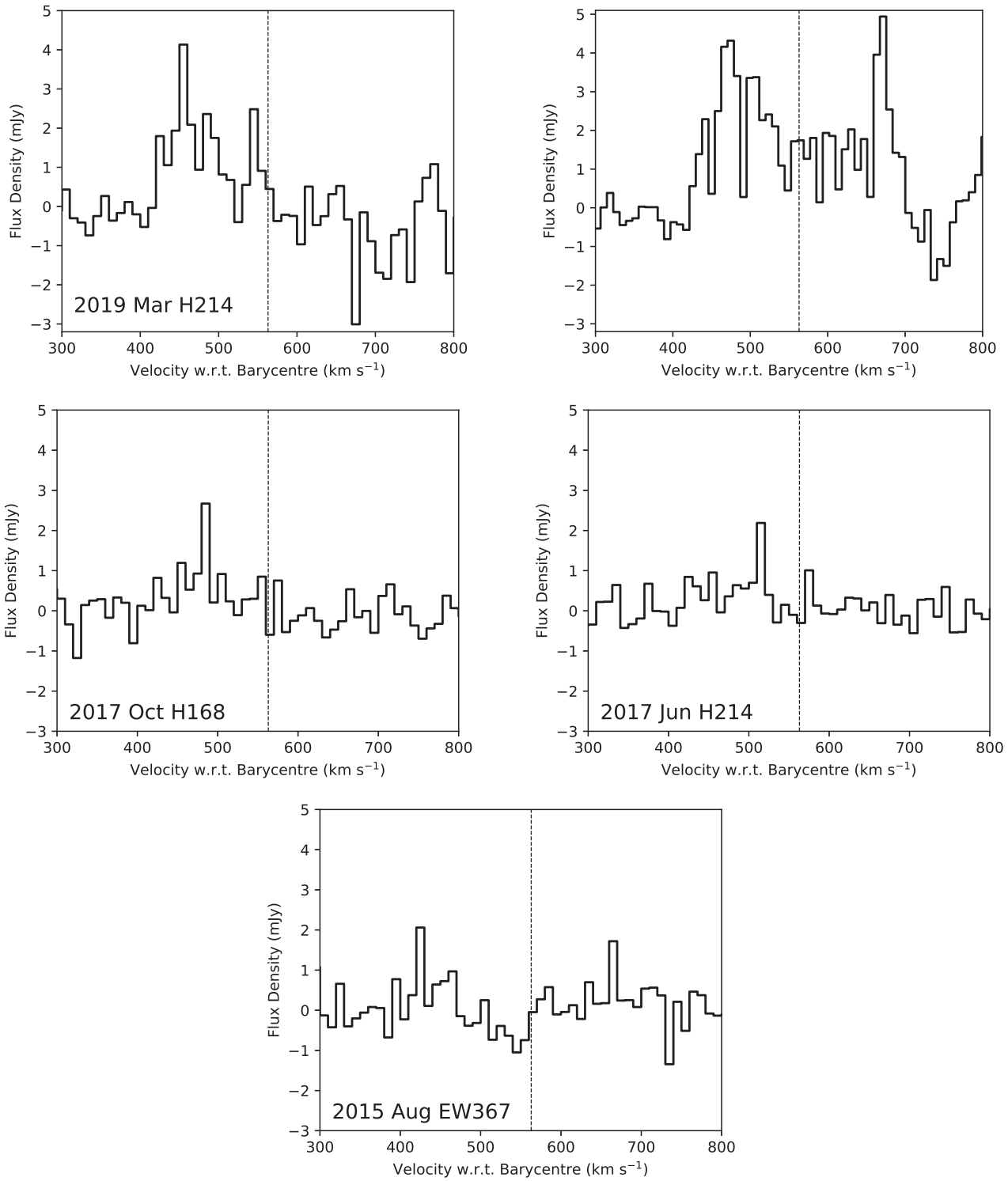

Figure 5: Spectra of 36.2-GHz emission at M2 toward NGC 4945 from each individual observation epoch (two epochs presented in this paper and the three from McCarthy et al. (2018a)). Vertical scales have all been set to the same range for ease of comparison. Note for the 2017 Jul H75 spectrum, the emission at ∼670km s^{-1} is due to the larger synthesised beam capturing emission from the main maser component in NGC 4945. The vertical dashed line indicates the systemic velocity of NGC 4945 (Chou et al. 2007).

Table 7: Table of flux density values from each epoch for the emission at M1, M2 and the continuum for NGC 4945, including the phase calibrator for these observations. Peak values are given, with integrated values given in parentheses. The peak values at both region M1 and M2 are given with a channel size of 10 km s^{-1}. It should be noted that these flux density values have an uncertainty of approximately 30% due to flux density calibration and continuum subtraction (see Section 2.6). We have left the random fitting errors off these values in order to facilitate easier reading, in general these random errors are around 5%.

Epoch	Flux density source (mJy)				Angular Scale
	M1	M2	Continuum	Phase Cal.	Min/Max (arcsec).
2015 Aug (EW352)	27.9 (289)	2.1 (44)	313 (414)	3328	3.6/55.8
2017 Jun (H214)	27.4 (305)	2.3 (65)	236 (348)	1369	4.4/20.7
2017 Jul (H75)	21.3 (450)	4.4 (279)	452 (447)	935	12.0/55.8
2017 Oct (H168)	30.4 (346)	2.8 (71)	385 (489)	1141	5.0/27.9
2019 Mar (H214)	25.7 (397)	4.3 (215)	246 (356)	1110	4.4/20.7

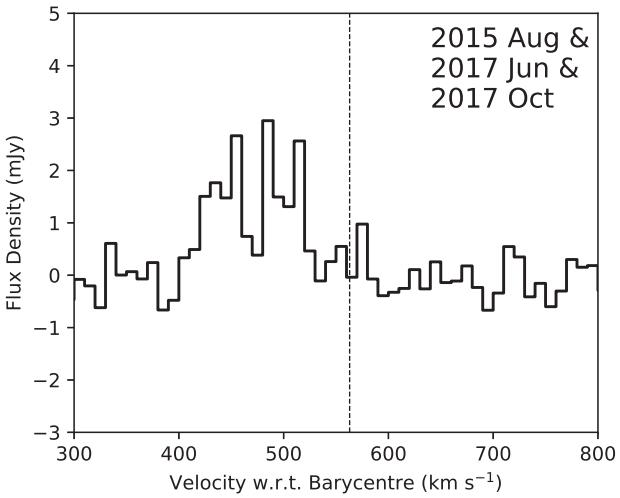

Figure 6: The spectrum from the M2 methanol maser region in NGC 4945 using the combined data from the three epochs reported in McCarthy et al. (2018a).

ted) targetted Arp 220 with the Effelsberg 100m telescope and report no detection of 36.2-GHz emission (with an upper limit of 4.2 mJy).

4.5 Sample discussion

When considering the non-detections toward most of our targets, it is important to note that the observations conducted under project C2879 were also responsible for discovering the first extragalactic methanol masers. Hence at the time the observations were made there was no information on the luminosity, nor likely environments to host extragalactic class I methanol masers. This results in many of the target sources not having a high enough sensitivity to detect methanol masers of comparable luminosity to those observed toward our known hosts (see Figure 4). This was not a problem for the subsequent searches, which uses much higher sensitivity levels, based on the currently known extragalactic class I maser sources.

Of the 12 sources for which we report 36.2-GHz methanol upper limits (C2879 and C3263 targets), only four have sensitivity levels adequate for detecting masers with the same luminosity as those detected toward NGC 4945, with the sensitivity of the majority over an order of magnitude too low (see Figure 4). When combining the non-detections with detections for analysis of the sample, the majority of the time we will include only these sources with appropriate sensitivity levels. This means our primary sample for discussion will include: NGC 4945, NGC 253, NGC 6946, NGC 1068, NGC 1097, NGC 1792, NGC 1808, IC 342 and the Circinus Galaxy.

Considering the general properties of the galaxies with detections we see three common factors: They are all barred, spiral galaxies with elevated levels of star-formation toward their nucleus (when compared to the Milky Way). However, it is important to note that searches for extragalactic methanol masers have been biased toward these types of sources based on the first detections in NGC 253 and NGC 1068 (Ellingsen et al. 2014; Wang et al. 2014). As of yet no statistically complete search for these masers has been undertaken, and as such, it is hard to determine the most relevant properties for future target selection. The observations for project C3263, reported in this paper, used the above properties to target nearby southern sources. Despite that, the three sources observed so far as part of that project (NGC 1097, NGC 1792 and NGC 1808) have not shown any sign of methanol maser emission. The only other source observed with appropriate sensitivity is the Circinus Galaxy, which is a spiral galaxy with no bar, however it does show evidence of molecular outflows from its type 2 Seyfert AGN.

In order to determine the most efficient way, in terms of target selection and telescope time, to search for extragalactic 36.2-GHz methanol masers, we must determine the luminosity levels of a 'typical' region. The currently reported extragalactic 36.2-GHz methanol masers (in NGC 4945, NGC 253, NGC 6946 and IC 342) all have varying peak and integrated luminosity levels. In this discussion we consider the peak and integrated flux density from a single emission component at our resolution (rather than the combined emission across the whole source) as these are what will be detected when searching using interferometers like the VLA or the ATCA. Peak luminosities (in a 10 km s^{-1} channel) for the brightest region in each source vary from 1.1×10^6 Jy kpc^2 in IC 342 to 5.2×10^6 Jy kpc^2 toward NGC 4945, with integrated luminosities ranging from 2.8×10^7 Jy km s^{-1} kpc^2 in IC 342 to 1.6×10^8 Jy km s^{-1} kpc^2 toward NGC 253. It must be noted that the flux density values for IC 342 and NGC 6946 are from observations with much higher spatial-resolution than the ATCA observations

(VLA C-configuration) of NGC 4945 and NGC 253 (∼1 arcsec compared to ∼5 arcsec). We calculate an average peak luminosity of 3.0×10^6 Jy kpc^2 across these 4 sources. With a sensitivity of 0.5 mJy (in a 10 km s^{-1} channel), a 5σ detection of a maser with this luminosity can be made out to a distance of ∼34 Mpc. Assuming the ability to self-calibrate off a continuum source, this sensitivity can be achieved with about 4 hours of on-source time with the ATCA in an intermediate resolution array configuration (H168 – EW367) or 45 minutes of on-source time with VLA D-configuration (VLA D-configuration will allow detection of any extended emission, such as that seen toward NGC 253). A 10 km s^{-1} channel width is appropriate for searching for these masers as this will allow multiple, above noise level, consecutive channels across the FWHM of the spectral profile for the vast majority of known extragalactic 36.2 GHz methanol sources. The only exception to this is the spectral profile of the M1 region in NGC 4945, which has a FWHM of ∼20 km s^{-1}. Though this source has a much higher peak luminosity then the other sources, so the ability to image with narrower channel widths will still allow flexibility for detecting these sources. However, it should be noted that our analysis of optimal search parameters for these 36.2-GHz masers is based off a sample size of four sources, and as such is susceptible to small number statistics.

4.6 Galaxy-wide star-formation as a predictor for class I methanol masers

Within our Galaxy, methanol masers (both class I and II) provide useful sign-posts for the location of star-formation regions (Caswell 1997; Kurtz et al. 2004; Voronkov et al. 2006; Breen et al. 2010, 2011). It was initially hypothesised that these extragalactic class I masers may be useable in the same manner, identifying starburst galaxies at cosmologically interesting distances (Chen et al. 2016). However, that speculation was largely predicated on the more luminous emission reported toward Arp 220. Reanalysis showing no 36.2-GHz methanol emission stronger than 3.5 mJy (peak luminosity of $\sim 2 \times 10^{10}$ Jy kpc^2) toward Arp 220, means that at present the known extragalactic methanol sources are not readily detectable at cosmologically interesting distances with current generation facilities. Even considering only the sources that meet our detection threshold in Figure 4, we have four sources with star-formation rates (SFR) at the same level or higher than those observed toward NGC 253 or NGC 4945 with confident non-detections for 36.2-GHz class I methanol masers.

When considering known examples of extragalactic class I methanol masers, we see that locally, there is no clear link to star-formation rates in the regions where they are detected. The M1 region toward NGC 4945 and the masers toward NGC 253 are all likely associated with giant molecular clouds in these sources, however, these regions do not necessarily display enhanced star-formation rates when compared to the rest of the nuclear region (Ellingsen et al. 2017; McCarthy et al. 2018a). M1 in NGC 4945 may be associated with the star-formation from Knot B, though even if this is correct, we do not observe class I maser emission from other regions in NGC 4945 with enhanced star-formation levels. Instead of tracing current star-formation, based on our current understanding of the environments of these masers (dense-gas and low-velocity shocks), we believe they may indicate regions that are soon to experience higher levels of star-formation, essentially the class I maser emission is associated with the triggering of the star-formation.

The presence, or lack-thereof, of class I methanol masers may not directly infer information about the star-formation rate of its host, however, it can still provide useful information about the mechanism triggering the star-formation. The morphological features that these class I masers have been observed toward (Ellingsen et al. 2017; Gorski et al. 2018; McCarthy et al. 2018a) can be related to the star-formation in a galaxy and, therefore, the class I masers (and their association with low-velocity shocks) can help identify mechanisms that are providing the gas fueling these starburst regions (Ellingsen et al. 2017).

5 CONCLUSIONS

We present the results of new observations toward NGC 4945 and NGC 253, detecting new components of methanol emission toward both galaxies. Evidence of variability, especially toward the new region in NGC 4945, indicates that this emission is likely the result of a maser process. This is the first reported example of variability in an extragalactic class I methanol maser and we recommend continued monitoring of these sources in order to both confirm and further quantify this variability.

We provide flux density upper-limits for the 36.2-GHz class I and 37.7-GHz class II methanol transitions toward 9 galaxies, observed as part of the original extragalactic class I methanol searches which detected NGC 253 and NGC 4945, and 3 more sources observed more recently. In the majority of sources from the older observations (C2879), sensitivity levels are not sufficient in order to rule out maser emission of the same order as is observed toward NGC 4945 or NGC 253.

We also report the results of a re-analysis of the ATCA data on Arp 220. We do not find any evidence of the 36.2-GHz methanol maser emission toward this source. It appears a combination of poor data quality and sub-optimal imaging procedures may have resulted in the original reported detection. We place a 5σ upper limit on the 36.2-GHz line of 3.5 mJy.

ACKNOWLEDGEMENTS

We thank the referee for the valuable comments which have helped improve the manuscript. The ATCA is part of the Australia Telescope which is funded by the Commonwealth of Australia for operation as a National Facility managed by CSIRO. This research has made use of NASA's Astrophysics Data System Abstract Service. This research has made use of the NASA/IPAC Extragalactic Database (NED), which is operated by the Jet Propulsion Laboratory, California Institute of Technology, under contract with the National Aeronautics and Space Administration. This research also utilised APLPY, an open-source plotting package for PYTHON hosted at http://aplpy.github.com. This research made use of Astropy, a community-developed core Python package for Astronomy (Astropy Collaboration et al. 2013).

REFERENCES

Araya E. D., Hofner P., Goss W. M., Kurtz S., Richards A. M. S., Linz H., Olmi L., Sewiło M., 2010, ApJ, 717, L133

Astropy Collaboration et al., 2013, A&A, 558, A33

Bendo G. J., Henkel C., D'Cruze M. J., Dickinson C., Fuller G. A., Karim A., 2016, MNRAS, 463, 252

Bottinelli L., Gouguenheim L., Paturel G., de Vaucouleurs G., 1985, A&AS, 59, 43

Breen S. L., Ellingsen S. P., Caswell J. L., Lewis B. E., 2010, MNRAS, 401, 2219

Breen S. L., Ellingsen S. P., Caswell J. L., Green J. A., Fuller G. A., Voronkov M. A., Quinn L. J., Avison A., 2011, ApJ, 733, 80

Breen S. L., Ellingsen S. P., Contreras Y., Green J. A., Caswell J. L., Stevens J. B., Dawson J. R., Voronkov M. A., 2013, MNRAS, 435, 524

Caswell J. L., 1997, MNRAS, 289, 203

Chen X., Ellingsen S. P., Baan W. A., Qiao H.-H., Li J., An T., Breen S. L., 2015, ApJ, 800, L2

Chen X., Ellingsen S. P., Zhang J.-S., Wang J.-Z., Shen Z.-Q., Wu Q.-W., Wu Z.-Z., 2016, MNRAS, 459, 357

Chen X., Ellingsen S. P., Shen Z.-Q., McCarthy T. P., Zhong W.-Y., Deng H., 2018, ApJ, 856, L35

Chou R. C. Y., et al., 2007, ApJ, 670, 116

Cyganowski C. J., Brogan C. L., Hunter T. R., Churchwell E., 2009, ApJ, 702, 1615

Cyganowski C. J., Brogan C. L., Hunter T. R., Zhang Q., Friesen R. K., Indebetouw R., Chandler C. J., 2012, preprint, (arXiv:1210.3366)

Dalcanton J. J., et al., 2009, ApJS, 183, 67

Ellingsen S. P., Breen S. L., Caswell J. L., Quinn L. J., Fuller G. A., 2010, MNRAS, 404, 779

Ellingsen S. P., Chen X., Qiao H.-H., Baan W., An T., Li J., Breen S. L., 2014, ApJ, 790, L28

Ellingsen S. P., Chen X., Breen S. L., Qiao H.-H., 2017, MNRAS, 472, 604

Felli M., et al., 2007, Astronomy & Astrophysics, 476, 373–664

Gao F., et al., 2016, ApJ, 817, 128

Goedhart S., Gaylard M. J., van der Walt D. J., 2003, MNRAS, 339, L33

Gorski M., Ott J., Rand R., Meier D. S., Momjian E., Schinnerer E., 2017, ApJ, 842, 124

Gorski M., Ott J., Rand R., Meier D. S., Momjian E., Schinnerer E., 2018, ApJ, 856, 134

Green J. A., et al., 2008, MNRAS, 385, 948

Haschick A. D., Baan W. A., 1990, ApJ, 355, L23

Henkel C., et al., 2018, A&A, 615, A155

Hollenbach D., Elitzur M., McKee C. F., 2013, preprint, (arXiv:1306.5276)

Jensen J. B., Tonry J. L., Barris B. J., Thompson R. I., Liu M. C., Rieke M. J., Ajhar E. A., Blakeslee J. P., 2003, ApJ, 583, 712

Kurtz S., Hofner P., Álvarez C. V., 2004, ApJS, 155, 149

Leurini S., Menten K. M., Walmsley C. M., 2016, A&A, 592, A31

McCallum J. N., Ellingsen S. P., Lovell J. E. J., 2007, MNRAS, 376, 549

McCarthy T. P., Ellingsen S. P., Chen X., Breen S. L., Voronkov M. A., Qiao H.-h., 2017, ApJ, 846, 156

McCarthy T. P., Ellingsen S. P., Breen S. L., Henkel C., Voronkov M. A., Chen X., 2018a, MNRAS, 480, 4578

McCarthy T. P., Ellingsen S. P., Breen S. L., Voronkov M. A., Chen X., 2018b, ApJ, 867, L4

McEwen B. C., Pihlström Y. M., Sjouwerman L. O., 2014, ApJ, 793, 133

Moran J. M., Greenhill L. J., Herrnstein J. R., 1999, Journal of Astrophysics and Astronomy, 20, 165

Olech M., Szymczak M., Wolak P., Sarniak R., Bartkiewicz A., 2019, MNRAS, 486, 1236

Sakamoto K., Mao R.-Q., Matsushita S., Peck A. B., Sawada T., Wiedner M. C., 2011, ApJ, 735, 19

Sjouwerman L. O., Murray C. E., Pihlström Y. M., Fish V. L., Araya E. D., 2010, ApJ, 724, L158

Sobolev A. M., et al., 2007, in Chapman J. M., Baan W. A., eds, IAU Symposium Vol. 242, Astrophysical Masers and their Environments. pp 81–88 (arXiv:0706.3117), doi:10.1017/S1743921307012616

Sorce J. G., Tully R. B., Courtois H. M., Jarrett T. H., Neill J. D., Shaya E. J., 2014, MNRAS, 444, 527

Tsunekawa S., Ukai T., Toyama A., Takagi K., 1995, Department of Physics, Toyama Univerity, Japan

Tully R. B., Fisher J. R., 1988, Catalog of Nearby Galaxies

Tully R. B., Rizzi L., Shaya E. J., Courtois H. M., Makarov D. I., Jacobs B. A., 2009, AJ, 138, 323

Tully R. B., et al., 2013, AJ, 146, 86

Tully R. B., Courtois H. M., Sorce J. G., 2016, AJ, 152, 50

Voronkov M. A., Brooks K. J., Sobolev A. M., Ellingsen S. P., Ostrovskii A. B., Caswell J. L., 2006, MNRAS, 373, 411

Voronkov M. A., Caswell J. L., Ellingsen S. P., Green J. A., Breen S. L., 2014, MNRAS, 439, 2584

Wang J., Zhang J., Gao Y., Zhang Z.-Y., Li D., Fang M., Shi Y., 2014, Nature Communications, 5, 5449

Whiting M. T., 2012, MNRAS, 421, 3242

Wilson W. E., et al., 2011, MNRAS, 416, 832

Yamauchi A., Nakai N., Ishihara Y., Diamond P., Sato N., 2012, PASJ, 64, 103

Yusef-Zadeh F., Cotton W., Viti S., Wardle M., Royster M., 2013, ApJ, 764, L19

van der Walt D. J., 2011, AJ, 141, 152

Table A.1: Details of the 2014 March sources excluded due to poor data quality. Recession velocities have been taken from the *NASA/IPAC Extragalactic Database*† (NED). Redshift-independent distances have been provided where possible, otherwise distances reported are the luminosity distances provided by NED.

Target Source	Right Ascension h m s	Declination $^\circ$ $'$ $''$	V_{helio} (km s^{-1})	D (Mpc)
MRK 1029	02 17 03.57	+05 17 31.40	9076	133
NGC 1052	02 41 04.80	–08 15 21.00	1510	18.0[1]
J0350–0127	03 50 00.35	–01 27 57.70	12322	185
UGCA 116	05 55 42.63	+03 23 31.80	789	10.3[2]
NGC 5765b	14 50 51.50	+05 06 52.00	8333	126[3]
TXS 2226–184	22 29 12.50	–18 10 47.00	7520	108

Note: [1]Jensen et al. (2003), [2]Tully & Fisher (1988), and [3]Gao et al. (2016)

Chapter 7

Discussion, conclusions and future work

In this final chapter we will discuss the results of Chapters 2 through 6 and how they have impacted our current knowledge on extragalactic class I methanol masers. As this thesis contains the exact published works as the individual chapters, much of this conclusion chapter will be focussed on the results from the later published works as our understanding of these masers has changed throughout the course of this project. The field has evolved significantly over the past three and a half years and so this chapter will also act as a review of the current state of extragalactic class I methanol masers, as of the end of this project (late 2019).

7.1 The methanol maser emission of NGC 4945

We presented the original detection of class I methanol maser emission toward NGC 4945, along with four epochs of follow-up observations investigating this emission. This emission toward NGC 4945 is the second confirmed detection of 36.2-GHz class I maser emission toward an external galaxy. This section will collate the results of the most recent papers on NGC 4945 (Chapters 4 and 6) and present our current understanding of the class I maser emission from this source.

The class I maser emission in NGC 4945 is distributed between two separate regions, the primary offset to the south-east of the galactic centre by approximately 10 arcsec-

onds (M1) and the secondary region located south-west of the nucleus, with a much more modest offset of 3 arcseconds (M2). The maser emission from M1 has a spectral profile much narrower than is observed towards any other extragalactic 36.2-GHz methanol maser, with a FWHM of approximately 12 km s^{-1}. There also appears to be evidence of 3 or 4 spectral components from M1, though no spatial offset between these has been detected yet. M1 has the highest peak luminosity of any known extragalactic class I maser at 5.2×10^6 Jy kpc^2, and an isotropic integrated luminosity less than a factor of 2 lower than the brightest (in NGC 253) at 6.9×10^7 Jy km s^{-1} kpc^2. This isotropic luminosity is over five orders of magnitude greater than a typical Galactic 36.2-GHz methanol maser. Unlike M1, the spectral profile of the emission from M2 is much broader and weaker, with what appears to be two or more maser components with FWHM of 20–30 km s^{-1}. Despite the peak flux density being much lower for M2 (by an order of magnitude), the integrated flux density is only a factor of 2 lower. Evidence for variability in the emission from M2 seems to suggest it is the result of a maser process, however, as this is the first example of variability detected in an extragalactic class I maser, further long-term investigation is required. The mechanism required to produce the necessary methanol abundances are unclear, however it is thought to likely arise from heightened levels of cosmic rays in the nuclear regions of these galaxies interacting with cold dust grains (Yusef-Zadeh et al., 2013a).

The class I maser emission from M1 appears to be associated with a giant molecular cloud at the interface region between the end of the galactic bar and beginning of the south-eastern spiral arm in NGC 4945. Dynamical interaction at this interface could be providing the shocks necessary to drive population inversion and allow masing. Observations that show that any 44 GHz methanol emission associated with M1 is at least an order of magnitude lower in luminosity than the 36.2 GHz emission allows us to confidently conclude that the maser at M1 is not simply the result of many star-formation regions in a tight cluster. If this was the case we would not expect to see such an extreme flux density ratio between the 36.2- and 44.1-GHz class I maser transitions. These flux density ratios are similar to what is observed towards the dense

Galactic giant molecular cloud G 1.6-0.025 (referred to hereafter as G 1.6; Jones et al., 2013). This similarity in line ratios may be an indication that M1 in NGC 4945 and G 1.6 share a similar pumping regime. Interestingly G 1.6 displays very little evidence of star-formation, yet it is a strong 36.2-GHz maser source. This is not necessarily dissimilar to M1 (or any known extragalactic class I maser for that matter), however, there is some evidence that M1 is associated with the star-formation feature known as 'Knot B'. Henkel et al. (2018) suggest that Knot B may be the star-forming front side of the same giant molecular cloud that M1 is associated with.

The location of M2 presents more of a mystery, as typically these masers are observed more significantly offset from the nucleus of the galaxy, whereas M2 has a projected linear offset of only $\sim 50\,\mathrm{pc}$. It should be noted that the geometry of NGC 4945 means that the actual offset may be significantly larger than this depending on where the emission is located within the galaxy along the line of sight. It may be that the emission from M2 is similar to that seen toward the central molecular zone (CMZ) of the Milky Way, where combined emission from many 36.2-GHz masers is observed in a relatively compact region (Yusef-Zadeh et al., 2013a). The lower limit of the 36.2-/44.1-GHz line also does not exclude the interpretation that the 36.2-GHz maser emission at M2 is the result of combined emission from star-forming regions, however, further high-sensitivity observations of the 44.1-GHz transition are required to constrain this line ratio value. Further modelling of the emission, or methanol line surveys towards NGC 4945 would be useful for determining what other methanol transitions are strong in the conditions where the 36.2-GHz transition is much stronger than the 44.1-GHz line.

7.2 Three class I transitions toward NGC 253

We presented the first high-resolution observations of the 84.5-GHz methanol emission towards NGC 253. These observations identified that this emission was coming from the same location as previously reported 36.2- and 44.1-GHz class I maser emission

and determined that a maser process is the most likely mechanism producing this emission. We also presented two epochs of follow-up observations on the 36.2-GHz emission toward NGC 253. In this section we will summarise the contents of Chapter 5 and 6 that pertain to NGC 253.

NGC 253 is the only extragalactic source so far that has emission detected from more than one methanol maser transition. The 36.2-GHz emission of NGC 253 is spread over at least 7 distinct sites (Ellingsen et al., 2017a; Gorski et al., 2019), with a further two tentatively detected in our most recent observations (see Chapter 6). Emission from the other two class I lines, at 44.1 and 84.5 GHz, are much more conservatively distributed. Narrow emission from the 44.1-GHz class I transition is detected toward two of the brightest 36.2-GHz class I maser regions (MM1 and MM4; Ellingsen et al., 2017a). The 84.5-GHz class I emission we report is also detected toward MM4, and all three maser lines at this location share overlapping velocity ranges. High resolution VLA observations ($0.1''$) toward MM4 determined a brightness temperature exceeding 1000 K for the 36.2-GHz emission, indicating that a maser process must be responsible for the emission from this transition (Chen et al., 2018). We determine an isotropic luminosity of $\sim 10^8$ Jy km s^{-1} kpc^2 (including the factor of 4π), which is five orders of magnitude greater than a typical Galactic 84.5-GHz methanol maser (with integrated flux density of 29.4 Jy km s^{-1}; Breen et al., 2019). This implies that the single region of 84.5-GHz emission in NGC 253 has a higher isotropic luminosity than all known Galactic 84.5-GHz masers combined. This extreme isotropic luminosity, combined with a narrow FWHM (compared to thermal lines) and the presence of two other class I methanol maser lines at the same location indicate that the 84.5-GHz emission is also masing. For a more extended discussion on the maser nature of this emission, please refer to Chapter 5.

Multiple class I transitions toward the same region of NGC 253 provide some insight into the physical conditions of the maser environment. The line ratio of 1.2 observed between the 36.2- and 84.5-GHz class I maser lines is strikingly similar to the median

ratio observed toward Galactic sources (1.4; Breen et al., 2019). Modeling of the relationship between class I methanol transitions predominantly focuses on their common Galactic environments, such as high-mass star formation (HMSF) regions and supernova remnants (McEwen et al., 2014; Leurini et al., 2016). In these environments the 36.2- and 84.5-GHz transitions (as members of the same family) favour higher density regions than the 44.1-GHz line. Based on these studies it would appear that the 36.2/84.5 GHz line ratio is maximised ($>> 1$) at lower densities and approaches 0 as density increases. Our 36.2/84.5 GHz line ratio would then imply a H_2 number density of $\sim 10^6 - 10^7 \mathrm{cm}^{-3}$ for this class I methanol environment (McEwen et al., 2014). This implied density does not agree with the interpretation, as outlined by Ellingsen et al. (2017a), that these masers are the result of low-gain, diffuse emission across large regions of shocked gas. Instead, it may suggest these masers are associated with giant molecular clouds, similar to Sagittarius B2, which are able to achieve these densities (Huttemeister et al., 1993). However, again it should be noted that these models are based on Galactic sources, and further modelling of lower density environments is required in order to determine the class I methanol behaviour in the context of extragalactic sources.

7.3 The current state of extragalactic methanol masers

As of this time, extragalactic class I masers have been detected in NGC 253 (36.2-, 44.1- and 84.5-GHz; Ellingsen et al., 2014, 2017a; McCarthy et al., 2018b), NGC 4945 (36.2-GHz; McCarthy et al., 2017), NGC 6946 (36.2-GHz; Gorski et al., 2018), NGC 1068 (84.5-GHz; Wang et al., 2014), IC 342 (36.2-GHz; Gorski et al., 2018) and Maffei 2 (36.2-GHz; Humire et al., 2019, Chen et al. in preparation). In this section we will cover the maser emission in each of these sources (excluding NGC 4945 as it is already covered in detail above) and review our current interpretation of this phenomenon.

7.3.1 NGC 253

Of all extragalactic sources currently observed, NGC 253 has 36.2-GHz methanol emission distributed across the largest number of discrete sites (Ellingsen et al., 2017a; Gorski et al., 2019). The current consensus is that these masers are the result of cloud-cloud interaction due to molecular inflow along the galactic bar (Ellingsen et al., 2017a; Gorski et al., 2019). High-resolution JVLA observations by Chen et al. (2018) and Gorski et al. (2019) resolve out much of the flux-density from these 36.2-GHz maser regions, though they determine brightness temperatures of > 1000 K for the emission that is detected. The majority of 36.2-GHz masers toward NGC 253 have line widths > 10 km s^{-1} (Ellingsen et al., 2017a; Gorski et al., 2017, 2019), however, a single region toward the centre of the galaxy has an unresolved line width of < 1 km s^{-1} (MM6a; Gorski et al., 2019) and is interpreted as being associated with high-mass star formation in the CMZ of NGC 253 (Gorski et al., 2019).

7.3.2 IC 342

IC 342 is a face-on spiral galaxy, approximately 3.3 Mpc away in the IC 342/Maffei group (Karachentsev et al., 2013). This source has two spiral arms, and a central molecular ring (Boker et al., 1997; Meier & Turner, 2005; Gorski et al., 2018). Some studies have suggested that there is a bar structure connecting the two spiral arms to the central molecular ring, however, this interpretation seems to have fallen out of favour in recent years, and instead the spiral arms connect directly to the central molecular ring (Ishizuki et al., 1990; Boker et al., 1997). The 36.2-GHz maser emission toward IC 342 was first reported by Gorski et al. (2018), using the JVLA in C configuration. Gorski et al. detected 6 individual 36.2-GHz maser components across a $30''$ stretch starting north-east, and extending south-west across the nucleus of the galaxy. These maser spots are constrained to the northern and southern spiral arms. The maser spots in IC 342 are around two orders of magnitude lower luminosity than those observed in NGC 4945 or NGC 253 (Gorski et al., 2017, 2018; Ellingsen et al.,

2017a; McCarthy et al., 2018a). Though this may be due to the smaller synthesised beam of JVLA in C configuration (when compared to JVLA D-configuration and typical ATCA array configurations), Effelsberg 100m observations of the emission by Humire et al. (in press) do not see a significant increase in integrated flux-density. This differs from NGC 253, where we see a substantial increase in flux-density as synthesised beam sizes increase (Ellingsen et al., 2014, 2017a; Gorski et al., 2017, 2019; McCarthy et al., 2018b). Similar to the class I methanol masers in NGC 253, there is a strong correlation between the HNCO emission (typically a tracer of low-velocity shocks) and the 36.2-GHz maser spots (Ellingsen et al., 2017a; Gorski et al., 2018; McCarthy et al., 2018a).

7.3.3 NGC 6946

The same JVLA observations responsible for the IC 342 detection also produced a detection of 36.2-GHz emission toward NGC 6946 (Gorski et al., 2018), another face-on spiral galaxy, approximately 5.9 Mpc away in the Virgo Supercluster (Karachentsev et al., 2013). The central region of NGC 6946 is well explained by multi-Gaussian-expansion model, which suggests the presence of an inner stellar bar, driving a starburst nucleus (Schinnerer et al., 2006). Two 36.2-GHz maser components are detected toward NGC 6946, offset by 90pc to the east of the dynamical centre (Gorski et al., 2018). This offset is close to the inner radius of the stellar bar modelled by Schinnerer et al. (2006), with the current interpretation that these masers are shocked by molecular infall along this bar (Gorski et al., 2018). As of yet no follow-up observations have been made of NGC 6946 and observations in a more compact array configuration (such as JVLA D array) would be valuable in order to investigate the 36.2-GHz emission on a larger scale.

7.3.4 Maffei 2

Maffei 2 is a spiral galaxy, at a distance of approximately 5.7 Mpc in the IC 342/Maffei group (Anand et al., 2019). Maffei 2 is host to a prominent kpc-scale bar which terminates at the central molecular ring (Meier & Turner, 2012). Effelsberg 100m observations by Humire et al. (in press) detect 36.2-GHz emission toward this galaxy. The spectral profile of this emission consists of two peaks, at local standard of rest velocities of approximately -99 and 7 km s^{-1}. Chen et al. (in preparation) see these same components in the spectrum from their JVLA interferometric observations. The red-shifted component appears to be located at the northern interface of the bar and nuclear ring, while the blue-shifted spectral component is the result of two separate emission spots in the southern bar. It is likely that this bar drives shocks in the central region, producing suitable conditions for extragalactic class I methanol masers to form.

7.3.5 NGC 1068

NGC 1068 (M 77) is a barred spiral galaxy $\sim$ 14.4 Mpc away in the M 77 group (Gallimore et al., 2001). So far only the 84.5-GHz class I methanol line has been detected toward this source (Wang et al., 2014). This detection was from IRAM 30m telescope, therefore, interferometric follow-up is required in order to determine the location of the emission relative to other morphological features in the galaxy. Throughout this project we made some attempt to image NGC 1068 at 36.2-GHz, however, the equatorial nature of the source made this not possible in our short observing windows. JVLA and/or ALMA follow-up at 7-mm and 3-mm respectively should be a priority in order to confirm the class I methanol emission from this source.

7.3.6 General discussion on extragalactic class I masers

One of the critical steps in increasing our understanding of these extragalactic class I masers is producing more detections of this phenomenon. Reflecting on our current

sample of six, we find three major common factors between all of these sources. They are all barred (except potentially IC 342), spiral type galaxies with star-formation levels elevated when compared to the Milky Way. This is potentially due to a bias in our target selection, rather than extragalactic methanol maser requiring these three specific properties. The first detection of extragalactic 36.2-GHz methanol emission was toward NGC 253, this combined with the subsequent detection of 84.5-GHz methanol maser emission in NGC 1068 has likely influenced target selection for recent searches, in favour of spiral galaxies with starburst nuclei. Of the sources we have searched as part of this project (see Chapter 6), we observed three sources that are starburst barred spirals (NGC 1097, NGC 1792 and NGC 1808) along with the Circinus galaxy (starburst, spiral with outflows) that have no detected 36.2-GHz emission at comparable luminosity to that observed from NGC 253 or NGC 4945. Although this is still a small sample size, it seems to indicate that these masers are not a common phenomenon in all barred, spiral galaxies. A way to combat this bias in target selection is to perform a quasi-statistically complete survey of nearby galaxies for 36.2-GHz maser emission, and speculation on how this could be performed will be included in the following 'future work' section.

It was previously suggested that extragalactic class I methanol masers may be good tools for studying star-formation at cosmologically interesting distances (Chen et al., 2016). This hypothesis is based on the relationship between the luminosity of 36.2-GHz emission and the infrared luminosity of the host galaxy (Chen et al., 2016). The discovery that the 36.2-GHz emission from Arp 220 is the result of imaging mistakes mostly invalidates this hypothesis as it was a key data point for the extreme luminosities (McCarthy et al., 2020). Additionally, many of the sources we have searched (with appropriate sensitivity) have star-formation rates higher than that of NGC 4945 and NGC 253 with no 36.2-GHz maser emission detected. In the majority of extragalactic class I sources the masers exist at the interface regions between galactic bars, spiral arms and the central molecular zones. Therefore, while these masers may not be good proxies for star-formation rates at cosmological distances, their presence

can instead inform us about the mechanisms fuelling the star-formation of their host galaxies. We see no real evidence of star-formation local to these methanol masers and instead, the dense, shocked gas in which these masers form may indicate regions soon to experience enhanced levels of star-formation.

7.4 Future work

There are three primary areas where future work in this field should focus, the first is searching for 36.2-GHz masers toward nearby galaxies (as previously mentioned), the second is searching known 36.2-GHz maser hosts for additional class I maser lines and the third is in-depth radiative transfer modelling of the extragalactic class I maser environments.

7.4.1 Searching for new extragalactic 36.2-GHz masers

In Chapter 6, we determine that 36.2-GHz masers could be detected with 4 hours of ATCA or 45 minutes of JVLA time out to a distance of 34 Mpc (McCarthy et al., 2020). If we prioritise nearest targets (for example out to 10 Mpc) first, even less on source time will be required per source. The Updated Nearby Galactic Catalogue contains all sources within 11 Mpc, or with corrected radial velocities < 600 km s^{-1} (Karachentsev et al., 2013). This catalogue consists of 1209 total sources, with 232 of these being non-dwarf galaxies. We can use this catalogue to determine the number of potential targets for future VLA and ATCA searches by determining all non-dwarf galaxy sources with a maximum distance of 10 Mpc. This catalogue lists B-band apparent magnitudes for all sources, we use these and the included distances to determine B-band absolute magnitudes for these sources. As we want to look at the most luminous nearby sources, we restrict our sample to those sources with B-band absolute magnitudes greater than that of our faintest source (IC 342). This cuts our potential target list down to 40 sources (excluding 5 sources already observed). Of these sources, 28 are observable with the VLA (declinations larger than -20 degrees),

Table 7.1: Potential targets for a 36.2-GHz search with the JVLA, based on discussion in Section 7.4.1. Galaxy T-Type refers to the galaxy morphology type classification presented in de Vaucouleurs et al. (1991). This T-type is represented by a number from –6 to 10, with lower values corresponding to early galaxy types (such as ellipticals) and larger numbers corresponding to late types (like irregulars and spirals). All data in this table is extracted from the 'The Catalog and Atlas of the LV galaxies' by Karachentsev et al. (2013).

Source Name	Right Ascension	Declination	B_{mag}	T-Type	V_{helio}	D
	h m s	° ′ ″			(km s^{-1})	(Mpc)
M 31	00 42 44.5	+41 16 09	4.3	3	–296	0.77
M 33	01 33 50.8	+30 39 37	6.3	6	–182	0.93
NGC 0891	2 22 32.8	+42 20 48	10.7	3	526	9.95
NGC 0925	02 27 16.0	+33 34 41	10.6	7	553	9.55
NGC 1637	04 41 28.2	–02 51 29	11.5	6	713	9.29
NGC 2403	07 36 51.4	+65 35 58	8.8	6	125	3.19
NGC 2683	8 52 40.9	+33 25 02	10.3	3	380	9.82
NGC 2903	09 32 09.6	+21 30 02	9.5	4	556	8.87
M 82	09 55 53.9	+69 40 57	9.1	8	183	3.61
NGC 3115	10 05 14.0	–07 43 07	9.9	-1	681	9.68
NGC 3344	10 43 30.2	+24 55 25	10.5	4	588	9.82
NGC 3351	10 43 57.7	+11 42 13	10.6	3	777	9.95
NGC 3384	10 48 16.9	+12 37 45	10.9	-1	704	9.42
NGC 3556	11 11 31.0	+55 40 26	10.7	6	696	9.90
NGC 3627	11 20 15.0	+12 59 29	9.7	4	716	8.32
NGC 4258	12 18 57.5	+47 18 14	9.1	4	447	7.66
NGC 4490	12 30 36.4	+41 38 37	9.8	7	586	8.91
NGC 4517	12 32 45.5	+00 06 54	11.1	7	1134	8.36
NGC 4559	12 35 57.7	+27 57 35	10.3	6	814	8.91
NGC 4594	12 39 59.1	–11 37 23	9.0	1	1090	9.55
NGC 4631	12 42 08.0	+32 32 29	9.8	7	583	7.35
NGC 4656	12 43 57.6	+32 10 13	11.0	8	638	7.98
NGC 4736	12 50 53.5	+41 07 10	8.7	2	308	4.41
NGC 4826	12 56 44.2	+21 41 05	9.3	2	409	4.41
NGC 5055	13 15 49.3	+42 01 45	9.3	4	500	9.04
NGC 5194	13 29 52.7	+47 14 04	8.6	5	446	8.40
NGC 5195	13 29 58.7	+47 16 05	10.5	0	455	7.66
M 101	14 03 12.8	+54 21 02	8.3	6	240	6.95

Table 7.2: Potential targets for a 36.2-GHz search with the ATCA, based on discussion in Section 7.4.1. Galaxy T-Type refers to the galaxy morphology type classification presented in de Vaucouleurs et al. (1991). This T-type is represented by a number from –6 to 10, with lower values corresponding to early galaxy types (such as ellipticals) and larger numbers corresponding to late types (like irregulars and spirals). All data in this table is extracted from the 'The Catalog and Atlas of the LV galaxies' by Karachentsev et al. (2013).

Source Name	Right Ascension	Declination	B_{MAG}	T-Type	V_{helio}	D
	h m s	$^\circ$ $'$ $''$			(km s^{-1})	(Mpc)
NGC 1291	03 17 18.6	–41 06 29	9.4	1	838	9.08
NGC 1313	03 18 15.4	–66 29 51	9.7	7	470	4.31
NGC 1744	4 59 58.2	–26 1 36	11.7	7	741	10.0
NGC 2784	9 12 19.4	–24 10 18	11.2	-2	687	9.82
NGC 3621	11 18 16.1	–32 48 42	10.2	7	730	6.64
NGC 5128	13 25 28.9	–43 01 00	7.8	-2	556	3.68
NGC 5236	13 37 00.1	–29 52 04	8.2	5	519	4.90
NGC 6684	18 48 57.9	–65 10 24	11.3	0	866	8.70
NGC 6744	19 09 45.9	–63 51 28	9.1	4	841	9.51
NGC 7090	21 36 28.6	–54 33 26	11.3	6	850	9.51
IC 5201	22 20 57.4	–46 02 03	11.3	6	915	8.80
IC 5332	23 34 27.5	–36 06 06	11.0	7	701	7.80

while 12 can only be observed with the ATCA (see Tables 7.1 and 7.2 for details on these sources).

7.4.2 Class I transition follow-up on known maser hosts

NGC 253 is the only extragalactic class I methanol maser source that shows emission from multiple class I transitions (Ellingsen et al., 2017a; McCarthy et al., 2018b) of the four current 36.2-GHz maser hosts that have been searched at 44.1-GHz (others being NGC 4945, Maffei 2 and IC 342; McCarthy et al., 2018b; Humire et al., 2019). Searching more of the known 36.2-GHz maser hosts for other class I transitions is important for our understanding of the nature of this phenomenon. Whether or not the various class I methanol transitions in these sources will be as commonly associated as in Galactic sources is still an open question. Additionally, comparison of the flux-density ratios between various methanol maser transitions in any particular region potentially allows us to infer the physical conditions within that region (McEwen et al., 2014; Leurini et al., 2016). Comparison of the different methanol lines allows us to test the hypothesis that these extragalactic masers are a different phenomenon with respect to their Galactic counterparts (Ellingsen et al., 2017a; McCarthy et al., 2018a). For Galactic sources the optimal conditions for 36.2-GHz methanol masers are also quite suitable for masers from the 44.1-GHz transition (McEwen et al., 2014). Therefore, a lack of association between the two most common class I transitions (36.2- and 44.1-GHz) may also indicate that these extragalactic methanol masers may result from different sets of optimal conditions than the Galactic 36.2-GHz class I masers. If this is the case, future methanol line surveys towards these source may reveal different transitions which come to dominate under these conditions.

7.4.3 Radiative transfer modelling

Investigation into the gas that hosts extragalactic class I methanol masers is a logical focus for extra work. The observational follow-up of additional class I methanol lines

goes partway to determining the physical conditions of the host molecular gas clouds, however, modelling based on both maser and thermal lines of various molecular species is required to develop the full picture. Modelling of the chemical composition, density and temperature of the masing gas in each source is important for determining the mechanisms responsible for producing the abundance of molecular methanol in these locations, as well as the pumping mechanisms driving these masers in extragalactic sources. This section will describe some of the recent analysis into the physical and chemical properties of our two primary sources (NGC 253 and NGC 4945), and identify research areas that should be further pursued.

The ATCA observations taken as part of this project did not have the sensitivity to detect weak thermal emission from the regions of the class I masers (McCarthy et al., 2018a). However, multi-line surveys of these sources from instruments such as the Atacama Large Millimetre/submillimetre Array (ALMA) have the potential to enable future detailed studies into the physical properties of this masing gas (Meier et al., 2015; Henkel et al., 2018). Leroy et al. (2015) have performed extensive line-ratio analysis toward the central region of NGC 253. Analysis of HCN-to-CO maps from this region reveal ten areas with enhanced dense gas (as traced by HCN) which are interpreted as giant molecular cloud (GMC) complexes. Many of these GMCs align in position with the class I methanol maser emission observed from the nuclear region of NGC 253 (Ellingsen et al., 2017a). Leroy et al. find radii for these GMCs are consistent with those observed toward other extragalactic and Galactic GMC sources, however, the masses and linewidths are much larger. If a direct connection exists between these cloud complexes and the methanol maser emission, investigation of the larger scale clouds can help infer physical conditions at the location of the masers.

Henkel et al. (2018) investigated the central region of NGC 4945, observing many molecular species between 85 and 98 GHz with ALMA Band 3. Their observations of dense gas tracers (HCN and CS) completely changed our understanding of the dynamics of NGC4945's nucleus, revealing details about the spiral arms and galactic

bar completely counter to what was previously understood based on observations of neutral hydrogen (Ott et al., 2001). Although Henkel et al. (2018) provide some preliminary analysis of line intensity ratios toward NGC 4945, their investigation was not focussed on a robust chemical analysis of NGC 4945. An example of the chemical analysis possible with ALMA can be seen in the work by McCoy et al. (2017) toward Centaurus A. They provide an insight into both the physical and chemical conditions within the nuclear region of Centaurus A, investigating temperatures and densities throughout this domain.

Although this ALMA data exists (with additional data soon to be available) and some investigation of the gas dynamics and chemistry has been completed, analysis with respect to the specific volumes of gas hosting the class I maser emission in NGC 253 and NGC 4945 has not yet been performed. For the three northern sky class I maser hosts (NGC 6946, IC 342 and Maffei 2) similar studies could be undertaken using the Karl G. Jansky Very Large Array observing 7-mm molecular thermal lines such as CS ($J = 1 \rightarrow 0$).

In addition to the typically observed tracers of molecular hydrogen (CO), dense gas (e.g. HCN, CS) and shock tracers (e.g. HNCO, SiO), observations of thermal methanol transitions may prove to be a valuable tool for studying physical conditions at the class I maser locations. An excellent example of this analysis toward a Galactic source can be found from Torstensson et al. (2011), who observe 25 thermal methanol lines at high frequency ($\sim$338 GHz) toward the star-formation region Cepheus A. Their analysis of rotational diagrams and non-LTE analysis reveals methanol abundances and distributions, along with temperatures and identification of outflows. Thermal methanol lines are plentiful and distributed across the frequency bands covered by current millimetre and sub-millimetre interferometers. Additionally, analysis of thermal methanol lines can be reasonably confidently linked to the location of the extragalactic class I methanol masers even in cases where synthesised beam sizes may be much larger than the maser regions (this is further discussed in the following paragraph).

There are some limitations in using radiative transfer modelling for understanding the class I methanol maser environments. Existing ALMA observations of thermal lines toward NGC 253 and NGC 4945 have had synthesised beam sizes of approximately 2 arcseconds. This corresponds to linear sizes of approximately 30 parsecs at the distance of NGC 253 (3.3 Mpc) and therefore, any analysis of physical conditions is going to be an average over this linear size. At present the scale on which the extragalactic class I methanol masers are produced is uncertain. JVLA observations by Chen et al. (2018) determined typical length scales of approximately 1 parsec for the compact regions of class I methanol emission toward NGC 253. Similarly, our preliminary results on methanol maser variability toward NGC 4945 indicate a linear scale of less than 1 parsec for the maser region M2 (McCarthy et al., 2020). In addition to the compact maser components, larger-scale maser emission which becomes resolved on baselines larger than a few hundred metres has been observed toward NGC 253 (linear scales of $\sim$ 80 pc; Chen et al., 2018). Consequently, radiative transfer modelling does not allow us to probe the individual environments of compact masers but instead the large scale structures they may be associated with. Instead, probing of the direct environment of the maser emission is more easily achieved through analysis of multiple associated methanol maser transitions as described in Section 7.4.2. These two techniques can provide complementary data in order to understand the physical conditions in these environments.

7.5 Concluding remarks

Although we are only just beginning to understand these extragalactic class I masers, excellent progress has been made in the last few years. The total number of known sources has increased from two to six and class I masers have been detected in two new transitions towards NGC 253. In addition to ongoing searches, evidence of variability in the class I masers of NGC 4945 has also shown that consistent monitoring of these masers is required. Observation of multiple transitions towards NGC 253, NGC 4945

and Maffei 2 have conclusively shown that these masers are a distinct phenomenon from those observed towards our Galaxy. Additionally, in all cases where we have interferometric data on these masers, it appears that these masers are tracing environments consisting of wide-scale low-velocity shocks, such as at the interface regions of spiral arms, galactic bars and nuclear rings.

As the sensitivity of modern interferometers increases, detections of these extragalactic class I masers will hopefully become increasingly common. After the Band 1 (and to a lesser extent Band 2) receiver is completed at the Atacama Large Millimetre/submillimetre Array (ALMA), ALMA will become the premiere instrument for searching southern sky galaxies for 36.2-GHz methanol masers, and allowing statistically complete searches with minimal time investment. An unbiased survey for these masers is one of the most important next steps in developing our understanding of this phenomenon, as it will increase our sample of searched galaxies and allow for meaningful detection statistics and analysis to be undertaken. Further study of additional methanol maser and thermal transitions should be undertaken toward all known hosts of extragalactic class I methanol masers. These studies will enhance our understanding of the environments of 36.2-GHz methanol masers, which will in turn allow for more intelligent source selection in future targeted searches.

Appendix A

Galactic 95-GHz Maser Field Images and Spectra

These field images and spectra were originally included as supplementary online data alongside the paper *'The relationship between Class I and Class II methanol masers at high angular resolution'*, which is presented in Chapter 2.

A.1 95-GHz maser field images

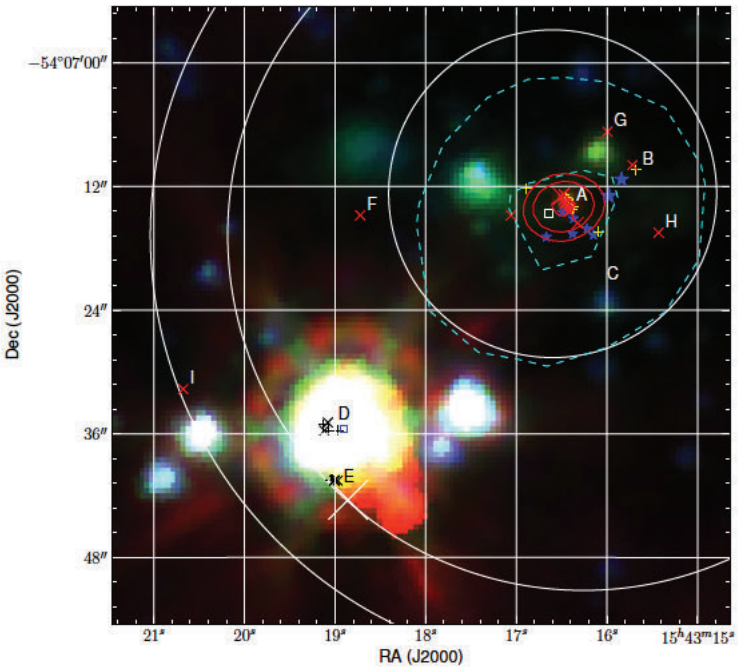

G326.48+0.70

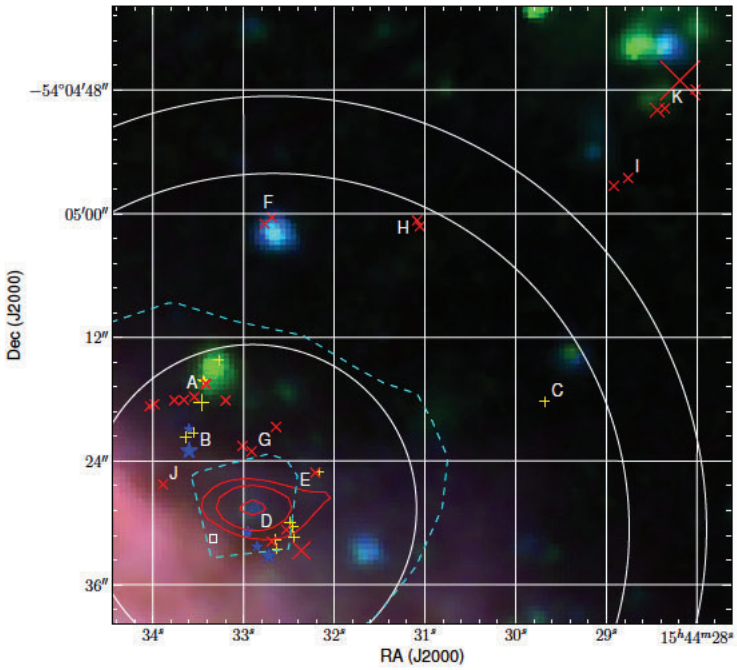

G326.64+0.61

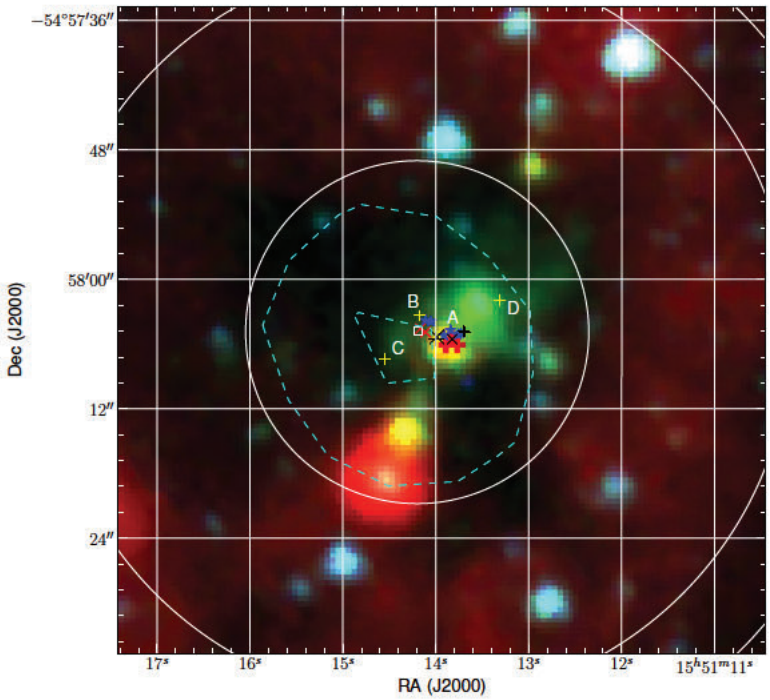

G326.86-0.68

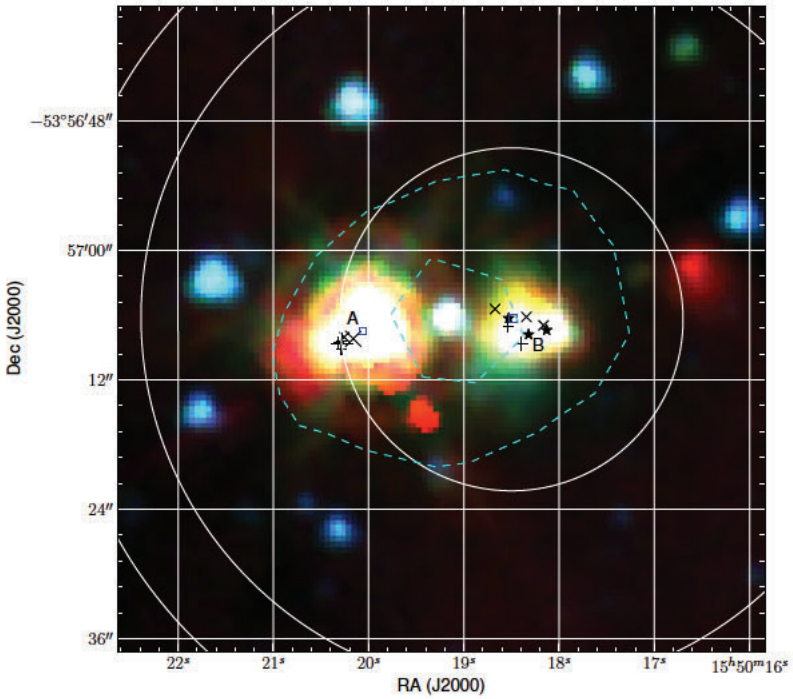

G327.39+0.20

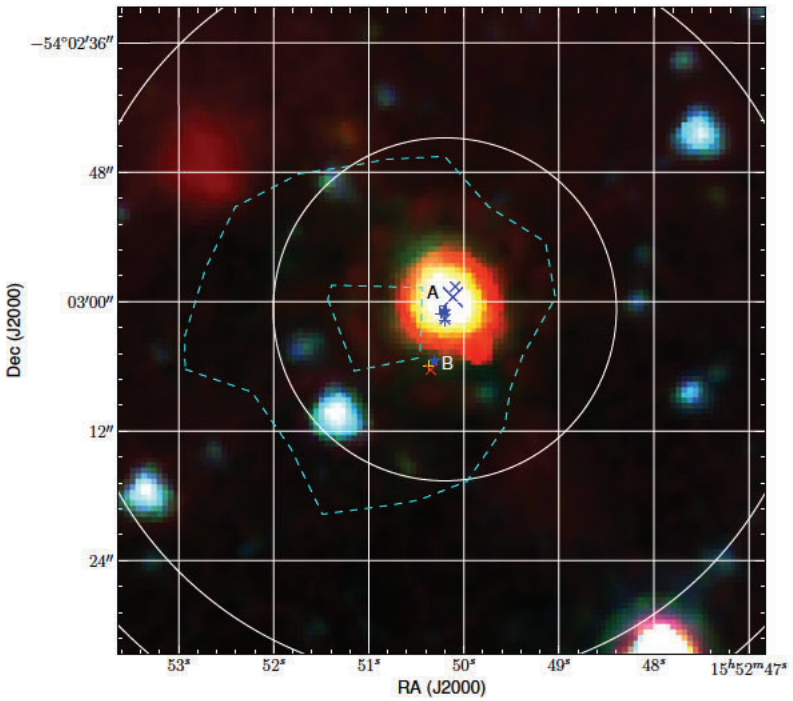

G327.62-0.11

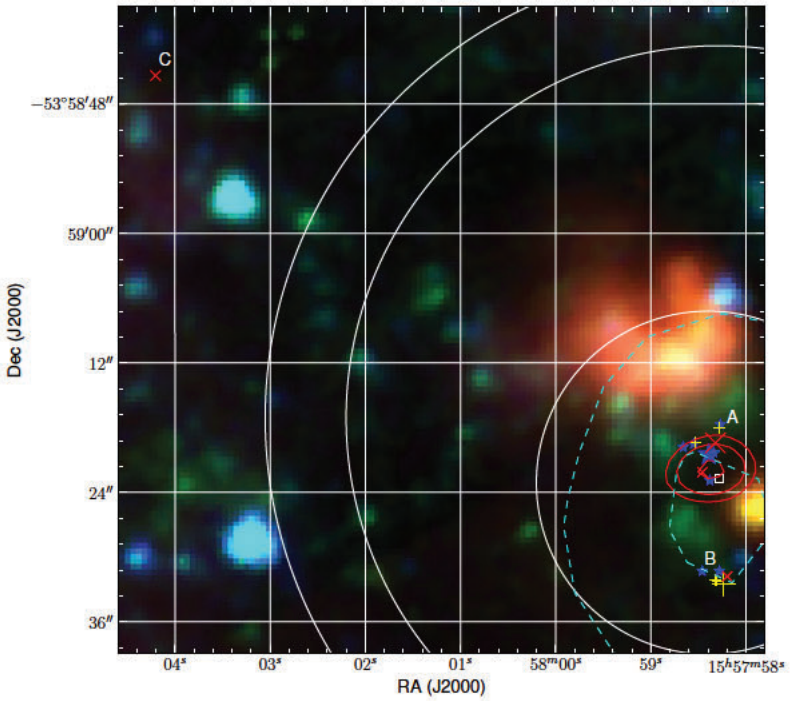

G328.24-0.55

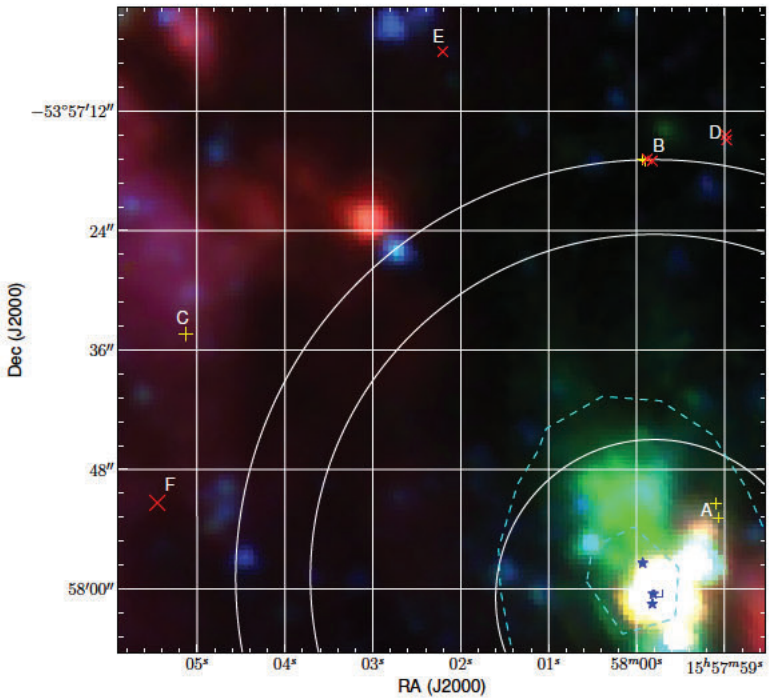

G328.25-0.53

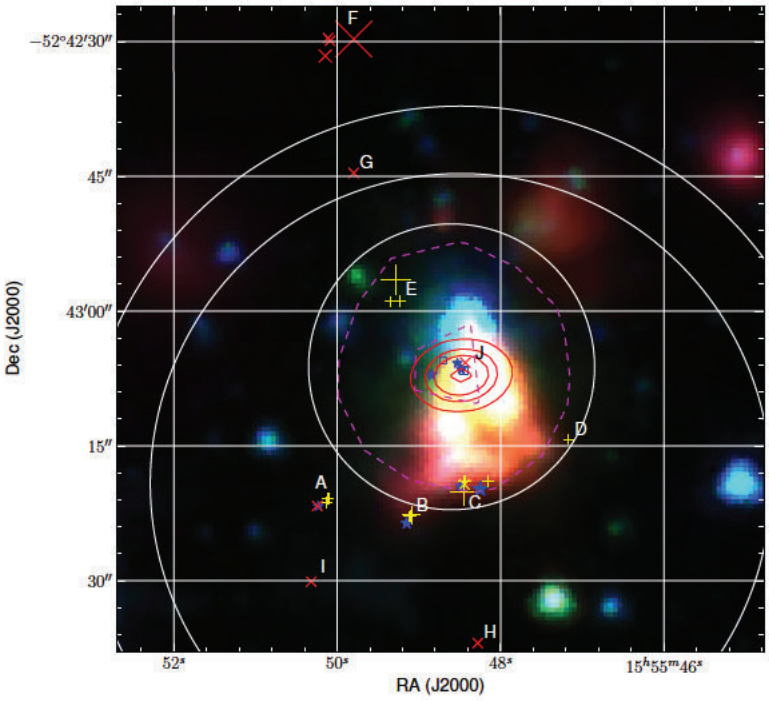

G328.81+0.63

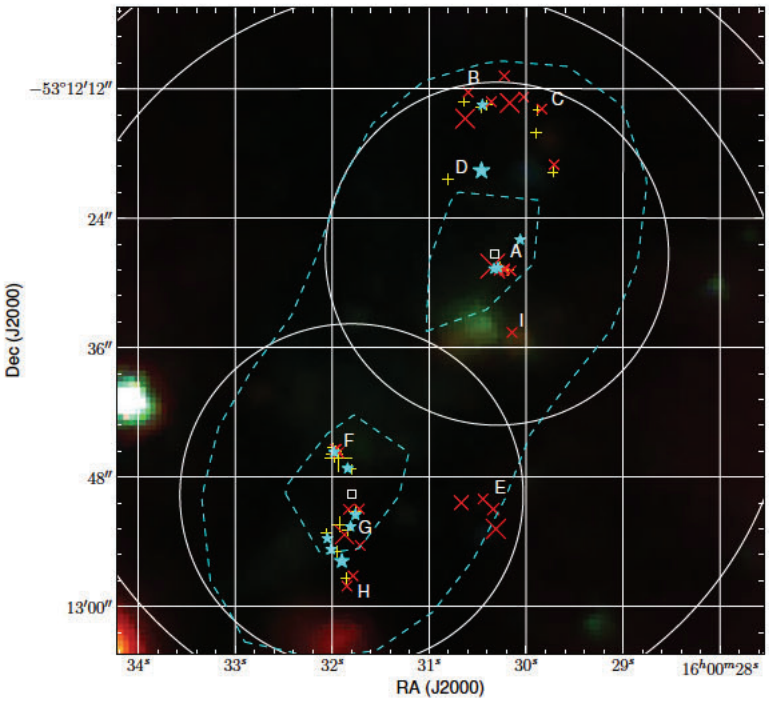

G329.03-0.20

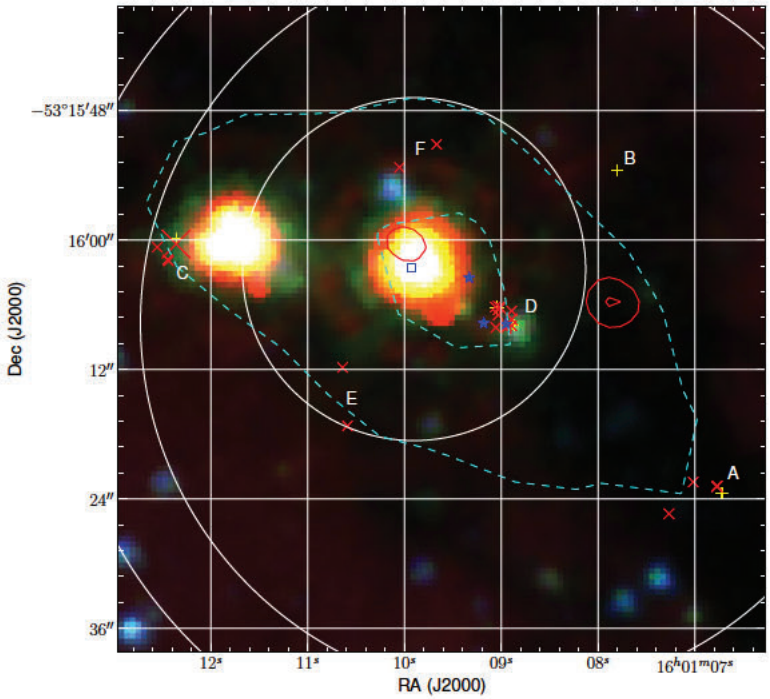

G329.07+0.31

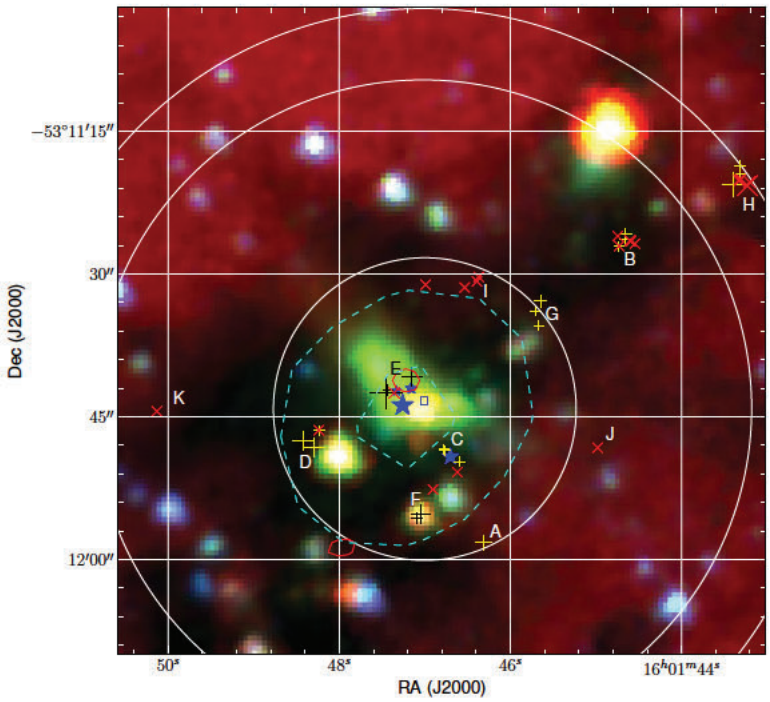

G329.18-0.31

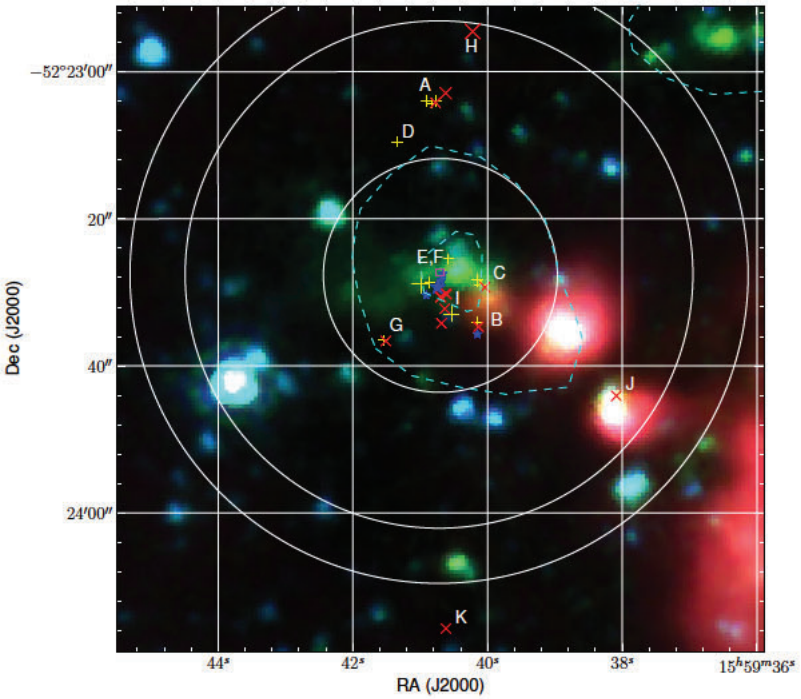

G329.47+0.50

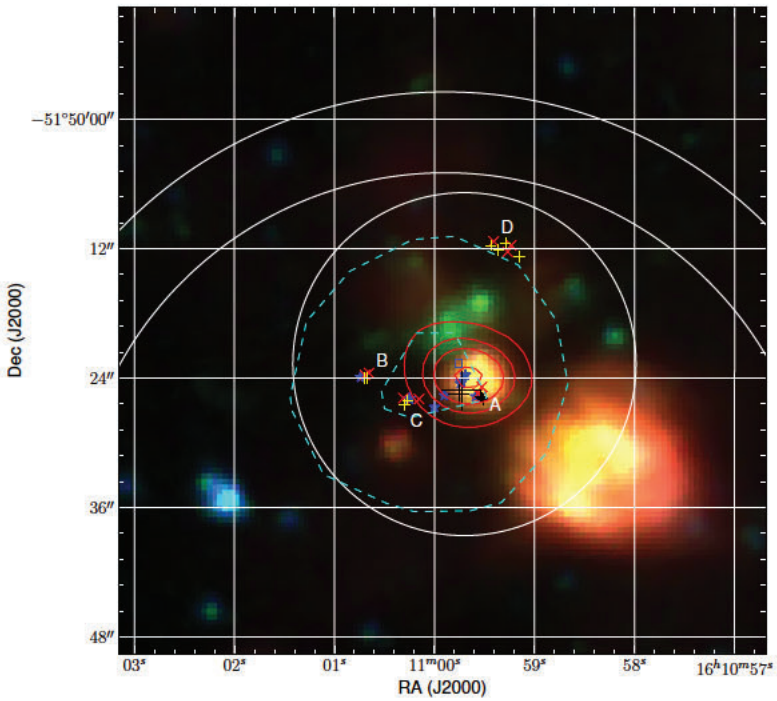

G331.13-0.24

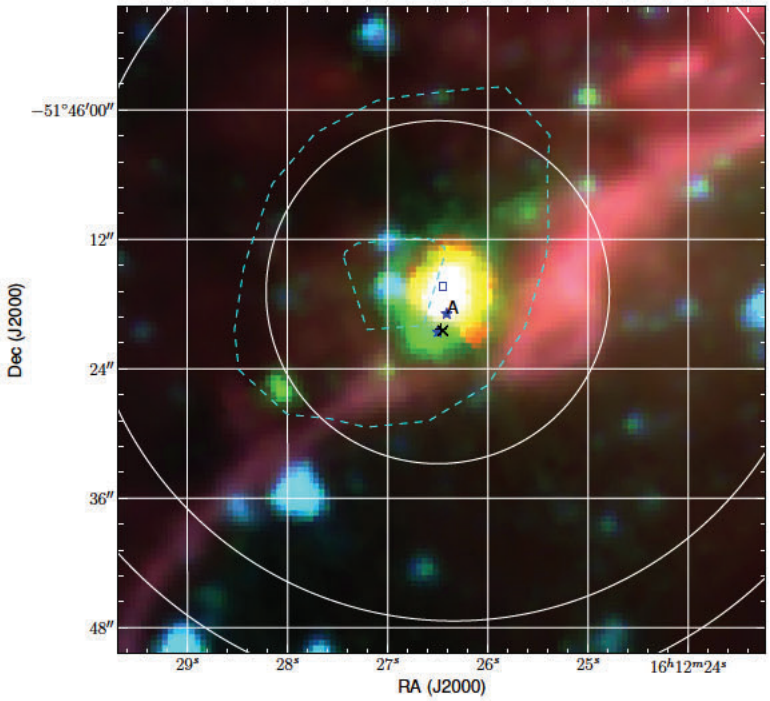

G331.34-0.35

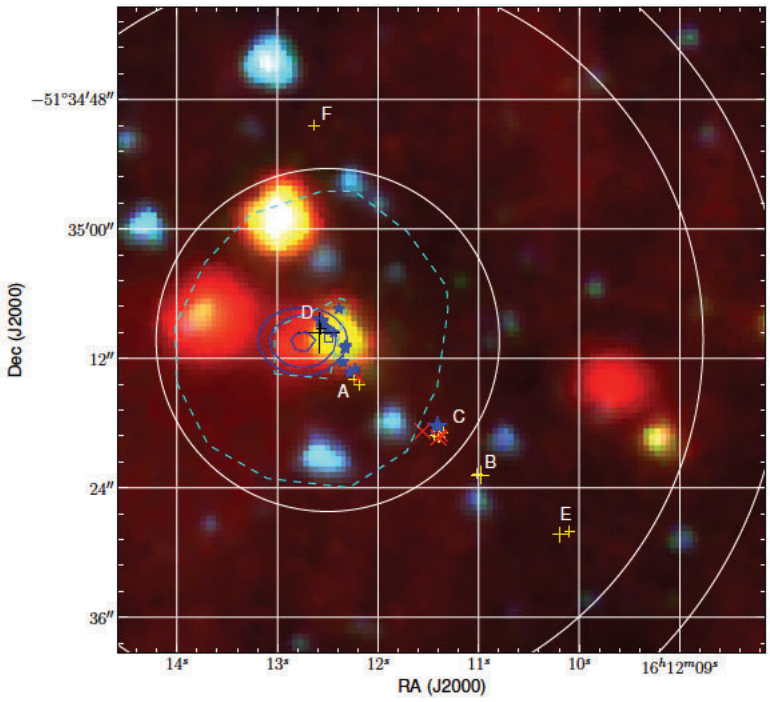

G331.44-0.19

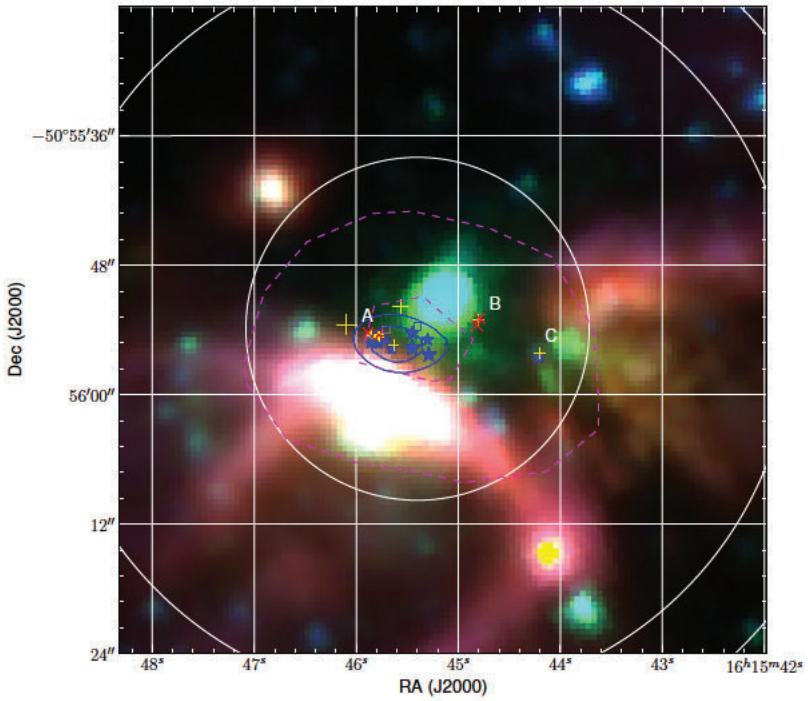

G332.30-0.09

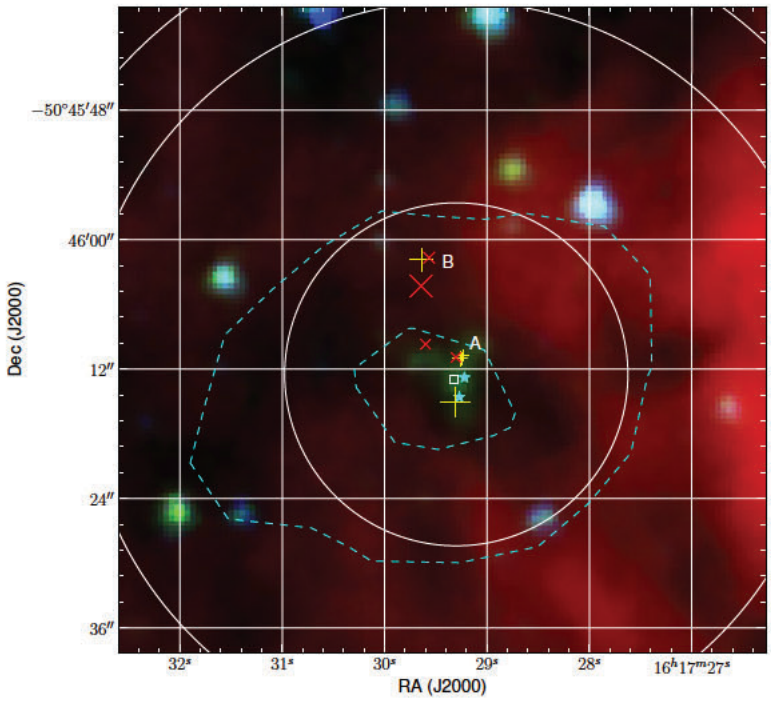

G332.60-0.17

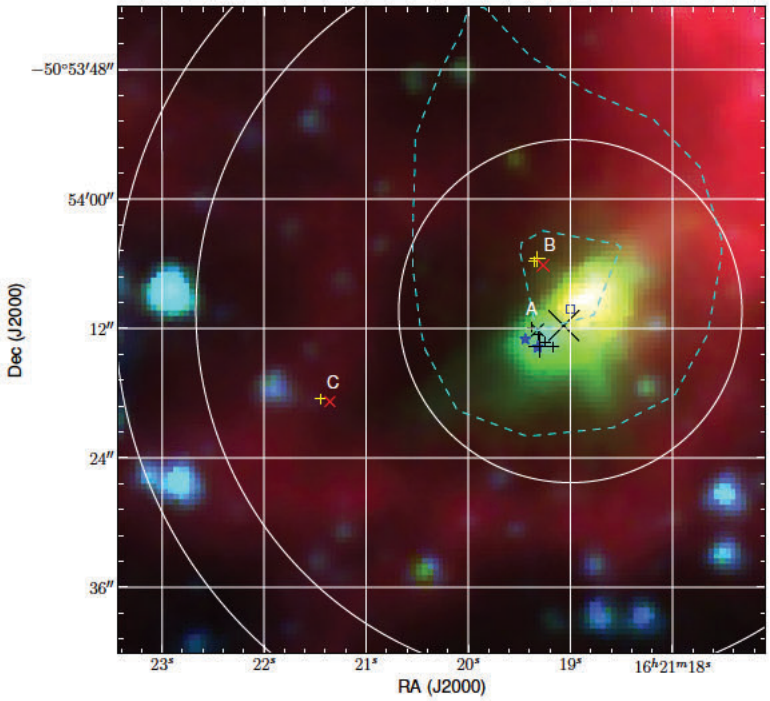

G332.94-0.69

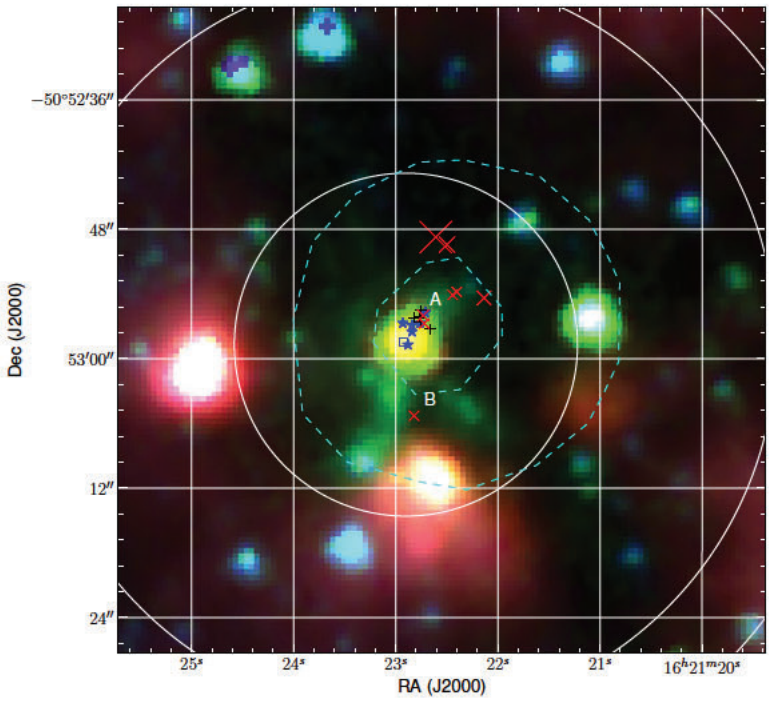

G332.96-0.68

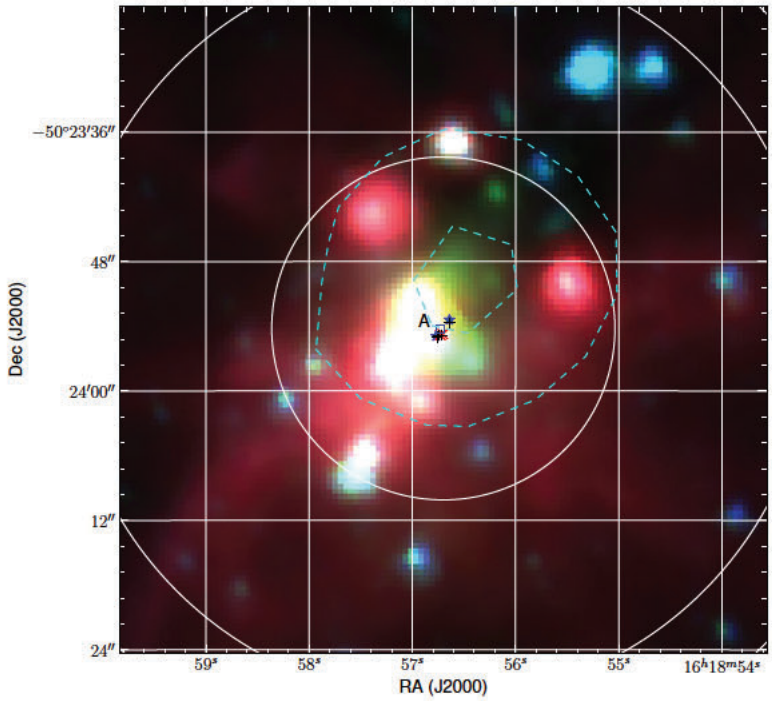

G333.03-0.06

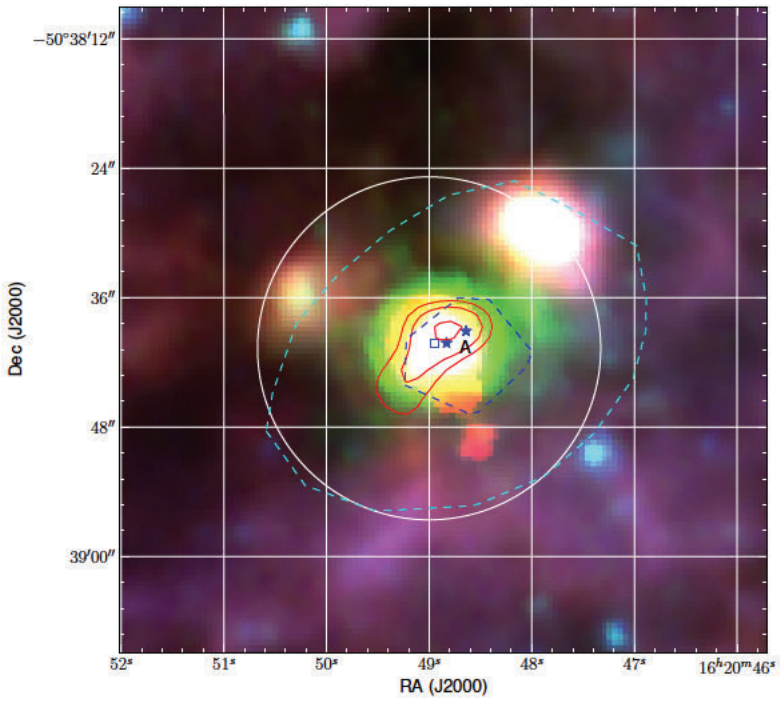

G333.07-0.45

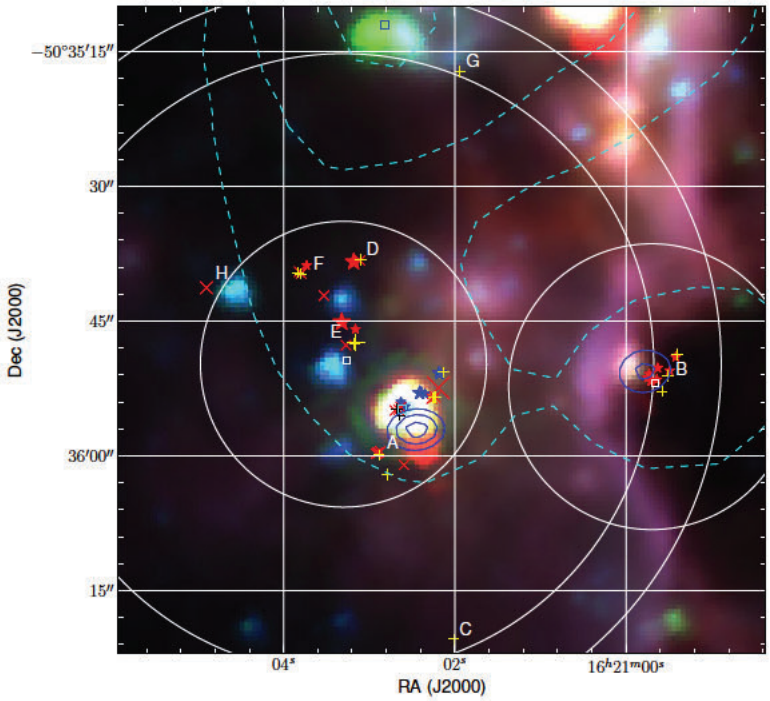

G333.13-0.44

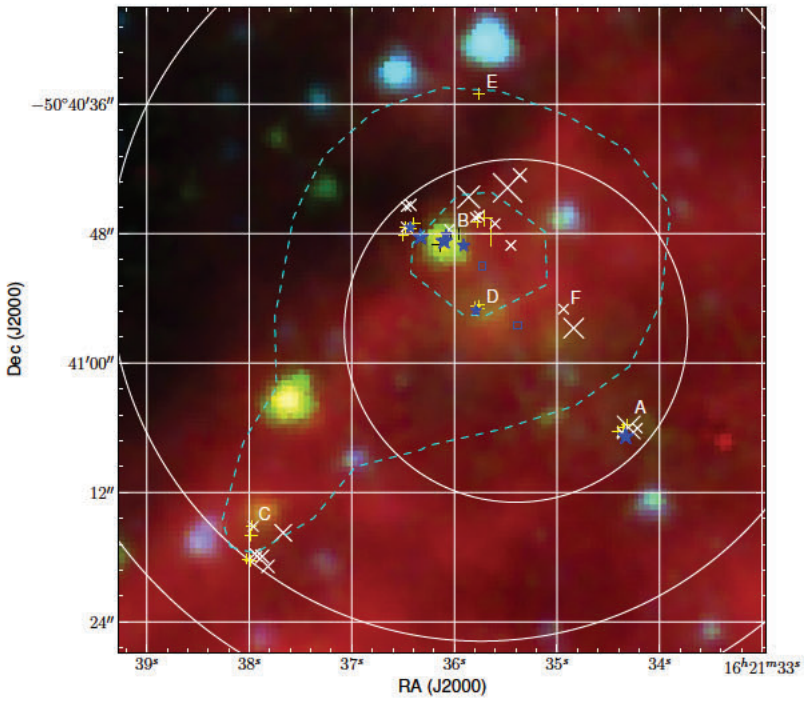

G333.13-0.56

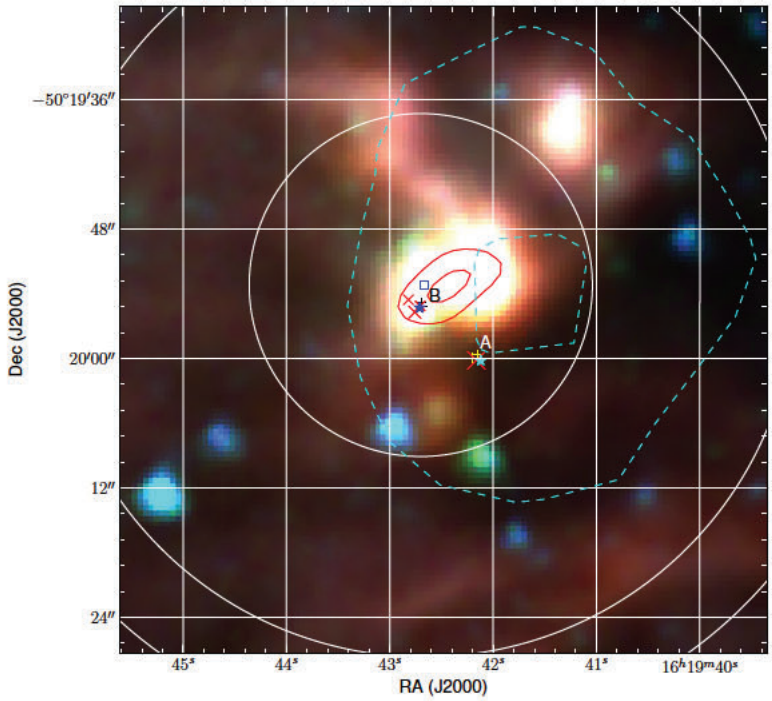

G333.16-0.10

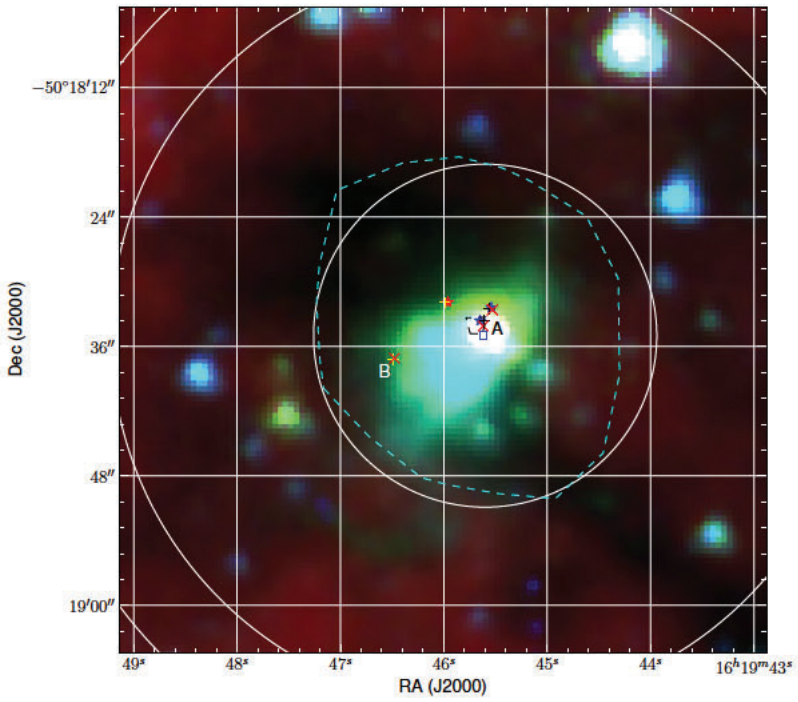

G333.18-0.09

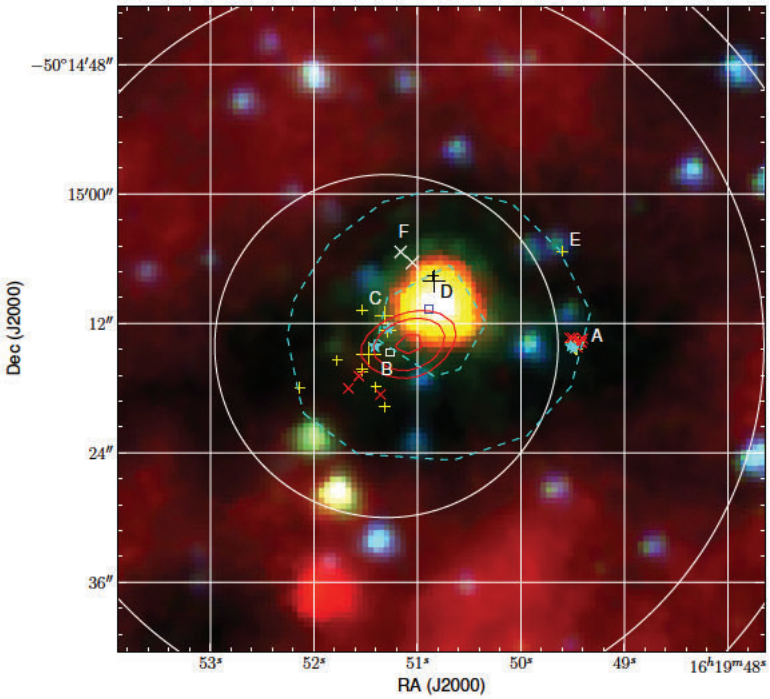

G333.23-0.06

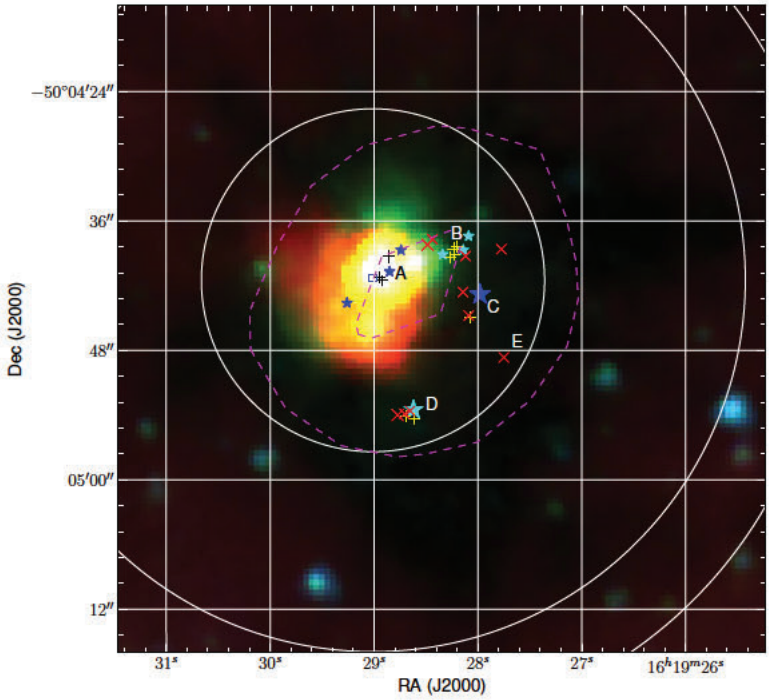

G333.32+0.11

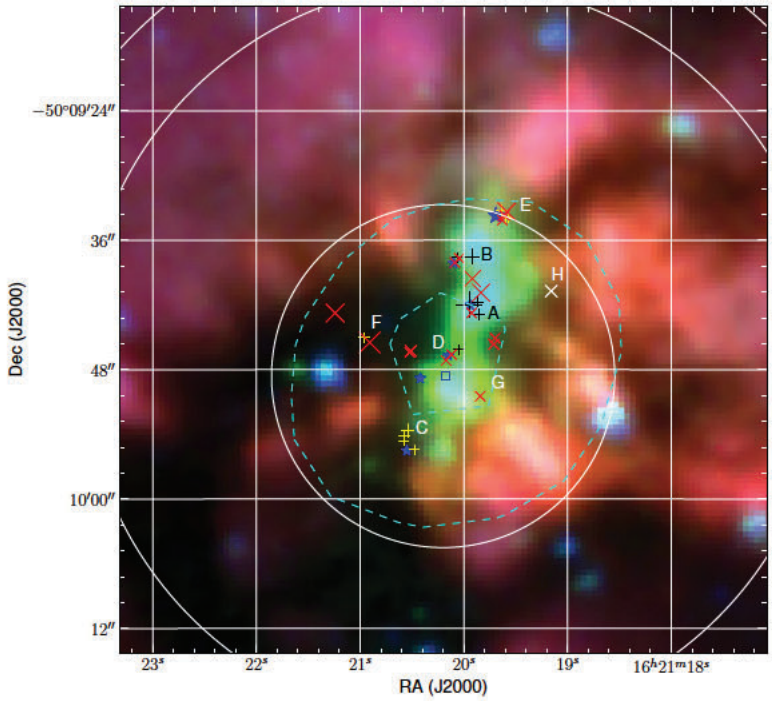

G333.47-0.16

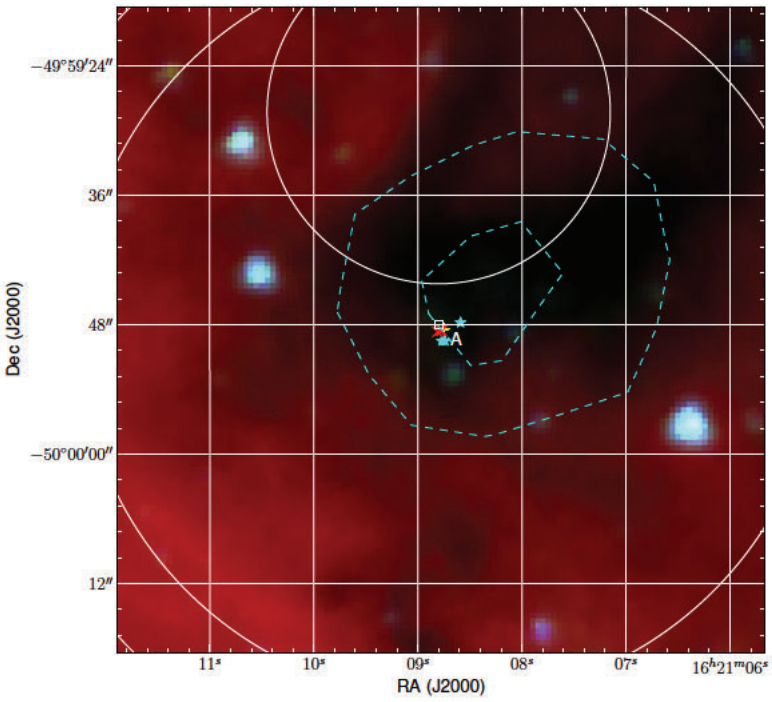

G333.56-0.02

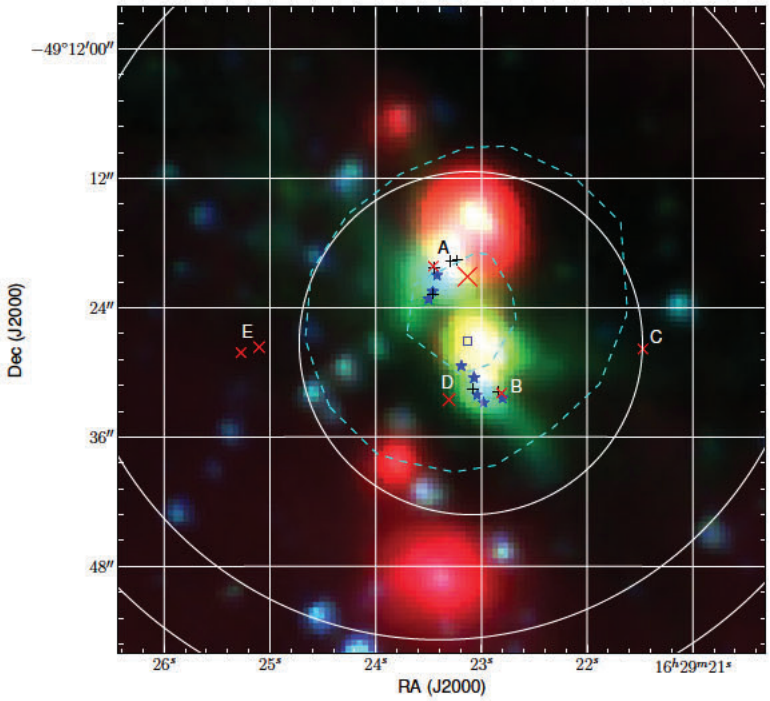

G335.06-0.43

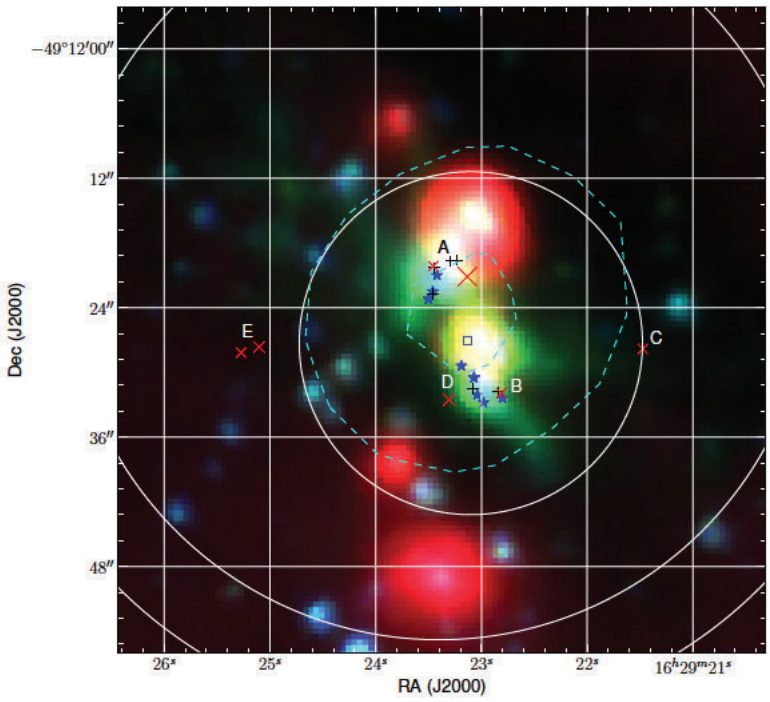

G335.06-0.43

A.2 95-GHz maser spectra

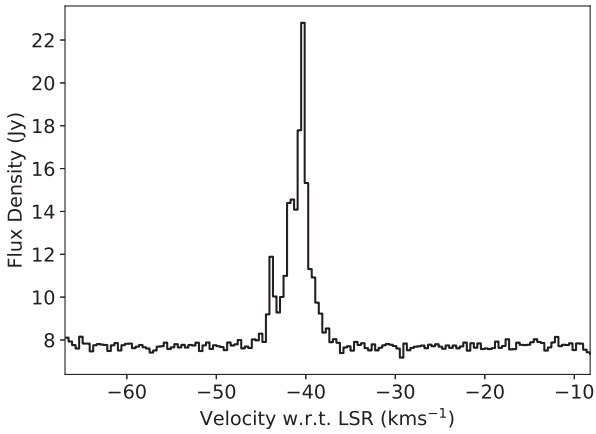

G326.475+0.70

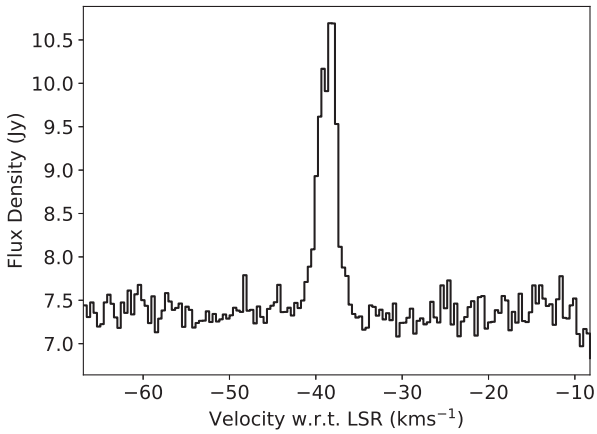

G326.641+0.61

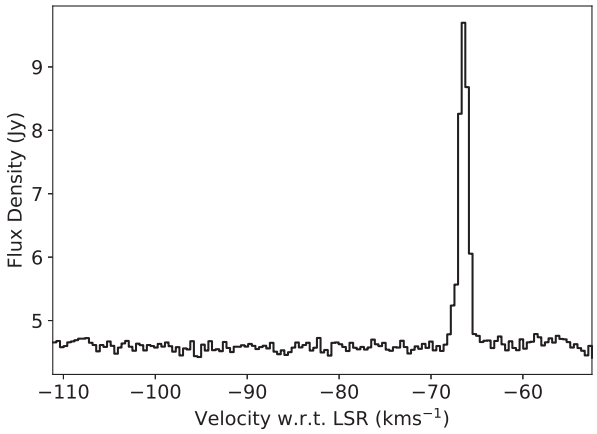

G326.859-0.67

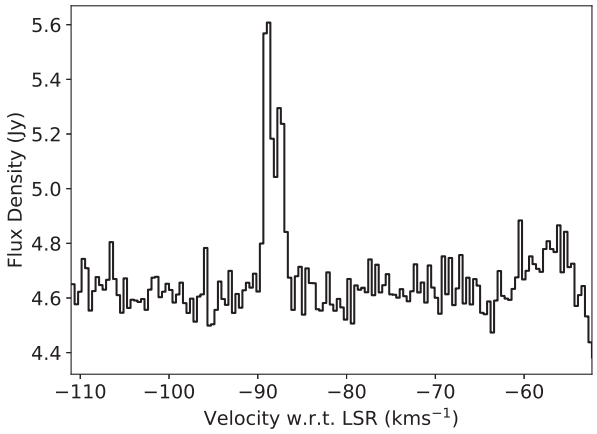

G327.392+0.19

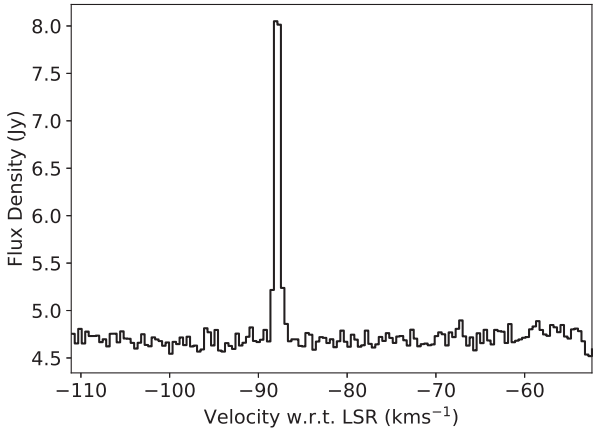

G327.618-0.11

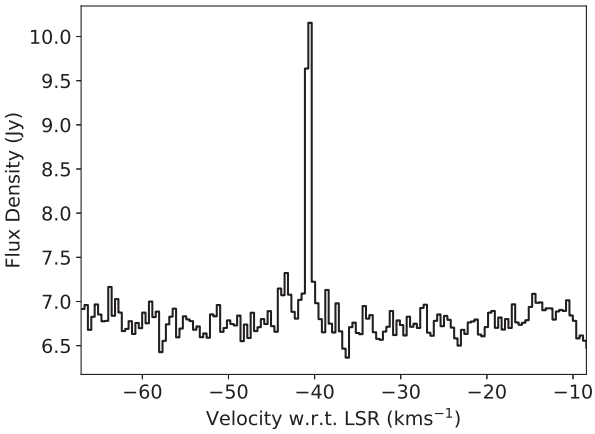

G328.237-0.54

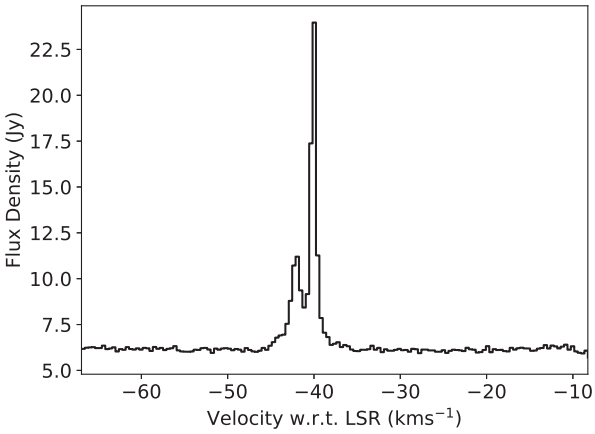

G328.809+0.63

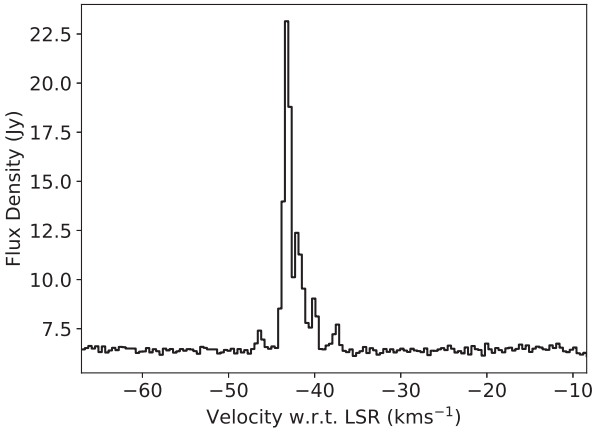

G329.029-0.20

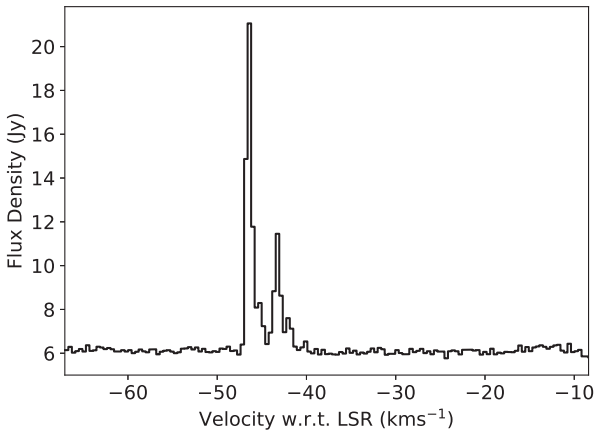

G329.031-0.19

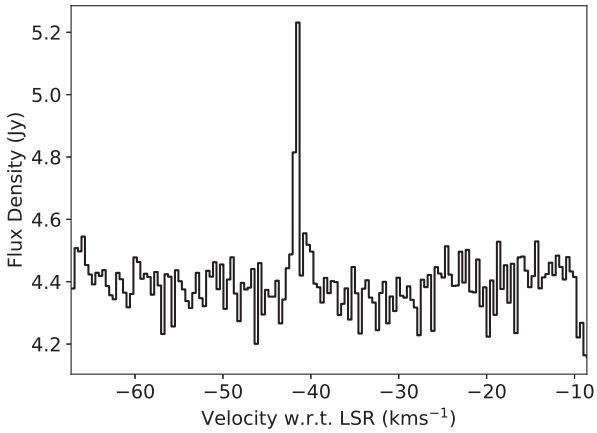

G329.066-0.30

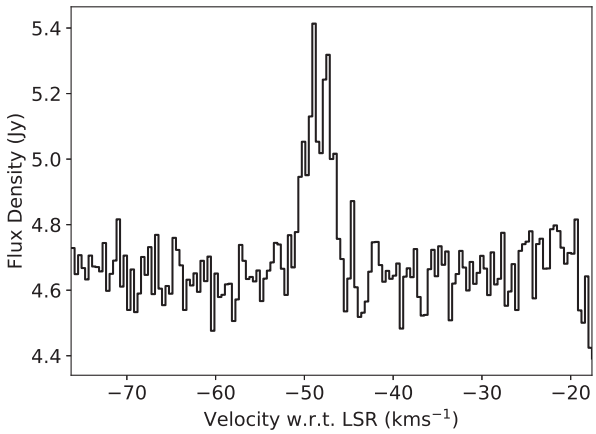

G329.183-0.31

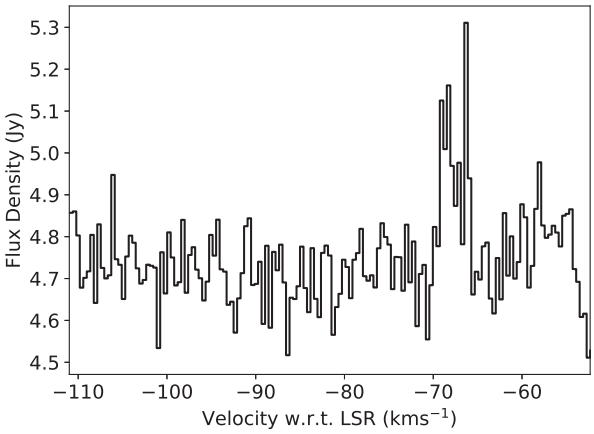

G329.469+0.50

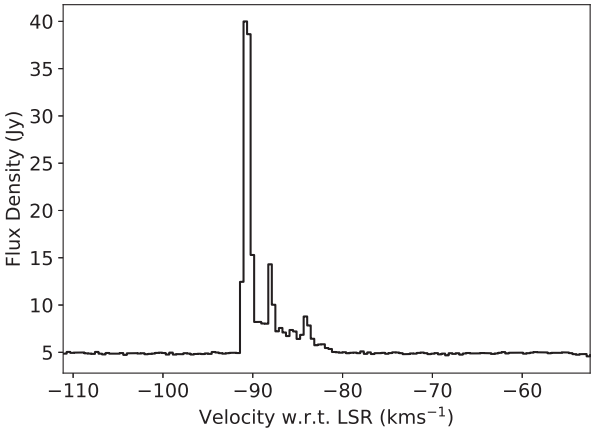

G331.132-0.24

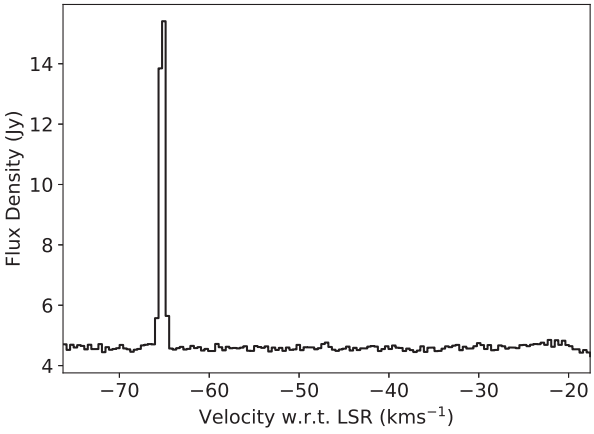

G331.342-0.34

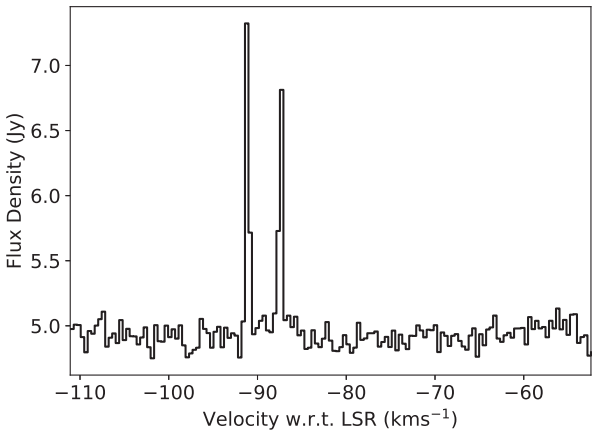

G331.442-0.18

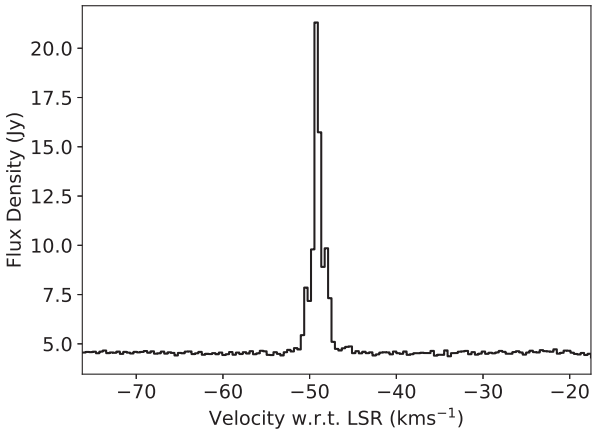

G332.295-0.09

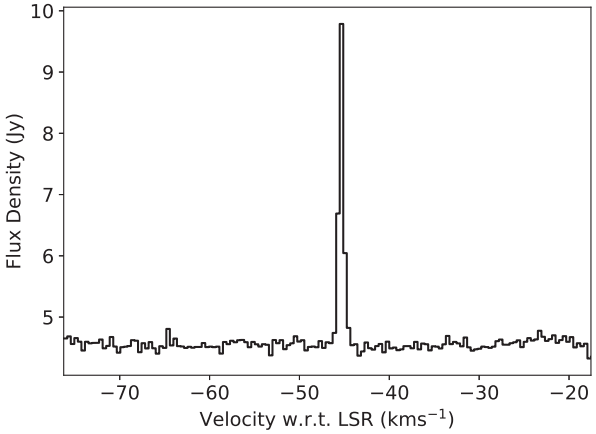

G332.604-0.16

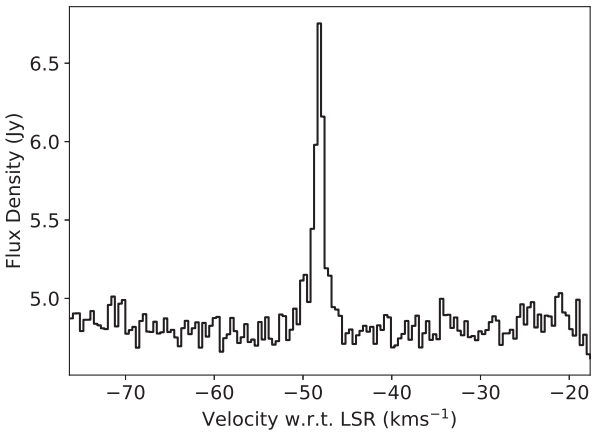

G332.942-0.68

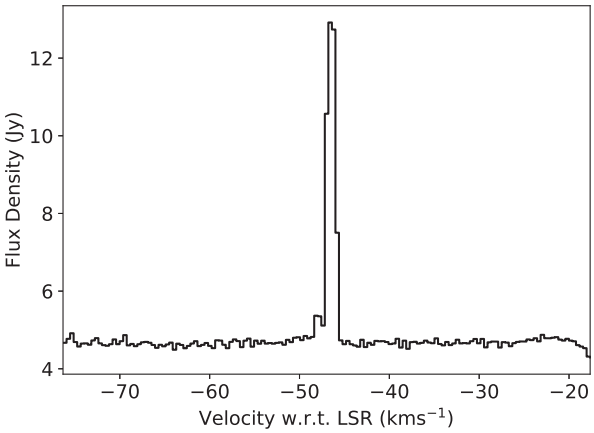

G332.963-0.67

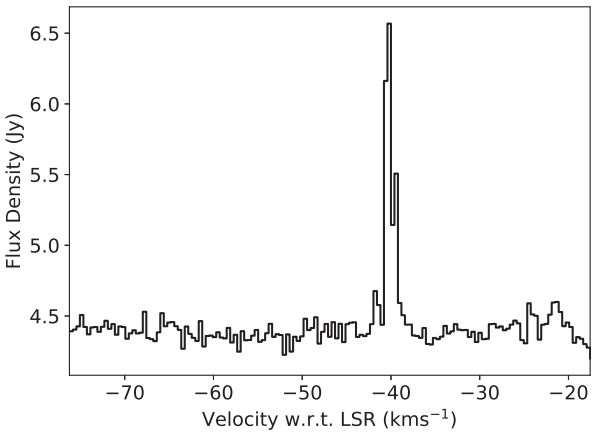

G333.029-0.06

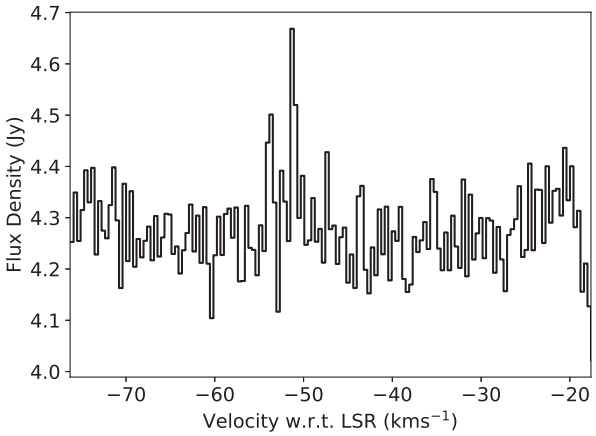

G333.068-0.44

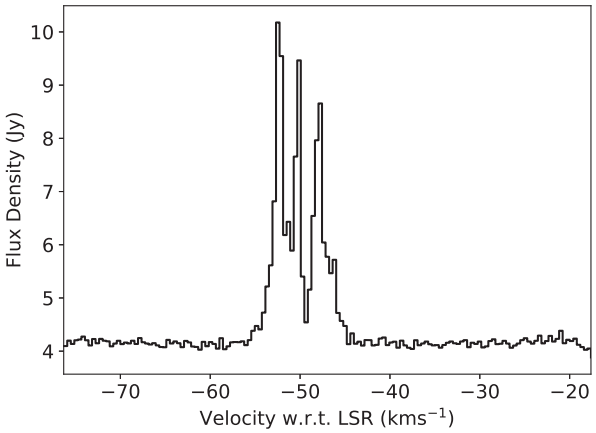

G333.121-0.43

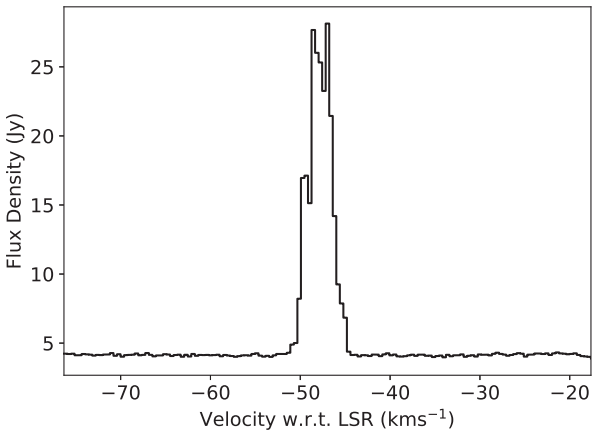

G333.128-0.44

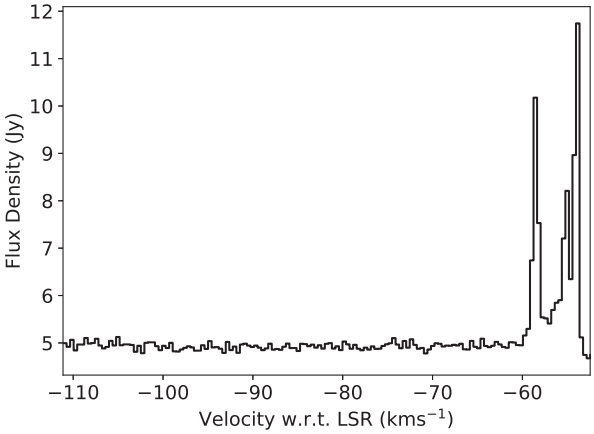

G333.128-0.56

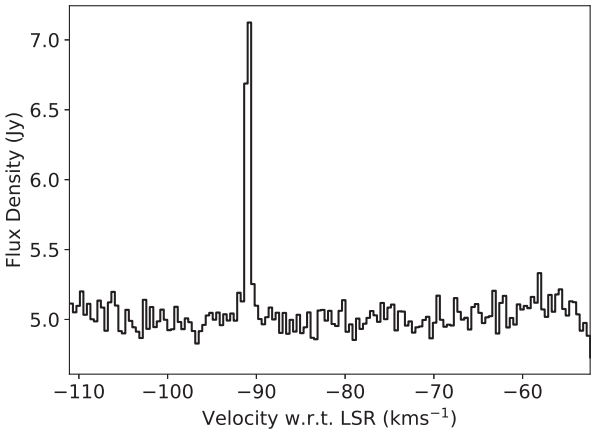

G333.163-0.10

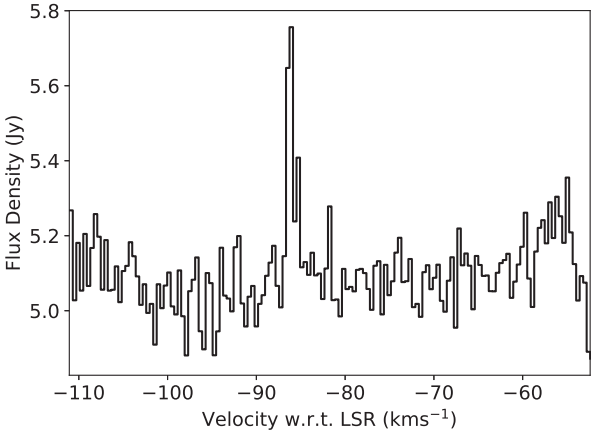

G333.184-0.09

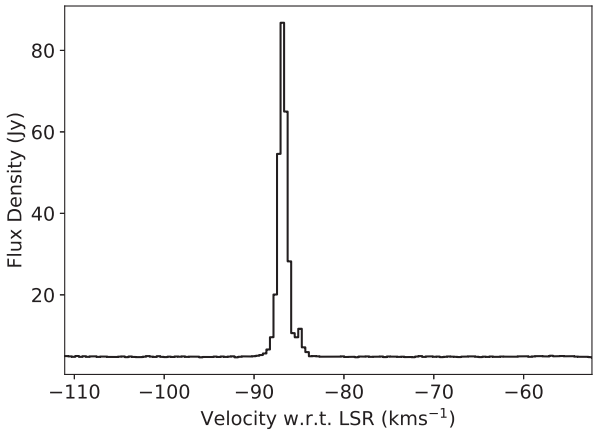

G333.234-0.06

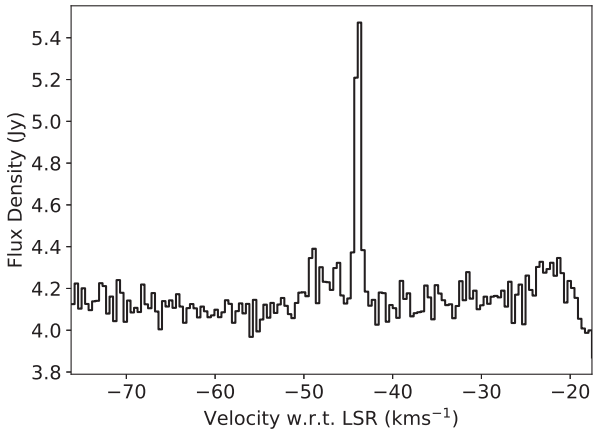

G333.315+0.10

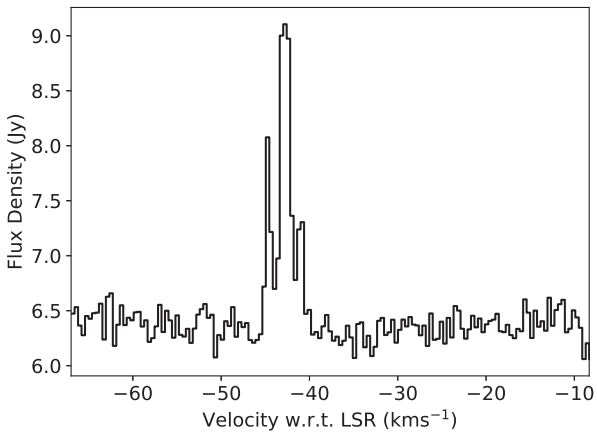

G333.466-0.16

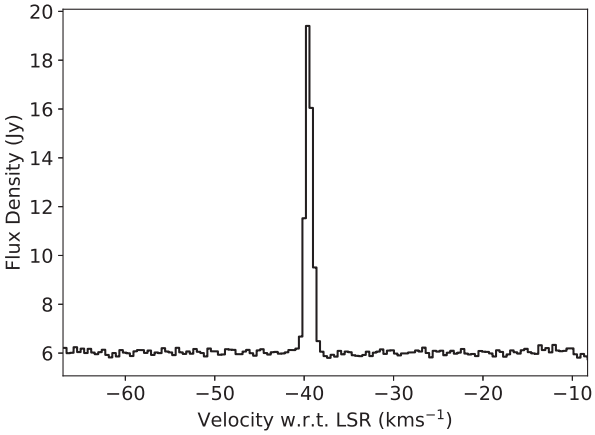

G333.562-0.02

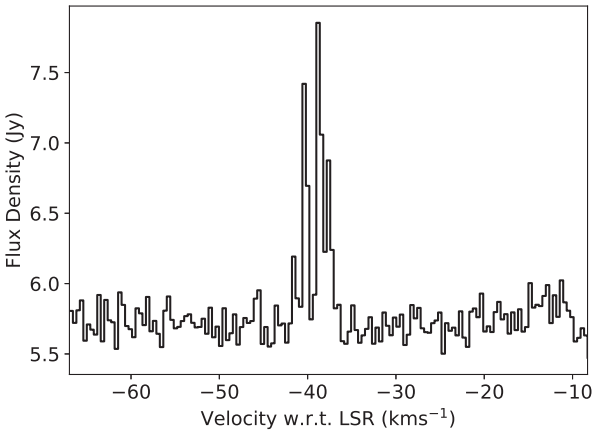

G335.060-0.42

BIBLIOGRAPHY

Anand, G. S., Tully, R. B., Rizzi, L., & Karachentsev, I. D. 2019, Astrophysical Journal, Letters to the Editor, 872, L4

Argon, A. L., Reid, M. J., & Menten, K. M. 2002, in IAU Symposium, Vol. 206, Cosmic Masers: From Proto-Stars to Black Holes, ed. V. Migenes & M. J. Reid, 367

Ashby, M. L. N., Mahajan, S., Smith, H. A., et al. 2011, Publications of the ASP, 123, 1011

Baan, W. A., Wood, P. A. D., & Haschick, A. D. 1982, Astrophysical Journal, Letters to the Editor, 260, L49

Baart, E. E., & Cohen, R. J. 1985, Monthly Notices of the RAS, 213, 641

Bagdonaite, J., Jansen, P., Henkel, C., et al. 2013, Science, 339, 46

Barrett, A. H., Schwartz, P. R., & Waters, J. W. 1971, Astrophysical Journal, Letters to the Editor, 168, L101

Batrla, W., Matthews, H. E., Menten, K. M., & Walmsley, C. M. 1987, Nature, 326, 49

Beasley, A. J., Ellingsen, S. P., Claussen, M. J., & Wilcots, E. 1996, Astrophysical Journal, 459, 600

Bendo, G. J., Beswick, R. J., D'Cruze, M. J., et al. 2015, Monthly Notices of the RAS, 450, L80

Boboltz, D. A., & Claussen, M. J. 2004, Astrophysical Journal, 608, 480

Boker, T., Forster-Schreiber, N. M., & Genzel, R. 1997, Astronomical Journal, 114, 1883

Bolatto, A. D., Warren, S. R., Leroy, A. K., et al. 2013, Nature, 499, 450

Braatz, J. A., & Gugliucci, N. E. 2008, Astrophysical Journal, 678, 96

Breen, S., Ellingsen, S., Caswell, J., et al. 2012a, Monthly Notices of the RAS, 426, 2189

Breen, S. L., Ellingsen, S. P., Caswell, J. L., et al. 2011, Astrophysical Journal, 733, 80

—. 2012b, Monthly Notices of the RAS, 421, 1703

Breen, S. L., Ellingsen, S. P., Caswell, J. L., & Lewis, B. E. 2010, Monthly Notices of the RAS, 401, 2219

Breen, S. L., Ellingsen, S. P., Contreras, Y., et al. 2013, Monthly Notices of the RAS, 435, 524

Breen, S. L., Sobolev, A. M., Kaczmarek, J. F., et al. 2019, Astrophysical Journal, Letters to the Editor, 876, L25

Breen, S. L., Fuller, G. A., Caswell, J. L., et al. 2015, Monthly Notices of the RAS, 450, 4109

Brock, D., Joy, M., Lester, D. F., Harvey, P. M., & Ellis, H. Benton, J. 1988, Astrophysical Journal, 329, 208

Brogan, C. L., Goss, W. M., Hunter, T. R., et al. 2013, Astrophysical Journal, 771, 91

Brown, P. D., Charnley, S. B., & Millar, T. J. 1988, Monthly Notices of the RAS, 231, 409

Buhl, D., Snyder, L. E., Lovas, F. J., & Johnson, D. R. 1974, Astrophysical Journal, Letters to the Editor, 192, L97

Carlstrom, J. E., Jackson, J. M., Ho, P. T. P., & Turner, J. L. 1990, in NASA Conference Publication, ed. D. J. Hollenbach & J. Thronson, Harley A., Vol. 3084, 337

Caswell, J. L. 1997, Monthly Notices of the RAS, 289, 203

—. 1998, Monthly Notices of the RAS, 297, 215

Caswell, J. L., & Haynes, R. F. 1987, Australian Journal of Physics, 40, 215

Caswell, J. L., Fuller, G. A., Green, J. A., et al. 2010, Monthly Notices of the RAS, 404, 1029

—. 2011, Monthly Notices of the RAS, 417, 1964

Chen, X., Ellingsen, S. P., Baan, W. A., et al. 2015, Astrophysical Journal, Letters to the Editor, 800, L2

Chen, X., Ellingsen, S. P., Shen, Z.-Q., et al. 2018, Astrophysical Journal, Letters to the Editor, 856, L35

Chen, X., Ellingsen, S. P., Shen, Z.-Q., Titmarsh, A., & Gan, C.-G. 2011, Astrophysical Journal, Supplement Series, 196, 9

Chen, X., Ellingsen, S. P., Zhang, J.-S., et al. 2016, Monthly Notices of the RAS, 459, 357

Cheung, A. C., Rank, D. M., Townes, C. H., Thornton, D. D., & Welch, W. J. 1969, Nature, 221, 626

Churchwell, E., Witzel, A., Huchtmeier, W., et al. 1977, Astronomy and Astrophysics, 54, 969

Claussen, M. J., Diamond, P. J., Braatz, J. A., Wilson, A. S., & Henkel, C. 1998, Astrophysical Journal, Letters to the Editor, 500, L129

Claussen, M. J., Heiligman, G. M., & Lo, K. Y. 1984, Nature, 310, 298

Claussen, M. J., & Lo, K. Y. 1986, Astrophysical Journal, 308, 592

Cragg, D. M., Johns, K. P., Godfrey, P. D., & Brown, R. D. 1992, Monthly Notices of the RAS, 259, 203

Cragg, D. M., Sobolev, A. M., Ellingsen, S. P., et al. 2001, Monthly Notices of the RAS, 323, 939

Cragg, D. M., Sobolev, A. M., & Godfrey, P. D. 2002, Monthly Notices of the RAS, 331, 521

—. 2005, Monthly Notices of the RAS, 360, 533

Cunningham, M. R., & Whiteoak, J. B. 2005, Monthly Notices of the RAS, 364, 37

Cyganowski, C. J., Brogan, C. L., Hunter, T. R., & Churchwell, E. 2009, Astrophysical Journal, 702, 1615

Cyganowski, C. J., Brogan, C. L., Hunter, T. R., et al. 2012, ArXiv e-prints, arXiv:1210.3366

Dahlem, M., Golla, G., Whiteoak, J. B., et al. 1993, Astronomy and Astrophysics, 270, 29

Dalcanton, J. J., Williams, B. F., Seth, A. C., et al. 2009, Astrophysical Journal, Supplement Series, 183, 67

Darling, J., & Giovanelli, R. 2002, Astrophysical Journal, 572, 810

de Vaucouleurs, G., de Vaucouleurs, A., Corwin, Jr., H. G., et al. 1991, Third Reference Catalogue of Bright Galaxies. Volume I: Explanations and references. Volume II: Data for galaxies between 0^h and 12^h. Volume III: Data for galaxies between 12^h and 24^h.

Deguchi, S. 1977, Publications of the ASJ, 29, 669

Dos Santos, P. M., & Lepine, J. R. D. 1979, Nature, 278, 34

Edris, K. A., Fuller, G. A., & Cohen, R. J. 2007, Astronomy and Astrophysics, 465, 865

Eisner, B. A., Ott, J., Meier, D. S., & Cannon, J. M. 2019, Astrophysical Journal, 882, 95

Elitzur, M. 1982, Reviews of Modern Physics, 54, 1225

—. 1992, Annual Review of Astronomy and Astrophysics, 30, 75

Elitzur, M., & de Jong, T. 1978, Astronomy and Astrophysics, 67, 323

Ellingsen, S., Voronkov, M., & Breen, S. 2011a, Physical Review Letters, 107, 270801

Ellingsen, S. P., Breen, S. L., Caswell, J. L., Quinn, L. J., & Fuller, G. A. 2010, Monthly Notices of the RAS, 404, 779

Ellingsen, S. P., Breen, S. L., Sobolev, A. M., et al. 2011b, Astrophysical Journal, 742, 109

Ellingsen, S. P., Chen, X., Breen, S. L., & Qiao, H.-H. 2017a, Monthly Notices of the RAS, 472, 604

Ellingsen, S. P., Chen, X., Breen, S. L., & Qiao, H.-h. 2017b, Astrophysical Journal, Letters to the Editor, 841, L14

Ellingsen, S. P., Chen, X., Qiao, H.-H., et al. 2014, Astrophysical Journal, Letters to the Editor, 790, L28

Ellingsen, S. P., Norris, R. P., Whiteoak, J. B., et al. 1994, Monthly Notices of the RAS, 267, 510

Ellingsen, S. P., Shabala, S. S., & Kurtz, S. E. 2005, Monthly Notices of the RAS, 357, 1003

Ellingsen, S. P., Voronkov, M. A., Breen, S. L., & Lovell, J. E. J. 2012, Astrophysical Journal, Letters to the Editor, 747, L7

Felli, M., Brand, J., Cesaroni, R., et al. 2007, Astronomy and Astrophysics, 476, 373

Fish, V. L., & Reid, M. J. 2006, Astrophysical Journal, Supplement Series, 164, 99

Forster, J. R., & Caswell, J. L. 1989, Astronomy and Astrophysics, 213, 339

Frayer, D. T., Seaquist, E. R., & Frail, D. A. 1998, Astronomical Journal, 115, 559

Furuya, R. S. 2003, in Astronomical Society of the Pacific Conference Series, Vol. 287, Galactic Star Formation Across the Stellar Mass Spectrum, ed. J. M. De Buizer & N. S. van der Bliek, 367–372

Gallimore, J. F., Henkel, C., Baum, S. A., et al. 2001, Astrophysical Journal, 556, 694

Garay, G., Mardones, D., Rodríguez, L. F., Caselli, P., & Bourke, T. L. 2002, Astrophysical Journal, 567, 980

García-Burillo, S., Martín-Pintado, J., Fuente, A., & Neri, R. 2000, Astronomy and Astrophysics, 355, 499

Gardner, F. F., & Whiteoak, J. B. 1975, Monthly Notices of the RAS, 173, 77P

—. 1982, Monthly Notices of the RAS, 201, 13P

Gorski, M., Ott, J., Rand, R., et al. 2018, ArXiv e-prints, arXiv:1804.00578

—. 2017, Astrophysical Journal, 842, 124

Gorski, M. D., Ott, J., Rand, R., et al. 2019, Monthly Notices of the RAS, 483, 5434

Gray, M. 2012, Maser Sources in Astrophysics

Gray, M. D., Howe, D. A., & Lewis, B. M. 2005, Monthly Notices of the Royal Astronomical Society, 364, 783

Green, C. E., Cunningham, M. R., Green, J. A., et al. 2016, Monthly Notices of the RAS, 457, 2470

Green, J. A., Caswell, J. L., Fuller, G. A., et al. 2008, Monthly Notices of the RAS, 385, 948

—. 2009, Monthly Notices of the RAS, 392, 783

—. 2010, Monthly Notices of the RAS, 409, 913

—. 2012, Monthly Notices of the RAS, 420, 3108

Greenhill, L. J., Colomer, F., Moran, J. M., et al. 1995a, Astrophysical Journal, 449, 365

Greenhill, L. J., Henkel, C., Becker, R., Wilson, T. L., & Wouterloot, J. G. A. 1995b, Astronomy and Astrophysics, 304, 21

Greenhill, L. J., Moran, J. M., & Herrnstein, J. R. 1997, Astrophysical Journal, Letters to the Editor, 481, L23

Günthardt, G. I., Agüero, M. P., Camperi, J. A., et al. 2015, Astronomical Journal, 150, 139

Hagiwara, Y., Horiuchi, S., Doi, A., Miyoshi, M., & Edwards, P. G. 2016, Astrophysical Journal, 827, 69

Hartquist, T. W., Menten, K. M., Lepp, S., & Dalgarno, A. 1995, Monthly Notices of the RAS, 272, 184

Heckman, T. M., Armus, L., & Miley, G. K. 1990, Astrophysical Journal, Supplement Series, 74, 833

Henkel, C., Tarchi, A., Menten, K. M., & Peck, A. B. 2004, Astronomy and Astrophysics, 414, 117

Henkel, C., Muehle, S., Bendo, G., et al. 2018, ArXiv e-prints, arXiv:1802.09852

Hofner, P., Baan, W. A., & Takano, S. 2006, Astronomical Journal, 131, 2074

Hollenbach, D., Elitzur, M., & McKee, C. F. 2013, ArXiv e-prints, arXiv:1306.5276

Huchtmeier, W. K., Witzel, A., Kuehr, H., Pauliny-Toth, I. I., & Roland, J. 1978, Astronomy and Astrophysics, 64, L21

Humire, P., Henkel, C., Gong, Y., et al. 2019, arXiv e-prints, arXiv:1911.06776

Humphreys, E. M. L., Vlemmings, W. H. T., Impellizzeri, C. M. V., et al. 2016, Astronomy and Astrophysics, 592, L13

Hüttemeister, S., Mauersberger, R., & Henkel, C. 1997, Astronomy and Astrophysics, 326, 59

Huttemeister, S., Wilson, T. L., Henkel, C., & Mauersberger, R. 1993, Astronomy and Astrophysics, 276, 445

Immer, K., Menten, K. M., Schuller, F., & Lis, D. C. 2012, Astronomy and Astrophysics, 548, A120

Impellizzeri, C. M. V., Henkel, C., Roy, A. L., & Menten, K. M. 2008, Astronomy and Astrophysics, 484, L43

Iodice, E., Arnaboldi, M., Rejkuba, M., et al. 2014, Astronomy and Astrophysics, 567, A86

Ishizuki, S., Kawabe, R., Ishiguro, M., Okumura, S. K., & Morita, K.-I. 1990, Nature, 344, 224

Iwasawa, K., Koyama, K., Awaki, H., et al. 1993, Astrophysical Journal, 409, 155

Jansen, P., Xu, L.-H., Kleiner, I., Ubachs, W., & Bethlem, H. L. 2011, Physical Review Letters, 106, 100801

Jones, P. A., Burton, M. G., Cunningham, M. R., Tothill, N. F. H., & Walsh, A. J. 2013, Monthly Notices of the RAS, 433, 221

Jordan, C. H., Walsh, A. J., Lowe, V., et al. 2015, Monthly Notices of the RAS, 448, 2344

Kanekar, N. 2011, Astrophysical Journal, Letters to the Editor, 728, L12

Karachentsev, I. D., Makarov, D. I., & Kaisina, E. I. 2013, The Astronomical Journal, 145, 101

Krieger, N., Bolatto, A. D., Walter, F., et al. 2019, Astrophysical Journal, 881, 43

Kurtz, S., Hofner, P., & Álvarez, C. V. 2004, Astrophysical Journal, Supplement Series, 155, 149

Leroy, A. K., Bolatto, A. D., Ostriker, E. C., et al. 2015, Astrophysical Journal, 801, 25

—. 2018, Astrophysical Journal, 869, 126

Leurini, S., Menten, K. M., & Walmsley, C. M. 2016, Astronomy and Astrophysics, 592, A31

Levshakov, S. A., Kozlov, M. G., & Reimers, D. 2011, Astrophysical Journal, 738, 26

Lo, K. Y. 2005, Annual Review of Astronomy and Astrophysics, 43, 625

Lockett, P., Gauthier, E., & Elitzur, M. 1999, Astrophysical Journal, 511, 235

Martín, S., Mauersberger, R., Martín-Pintado, J., Henkel, C., & García-Burillo, S. 2006, Astrophysical Journal, Supplement Series, 164, 450

McCarthy, T. P., Ellingsen, S. P., Breen, S. L., et al. 2018a, Monthly Notices of the RAS, 480, 4578

McCarthy, T. P., Ellingsen, S. P., Breen, S. L., Voronkov, M. A., & Chen, X. 2018b, Astrophysical Journal, Letters to the Editor, 867, L4

McCarthy, T. P., Ellingsen, S. P., Breen, S. L., et al. 2020, Monthly Notices of the RAS, 491, 4642

McCarthy, T. P., Ellingsen, S. P., Chen, X., et al. 2017, Astrophysical Journal, 846, 156

McCoy, M., Ott, J., Meier, D. S., et al. 2017, Astrophysical Journal, 851, 76

McEwen, B. C., Pihlström, Y. M., & Sjouwerman, L. O. 2014, Astrophysical Journal, 793, 133

Meier, D. S., & Turner, J. L. 2005, Astrophysical Journal, 618, 259

—. 2012, Astrophysical Journal, 755, 104

Meier, D. S., Walter, F., Bolatto, A. D., et al. 2015, Astrophysical Journal, 801, 63

Menten, K. M. 1991a, in Astronomical Society of the Pacific Conference Series, Vol. 16, Atoms, Ions and Molecules: New Results in Spectral Line Astrophysics, ed. A. D. Haschick & P. T. P. Ho, 119–136

Menten, K. M. 1991b, Astrophysical Journal, Letters to the Editor, 380, L75

Miyoshi, M., Moran, J., Herrnstein, J., et al. 1995, Nature, 373, 127

Monje, R. R., Lord, S., Falgarone, E., et al. 2014, Astrophysical Journal, 785, 22

Morimoto, M., Ohishi, M., & Kanzawa, T. 1985, Astrophysical Journal, Letters to the Editor, 288, L11

Muller, S., Beelen, A., Guélin, M., et al. 2011, Astronomy and Astrophysics, 535, A103

Nakai, N. 1989, Publications of the ASJ, 41, 1107

Nguyen-Q-Rieu, Mebold, U., Winnberg, A., Guibert, J., & Booth, R. 1976, Astronomy and Astrophysics, 52, 467

Norris, R. P. 1985, Monthly Notices of the RAS, 216, 701

Ott, J., Weiss, A., Henkel, C., & Walter, F. 2005, Astrophysical Journal, 629, 767

Ott, M., Whiteoak, J. B., Henkel, C., & Wielebinski, R. 2001, Astronomy and Astrophysics, 372, 463

Paglione, T. A. D., Yam, O., Tosaki, T., & Jackson, J. M. 2004, Astrophysical Journal, 611, 835

Parra, R., Conway, J., & Elitzur, M. 2005, Astrophysics and Space Science, 295, 325

Pesce, D. W., Braatz, J. A., & Impellizzeri, C. M. V. 2016, Astrophysical Journal, 827, 68

Puche, D., Carignan, C., & van Gorkom, J. H. 1991, Astronomical Journal, 101, 456

Roberts, J. F., Rawlings, J. M. C., & Stace, H. A. W. 2007, in Molecules in Space and Laboratory, 111

Salter, C. J., Catinella, B., Ghosh, T., et al. 2007, in American Astronomical Society Meeting Abstracts, Vol. 211, 141.06

Scalise, E., J., & Lepine, J. R. D. 1978, Astronomy and Astrophysics, 65, L7

Schinnerer, E., Böker, T., Emsellem, E., & Lisenfeld, U. 2006, Astrophysical Journal, 649, 181

Schwartz, P. R., Zuckerman, B., & Bologna, J. M. 1982, Astrophysical Journal, Letters to the Editor, 256, L55

Sinclair, M. W., Carrad, G. J., Caswell, J. L., Norris, R. P., & Whiteoak, J. B. 1992, Monthly Notices of the RAS, 256, 33P

Sjouwerman, L. O., Murray, C. E., Pihlström, Y. M., Fish, V. L., & Araya, E. D. 2010, Astrophysical Journal, Letters to the Editor, 724, L158

Slysh, V. I., Kalenskii, S. V., Valtts, I. E., & Otrupcek, R. 1994, Monthly Notices of the RAS, 268, 464

Snyder, L. E., & Buhl, D. 1974, Astrophysical Journal, Letters to the Editor, 189, L31

Sobolev, A. M., Cragg, D. M., & Godfrey, P. D. 1997, Astronomy and Astrophysics, 324, 211

Sutton, E. C., Sobolev, A. M., Ellingsen, S. P., et al. 2001, Astrophysical Journal, 554, 173

Telesco, C. M., & Harper, D. A. 1980, Astrophysical Journal, 235, 392

Tielens, A. G. G. M., & Whittet, D. C. B. 1997, in IAU Symposium, ed. E. F. van Dishoeck, Vol. 178, 45

Torrelles, J. M., Patel, N. A., Gómez, J. F., & Anglada, G. 2002, in Revista Mexicana de Astronomia y Astrofisica Conference Series, ed. W. J. Henney, W. Steffen, L. Binette, & A. Raga, Vol. 13, 108–113

Torstensson, K. J. E., van der Tak, F. F. S., van Langevelde, H. J., Kristensen, L. E., & Vlemmings, W. H. T. 2011, Astronomy and Astrophysics, 529, A32

Tully, R. B., Courtois, H. M., Dolphin, A. E., et al. 2013, Astronomical Journal, 146, 86

Turner, B. E. 1985, Astrophysical Journal, 299, 312

Val'tts, I. E., Ellingsen, S. P., Slysh, V. I., et al. 2000, Monthly Notices of the RAS, 317, 315

Van Der Walt, D. J., Goedhart, S., & Gaylard, M. J. 2009, Monthly Notices of the Royal Astronomical Society, 398, 961

van Dishoeck, E. F., & Hogerheijde, M. R. 1999, in NATO Advanced Science Institutes (ASI) Series C, Vol. 540, NATO Advanced Science Institutes (ASI) Series C, ed. C. J. Lada & N. D. Kylafis, 97

Voronkov, M. A., Brooks, K. J., Sobolev, A. M., et al. 2006, Monthly Notices of the RAS, 373, 411

Voronkov, M. A., Caswell, J. L., Britton, T. R., et al. 2010a, Monthly Notices of the RAS, 408, 133

Voronkov, M. A., Caswell, J. L., Ellingsen, S. P., et al. 2012, in IAU Symposium, Vol. 287, Cosmic Masers - from OH to H0, ed. R. S. Booth, W. H. T. Vlemmings, & E. M. L. Humphreys, 433–440

Voronkov, M. A., Caswell, J. L., Ellingsen, S. P., Green, J. A., & Breen, S. L. 2014, Monthly Notices of the RAS, 439, 2584

Voronkov, M. A., Caswell, J. L., Ellingsen, S. P., & Sobolev, A. M. 2010b, Monthly Notices of the RAS, 405, 2471

Voronkov, M. A., Sobolev, A. M., Ellingsen, S. P., & Ostrovskii, A. B. 2005, Monthly Notices of the RAS, 362, 995

Walsh, A. J., Burton, M. G., Hyland, A. R., & Robinson, G. 1998, Monthly Notices of the RAS, 301, 640

Wang, J., Zhang, J., Gao, Y., et al. 2014, Nature Communications, 5, 5449

Watanabe, N., & Kouchi, A. 2002, Astrophysical Journal, Letters to the Editor, 571, L173

Weaver, H., Williams, D. R. W., Dieter, N. H., & Lum, W. T. 1965, Nature, 208, 29

Wilson, T. L., Walmsley, C. M., Menten, K. M., & Hermsen, W. 1985, Astronomy and Astrophysics, 147, L19

Wilson, T. L., Walmsley, C. M., Snyder, L. E., & Jewell, P. R. 1984, Astronomy and Astrophysics, 134, L7

Yusef-Zadeh, F., Cotton, W., Viti, S., Wardle, M., & Royster, M. 2013a, Astrophysical Journal, Letters to the Editor, 764, L19

Yusef-Zadeh, F., Hewitt, J. W., Wardle, M., et al. 2013b, Astrophysical Journal, 762, 33

Zschaechner, L. K., Bolatto, A. D., Walter, F., et al. 2018, Astrophysical Journal, 867, 111